α-Arrestin phospho-regulation and control of autophagosome formation

by

Ray Wesley Bowman II

Bachelor of Science, Seton Hill University, 2010

Submitted to the Graduate Faculty of the

Dietrich School of Arts and Sciences in partial fulfillment

of the requirements for the degree of

Doctor of Philosophy

University of Pittsburgh

2022

UNIVERSITY OF PITTSBURGH

DIETRICH SCHOOL OF ARTS AND SCIENCES

This thesis was presented

by

Ray Wesley Bowman II

It was defended on

July 21, 2022

and approved by

Kirill Kiselyov, Ph.D., Associate Professor, Department of Biological Sciences

Karen Arndt, Ph.D., Professor, Department of Biological Sciences

Jeffrey Brodsky, Ph.D., Professor, Department of Biological Sciences

Nava Segev, Ph.D., Professor, Department of Biochemistry and Molecular Genetics

Thesis Advisor/Dissertation Director: Allyson F. O'Donnell, Ph.D., Department of Biological Sciences

α-Arrestin phospho-regulation and control of autophagosome formation

Ray Wesley Bowman II, PhD

University of Pittsburgh, 2022

Cells selectively reorganize their proteome in response to environmental stressors. For membrane proteins, this reshuffling is controlled by selective protein trafficking. Studies in yeast demonstrate that the α-arrestins, a highly conserved family of protein trafficking adapters, are critical players in the selective movement of membrane proteins. In response to cell signaling, α-arrestins are post-translationally modified and bind specific membrane proteins. In doing so, they recruit with them the ubiquitin ligase Rsp5, acting as a bridge between the ligase and the membrane protein. Ubiquitination of the membrane protein promotes sorting into endocytic vesicles. There are many outstanding questions in the field of α-arrestins, and my research focuses on defining a new role for α-arrestins in influencing autophagy and expanding our understanding of α-arrestin phospho-regulation. Autophagy is a highly conserved self-degradative process controlled by the TORC1 signaling complex that is utilized by cells to survive periods of nutrient limitation through the bulk-transport of cellular components to the vacuole for degradation. We employ a targeted genetic screen to uncover a series of mutations that alter α-arrestins' ability to confer resistance to the TORC1-inhibiting drug rapamycin, revealing a complex genetic tie between the α-arrestins and autophagy. We further show that the absence of α-arrestins results in impaired autophagic flux to the vacuole, a defect in the ability of α-arrestin mutants to form autophagy-dedicated membrane-bound vesicles (autophagosomes), as well as an aberrant retention of autophagic machinery to the vacuolar membrane that coincides with defects in the localization of phospholipid species and their

modifying enzymes. Furthermore, phosphorylation of α-arrestins alters their protein trafficking function. We therefore performed a second targeted screen to identify α-arrestin phospho-regulators, finding the TORC1-Sit4-Npr1 signaling network to possess a prominent role in controlling α-arrestin phosphorylation and stability, as well as establishing a novel link between α-arrestin stability and vacuolar degradation. Together, my work forges new connections between the α-arrestins and the maintenance of the vacuolar membrane's composition, the ability of the cell to properly respond to TORC1 inhibition in their absence, as well as the post-translational regulation and stability of the α-arrestins themselves.

Table of Contents

List of Tables

List of Figures

List of Abbreviations

Below is a list of abbreviations used in this dissertation, with common abbreviations (*i.e.*, DNA, pH) omitted.

5-FOA: 5-Fluoroorotic Acid Monohydrate
a.u.: Arbitrary Units
AB: Autophagic Body
AP-1: Adapter Protein Complex 1
AP-2: Adapter Protein Complex 2
AP-3: Adapter Protein Complex 3
AP: Autophagosome
ARRDC: Arrestin Domain-Containing
ART: Arrestin-Related Trafficking adaptor
ATG: Autophagy Related Gene
AzC: Azetidine-2-carboxylic Acid
BODIPY: Boron-Dipyrromethane
CHX: Cycloheximide
CMAC: 7-amino-4-chloromethylcoumarin
COP: Coat Protein Complex
CURE: Course-Based Undergraduate Research Experience
CVT: Cytoplasm-to-Vacuole Targeting
DMSO: Dimethyl Sulfoxide
DUB: DeUbiquitinating enzyme
EM: Electron Microscopy
ER: Endoplasmic Reiticulum
ERAD: ER-Associated Degradation
ESCRT: Endosomal Sorting Complex Required for Transport
GAAC: General Amino Acid Control
GFP: Green Fluorescent Protein
GO: Gene Ontology
GPCR: G-Protein Coupled Receptor
GPI: Glycerophosphoinositol
HOPS: Homotypic Vacuole Fusion and Protein Sorting
kDa: Kilodalton
KinDel: Kinase and Phosphatase Deletion
LD: Lipid Droplet
MCS: Membrane Contact Site
MG: Methylglyoxal
MVB: Multi-Vesicular Body
n.s.: Not Significant
NVJ: Nuclear-Vacuolar Junction
OD: Optical Density
PAS: Phagophore Assembly Site

PCR: Polymerase Chain Reaction
PE: Phosphatidylethanolamine
PI: Phosphoinositides
PI(3,5)P_2: Phosphatidylinositol 3,5 bisphosphate
PI3K: Phosphatidylinositol 3-kinase
PI3P: Phosphatidylinositol 3-phosphate
PMN: Piecemeal Microautophagy of the Nucleus
PP1: Protein Phosphatase 1
UBS: Ubiquitin Binding Site

1.0 Introduction

1.1 Arrestins

1.1.1 Yeast and Protein Trafficking

The unicellular eukaryotic organism *Saccharomyces cerevisiae*, commonly referred to as baker's or brewer's yeast, shares remarkably similar machinery with other eukaryotic cells and has been extensively studied to provide fundamental insights into many aspects of cellular biology, including lipid metabolism, cell signaling, and membrane trafficking [1–3]. Eukaryotic cells synthesize both soluble and membrane-bound proteins, many of which are imported into the endoplasmic reticulum (ER), requiring transport via the endo-membrane system to be trafficked to their appropriate locale [4]. Nobel Prize-winning work from Dr. Randy Schekman (Univ. of California at Berkeley) used the powerful genetic tools available in yeast to perform foundational work in defining the machinery needed for membrane protein trafficking, identifying over 50 *SEC* proteins involved in various stages of the secretory pathway, prominently including those involved in ER-to-Golgi transport [5–7].

To survive ever-changing environmental conditions, cells must carefully control the abundance and distribution of their proteome through a balance of protein synthesis, trafficking, and degradation. Newly synthesized proteins in the ER transit to the Golgi for sorting and subsequent direction to their appropriate destination. While some of these proteins are trafficked directly to the vacuole, others travel to the cell surface for integration with the plasma membrane or excretion into the extra-cellular environment. Plasma membrane proteins can subsequently be

removed through endocytosis and packed into endocytic vesicles, or endosomes, for further sorting and transport, either to the vacuole for degradation or back to the Golgi for recycling and return to the cell surface. Importantly, many of these pathways and their effectors were characterized using the yeast model system and are conserved among higher eukaryotes [8–11].

1.1.2 The arrestin clan

Representing the largest family of signaling proteins in eukaryotes, G-protein coupled receptors (GPCRs) control the cellular response to a variety of stimuli, including extracellular ions like calcium, biological compounds like hormones and pheromones, and even light [12]. Study of the light-sensitive GPCR rhodopsin yielded the first characterization of an arrestin protein, arrestin-1 (Arr1), so named for its ability to inhibit (or 'arrest') rhodopsin signaling [13]. Further work led to identification of another rhodopsin regulator, arrestin-4 (Arr4), as well as two regulators of the GPCR β-adrenergic receptor, arrestin-2 (β-arrestin-1) and arrestin-3 (β-arrestin-2), forming the visual- and β-arrestin sub-groups, respectively [14].

The visual- and β-arrestins have been studied extensively in the regulation of GPCR signaling, as cell signaling scaffolds, and as cargo-selective adaptors in clathrin-mediated endocytosis [15–17]. The arresting, or desensitization, of GPCR signaling is accomplished by the binding of β-arrestins to G proteins following GPCR stimulation and phosphorylation [18–20]. This binding sterically inhibits G-proteins from interacting with their associated GPCR, functionally uncoupling the two and preventing G-protein signal transduction to secondary messengers [21–23]. The β-arrestins further regulate many GPCRs by serving as scaffolds for trafficking factors like clathrin and AP-2 to target these receptors to clathrin-coated pits and induce

their internalization and lysosomal degradation [24–26]. Once removed from the cell surface, GPCRs transit the endocytic pathway, where β-arrestins can further serve to prevent their lysosomal delivery and recycle them back to the plasma membrane [27]. Similarly, these arrestins can participate in inducing the endocytic trafficking of nutrient transporters by mediating the binding of NEDD4-family ubiquitin ligases [28,29].

Along with visual- and β-arrestins, phylogenetic analysis further identified the bacterial Spo0M family, the Vps26 family, and, most notably for my studies, the α-arrestins as members of the arrestin clan [14]. Crystal structure analyses of these family members have identified the presence of conserved N- and C-terminal arrestin-fold domains, each of which contains seven anti-parallel β-sheets. The arrestin-fold domains are connected by variable linker regions, and most arrestins have a C-terminal tail extension of variable length that is an important site of regulation [30–35].

1.1.3 The α-arrestin family

First described in 2008, the previously unrecognized α-arrestins were discovered as part of a phylogenetic analysis of eukaryotes and represent a distinct evolutionary branch of the arrestin family. Gaining their name due to being evolutionary predecessors to the visual and β-arrestins, α-arrestins are highly conserved, with 6 members in humans and 14 in *Saccharomyces cerevisiae*, each possessing paired N- and C-terminal arrestin fold domains (Figure 1A-B) [14]. While β-arrestins possess a characteristic N-terminal helix along with binding sites for clathrin, clathrin-adaptor complexes, and phosphoinositides, the α-arrestins similarly bind both the AP-1 and AP-2 clathrin adapters, and further contain binding regions known as $^{L}/_{P}$PXY motifs that are recognized

by the WW-domains of NEDD4-family ubiquitin ligases (Rsp5 in yeast) (Figure 1A-B) [14,36,37].

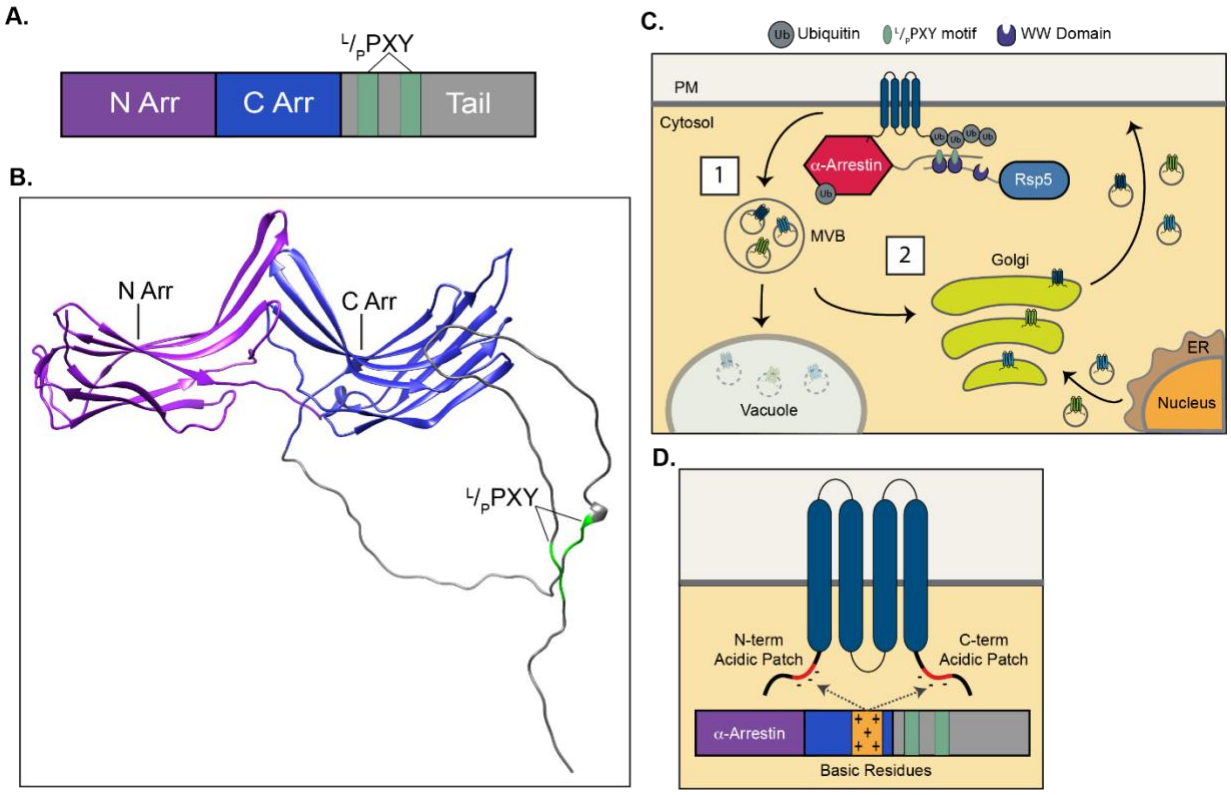

Figure 1. α-Arrestins structure, trafficking functions, and substrate recognition in yeast

(**A**) A basic diagram of α-arrestin structure. α-Arrestins are defined by the presence of N-terminal (purple) and C-terminal (blue) arrestin fold domains, each composed of 7 anti-parallel beta sheets. α-Arrestins further possess L/PPXY domains in the C-terminal tail regions that are used to recruit the ubiquitin ligase Rsp5 through interaction with its WW domains. (**B**) An predictive structural model of the mammalian α-arrestin TXNIP generated using AlphaFold (credit: Mitchell A. Lesko) [38]. Structural features are denoted by colored regions, including the N-terminal arrestin fold (purple), the C-terminal-arrestin fold (blue) and $^{L}/_{P}$PXY motifs (green). (**C**) A model of α-arrestin-mediated trafficking. α-Arrestins bind the ubiquitin ligase Rsp5 and membrane-bound proteins at the cell surface, serving as a bridge between the Ub ligase and the membrane cargo. This recruitment leads to the ubiquitination of both the α-arrestin and its membrane cargo, resulting in the cargo's internalization and packaging into multi-vesicular bodies (MVBs) for transit to the vacuole and their subsequent degradation (1). Alternatively, α-

arrestins can also serve to rescue these cargo proteins from the endocytic pathway, rerouting them to the Golgi to facilitate their return to the cell surface (2) (**D**) α-Arrestins recognize their membrane-bound protein substrates through interactions between acidic patches (red) in the N- or C-terminal cytosolic tails of these cargo with basic residues (orange) found in the α-arrestin's C-terminal arrestin fold domain (blue).

1.1.3.1 Human α-arrestins (ARRDCs)

Humans possess six α-arrestins members: five arrestin domain-containing proteins (ARRDC1-5) and a thioredoxin-interacting protein (TXNIP) [14]. Though the family remains largely understudied, some molecular details of human α-arrestin function have begun to emerge. ARRDC3, for example, mediates the ubiquitination of the endosomal sorting complex required for transport III (ESCRT-III) related apoptosis-linked gene 2 interacting protein (ALIX), and, along with ARRDC4 and TXNIP, can interact with both clathrin and their β-arrestin relatives [39–41]. In perhaps the best described example of α-arrestin-mediated regulation of a nutrient transporter in humans, TXNIP controls the trafficking of glucose transporters, GLUT1 and GLUT4,, inducing their clathrin-mediated endocytosis to regulate glucose import in muscle and fat cells [40,42]. The expression of TXNIP can be modulated by changes in sugar availability, while its endocytic function and stability is controlled by phosphorylation [40,42–44]. Though many molecular details of this trafficking relationship, such as the ubiquitin ligase required for TXNIP's regulation of GLUT1/4, have yet to be identified, the regulation of glucose transporters by this mammalian α-arrestin bears a striking resemblance to what occurs in the control of HXT glucose transporters by yeast α-arrestins Rod1 and Rog3 (discussed further in Section 1.1.3.2.2).

Interestingly, several studies establish links to broader functionality for the α-arrestins. For example, the human α-arrestin ARRDC1 recruits endosomal sorting complex required for transport-0 (ESCRT-0) to the cell surface to control the extracellular release of ARRDC1-mediated

microvesicles (ARMMs) [45,46]. ARRDC1 utilizes this pathway to mediate the release of the divalent metal ion transporter (DMT1) in extracellular vesicles following its ubiquitination by NEDD4-2, potentially as a non-degradative alternative method of protein clearance. ARRDC4 also mediates the NEDD4-2 ubiquitination and extracellular transport of DMT1, but through an ESCRT-independent viral budding pathway that is also important for sperm maturation in mice [47,48]. Human α-arrestins are linked to cancer, with TXNIP playing an important role in tumor suppression through its pro-apoptotic function [49], and ARRDC3 is tied to metastasis suppression and the inhibition of cell proliferation through the regulation of factors important for cancer progression like PAR1 and Itgβ4 [50–53]. Furthermore, ARRDC3 expression is suppressed in invasive basal-like breast carcinomas, resulting in the defective lysosomal degradation and subsequent Hippo-pathway signaling of the metastatic cancer-related GPCR PAR1 [54]. ARRDC3 controls PAR1-Hippo pathway signaling independently of PAR1 trafficking by binding to and preventing the signaling activity of the GPCR-effector and transcriptional co-activating protein TAZ, which plays important roles in triple-negative breast carcinoma [55]. Furthermore, the only human α-arrestin shown to regulate redox state in cells, TXNIP binds to and negatively regulates thioredoxin and is capable of inducing apoptosis following its translocation to the mitochondria to influence the intrinsic mitochondrial pathway [56,57].

1.1.3.2 Yeast α-Arrestins

Studies of yeast α-arrestins provide a more detailed understanding of α-arrestin function and regulation. There are 14 yeast α-arrestins, or arrestin-related trafficking adaptors (ARTs), identified to date: Ldb19/Art1, Ecm21/Art2, Aly2/Art3, Rod1/Art4, Art5, Aly1/Art6, Rog3/Art7, Csr2/Art8, Rim8/Art9, Art10, Bul1, Bul2, Bul3, and Spo23 [34,58–60]. As the ART moniker

suggests, yeast α-arrestins are best-characterized as protein trafficking adaptors, utilizing their $^{L}/_{P}$PXY motifs to bind the WW domains of the NEDD4-family ubiquitin ligase Rsp5 to facilitate the removal of proteins from the cell surface following ligand/substrate binding or exposure to stressors, like heat or nutrient starvation (Figure 1A-B) [37,61–64].

Like their human orthologs, yeast α-arrestins localize primarily to the cytosol, Golgi, and plasma membrane [65–68]. Additionally, nuclear localization has been described for multiple α-arrestins, with Csr2 acting in the transcriptional repression of genes that regulate carbon source metabolism, and Bul1/Bul2 acting in the response to DNA damage [69–72]. While relatively little is known about the transcriptional control of yeast α-arrestins themselves, activation of the general amino acid control (GAAC) pathway activates the Gcn4 transcription factor, which in turn induces expression of *ECM21* [73]. This transcriptional control of *ECM21* has further effects on protein trafficking, as this α-arrestin is now available to induce the trafficking of multiple amino acid transporters [73]. Expression of α-arrestin *CSR2* is controlled by the transcriptional repressors Mig1 and Mig2, which are deactivated during glucose starvation when they become phosphorylated by Snf1 [74]. Expression of *CSR2* under these conditions then allows it to regulate the trafficking of hexose transporters and other sugar transporters [74,75].

1.1.3.2.1 α-Arrestin function in endocytosis:

The best described function of yeast α-arrestins is their ability to selectively bind transmembrane proteins (referred to as cargo) in response to cell signaling cues. Once bound to cargo, α-arrestins recruit Rsp5, linking this ligase to the membrane protein and stimulating the poly-ubiquitination of cargo (Figure 1D). Ubiquitination is a signal for cargo internalization, and α-arrestin-bound membrane proteins are internalized by clathrin-mediated endocytosis. Rsp5

ubiquitinates both the membrane protein and the α-arrestin (discussed further in Section 1.1.3.2.3) and mono-ubiquitination of α-arrestins is thought to be activating for their endocytic function [58,74,76–78]. α-Arrestins can also participate in clathrin-independent endocytosis (CIE). For example, Aly1, Aly2, and Art1 promote the CIE of the yeast **a**-factor receptor Ste3, independent of their interaction with Rsp5 [79]. Furthermore, Aly1, Aly2, Art1, Art5, Rod1, and Rog3 all directly interact with the Rho1 GTPase, which is a critical activator of CIE by driving formin-directed actin polymerization at sites of CIE [67,79–82]. While broadly focused mass spectroscopy efforts suggest the α-arrestins likely impact the trafficking of many membrane-bound proteins, a systematic identification of α-arrestin cargo has yet to be performed [83–86]. Instead, independent studies have identified the endocytic control of at least 28 membrane-bound proteins, many of which area nutrient or carbon source transporters [58,59,62,66,67,73,74,77,79,87–97]. Several α-arrestins also have roles in the recycling of membrane proteins, promoting post-endocytic trafficking of cargo from endosomes back to the Golgi to ultimately increase the abundance of membrane proteins at the cell surface, rescuing them from vacuolar degradation. Examples of such function include role of Aly1/Aly2 and Bul1/Bul2 in controlling the endocytic rescue of the general amino acid permease Gap1 and the arginine permease Can1, respectively. Rod1 similarly controls the intracellular sorting of the monocarboxylate transporter Jen1 [67,98].

α-Arrestin-mediated endocytosis of cargo proteins is induced following the selective binding of the α-arrestin and recruitment of Rsp5. α-Arrestin-cargo selectivity is likely achieved by conformational changes to the cargo proteins that reveal patches of acidic residues in their cytosolic tails that are recognized by the α-arrestin (Figure 1D) [98–102]. For example, substrate transport reveals an acidic patch in the cytosolic N-terminal tail of the high affinity methionine permease Mup1 that recruits Art1, though modification of this region in Mup1 is not sufficient for

degradation as a C-terminal region has also been implicated in this regulation [99,102]. Similarly, arginine transport reveals an N-terminal acidic patch in the cytosolic tail of the arginine transporter, Can1, that is recognized by Art1 to induce internalization [98–102]. Acidic patches have been identified as required for α-arrestin dependent endocytosis of Mup1 and Can1, the arsenite and antimonite transporter, Acr3, and the monocarboxylate transporter Jen1 by α-arrestins Ecm21, Art1, Aly2, and Rod1, respectively [73,96,103]. Furthermore, the specificity of these regions has been validated through the transposition of these degrons to alternate transporters (*e.g.*, the fusion of a 20-amino acid region of Jen1's C-terminal tail to Mup1, which is normally trafficked in response to excess methionine, is sufficient to induce aberrant Rod1-mediated endocytosis of Mup1 following glucose addition) [103]. Together, these studies demonstrate the emergence of a unifying theme for the recruitment of α-arrestins to their membrane-bound substrates driven by the unveiling of degrons and/or the presence of acidic residues in the cytosolic tails of α-arrestin's cargo.

1.1.3.2.2 α-Arrestin phospho-regulation

Cell signaling proteins control the post-translational modification of α-arrestins, enabling regulation of α-arrestin functions. Proteomic analyses have revealed many phosphorylated and ubiquitinated residues in all members of the yeast α-arrestin family (Figure 2) [68,84,86,104–134]. A central player in nutrient-dependent cell signaling is the Target of Rapamycin Complex 1 (TORC1). This prominent signaling kinase complex responds to changes in nutrients, including nitrogen, amino acids, glucose or cholesterol abundance, to control cell growth by regulating transcription, translation, ribosome biogenesis, nutrient transport, and autophagy [135]. It is therefore not surprising that TORC1 regulates α-arrestin-mediated trafficking of nutrient

permeases, including the substrate-induced endocytosis of Can1, Mup1, the lysine permease Lyp1, the uracil permease Fur4, and the high affinity tryptophan and tyrosine permease Tat2 [66,136,137].

One downstream branch of TORC1 controlling nutrient transport localization involves the nitrogen permease reactivator kinase (Npr1), which regulates the activity of cell surface amino acid transporters and exerts some of its influence through targeting of select α-arrestins. Amino acid influx activates TORC1, which, in turn, represses the activity of Npr1. Art1 is subsequently activated by Ppz1/2-mediated dephosphorylation at its Npr1-dependent phospho-sites, which promotes Art1 binding to its membrane-bound substrates [129]. Conversely, when TORC1 activity is repressed, activated Npr1 phosphorylates Art1, preventing its recruitment to plasma membrane proteins [66]. Npr1-dependent phosphorylation of α-arrestin Ecm21 similarly induces the Ecm21-dependent internalization of Fur4 and Tat2 [66,67,98,101]. The full details of Npr1-dependent phospho-regulation of α-arrestin-mediated trafficking remains unclear, however, as another study demonstrates the retention of the Can1 in *npr1*Δ cells treated with rapamycin [64]. This suggests that there may be Npr1-driven activation of Ecm21, as this α-arrestin controls the trafficking of Can1 in nitrogen starved cells, a condition that also inhibits TORC1 [73].

Another downstream effector of TORC1, the Sit4 protein phosphatase is a regulator of Npr1 kinases function and controls α-arrestins. Sit4 antagonizes Npr1-driven phosphorylation of Bul1 and Bul2, two paralogous α-arrestins that control the internalization of Gap1. Additionally, the substrate-induced internalization of the thiamine transporter Thi7 is controlled by Ecm21 and stimulated by Sit4, in a process that is thought to be independent of Npr1 [93]. Dephosphorylation of Buls is also induced by Sit4, releasing them from the inhibitory binding to 14-3-3 proteins Bmh1 and Bmh2 [77]. In Chapter 3, we find that the α-arrestins Aly1 and Aly2 are also regulated by Sit4

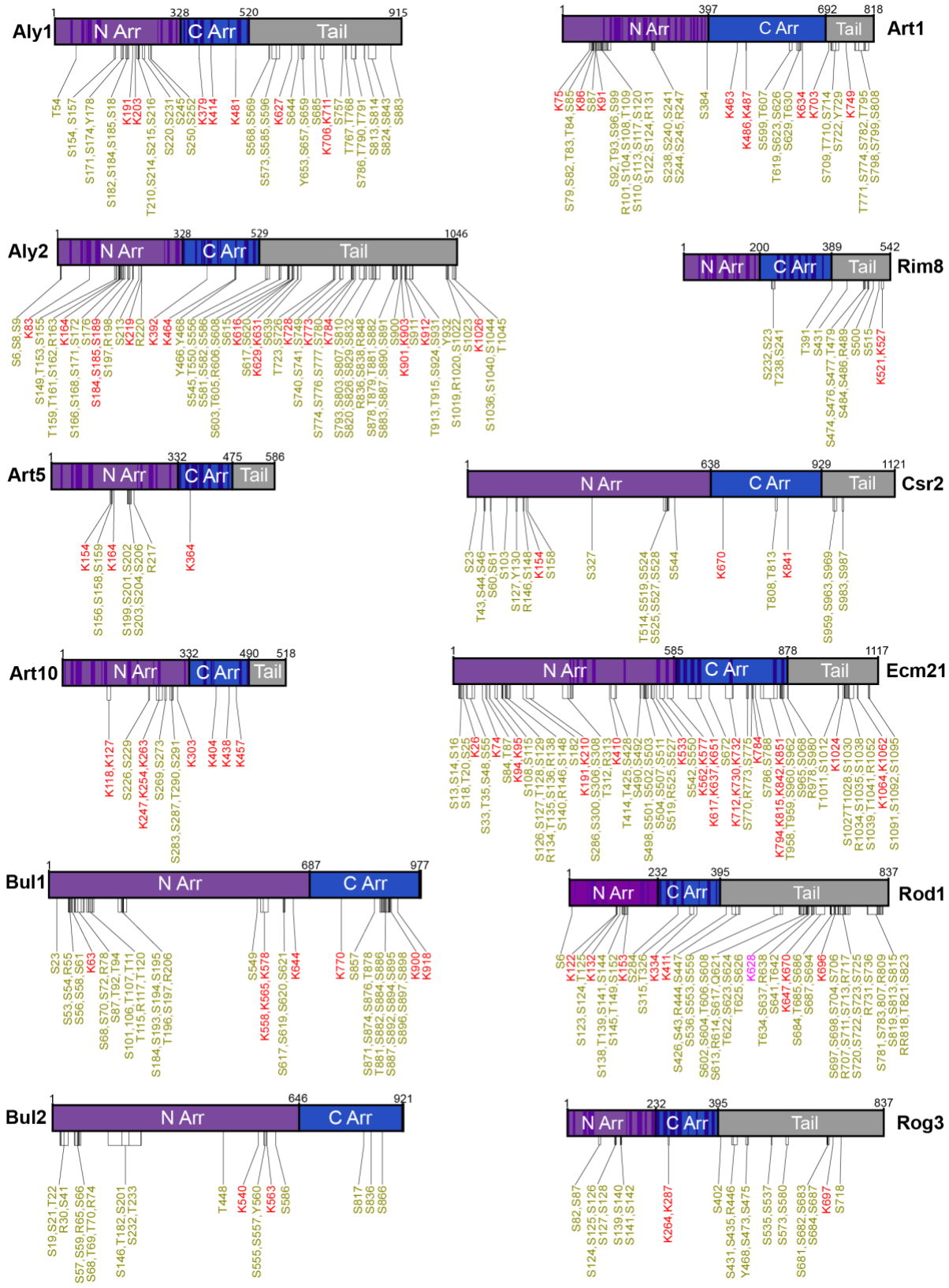

Figure 2. α-Arrestins are post-translationally modified by phosphorylation and ubiquitination

Depiction of α-arrestin structure and post-translational modification by residue. For each α-arrestin, the boundaries of the N-terminal arrestin fold (purple), C-terminal (blue) arrestin fold, and C-terminal tail (grey) are annotated with residue numbers (top). Predicted locations of beta-sheets within each arrestin fold domain are shown in either dark purple (N-term) or dark blue (C-term). Residues shown by mass spectroscopy to be either phosphorylated (green) or ubiquitinated (red) are indicated below each diagram. Mass spectroscopy data compiled from [68,84,86,104–134].

and Npr1, as in the absence of Sit4, Aly1 and Aly2 are hyper-phosphorylated and degraded in an Npr1-dependent manner. This effect leads to the PM stabilization of their membrane cargo Git1, which is a transporter that mediates the uptake of glycerophosphoinositol and glycerophosphocholine (described further in Chapter 2) [138].

α-Arrestins are not only regulated by TORC1 but are controlled by many other kinases and phosphatases. For example, the AMPK/Snf1 kinase, an energy and nutrient-level sensor, phosphorylates Rod1, Rog3, and Csr2 *in vivo*, and additionally Aly2 and Bul2 *in vitro* [133,139]. Snf1 phosphorylation of α-arrestins impedes α-arrestin-mediated endocytosis of nutrient transporters. Specifically, Snf1 phosphorylation of Rod1, Rog3 and Bul1 impedes their ability to endocytose Jen1 and hexose transporters, Hxt1, Hxt3, and Hxk6, respectively [59,76,89,90,140,141]. Further, like the TORC1 regulation of Buls, Snf1 phosphorylation of Rod1 stimulates Rod1 binding to 14-3-3 proteins Bmh1/2, and this prevents Rod1-Rsp5 complex formation, which is needed for endoyctosis [76]. Aside from the control of carbon-source transporters, Snf1 phosphorylation of Rod1 leads to stabilization of Ste2 by impeding Rod1-mediated endocytosis of Ste2, a mechanism that is antagonized by the activity of the calcium-dependent phosphatase calcineurin [62,142].

1.1.3.2.3 α-Arrestin ubiquitin-regulation

In addition to their complex phospho-regulation, nearly all α-arrestins are ubiquitinated (Figure 2) [85,132,143–148]. While α-arrestin phosphorylation appears to be largely inhibitory, their mono-ubiquitination stimulates α-arrestin-mediated endocytosis and appears to be antagonized by phosphorylation. For example, Rod1 is inhibited by Snf1-dependent phosphorylation subsequent 14-3-3 protein binding but is rapidly dephosphorylated by the protein phosphatase 1 (PP1) complex following glucose stimulation. Once freed from its phospho-inhibition, Rod1 is able to be mono-ubiquitinated by Rsp5 and stimulate the endocytic trafficking of Jen1 [76]. Similarly, Snf1-regulation of Csr2-driven endocytosis of Hxt transporters is coupled to Crs2 deubiquitination by the deubiquitinating enzyme (DUB) Ubp2, a mechanism proposed to control the length of Csr2's ubiquitin chains and maintaining it in a mono-ubiquitinated state [74,143]. Rsp5 also ubiquitinates Bul1 and Bul2 following their dephosphorylation to promote their control of Gap1 [77]. Ubiquitination and dephosphorylation are not always linked, however, as ubiquitination of Aly1, Aly2, Bul1, Bul2, and Art1 each occur independently of changes in phospho-status [58,65,66,129,149].

In one example relevant to my work, Aly1 and Aly2 were shown to be mono-ubiquitinated within their C-terminal arrestin-fold domains at a conserved lysine, K379 and K392, respectively (Figure 2) [86,150,151]. Mutation of this residue in its cognate α-arrestin is sufficient to block mono-ubiquitination. Similarly, the mono-ubiquitination of Art1 at K486 within its C-terminal arrestin-fold domain is critical for its ability to mediate trafficking of Can1, and its recruitment to the Golgi and cell surface (Figure 2) [58,76,152]. Underscoring the importance of mono-ubiquitination at these conserved residues in the C-terminal arrestin-fold domain, mutants of Aly1 or Aly2 where these key lysine residues were changed to arginine did not produce detectable

ubiquitin signal when grown under normal conditions. The same lack of ubiquitination, as well as a loss of function and an increase in stability, occurs in mutants lacking the Rsp5-binding $^{L}/_{P}$PxY motifs (see Section 1.1.3.2), implicating Rsp5 in their mono-ubiquitination [67,152]. Loss of ubiquitination does, however, impact their function, as evidenced by changes in sensitivity to TORC1 inhibition (discussed further in Chapter 2), or their ability to traffic ectopically expressed human potassium transporter Kir2.1[152]. Confoundingly, ubiquitin regulation of the α-arrestins does not appear to be a consistent requirement for activation of their trafficking activity, as Rod1 does not require its mono-ubiquitination site when trafficking glucose transporters in response to 2-deoxyglucose (2DG), nor is ubiquitination required for Art1's control of the GPCR Ste2 in response to pheromone signaling [62,90].

One possible mechanism by which mono-ubiquitination governs α-arrestin function is tied to the ubiquitin-binding capacity of Rsp5 itself. This model suggests that the mono-ubiquitination of Art1 and Rim8 helps to increase the binding of these α-arrestins to the ubiquitin-binding surface (UBS) domain of Rsp5, "locking" the proteins together and promoting an increase in their cooperative endocytic functions [153]. Similarly, these mono-ubiquitination sites can serve as recognition motifs for other protein-protein interactions. For example, Rim8 is mono-ubiquitinated in a Rsp5-dependent manner at K521 within its C-terminal tail (Figure 2). Loss of this modification reduces Rim8 binding to ESCRT-I subunits, Vps23 and Vps28, which in turn impairs the recruitment of the membrane-bound pH sensor Rim21[70,154]. While K521 does not lie within Rim8's predicted C-terminal arrestin-fold domain, it represents (along with closely neighboring K527) the only ubiquitinated residues, and at minimum demonstrates the potential for α-arrestin ubiquitination to control α-arrestin interactions with other proteins beyond the ubiquitination/deubiquitination machinery (Figure 2).

Multiple studies have identified functional roles linked to post-translational modification of α-arrestins, including mono-ubiquitination, yet a coherent model applicable to the entire family remains elusive. The most widely applicable model is that phosphorylation of α-arrestins is inhibitory and can be antagonized by mono-ubiquitination [59,66,74,76,77,140]. Mono-ubiquitination often occurs in a conserved region between two of the beta-strands that help form the C-terminal arrestin-fold domain (Figure 2). The exact functional implications of mono-ubiquitination, however, are not clear for each α-arrestin family member. Even for those α-arrestins whose mono-ubiquitination has been characterized, nuances remain. For example, stressors like rapamycin, heat shock, oxidative stress, and alcohol stress stimulate Gap1 internalization by Bul1/Bul2, yet they likely remain un-ubiquitinated in these conditions [27]. The dichotomy of functional outcomes for the mono-ubiquitination of the Aly1/Aly2 pair, as described above, further illustrates the complexity of α-arrestin regulation and function and underscores the work remaining to complete our understanding.

While mono-ubiquitination is a modifier of α-arrestin trafficking function, poly-ubiquitination instead regulates the abundance and stability of this adapter family. α-Arrestins characteristically control the delivery of their cargo to the vacuole for degradation, yet their own stability is closely tied to the 26S proteasome [143,154–156]. Csr2 is barely detectable until its transcription is released from repression, as occurs when cells transition from glucose (preferred) to lactate (nonpreferred) media. The abundance of Csr2 quickly declines again, however, when returned to media containing glucose, indicating a high rate of turnover [74]. Csr2 levels under these conditions are stabilized when cells are treated with the drug MG-132, a proteasomal inhibitor, implicating proteasomal degradation as the driver of that turnover. Notably, down-regulation of Csr2 does not require catalytically active Rsp5, nor the ability of Csr2 to bind Rsp5,

suggesting that an as-yet unidentified ubiquitin ligase governs the stability of at least this α-arrestin [74]. Other members of the α-arrestins, however, are directly tied to Rsp5-dependent K63-linked poly-ubiquitination, including Rod1, Art1, Ecm21, and Art10 [156]. Importantly, these modifications occur at residues separate from their sites of mono-ubiquitination, located within the α-arrestin's N- or C-terminal tail. The poly- and mono-ubiquitination sites are structurally distinct, eliciting different outcomes [156].

Though the direct binding of ubiquitin by the UBS domain of Rsp5 may help to prevent further ubiquitin chain linkage, the prolonged proximity of α-arrestins to a highly active ubiquitin ligase like Rsp5 likely requires antagonistic activity by DUBs to prevent constitutive degradation [153]. For example, a dramatic increase in K63-linked poly-ubiquitination occurs in α-arrestins Ecm21 and Csr2 in the absence of the DUB Ubp2, which directly binds Rsp5 [155]. Furthermore, Ubp2, as well as Ubp15, are directly tied to the stability of many α-arrestins [156]. Cells lacking these two DUBs have reduced levels of Aly1, Art10, Bul1, Csr2, Ecm21, Art1, Rod1, and Rog3 [74,143,155,156]. Interestingly, the instability of Art1 and Rod1 in the absence of Ubp2 and Ubp15 is reversed by the additional loss of DUBs Doa4 and, to a lesser extent, Ubp3 [156]. Ubp3 is not known to bind to or have activity towards α-arrestin, however it can bind directly to Rsp5 and regulates proteasomal degradation of proteins following heat stress [157]. Furthermore, while it has been suggested the Doa4 phenotype may be due to reduced free unconjugated ubiquitin pools direct activity of this DUB against Art1 has been demonstrated [158–160]. As with other facets of ubiquitin regulation for a-arrestins, additional study of DUB control of these proteins is required. Suggestive of additional functions, cells lacking both *ubp2*Δ *ubp15*Δ did not significantly destabilize Aly2 or Rim8, despite increasing the ubiquitination of at least Aly2. This finding

supports the idea that yet-unidentified ubiquitin-ligase or DUB machinery controls α-arrestin stability [156].

Providing appropriate specificity to protein trafficking events requires tight regulation of the α-arrestin adapters, both in terms of trafficking activity and overall protein abundance. The stability of α-arrestins appears to fall within the well-studied purview of the 26S proteasome. Proteasome-mediated degradation is signaled by addition of K63-linked polyubiquitin chains which are added to lysine residues. Multiple DUBs antagonize this modification, likely preventing both the constitutive degradation of the α-arrestin and over-consumption of available ubiquitin molecules. Further study of the signaling inputs and environmental cues capable of inducing changes in α-arrestin stability are needed to fully appreciate how α-arrestins are controlled. Indeed, my work and that of other members of the O'Donnell lab have implicated a novel role for the vacuole in the destabilization of Aly1 and Aly2, which is linked to their regulation by the Sit4 and Npr1 phosphatase and kinase, respectively (discussed further in Chapter 3) [138].

1.2 Autophagy

"Autophagy", derived from the Greek words for self (auto) and eating (phagy), is a self-degradative process conserved from yeast to humans and plants that is used by cells to survive periods of nutrient starvation [161,162]. Autophagy was first observed in mammals nearly 60 years ago by Christian De Duve as a system for the lysosomal degradation of cytosolic components and organelles, yet the molecular details of this process remained undefined for decades after [163,164]. Nobel Prize winning work from Yoshinori Ohsumi first identified autophagy in the

yeast model system and, utilizing the power of yeast genetics, he and others became the first to identify and characterize many of the genes required by the autophagic program [165–171].

Under basal conditions, the autophagy pathway utilizes cargo receptors to traffic immature forms of proteases to the vacuole for maturation as part of the selective cytoplasm-to-vacuole targeting (CVT) pathway [165,172–180]. Selective forms of autophagy are also utilized in the turnover of organelles, including mitochondria (mitophagy), peroxisomes (pexophagy), ribosomes (ribophagy), the ER (reticulophagy/ER-phagy), and the nucleus (nucleophagy) [181–188]. Bulk non-selective autophagy, or macro-autophagy, occurs primarily in response to restricted availability of nutrients like carbon and, more notably, nitrogen [189–193]. Macro-autophagy is also induced by a broad range of other stress conditions, including cholesterol limitation, oxidative stress, hypoxia, DNA damage, pathogen infection, and hormonal stimulation [194–199]. Macro-autophagy is supported by a broad group of gene products, including a dedicated subset of machinery organized into the autophagy-related gene family (ATG), which cooperate to accomplish the bulk transport of cytoplasmic cargo [166,200–202].

1.2.1 Mechanisms of macro-autophagy

Yeast macro-autophagy can be roughly broken down into 5 stages: 1) Initiation, 2) Phagophore nucleation, 3) Phagophore expansion, 4) Phagophore closure, and 5) Autophagosome fusion. In nutrient replete conditions, autophagy is inactivated by phosphorylation of Atg13 by the Target of Rapamycin Complex 1 (TORC1) (Figure 3). This inhibition is released when TORC1 is inactivated by nutrient restriction or direct inhibition by the drug rapamycin (discussed further in section 1.2.2) [203–205]. Dephosphorylation of Atg13 by protein phosphatases 2A and

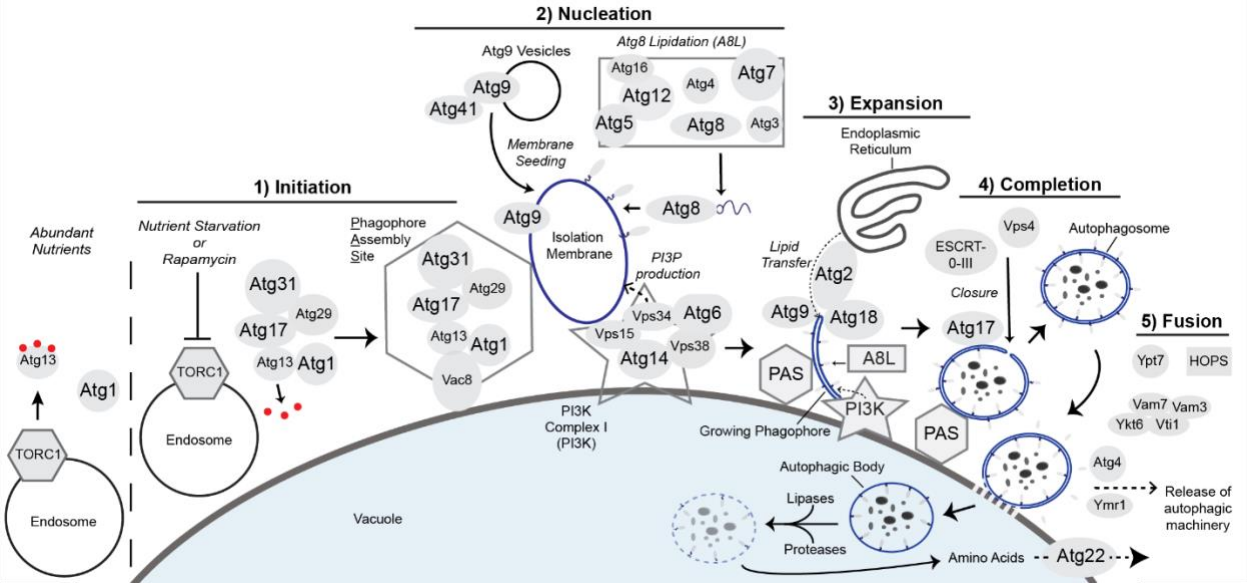

Figure 3. Mechanisms of autophagy in yeast

A simplified diagram of the machinery involved in macroautophagy divided into 5 stages: 1) Initiation, 2) Nucleation, 3) Expansion, 4) Completion, and 5) Fusion. In short, under abundant nutrient conditions, the endosomal population of the TORC1 signaling complex inhibits autophagy through phosphorylation of Atg13 (red circles). Once endosomal TORC1 is inhibited, either by nutrient starvation or treatment with the drug rapamycin, Atg13 is dephosphorylated, allowing for Atg1 activation and the recruitment of other autophagic machinery to form the PAS and initiate macroautophagy (1). Vesicles containing Atg9 are then recruited to the PAS, providing the seed for isolation membrane formation. The autophagy-specific PI3K is also recruited to the PAS, along with machinery to conjugate Atg8 to PE for incorporation into the isolation membrane (2). PI3K activity at the PAS produces PI3P on the isolation membrane, recruiting the Atg18-Atg2 complex. Atg2, bound to Atg9, tethers the tip of the growing phagophore to the ER and facilitates ER-to-phagophore lipid transfer which, along with Atg8 lipidation, drives phagophore expansion (3). Once fully expanded to encapsulate its cytosolic cargo, the phagophore is sealed through activity of Atg17, Vps4, and the ESCRT machinery to form a completed AP (4). The autophagic machinery is then released and Atg8 is cleaved from its PE anchor on the outer autophagic membrane. APs then fuse to the vacuolar membrane through the action of Rab GTPase Ypt7, the HOPS tethering complex, and various SNARE proteins, delivering the inner-membrane-bound autophagic body to the vacuolar lumen (5). There, vacuolar lipases and proteases degrade the autophagic body and its contents, producing free amino acids that are effluxed to the cytosol via Atg22.

2C allows it to interact with Atg1, Atg17, Atg31, and Atg29 to form the Atg1 complex and inducing Atg1 kinase activity to begin the initiation stage [203,206–208]. The Atg1 complex is then tethered to the vacuole membrane by Vac8 to form the phagophore assembly site (PAS) [209,210].

Once active, Atg1 phosphorylates and activates Atg9, the lone transmembrane protein in the core autophagy machinery, recruiting it to the PAS [130]. Atg9 cycles between the Golgi and endosomes, normally residing in cytoplasmic vesicles or membrane-bound reservoirs maintained through the activity of Atg23 and Atg27 [211–219]. Atg9-containing vesicles recruited to the PAS are thought to seed the initial formation of the phagophore's isolation membrane, though COPII-coated vesicles have also been implicated in contributing to the nucleation of the phagophore's isolation membrane [211,220–222]. Next, the autophagy-specific phosphatidylinositol-3 kinase complex I (PI3K-I), composed of the catalytic subunit Vps34, Vps15, Vps30/Atg6, Atg14, and Atg38, is recruited to the PAS [223–225]. Once recruited, PI3K-I produces phosphatidylinositol-3-phosphate (PI3P) on the phagophore's isolation membrane, thereby aiding in the recruitment of additional autophagic machinery [226–229]. Atg21 binds PI3P on the phagophore's isolation membrane to promote the recruitment and organization of the ubiquitin-like proteins Atg12 and Atg8 [230,231]. Atg12 is conjugated to Atg5 by the E1 enzyme Atg7 and the E2 enzyme Atg10, then binds to Atg16, forming the Atg12-5-16 complex, Atg17 and Atg21 at the PAS [232–235]. Atg8, following C-terminal cleavage by Atg4, is conjugated to phosphatidylethanolamine (PE) on the isolation membrane by Atg7, the E2 enzyme Atg3, and the E3 enzyme Atg16 as autophagosome (AP) formation transitions from nucleation to phagophore expansion [169,236–240]. Atg8-PE is distributed across both faces of the isolation membrane, and its abundance is a key factor in regulating the size of APs [241].

For the phagophore's isolation membrane to expand and encapsulate its cytosolic cargo, it requires membrane lipids, which are supplied in part by the Atg2-Atg18 lipid transfer complex. The Atg2-Atg18 complex is recruited to the PAS by Atg18 binding to PI3P and through Atg2's interaction with Atg9 [242–244]. Atg2 tethers the edge of the isolation membrane to the ER, likely at ER exit sites, and facilitates the transfer of lipids from the ER into the growing phagophore to promote phagophore expansion [244–249]. This process is thought to be supported by *de novo* fatty acid synthesis by the acyl-CoA synthetase Faa1 at ER-phagophore contacts to support phospholipid synthesis in the ER and their integration into growing phagophores [250]. Contribution of lipids to the expanding isolation membrane has also been attributed to other sources, like COPII vesicles, which are formed at ER exit sites and facilitate the transfer of transmembrane proteins from the ER to isolation membrane [5,222,248,249]. While other membrane sources have been implicated, their specific roles, especially in yeast, remain elusive. For example, the loss of vacuolar anchoring for the PAS results in reduced AP size in yeast, though the direct contribution of the vacuolar membrane to isolation membranes has not been demonstrated [210]. Similarly, lipid droplets are essential to produce APs, yet it remains unclear whether they represent a lipid source for isolation membranes themselves or are instead connected to regulation of lipids in the ER [251,252]. Further potential membrane sources have been implicated in mammals, with physical contacts identified between the growing phagophore and mitochondria, the Golgi, late endosomes, and lysosome, each of which require further characterization to uncover their true roles [253].

Once fully expanded, the phagophore's isolation membrane requires closure to form a completed autophagosome. Phagophore closure is thought to require membrane scission and the activity of the RAB5-related Vps21, Atg17, and the endosomal sorting complex required for

transport (ESCRT) complexes, though further study of this stage is still required as the ATPase ESCRT subunit Vps4 is not required for the accumulation of ABs in the vacuole [254–257]. Once sealed, completed APs must release the autophagic machinery present on the outer membrane before fusion to the vacuole can be accomplished. Atg8 is cleaved from its PE lipid anchor by the protease Atg4 and then is released back to the cytosol [258–260]. Additionally, PI3P must be removed from the autophagosomal membrane by the PI3P-specific hydrolase Ymr1, as well as the redundant phosphoinositide phosphatases Sjl2 and Sjl3 [228,261]. This step is thought to promote the release of PI3P-binding autophagic machinery, as hyper-activity of the PI3K Vps34 is linked to retention of these components on APs and delays AP fusion to the vacuole, while loss of the PI3P phosphatases leads to accumulation of APs in the cytosol [228,261,262].

Once sealed, the outer membrane of APs fuses with the vacuolar membrane to deliver the inner membrane-bound cargo to the vacuolar lumen as an autophagic body (AB). Fusion of APs to the vacuole requires similar machinery to that needed for endosomal fusion to the vacuole, including the RAB7-like GTPase Ypt7 and its guanine nucleotide exchange factors (GEF) Mon1-Ccz1, the homotypic vacuole fusion and protein sorting (HOPS) tethering complex, and multiple soluble NSF attachment protein receptors (SNAREs) [263–271]. Additionally, Atg17 binding to the SNARE Vam7 is required to promote efficient AP fusion, suggesting this member of the Atg1 complex plays an important role in fusion [272]. Once in the vacuolar lumen, ABs are degraded by vacuolar proteases like proteinase A (Pep4) and proteinase B (Prb1), and lipases like Atg15 [171,273–275]. Degraded autophagic cargo produces free amino acids, which can be returned to the cytosol via transport by the vacuolar membrane transporter Atg22, possibly aided by fellow transporters Avt3 and Avt4 [276–279]. These form the building blocks to help maintain essential processes during starvation conditions.

1.2.2 Macro-autophagy linked to TORC1 regulation

Key to my work in defining a new role for α-arrestins in autophagy, both the family of trafficking adapters and the bulk degradative program are controlled downstream of the TORC1 master signaling complex. TORC1 promotes growth in the presence of rich nutrient supply, and inhibits catabolic processes [135]. TOR regulation was first linked to autophagy using the direct TORC1 inhibiting drug rapamycin, which is sufficient to induce autophagy in the absence of nutrient starvation [171,280]. Under nutrient-replete conditions, TORC1 is active and directly phosphorylates Atg13, preventing the formation and activation of the Atg1 complex and thereby inhibiting macro-autophagy (Figure 3) [205,281,282]. However, when nutrients become limiting, or when TOR is directly inhibited by rapamycin, Atg13 is rapidly dephosphorylated in a manner dependent on two forms of protein phosphatase 2A (PP2A), releasing it from inhibition and inducing the autophagy program [203,205]. Furthermore, the nutrient permease reactivator kinase, Npr1, a downstream effector of TORC1, was recently linked to the regulation of autophagy through its modification of Atg9, though the mechanistic details of this regulation are yet to be described [104].

During periods of nutrient starvation, both autophagy and endocytosis deliver cellular components to the vacuole to be broken down and generate new building blocks to support essential processes [283,284]. In fact, there is a direct link between the endocytosis of cell surface nutrient transporters and autophagy; During the initial stages of starvation, the delivery of endocytosed cargos to the vacuole is required to ensure proper autophagic activation and survival in starvation [285]. As discussed in Section 1.1.3.2.1, the α-arrestins are best characterized as facilitating the endocytic turnover of plasma membrane transporters and are themselves substrates

of TORC1 regulation. Furthermore, the growth inhibition resulting from treatment with the autophagy-inducing drug rapamycin can be overcome by over-expression of select α-arrestins [68]. Despite the functional and regulatory overlap between the α-arrestins and autophagy, a direct connection between the two is only loosely established in the rice fungus *Magnaporthe oryzae,* where α-arrestin ARRDC1 was found to affect pathogenicity and co-localize with the autophagy protein Atg8, prior to the work I and others from the O'Donnell lab performed, as described in Chapter 2 [286].

2.0 α-Arrestins maintain phospholipid balance and Atg18 distribution to permit efficient autophagy

The contents of this chapter are adapted from an article submitted to the journal *PLOS Genetics (Ray W. Bowman II, Sydnie Davis, Eric M. Jordahl, Karandeep Chera, Nejla Ozbaki-Yagan, Jonathan Franks, Sarah Hawbaker, Annette Chiang, Omer Acar, Donna Beer-Stoltz, and Allyson F. O'Donnell)*. RWB completed Figures 4A-D, 5A, 5C-D, 6B-C, 8-10, 11A-B, 12, 13C-D, 14, 15B, 15C-E, 16A, 16C, 17, 18B-D, 19-20, and 21C. Further contributions to figures include:

- Sydnie Davis:5B-C, 6A-C, 7, 15A, 18A
- Eric Jordahl: 15C, 16B
- Karandeep Chera: 7
- Nejla Ozbaki-Yagan:11C, strain preparation for 12A, 14A, 19A,
- Jonathan Franks and Donna Beer-Stoltz: Sample preparation for 8A, 9
- Sarah Hawbaker:5C, 6B
- Annette Chiang:13A-B, 21A
- Omer Acar: 4E
- Allyson F. O'Donnell: 21B

2.1 Introduction

In order to properly grow and thrive, cells employ nuanced systems by which they control nutrient balance. Under rich nutrient conditions, the Target of Rapamycin Complex 1 (TORC1),

defined by the presence of the catalytic kinase subunit Tor1, heavily influences the catabolic processes that facilitate cell growth and division [135]. While macromolecule biosynthesis represents one major branch of TORC1's influence, another is represented by its role as a negative regulator for degradative pathways including autophagy and the endocytic turnover of nutrient transporters [137,138,205,281,287–290]. Nutrient starvation results in TORC1 inactivation, subsequently releasing its inhibitory effect on autophagy, a highly conserved pathway whose most prominent role lies in its ability to employ a dedicated set of proteins from the autophagy-related (ATG) gene family to encapsulate portions of the cytosol for transport to the vacuole/lysosome in double-layered membrane-bound structures called autophagosomes (APs) [200,291,292]. Under these same conditions, the loss of TORC1 activity further stimulates the internalization and vacuolar degradation of many membrane-bound proteins, like nutrient transporters, providing a temporary pool of molecular building blocks that are essential to cell survival prior to full activation of autophagy [283–285].

The endocytic trafficking of cell surface transporters and permeases is largely controlled by a conserved family of selective protein trafficking adapters called the α-arrestins [58,59,76,77]. Phospho-inhibition of these proteins, regulated by kinases and phosphatases like TORC1 and its downstream effectors Npr1 and Sit4, is released during periods of nutrient limitation or when TORC1 is directly inactivated by treatment with the drug rapamycin [77,93,94,138]. Activated α-arrestins are thus able to mediate the endocytosis and degradation of a wide range of membrane-bound proteins, including amino acid transporters and permeases [66,67,76,77,90,129,293,294]. These trafficking adapters are specific, recognizing discreete membrane cargo, and this specificity is accomplished via recognition of acidic patches of amino acids in the cytosolic tails of their intended cargo [73,96,98,101,103]. There, the α-arrestins induce the endocytic trafficking of these

cargo through the recruitment of Rsp5, a Nedd4-family E3 ubiquitin ligase [58,62,68,76,85,92]. In turn, Rsp5 serves to ubiquitinate both the membrane-bound cargo protein, helping to further recruit components of the endocytic machinery that recognize ubiquitin, and the α-arrestin itself [58,74,76–78,295–298]. Thus, α-arrestin-mediated trafficking helps reorganize the cell-surface proteome that is required for the adaptation of cells to changes in nutrient availability.

Given their relatively recent discovery, there remain significant gaps in our understanding of α-arrestin function [14,59]. I therefore endeavored to further define α-arrestin starvation-induced regulation through targeted genetic screening of a ubiquitin-related gene deletion library, which included gene deletions for those lacking autophagy-specific ubiquitin-like modifiers, in the presence of the TORC1-inhibiting drug rapamycin [169,237]. The O'Donnell lab previously demonstrated that the over-expression of either of the paralogous α-arrestins Aly1 or Aly2 confers resistance to rapamycin-induced growth inhibition, possibly by influencing the activity of TORC1 [68]. During my genetic screening, I discovered this α-arrestin-conferred rapamycin resistance is often altered when cells are additionally missing genes from the autophagy (ATG) gene family. Subsequent investigation further revealed a broad genetic link between the α-arrestins and the autophagic machinery, notably including: 1) the PROPPIN family member Atg18, which binds phosphoinositides (PIs) and regulates their abundance in the vacuolar membrane, while also aiding in the transfer of lipid components from the ER to enable AP production, and 2) Atg6/Vps30, an essential component of the phosphatidylinositol 3-kinase (PI3K) complexes I and II that are defined by the presence of the Vps34 kinase and responsible for the production of phosphatidylinositol 3-phosphate (PI3P) in autophagy and vacuolar protein sorting, respectively [223,242,244–246,299–301].

Autophagic flux is impaired by defects in the function of either Vps34 or Atg18 [223,262,299,302,303]. Recent work from the Weisman lab demonstrates that increased PI3P produced by hyperactive Vps34 mutants prolongs the lifetime of APs and delays their fusion to the vacuole [262]. Atg18 binds Atg2 to form an autophagy-specific lipid-transfer complex that is recruited, in part, by PI3P and facilitates the proper expansion of isolation membranes during AP formation at the phagophore assembly site (PAS) [242,299]. This complex tethers the ER to the tip of the growing phagophore via Atg2's interaction with the transmembrane protein Atg9, thus enabling the *de novo* formation of APs [130,220,244,245]. Both Atg18 and Vps34 further possess related functions outside of autophagy as well, including regulation of retromer dependent retrograde trafficking, vacuolar degradation linked to the endosomal sorting complexes required for transport proteins (ESCRTs), and vacuolar morphology [231,301,304–308].

Given the results of my genetic screening, we chose to further evaluate the potential connection between autophagy and the α-arrestins, finding that loss of *ALY1* and *ALY2*, or fellow α-arrestins *ART1*, delayed the autophagy-driven vacuolar delivery of GFP-tagged Atg8, an autophagy-specific ubiquitin-like protein embedded in autophagosomal membranes and often utilized as a bellwether of autophagic flux [238,241,291,309]. Furthermore, electron microscopy analyses revealed the loss of α-arrestins to result in a decrease in the size of autophagic bodies (ABs), single-membrane-bound structures delivered to the vacuolar lumen by the fusion of APs to this compartment. α-Arrestin mutants also exhibited prolonged AP lifetimes, like those associated with hyperactive Vps34, as well as an increased retention of the PI-binding Atg18 and Atg2 to the vacuolar membrane, potentially linked to elevated levels of PI3P at this structure. In contrast to these defects, we did not observe any α-arrestin-associated impairment in the release of Atg13's phospho-inhibition by TORC1, a transition required for the activation of autophagy, the

recruitment of Atg9 to the PAS, which acts to seed AP formation, nor the localization of the TORC1 complex itself. Collectively, this work leads us to propose a model where loss of α-arrestins results in: 1) an increased abundance of PI3P, and potentially phosphatidylinositol 3,5 bisphosphate ($PI(3,5)P_2$), at the limiting membrane of the vacuole due to an elevated abundance of the lipid kinases responsible for their production and at this structure; and 2) a subsequent over-retention of the PI-binding Atg18 and Atg2 at the vacuolar surface, potentially driving impaired phagophore expansion and, thus, AP production. These findings establish a new-found connection between the α-arrestins and autophagy, while underscoring the importance of further study into their impact on cellular metabolism and phospholipid balance.

2.2 Materials and methods

2.2.1 Yeast strains and growth conditions

The yeast strains used in this study are described in Table 1 and are derived from the BY4741 genetic background of *S. cerevisiae* (S288C in origin). Yeast cells were grown in either synthetic complete (SC) medium lacking the appropriate amino acid for plasmid selection and using ammonium sulfate as a nitrogen source [310] or YPD medium where indicated. Unless otherwise indicated, yeast cells were grown at 30°C. Liquid medium was filter-sterilized and solid medium for agar plates had 2% agar w/v added before autoclaving.

Table 1. Strains used in Chapter 2

The *MAT* **a** deletion collection [311] was used for the strains in the ScUbI library and the mini-library information can be found at odonnelllab.com. For simplicity, only strains used for experiments other than the initial screens are listed in the table below.

Strain	Genotype	Source
BY4741	*MAT* **a** *his3Δ1 leu2Δ0 ura3Δ0 met15Δ0*	[311]
aly1Δ aly2Δ (aka D2-6a)	*MAT* **a** *aly1Δ::KanMX aly2Δ::KanMX his3Δ1 leu2Δ0 ura3Δ0 met15Δ0 lys2Δ0*	[67]
9Arrδ (EN60)	*ecm21Δ::KanMX csr2Δ::KanMX bsd2Δ rog3Δ::NatMX rod1Δ ygr068cΔ aly1Δ aly2Δ ldb19Δ ylr392cΔ::HIS3 his3Δ0 ura3Δ0 leu2Δ0*	[59]
art1Δ	*MAT* **a** *art1Δ::KanMX his3Δ1 leu2Δ0 ura3Δ0 met15Δ0*	[311]
csr2Δ	*MAT* **a** *csr2Δ::KanMX his3Δ1 leu2Δ0 ura3Δ0 met15Δ0*	[311]
rog3Δ	*MAT* **a** *rog3Δ::KanMX his3Δ1 leu2Δ0 ura3Δ0 met15Δ0*	[311]
rim8Δ	*MAT* **a** *rim8Δ::KanMX his3Δ1 leu2Δ0 ura3Δ0 met15Δ0*	[311]
art5Δ	*MAT* **a** *art5Δ::KanMX his3Δ1 leu2Δ0 ura3Δ0 met15Δ0*	[311]
art10Δ	*MAT* **a** *art10Δ::KanMX his3Δ1 leu2Δ0 ura3Δ0 met15Δ0*	[311]
rod1Δ	*MAT* **a** *rod1Δ::KanMX his3Δ1 leu2Δ0 ura3Δ0 met15Δ0*	[311]
ecm21Δ	*MAT* **a** *ecm21Δ::KanMX his3Δ1 leu2Δ0 ura3Δ0 met15Δ0*	[311]
bul1Δ bul2Δ (aka spore3A)	*MAT* **a** *bul1Δ::KanMX bul2Δ::KanMX his3Δ1 leu2Δ0 lys2Δ0 met15Δ0 ura3Δ0*	[91]
atg1Δ	*MAT* **a** *atg1Δ::KanMX his3Δ1 leu2Δ0 ura3Δ0 met15Δ0*	[311]
atg2Δ	*MAT* **a** *atg2Δ::KanMX his3Δ1 leu2Δ0 ura3Δ0 met15Δ0*	[311]
atg5Δ	*MAT* **a** *atg5Δ::KanMX his3Δ1 leu2Δ0 ura3Δ0 met15Δ0*	[311]
atg6Δ	*MAT* **a** *atg6Δ::KanMX his3Δ1 leu2Δ0 ura3Δ0 met15Δ0*	[311]
atg8Δ	*MAT* **a** *atg8Δ::KanMX his3Δ1 leu2Δ0 ura3Δ0 met15Δ0*	[311]
atg9Δ	*MAT* **a** *atg9Δ::KanMX his3Δ1 leu2Δ0 ura3Δ0 met15Δ0*	[311]
atg11Δ	*MAT* **a** *atg11Δ::KanMX his3Δ1 leu2Δ0 ura3Δ0 met15Δ0*	[311]
atg12Δ	*MAT* **a** *atg12Δ::KanMX his3Δ1 leu2Δ0 ura3Δ0 met15Δ0*	[311]
atg14Δ	*MAT* **a** *atg14Δ::KanMX his3Δ1 leu2Δ0 ura3Δ0 met15Δ0*	[311]
atg17Δ	*MAT* **a** *atg17Δ::KanMX his3Δ1 leu2Δ0 ura3Δ0 met15Δ0*	[311]
atg18Δ	*MAT* **a** *atg18Δ::KanMX his3Δ1 leu2Δ0 ura3Δ0 met15Δ0*	[311]
atg19Δ	*MAT* **a** *atg19Δ::KanMX his3Δ1 leu2Δ0 ura3Δ0 met15Δ0*	[311]
atg22Δ	*MAT* **a** *atg22Δ::KanMX his3Δ1 leu2Δ0 ura3Δ0 met15Δ0*	[311]
atg31Δ	*MAT* **a** *atg31Δ::KanMX his3Δ1 leu2Δ0 ura3Δ0 met15Δ0*	[311]
atg34Δ	*MAT* **a** *atg34Δ::KanMX his3Δ1 leu2Δ0 ura3Δ0 met15Δ0*	[311]
atg41Δ	*MAT* **a** *atg41Δ::KanMX his3Δ1 leu2Δ0 ura3Δ0 met15Δ0*	[311]
pep4Δ	*MAT* **a** *pep4Δ::HphNT* I *his3Δ1 leu2Δ0 ura3Δ0 met15Δ0*	This Study
aly1Δ aly2Δ pep4Δ	*MAT* **a** *aly1Δ::KanMX aly2Δ::KanMX pep4Δ::HphNT I his3Δ1 leu2Δ0 ura3Δ0 met15Δ0 lys2Δ0*	This Study
art1Δ pep4Δ	*MAT* **a** *art1Δ::KanMX pep4::HphNT I his3Δ1 leu2Δ0 ura3Δ0 met15Δ0*	This Study
9Arrδ *pep4Δ*	*MAT* **a** *ecm21Δ::KanMX csr2Δ::KanMX bsd2Δ rog3Δ::NatMX rod1Δ ygr068cΔ aly1Δ aly2Δ ylr392cΔ::HIS3 pep4Δ::HphNT I his3Δ0 ura3Δ0 leu2Δ0*	This Study
atg8Δ pep4Δ	*MAT* **a** *atg8Δ::KanMX pep4Δ::HphNT I his3Δ1 leu2Δ0 ura3Δ0 met15Δ0*	This Study
vam3Δ pep4Δ	*MAT* **a** *vam3Δ::KanMX pep4Δ::HphNT I his3Δ1 leu2Δ0 ura3Δ0 met15Δ0*	This Study
BY4741 *ATG2-mNG*	*MAT* **a** Atg2-mNG::*HPH his3Δ1 leu2Δ0 ura3Δ0 met15Δ0*	This Study
aly1Δ aly2Δ ATG2-mNG	*MAT* **a** *aly1Δ::KanMX aly2Δ::KanMX* Atg2-mNG::*HPH his3Δ1 leu2Δ0 ura3Δ0 met15Δ0 lys2Δ0*	This Study

*art1*Δ *ATG2-mNG*	*MAT* **a** *art1Δ::KanMX* Atg2-mNG::*HPH his3Δ1 leu2Δ0 ura3Δ0 met15Δ0 lys2Δ0*	This Study
9arrΔ *ATG2-mNG*	*MAT* **a** *ecm21*Δ*::KanMX csr2*Δ*::KanMX bsd2*Δ *rog3*Δ*::NatMX rod1*Δ *ygr068c*Δ *aly1*Δ *aly2*Δ *ldb19*Δ *ylr392c*Δ*::HIS3* Atg2-mNG::*HPH his3Δ0 ura3Δ0 leu2Δ0*	This Study
BY4741 *ATG9-mNG*	*MAT* **a** Atg9-mNG::*HPH his3Δ1 leu2Δ0 ura3Δ0 met15Δ0*	This Study
*aly1*Δ *aly2*Δ *ATG9-mNG*	*MAT* **a** *aly1Δ::KanMX aly2Δ::KanMX* Atg9-mNG::*HPH his3Δ1 leu2Δ0 ura3Δ0 met15Δ0 lys2Δ0*	This Study
*art1*Δ *ATG9-mNG*	*MAT* **a** *art1Δ::KanMX* Atg9-mNG::*HPH his3Δ1 leu2Δ0 ura3Δ0 met15Δ0 lys2Δ0*	This Study
9ArrΔ *ATG9-mNG*	*MAT* **a** *ecm21*Δ*::KanMX csr2*Δ*::KanMX bsd2*Δ *rog3*Δ*::NatMX rod1*Δ *ygr068c*Δ *aly1*Δ *aly2*Δ *ldb19*Δ *ylr392c*Δ*::HIS3* Atg9-mNG::*HPH his3Δ0 ura3Δ0 leu2Δ0*	This Study
*atg8*Δ *ATG9-mNG*	*MAT* **a** *atg8Δ::KanMX* Atg9-mNG::*HPH his3Δ1 leu2Δ0 ura3Δ0 met15Δ0 lys2Δ0*	This Study
*aly1*Δ *aly2*Δ *atg8*Δ *ATG9-mNG*	*MAT* **a** *aly1Δ::KanMX aly2Δ::KanMX atg8*Δ::*LEU2* Atg9-mNG::*HPH his3Δ1 ura3Δ0 met15Δ0 lys2Δ0*	This Study
*art1*Δ *atg8*Δ *ATG9-mNG*	*MAT* **a** *art1*Δ*::KanMX atg8*Δ::*LEU2* Atg9-mNG::*HPH his3Δ1 ura3Δ0 met15Δ0 lys2Δ0*	This Study
9ArrΔ *atg8*Δ *ATG9-mNG*	*MAT* **a** *ecm21*Δ*::KanMX csr2*Δ*::KanMX bsd2*Δ *rog3*Δ*::NatMX rod1*Δ *ygr068c*Δ *aly1*Δ *aly2*Δ *ldb19*Δ *ylr392c*Δ*::HIS3 atg8*Δ::*LEU2* Atg9-mNG::*HPH his3Δ0 ura3Δ0*	This Study
*atg1*Δ *atg8*Δ *ATG9-mNG*	*MAT* **a** *atg1*Δ::*KanMX* Atg9-mNG*::HPH his3Δ1 leu2Δ0 ura3Δ0 met15Δ0 lys2Δ0*	This Study
BY4741 *VPS10-ENVY*	*MAT* **a** *VPS10-ENVY*::*HIS3 leu2Δ0 ura3Δ0 met15Δ0*	This study
*aly1*Δ *aly2*Δ *VPS10-ENVY*	*MAT* **a** *aly1Δ::KanMX aly2Δ::KanMX VPS10-ENVY*::*HIS3 his3Δ1 leu2Δ0 ura3Δ0 met15Δ0 lys2Δ0*	This study
*art1*Δ *VPS10-ENVY*	*MAT* **a** *art1*Δ::*KanMX VPS10-ENVY*::*HIS3 leu2Δ0 ura3Δ0 met15Δ0 lys2Δ0*	This study
9ArrΔ *VPS10-ENVY*	*MAT* **a** *ecm21*Δ*::KanMX csr2*Δ*::KanMX bsd2*Δ *rog3*Δ*::NatMX rod1*Δ *ygr068c*Δ *aly1*Δ *aly2*Δ *ldb19*Δ *ylr392c*Δ::*LEU2 his3Δ0 ura3*Δ *VPS10-ENVY*::*HIS3*	This study
BY4741 *VPS17-ENVY*	*MAT* **a** Vps17-ENVY::*HIS3 leu2Δ0 ura3Δ0 met15Δ0*	This study
*aly1*Δ *aly2*Δ *VPS17-ENVY*	*MAT* **a** *aly1*Δ::KanMX *aly2*Δ::KanMX Vps17-ENVY::*HIS3 his3Δ1 leu2Δ0 ura3Δ0 met15Δ0 lys2Δ0*	This study
*art1*Δ *VPS17-ENVY*	*MAT* **a** *art1*Δ::KanMX Vps17-ENVY::*HIS3 his3Δ1 leu2Δ0 ura3Δ0 met15Δ0 lys2Δ0*	This study
9ArrΔ *VPS17-ENVY*	*MAT* **a** *ecm21*Δ*::KanMX csr2*Δ*::KanMX bsd2*Δ *rog3*Δ*::NatMX rod1*Δ *ygr068c*Δ *aly1*Δ *aly2*Δ *ldb19*Δ *ylr392c*Δ::LEU2 *his3Δ0 ura3Δ0* Vps17-ENVY::*HIS3*	This study

2.2.2 Plasmids and DNA manipulations

Plasmids used in this work are described in Table 2. PCR amplifications for building plasmid DNA inserts were performed using Phusion High Fidelity DNA polymerase (ThermoFisher Scientific, Waltham, MA) and confirmed by DNA sequencing. Plasmids were transformed into yeast cells using the lithium acetate method [312] and transformants were selected for on SC medium lacking a specific nutrient.

Table 2. Plasmids used in Chapter 2

Plasmid	Genotype	Description (Reference)
pRS426	2μ, *URA3*	[313]
pRS426-Aly1	*ALY1prom-ALY1*, 2μ, *URA3*	[67]
pRS426-Aly2	*ALY2prom-ALY2*, 2μ, *URA3*	[67]
pRS426-Aly1^{K379R}	*ALY1prom-aly1^{K379R}*, 2μ, *URA3*	[152]
pRS426-Aly2^{K392R}	*ALY2prom-aly2K392R*, 2μ, *URA3*	[152]
pRS426-Aly1^{PPxYless}	*ALY1prom-aly1^{PPxYless}*, 2μ, *URA3*	[79]
pRS426-Aly2^{PPxYless}	*ALY2prom-aly2^{PPxYless}*, 2μ, *URA3*	[79]
pRS426-Art1	*ART1prom-ART1*, 2μ, *URA3*	[62]
pRS426-Art5	*ART5prom-ART5*, 2μ, *URA3*	[79]
pRS416-GFP-Atg8	*ATG8prom*-GFP-*ATG8*, *CEN*, *URA3*	[302]
pRS316-GFP-Tor1	*TOR1prom*-GFP-*TOR1*, *CEN*, *URA3*	[314]
pRS416-mCherry-Ape1	*ADH1prom*-mCherry-APE1, *CEN*, *URA3*	[315]
pRS315-BFP-Ape1	*CUP1prom*-BFP-*APE1*, *CEN*, *LEU2*	[245]
pRS416-Atg18-GFP	*ATG18prom*-GFP-*ATG18*, *CEN*, *URA3*	[300]
pRS426-GFP-Vps34	*VPS34prom*-GFP-*VPS34*, 2μ, *URA3*	[262]
pRS416-Fab1-ENVY	*FAB1prom-FAB1*-ENVY, *CEN*, *URA3*	[262]
pRS415-Ypq2-GFP	*TEF1prom-Ypq2YPQ2*-GFP, *CEN*, *LEU2*	This study. The coding region of Ypq2 lacking its stop codon was PCR amplified from the genome using XbaI and PstI restriction site adapters. This was then subcloned into pRS415-*TEF1prom*-GFP at the XbaI and PstI sites.
pRS416-GFP-Yck3	*CEN*, *URA3*	[262]
pRS426-GFP-FYVE(Eea1)	*PRC1prom*-GFP-FYVE(Eea1), 2μ, *URA3*	[91]

2.2.3 Yeast protein extraction and immunoblot analyses

Whole-cell extracts of yeast proteins were prepared using the trichloroacetic acid (TCA) extraction method as previously described [152]and as modified from [316]. In brief, cells were grown in SC medium to mid-exponential log phase at 30°C (A_{600}= 0.6-1.0) and an equal density of cells was harvested by centrifugation. Cell pellets were flash frozen in liquid nitrogen and stored at -80°C until processing. Cells were lysed using sodium hydroxide and proteins were precipitated using 50% TCA. Precipitated proteins were solubilized in SDS/Urea sample buffer [8M Urea, 200mM Tris-HCl (pH 6.8), 0.1mM EDTA (pH 8), 100mM DTT, Tris 100mM (not pH adjusted)] and heated to 37°C for 15 minutes. Samples were then precipitated using 50% TCA and solubilized in SDS/Urea sample buffer as above. Proteins were resolved by SDS-PAGE and identified by immunoblotting with a mouse anti-green fluorescent protein (GFP) (Santa Cruz Biotechnology, Santa Cruz, CA), or anti-Atg13 [209] antibody to detect tagged or endogenous proteins. As a protein loading control, immunoblot membranes were stained after transfer with Revert™ (Li-Cor Biosciences, Lincoln, NE) total protein stain and detected using the Odyssey™ CLx Infrared imaging system (Li-Cor Biosciences). Anti-mouse or anti-rabbit secondary antibodies, conjugated to IRDye-800 or IRDye-680 (Li-Cor Biosciences) were used to detect primary antibodies on the Odyssey™ CLx (Li-Cor Biosciences).

2.2.4 Serial dilution growth assays

For the serial dilution growth assays on solid medium, cells were grown to saturation in liquid YPD or SC medium overnight and the A_{600} determined. Starting with an A_{600} of 1.0 (approximately 1.0 x 10^7 cells/ml), 5-fold serial dilutions were generated and transferred to solid

medium using a sterile replica-pinning tool. Cells were grown at 30°C for 3-6 days and images captured using a Chemidoc XRS+ imager (BioRad, Hercules, CA). All images were evenly adjusted in Photoshop (Adobe Systems Incorporated, San Jose, CA). For rapamycin (LC Laboratories, Woburn, MA) containing plates, the stock solution of 0.5 mg/ml in ethanol was diluted in growth medium to the final concentration indicated in each figure panel (typically 50 ng/ml).

2.2.5 ScUbI library screen

The *Saccharomyces cerevisiae* Ubiquitin Interactome (ScUbI) library contains 323 unique non-essential gene deletions, each of which is annotated as being non-essential in the *Saccharomyces* Genome Database (SGD). This library initially was constructed as the Targeted Ubiquitin System (TUS) yeast gene deletion library [317] We then used YeastMine, populated by SGD and powered by InterMine, and searched for 'ubiquitin'. These searches returned over 2,000 candidates before duplicates, essential genes, and targets of ubiquitin were removed. The remaining list was combined with the TUS library to produce the final ScUbI library. The 323 gene deletion mutants were arrayed over four 96-well plates. The library is available upon request and is further documented at https://www.odonnelllab.com/yeast-libraries.

To screen for modifiers of α-arrestins Aly1 and Aly2 function, the ScUbI library was transformed with either pRS426-vector or pRS426-Aly1 or -Aly2 plasmids, each of which over-express Aly1 or Aly2 as they are present on a on a 2-micron plasmid backbone but expressed from their endogenous promoter. Transformations were performed as described in [312] and were done with the aid of the Benchtop RoToR HAD robotic plate handler (Singer Instruments Co. Ltd, Roadwater, UK) and the Multidrop Combi (ThermoFisher Scientific, Waltham, MA) in the

laboratory of Dr. Anne-Ruxandra Carvunis (Univ. of Pittsburgh). Each transformed version of the library was stamped in technical triplicate to SC medium lacking uracil (as a control), or the same medium containing 50 ng/ml rapamycin. Plates were grown at 30°C for 2-4 days and white light images were captured using the BioRad ChemiDoc XRS+ imager (Hercules, CA) on days 1-4 of incubation. Images were converted to *.jpg* file format and the pixel size of colonies were measured using the DissectionReader macro [generously provided by Dr. Kara Bernstein's laboratory (Univ. of Pittsburgh) and developed by John C. Dittmar and Robert J.D. Reid in Dr. Rodney Rothstein's laboratory (Columbia Univ.)] in Image J (National Institutes of Health, Bethesda, MA, USA). More information on this plugin can be found at: https://github.com/RothsteinLabCUMC/dissectionReader. Colony sizes were converted into individual sets of Z-scores for each transformed version of the library (this allowed for comparisons between pRS426 vs pRS426-Aly1 or -Aly2 colony sizes). The Z-scores for each gene deletion strain containing pRS426 was subtracted from the Z-score for that gene deletion when over-expressing Aly1 or Aly2 to produce the 'change from vector' or ΔV value (Sup. File 1, available in 'Chapter 2' folder at OneDrive link: Supplemental Thesis Documents - Bowman). A ΔV cutoff of +/- 1.0 was arbitrarily used to identify a targeted list of gene deletion candidates for further study. This list was used to perform Gene Onotology (GO) enrichment analysis described below.

2.2.6 Gene ontology enrichment analysis

GO trees (file: *go-basic.obo*) and annotations (files: *sgd.gaf*) were downloaded from http://geneontology.org/ on April 20, 2022. We used *BINGO* from the *Cytoscape* application library to calculate the number of genes associated with each GO term in the group with strongest

Z-score change (positive or negative) and the overall population of (all) genes we tested (see Section 2.2.5 above, Sup. File 1, available in 'Chapter 2' folder at OneDrive link: Supplemental Thesis Documents - Bowman) [318,319]. We excluded annotations based on the evidence codes ND (no biological data available). We identified GO term enrichments by calculating the likelihood of the ratio of the genes associated with a GO term within a study group given the total number of genes associated with the same GO term in the background set of all genes in our population. We applied a hypergeometric test to calculate *p*-values for the enrichment of GO terms. *p*-value < 0.05 was taken as a requirement for significance.

To visualize GO terms, we removed redundant information by selecting parent GO terms of multiple similar terms. Then we calculated average Z-score change for the genes associated with the GO term and plotted representative GO terms based on the associated p-values and average Z-score changes using R package ggplot2 v3.3.5 [320].

2.2.7 Quantification of serial dilution growth assays

Serial dilution growth assays in S1-2 Figs) were quantified using a CellProfiler (Broad Institute, Cambridge, MA) automated pipeline (available at https://www.odonnelllab.com/automated-quantification-pipelines). White light images of serial dilution growth assay plates were obtained using a BioRad ChemiDoc XRS+ imager (Hercules, CA, USA) after 5 days growth. Images were then cropped, converted to binary, and resized to equivalent pixel densities. The CellProfiler automated pipeline segmented the rows and columns for each image and measured the pixel intensity for each spot of yeast growth, aggregating the values for each row. Using this approach, we defined a quantitative measure of the growth present for each row in a serial dilution growth assay. These values were converted into a heat map using

Prism (GraphPad Software, San Diego, CA). Data derived from this analysis is presented in Figures 5-6.

2.2.8 Electron microscopy

We grew cells overnight in SC medium in culture tubes on a rotating drum at 30°C. We then diluted cells (~A_{600} = 0.3) and regrew them in culture tubes for 4 h on a rotating drum at 30°C. For cells treated with rapamycin (LC Laboratories, Woburn, MA), 200 ng/ml rapamycin was added to 15ml of cells, then incubated at 30˚C for four hours. We used an osmium tetroxide (OsO4) substitution method to prepare yeast cells for EM [321]. Concentrated live yeast cells were placed in 1.5 mm wide by 0.2 mm deep brass planchets (Leica 707899) and frozen using a Leica EM PACT2 High pressure freezer (Leica Microsystems, Buffalo Grove, IL). Frozen samples were then placed in a Leica EM AFS2 Freeze Substitution device (Leica Microsystems, Buffalo Grove, IL). A solution of 2% OsO_4 in 100% acetone was placed on the samples for 110 hours at -90ºC. The samples were then left in the OsO_4 solution and was allowed to rise 5°C every hour the solution reached 0°C. Samples remained at 0°C and were dehydrated further with 3 x 30-minute acetone washes and 3 x 1-hour ethanol washes (Pharmco, Brookefield, CT). Samples were then removed from the Freeze Substitution device and allowed to come to room temperature. Samples were washed twice in propylene oxide (Electron Microscopy Sciences, Hatfield, PA) and embedded in Poly/Bed® 812 (Luft formulation, Warrington, PA). Samples were allowed to cure for 24 hours at 37°C and 48 hours at 65°C. The brass planchets were carefully removed from the polymerized resin and semi-thin (300 nm) sections were cut on a Leica Reichart Ultracut (Leica Microsystems, Buffalo Grove, IL), stained with 0.5% Toluidine Blue in 1% aqueous sodium borate (Fisher, Pittsburgh, PA) and examined using light microscopy. Ultrathin sections (65 nm) were taken,

placed on 200 mesh copper TEM grids and were stained with 2% uranyl acetate (Electron Microscopy Sciences, Hatfield, PA) and Reynold's lead citrate (Fisher, Pittsburgh, PA) and examined on JEOL 1400 Plus transmission electron microscope (JEOL Peabody, MA) with a side mount AMT 2k digital camera (Advanced Microscopy Techniques, Danvers, MA).

2.2.9 Quantification of electron micrographs

The number of autophagic bodies (AB) per cell was determined manually by counting the number of membrane-bound structures inside the vacuoles of complete cells for each electron micrograph. The diameter of ABs measurement was performed using Image J software (NIH, Bethesda, MD). The distance scale was calibrated using the scale bar on the electron micrograph and the furthest distance across each AB was determined. Data derived using this method is presented in Figure 8.

2.2.10 Fluorescence microscopy

Fluorescent protein localization was assessed using epifluorescent and confocal microscopy. We grew cells overnight in SC medium in culture tubes on a rotating drum at 30°C. We then diluted cells (~A_{600} = 0.3) and regrew them in culture tubes for 4 h on a rotating drum at 30°C. For cells treated with rapamycin (LC Laboratories, Woburn, MA), 200 ng/ml rapamycin was added to 1ml of cells in a microcentrifuge tube and incubated in an end-over-end rotator at 30˚C for indicated times. Prior to imaging, FM4-64 or CMAC stains were used to mark the vacuole membrane or lumen, respectively. For cells stained with FM4-64 (ThermoFisher Scientific, Waltham, MA), 1 ml of cells were treated with 100 μg/ml FM4-64 for 30 minutes at 30˚C. Cells

were then washed, resuspended in 1 ml SC medium, and incubated at 30˚C for 1h. For cells stained with CMAC, 20 μM Cell Tracker Blue CMAC (7-amino-4-chloromethylcoumarin) dye (Life Technologies, Carlsbad, CA) was added to 1 ml of mid-log cells 1 hour prior to imaging. Cells were then inoculated to low density (~A_{600} = 0.15) onto 35 mm glass bottom microwell dishes (MatTek Corporation, Ashland, MA) that were either poly-D-lysine coated or had been treated with 50 μl of 0.2 mg/ml concanavalin A (MP Biomedicals, Solon, OH). Cells were imaged by confocal microscopy using a Nikon Eclipse Ti2-E A1R inverted microscope (Nikon, Chiyoda, Tokyo, Japan) outfitted with a 100x objective (NA 1.49) and images were detected using GaAsP or multi-alkali photomultiplier tube detectors as single median planes or as a series of images in an 8-10 μm Z-stack with 0.125-0.25 μm step sizes. Data derived using this method is presented in Figures 10-12, 14-20. Alternatively, cells were imaged by epifluorescent microscopy using a Nikon Eclipse Ti2 inverted microscope (Nikon, Chiyoda, Tokyo, Japan) outfitted with a Teledyne Photometics Prime BSI CMOS (sCMOS) camera (Teledyne Photometics, Tucson, AZ) and a 100x objective (NA 1.45). Data derived using this method is presented in Figures 13 and 21.

In both cases, acquisition was controlled using NIS-Elements software (Nikon, Chiyoda, Tokyo, Japan) and all images within an experiment were captured using identical settings. Confocal images were deconvolved using the Richardson-Lucy algorithm. All images were cropped and adjusted evenly using NIS-Elements.

2.2.11 Fluorescent image quantification and statistical analyses

Quantification of whole cell fluorescence intensity was done using the Nikon General Analysis 3 software (Nikon, Chiyoda, Tokyo, Japan) using segmentation from NIS-Elements.*ai* (Artificial Intelligence) software (Nikon, Chiyoda, Tokyo, Japan) unless otherwise described

below. For quantification of whole-cell signal, the NIS.*ai* software was trained on a ground truth set of samples where cells had been manually segmented using DIC channel images. Next, the NIS.*ai* software performed iterative training until it achieved a training loss threshold of <0.02, which is indicative of a high degree of agreement between the initial ground truth provided and the output generated by the NIS.*ai* software. Fields of images captured via confocal imaging were then processed so that the individual cells in a field of view were segmented using the DIC. Any partial cells at the edges of the image were removed. The sum fluorescence intensity and pixel count for each cell was defined in the appropriate channel, with the mean fluorescence intensity being calculated by dividing the sum intensity by the number of pixels. Data derived from these kinds of analyses are presented in Figures 11-12.

To measure the vacuolar lumen or membrane fluorescence or length, we trained the NIS.*ai* software to identify the vacuolar lumen or membrane using CMAC or FM4-64, respectively, as fiducial markers. The NIS.*ai* software was trained using a manually defined 'ground truth' set of vacuole segmentations selecting either the entire vacuole or just the vacuolar membrane and trained as above. Then, fields of images captured via confocal imaging were processed so that the individual vacuole objects in a field of view were segmented using the 405nm (CMAC) or 561nm (FM4-64) channel. Using General Analysis 3 software, individual cells were segmented by the same trained NIS.*ai* module described above using the DIC channel. A parent-child relationship was applied to individual vacuolar objects (child) within the same cell (parent) to aggregate them as single objects and pair them to the appropriate whole cell. Any partial cells at the edges of the image were removed along with their child-objects. Then the sum fluorescence intensity and pixel count for each parent or child object was defined in the appropriate channel. Mean intensities were determined by dividing the sum intensity by the number of pixels for all child objects inside a

parent. Mean vacuolar lengths were determined by dividing the sum intensity by the sum pixel counts for each child object inside a parent. Data derived from these kinds of analyses are presented in Figure 11, and 15-20.

Manual image quantification to measure the vacuolar membrane fluorescence or length was performed using ImageJ software (National Institutes of Health, Bethesda, MD). A 2-pixel thick line was hand drawn over the vacuolar membrane using images captured of cells stained with FM4-64 which was then overlaid on the GFP images and the median GFP signal or total length of the line was measured. The median background fluorescence intensity was then subtracted for the vacuolar membrane intensity measures. Data derived from these kinds of analyses are presented in Figure 15 and 16.

Manual image quantification to measure the number of vacuole lobes was performed using ImageJ software (National Institutes of Health, Bethesda, MD). The number of vacuole lobes was determined using images capture of cells stained with FM4-64. Data derived from this kind of analysis is presented in Figure 16.

To determine the lifetimes of GFP-Atg8 AP structures, we used time-lapse confocal microscopy to obtain Z-stack image series acquired every 30 seconds for 20-25 minutes per single field of cells. Following Richardson-Lucy deconvolution, images were manually assessed to identify newly formed GFP-Atg8 puncta which were then tracked over time until they merged with the vacuole (stained with CMAC), recording the total lifetime of the puncta. Representative cells displayed as maximum intensity projections of the entire Z-series (Figure 10), or as 3D projection movies (S1-4 Movies) were created using NIS Elements software.

To measure Atg9-mNG intensity at the PAS, we relied on the autophagy cargo protein Ape1, which is recruited to the PAS upon autophagy induction [130]. We trained the NIS.*ai*

software to segment the PAS using the signal from puncta formed by mCherry-Ape1 expressing cells. The NIS.*ai* software was trained using a manually defined 'ground truth' set of mCherry-Ape1 PAS segmentations as above. Fields from images captured via confocal imaging were then processed so that individual PAS objects in a field of view were segmented using the 561nm channel. Parent-child relationships were used to pair PAS to their respective whole as above, and any partial cells at the edges of the image were removed along with their child-objects. The sum fluorescence intensity for each PAS was defined in the 488nm channel to assess the abundance of Atg9-mNG recruited following 3h rapamycin treatment. Data derived from this analysis is presented in Fig 14B.

To evaluate the ability of isolation membranes to expand, we utilized the giant Ape1 assay [174,248]. We used confocal microscopy to obtain Z-stack image series acquired following 1h treatment with rapamycin. Following Richardson-Lucy deconvolution, BFP-Ape1 puncta were manually assessed for the presence of GFP-Atg8 structures. When present, these structures were manually binned into categories of 'patch' and 'elongated' based on their shape and size. Data derived from this analysis is presented in Figure 14D-E.

Fluorescent quantification was assessed statistically using Prism (GraphPad Software, San Diego, CA). Unless otherwise indicated, we performed the Kruskal-Wallis statistical test with Dunn's post hoc correction for multiple comparisons. In all cases, significant p-values from these tests are represented as: *, p value <0.1; ** p value <0.01; ***, p value <0.001; ****, p value <0.0001; ns, p value >0.1. In some instances where multiple comparisons are made, the † symbol may additionally be used in place of the * with the same p value meanings but indicating comparisons to a different reference sample.

2.3 Results

2.3.1 Identifying genes that alter Aly-mediated growth on rapamycin

α-Arrestins facilitate the ubiquitination, internalization, and vacuolar degradation of plasma membrane proteins by mediating the binding of the E3 ubiquitin ligase Rsp5 to these membrane-bound cargo (Figure 4A) [58,62,68,76,85,92]. As a consequence of their Rsp5 recruitment, achieved through the binding of Rsp5's WW-domains to α-arrestin $^{L}/_{P}$PXY motifs, the α-arrestins undergo their own mono-ubiquitination, which promotes their endocytic trafficking roles, or poly-ubiquitination, a modification resulting in their degradation (Figure 4B) [58,74,76,77,143,154–156]. Previous work from the O'Donnell lab used mass spectroscopy to identify residues targeted for the mono-ubiquitination on α-arrestins Aly1 and Aly2, allowing for the generation of mutants that cannot be mono-ubiquitinated (K397R and K392R, respectively) [152]. Similarly, earlier work produced Aly1 and Aly2 mutants lacking their $^{L}/_{P}$PXY motifs (PPXYless), resulting in a loss of both their ubiquitination and trafficking functions by rendering them incapable of binding Rsp5 (Figure 4B) [68].

In rich nutrient conditions, the activity of the TORC1 signaling complex promotes cell growth [135]. TORC1 is inhibited, however, during periods of nutrient limitation or by treatment with the drug rapamycin, triggering a transition in cellular metabolism that inhibits cell growth and protein synthesis, while activating the self-degradative autophagy program [135]. TORC1 also controls the α-arrestins, thereby regulating endocytosis of cell surface nutrient transporter endocytosis [66,77,138]. The intertwined relationship between TORC1 and the α-arrestins is further supported by the previously reported resistance to rapamycin-induced cell growth

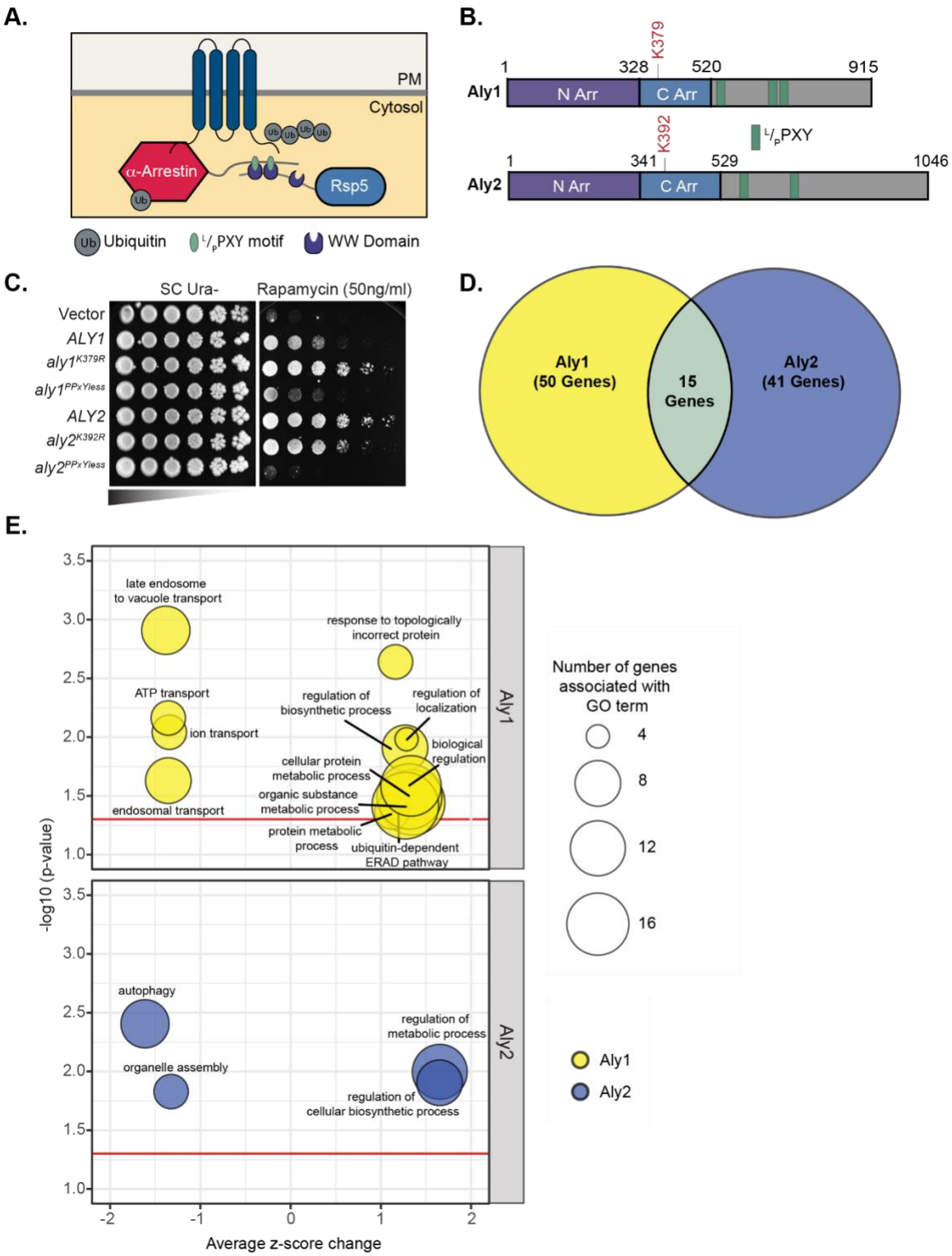

Figure 4. Genetic screen of the ScUbI library identifies modifiers of α-arrestin-mediated resistance to rapamycin.

(A) Model of α-arrestin function. α-Arrestins bind selectively to membrane proteins and interact with the Rsp5 ubiquitin ligase. α-Arrestin $^{L}/_{P}$PXY motifs (green) interact with the WW domains of Rsp5 (purple). Rsp5 can ubiquitinate (Ub in grey) the α-arrestin, which regulates α-arrestin function, or the membrane protein, which helps stimulate its endocytosis. (B) A schematic of α-arrestins Aly1 and Aly2 depicting the N- and C-terminal arrestin-fold domains (purple and blue, respectively), $^{L}/_{P}$PXY motifs (green) and sites of mono-ubiquitination [152]. Numbers indicate amino acid positions in coding sequence. (C) Serial dilution growth assays of WT cells containing the pRS426-derived plasmid expressing either nothing (vector) or the indicated α-arrestin on SC medium lacking uracil, with and without 50ng/mL rapamycin, are shown. (D) Venn-diagrams indicating the number of ScUbI library gene deletions that altered Aly1 or Aly2-mediated resistance to rapamycin. (E) Representative gene ontology terms for the genes with the strongest Z-score changes in *ALY1* (top) or *ALY2* (bottom) overexpression backgrounds. The x-axis shows the average Z-score changes for the genes associated with a particular GO term and the y-axis represents the significance of the association. For GO terms with similarities, we only show the parent terms. Circle sizes represent the number of terms associated with the GO terms. Many genes with strong negative Z-score changes in Aly2 are related with autophagy.

inhibition conferred by the over-expression of either Aly1 or Aly2, an effect we found to be shared by the over-expression of either Art1 or Art5, but no other member of the α-arrestin family (Figure 5A) [68]. Notably, while the ability of the Alys to interact with Rsp5 is required for their ability to confer rapamycin resistance, these closely related paralogs display divergent effects resultant from the loss of their mono-ubiquitination, with this function being improved for Aly1 and impaired for Aly2 (Figure 4C). While this suggests that Rsp5-associated trafficking activities are critical to the α-arrestin's ability to affect the cell's resistance to rapamycin, the molecular details surrounding the role of their mono-ubiquitination remain unclear.

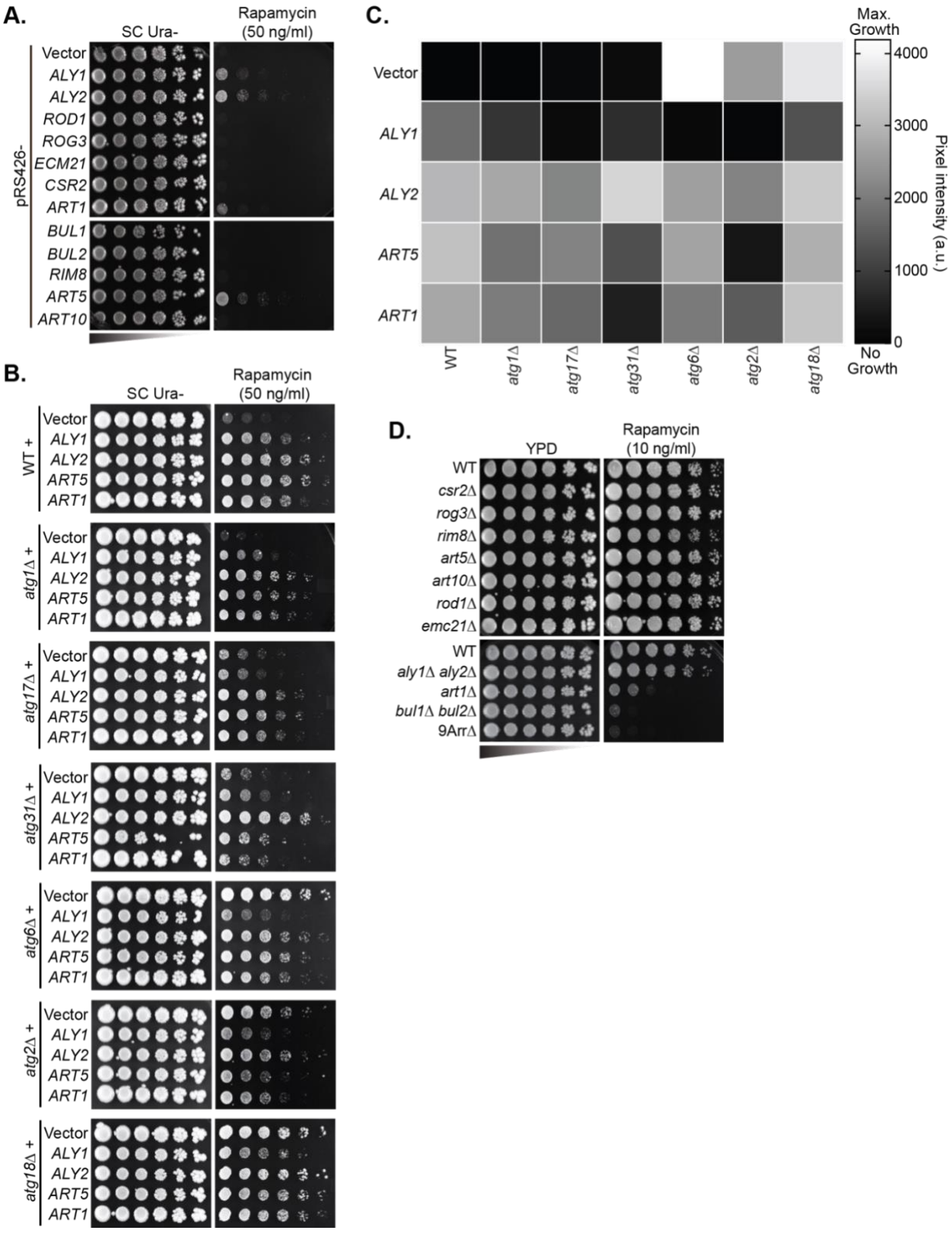

Figure 5. The loss of *ATG* family genes affects the rapamycin resistance conferred by α-arrestins.

(A) Serial dilution growth assays of WT cells containing a pRS426- derived plasmid expressing either nothing (vector) or the indicated α-arrestin on SC medium lacking uracil with or without 50ng/mL rapamycin are shown. (B) Serial dilution growth assays of WT cells or those lacking the *ATG* family gene indicated containing a pRS426-derived plasmid expressing either nothing (vector) or the indicated α-arrestin under the control of its own promoter on the medium indicated. (C) Heat map representing quantified (see Section 2.2.7) serial dilution growth assays from (B). (D) Serial dilution growth assays of WT and α-arrestin deletion mutant cells on YPD media with and without 10ng/mL rapamycin are shown.

In an effort to uncover potential regulators of Aly-mediated resistance to rapamycin, I constructed the *Saccharomyces cerevisiae* Ubiquitin Interactome (ScUbI) library, an array of 323 unique mutants derived from the yeast gene deletion collection annotated as relating to ubiquitin in the *Saccharomyces cerevisiae* Genome Database (SGD) (accessed 16, July 2016) (see Section 2.2.5) [311]. As part of an undergraduate laboratory course at the Univ. of Pittsburgh (BIOSC 0352), I conducted a genetic screen of the ScUbI library comparing the growth of each deletion mutant over-expressing either *ALY1*, *ALY2*, or an empty-vector control on rapamycin-containing media. Together, we isolated 76 genes whose Aly-mediated growth was most severely affected as compared to their corresponding vector-expressing colonies (ΔV +/- 1.0, see Section 2.2.5 and Sup. File 1, available in 'Chapter 2' folder at OneDrive link: Supplemental Thesis Documents - Bowman). Of these, we found 50 mutants that altered Aly1-dependent growth and 41 for Aly2, of which 15 gene deletions affected both (Figure 4D and Sup. File 1, available in 'Chapter 2' folder at OneDrive link: Supplemental Thesis Documents - Bowman). Subsequent Gene Ontology term analysis of these candidate genes revealed an enrichment of genes related to ER-associated degradation (ERAD) among those which improved Aly-mediated rapamycin resistance (see

Section 4.2), while genes associated with autophagy represented the largest group negatively affecting this phenotype (Figure 4E; O.A.).

2.3.2 A network of genetic interactions between autophagy genes and α-arrestins

Many autophagy-related candidates identified in our initial screen are involved in autophagy initiation and AP biogenesis. Thus, in an effort to further assess the genetic connections between autophagy and the α-arrestins, we conducted secondary screening using more sensitive serial dilution growth assays of a variety of *ATG* gene family mutants, focusing especially on those components known to operate early in autophagy [200,292]. These experiments not only validated many of the genetic interactions identified in my initial screen, but further identified additional links between the α-arrestins and early acting autophagy machinery (Figure 5B-C, 6A-B, and 7; R.W.B, S.D., and K.C.). In order to quantitatively assess these results (example in Figure 6A, full data in Figure 7; R.W.B, S.D., and K.C.), we developed an automated analysis pipeline using the Cell Profiler program to measure the pixel intensities derived from binary images of these growth assays (see Section 2.2.7). A heat map of these data is presented in Figures 5C and 6B, with maximum growth represented as a white square and the absence of growth represented by a black square. These results, and the genetic interactions they describe, are further put into the context of the autophagy pathway in the model presented in Figure 6C.

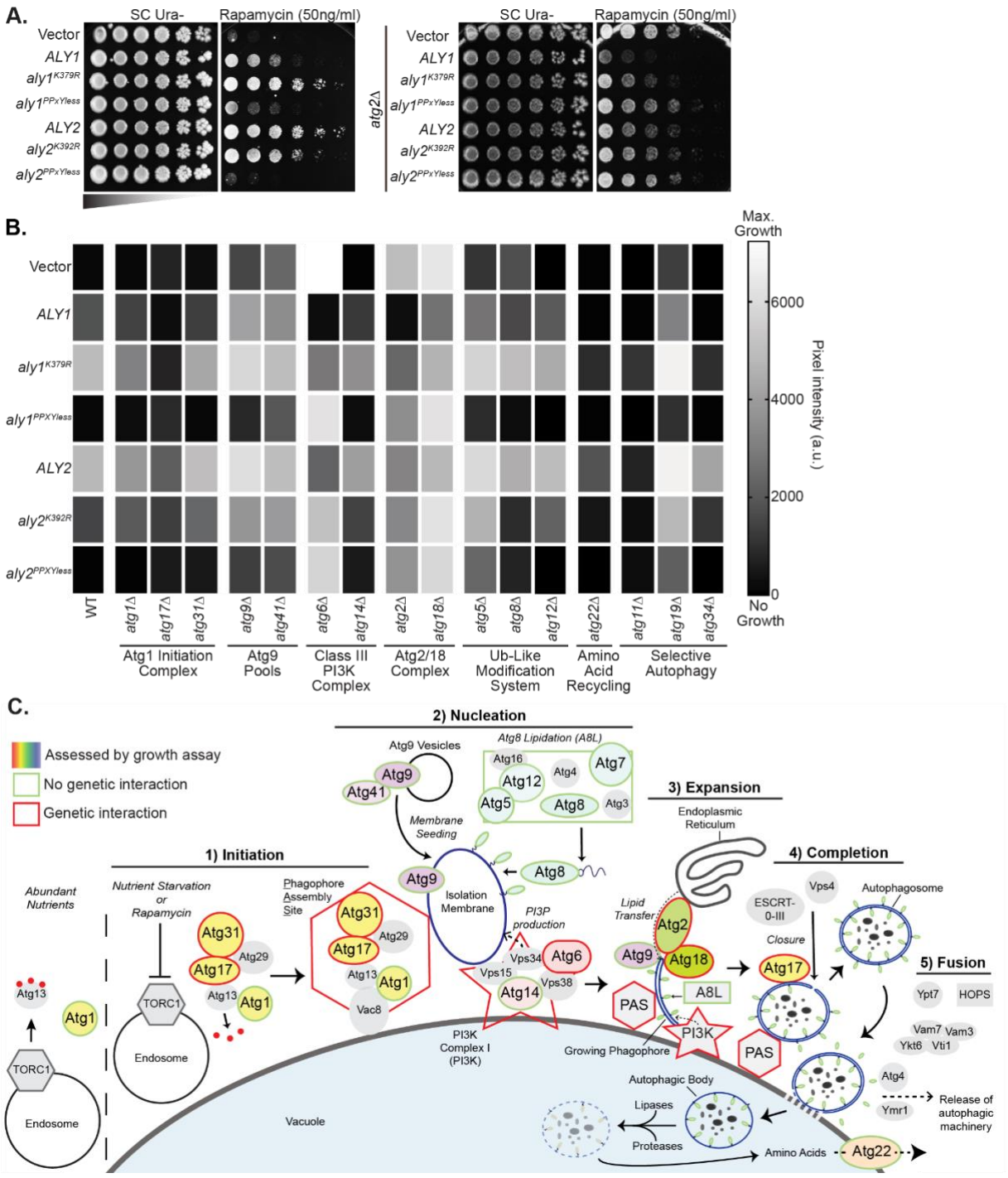

Figure 6. Genetic interactions between α-arrestins and the *ATG* gene family.

(**A**) Serial dilution growth assays of WT and *atg2*Δ cells containing a pRS426-derived plasmid expressing either nothing (vector) or an α-arrestin on SC medium lacking uracil with or without 50ng/mL rapamycin are shown. One representative example of the larger serial dilution growth assay set, which is found in Figure 7, is provided. (**B**) Heat

map representing quantified (see Section 2.2.5) serial dilution growth assays (for primary data see Figure 7) of WT or *atg*Δ cells containing a pRS426-derived plasmid expressing either nothing (vector) or the indicated α-arrestin on SC medium lacking uracil with or without 50ng/mL rapamycin. (**C**) A simplified diagram of the machinery involved in macroautophagy divided into 5 stages: 1) Initiation, 2) Nucleation, 3) Expansion, 4) Completion, and 5) Fusion. In short, under abundant nutrient conditions, the endosomal population of the TORC1 signaling complex inhibits autophagy through phosphorylation of Atg13 (red circles). Once endosomal TORC1 is inhibited, either by nutrient starvation or treatment with the drug rapamycin, Atg13 is dephosphorylated, allowing for Atg1 activation and the recruitment of other autophagic machinery to form the PAS and initiate macroautophagy (1). Vesicles containing Atg9 are then recruited to the PAS, providing the seed for isolation membrane formation. The autophagy-specific PI3K is also recruited to the PAS, along with machinery to conjugate Atg8 to PE for incorporation into the isolation membrane (2). PI3K activity at the PAS produces PI3P on the isolation membrane, recruiting the Atg18-Atg2 complex. Atg2, bound to Atg9, tethers the tip of the growing phagophore to the ER and facilitates ER-to-phagophore lipid transfer which, along with Atg8 lipidation, drives phagophore expansion (3). Once fully expanded to encapsulate its cytosolic cargo, the phagophore is sealed through activity of Atg17, Vps4, and the ESCRT machinery to form a completed AP (4). The autophagic machinery is then released and Atg8 is cleaved from its PE anchor on the outer autophagic membrane. APs then fuse to the vacuolar membrane through the action of Rab GTPase Ypt7, the HOPS tethering complex, and various SNARE proteins, delivering the inner-membrane-bound autophagic body to the vacuolar lumen (5). There, vacuolar lipases and proteases degrade the autophagic body and its contents, producing free amino acids that are effluxed to the cytosol via Atg22. Shapes filled with color were assessed with the serial dilution growth assays found in (B) and Figure 7, while those filled with grey were not. Those deletion mutants found to have a genetic interaction with α-arrestins are marked with a red outline, while those that marked with a green outline had no genetic interaction with α-arrestins.

We began by assessing genes involved in autophagy initiation, finding that loss of *ATG17*, which operates as a scaffold protein at the PAS and helps to stimulate the kinase activity of Atg1, resulted in a near complete loss of Aly1-mediated rapamycin resistance and a moderate decrease in that conferred by Aly2 or Aly2^{K392R}-conferred resistance to rapamycin (Figure 6B, column 3; R.W.B, S.D., and K.C.) [204,272]. Further evaluation of the *atg17*Δ impact on other α-arrestins revealed a comparable dampening of Art1- and Art5-mediated resistance to rapamycin (Figure 5B-C; R.W.B, S.D., and K.C.). Mutants lacking *ATG31*, a protein also required for autophagy initiation that binds to Atg17, similarly prevent Aly1, Art1, and Art5 from conferring rapamycin resistance, though they appear to enhance this ability for Aly2 (Figure 6B, column 4 and 5B-C; R.W.B, S.D., and K.C.). As both Atg17 and Atg31 are important members of the Atg1 initiation complex, we were surprised to find almost no effect on α-arrestin-mediated resistance in the absence of *ATG1*, a kinase required for autophagy whose activity regulates multiple downstream components of the pathway (Figure 6B, column 2 and Figure 5C; R.W.B, S.D., and K.C.) [208].

Following the initiation of autophagy, the PI3K Complex I is recruited to the PAS to allow for the incorporation of PI3P in the phagophore's isolation membrane to recruit additional autophagic machinery [223,226,322,323]. This complex is composed of multiple subunits, including Atg6/Vps30, whose deletion confers strong resistance to rapamycin itself. Unexpectedly, the over-expression of WT or K-R mutant α-arrestins in the *atg6*Δ cells reduced Aly-mediated resistance to rapamycin (Figure 6B, column 7, 6C, and 5B-C; R.W.B, S.D., and K.C.). The autophagy-specific PI3K Complex I is defined by the presence of Atg38 and Atg14 in place of Vps38, which is contained in the vacuolar protein sorting-related PI3K Complex II [223,224]. Atg14 helps anchor the complex to the PAS through its interactions with Atg9, Atg13, and Atg17 [226,323]. Unlike *atg6*Δ cells, however, which is present in both PI3K complex forms,

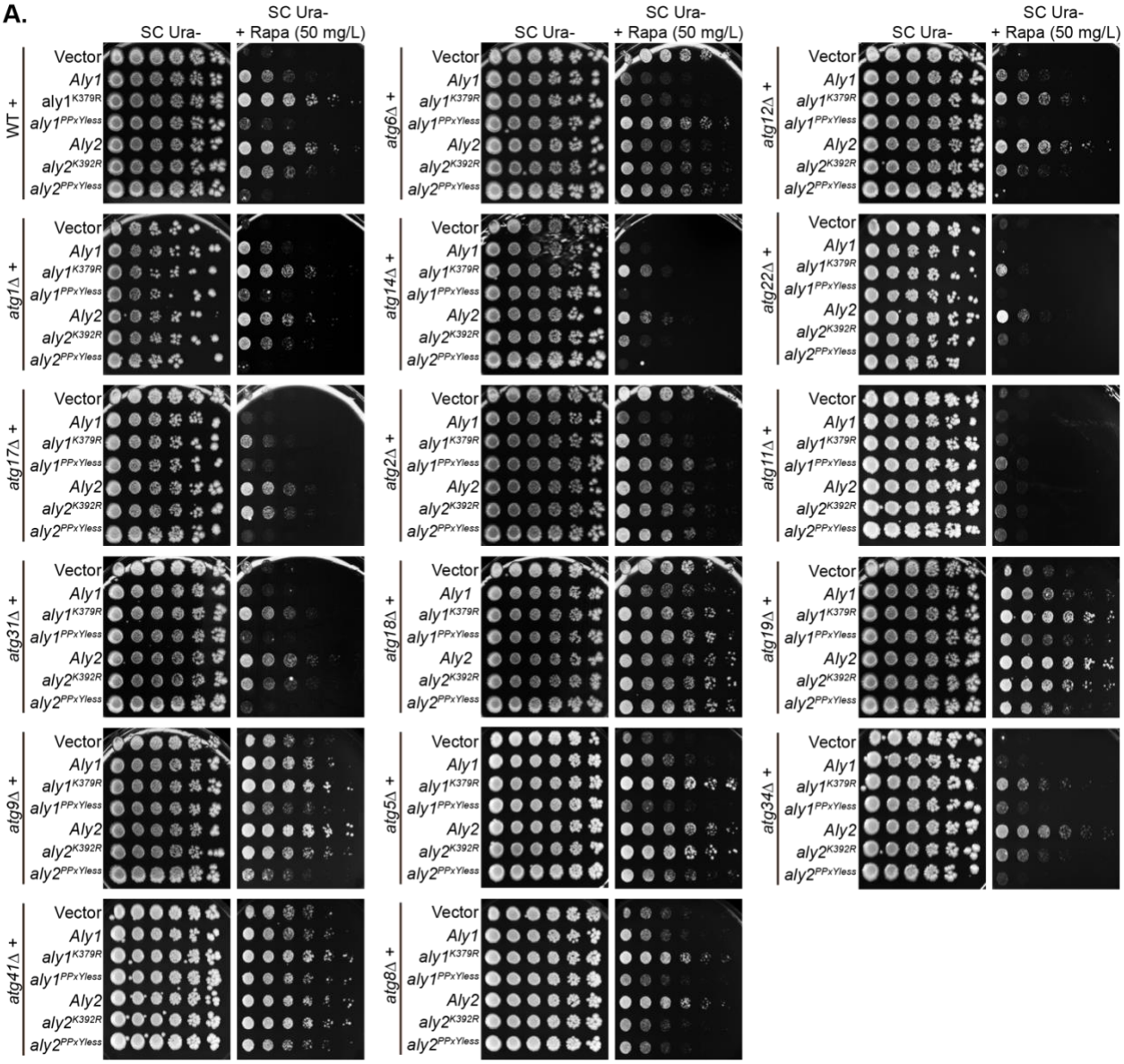

Figure 7. Loss of *ATG* family genes affects the ability of α-arrestins Aly1 and Aly2 to confer resistance to rapamycin.

(A) Serial dilution growth assays WT cells or those lacking the *ATG* family gene indicated containing a pRS426-derived plasmid expressing either nothing (vector) or the indicated α-arrestin or α-arrestin mutant under the control of its endogenous promoter on the medium indicated.

the loss of *ATG14* neither conferred its own rapamycin resistance nor exhibited any ability for α-arrestins to do the same (Figure 6B, column 8 and 5C; R.W.B, S.D., and K.C.). While the single concentration of rapamycin used in our evaluations may prevent identification of all genetic interactions, especially for those in this highly sensitive background, the differential effects observed in *atg6*Δ and *atg14*Δ cells suggest PI3K complexes I and II possess distinct roles in the cellular response to rapamycin treatment.

Once nucleated, the phagophore's isolation membrane requires an influx of lipid to efficiently expand and encapsulate cytosolic cargo. This feat is thought to be accomplished primarily by the PI3P-binding Vps13 family protein Atg2, which is localized to the tip of the growing phagophore through its interactions with Atg9 and Atg18 and facilitates lipid transfer from the ER [246,324,325]. As we observed in *atg6*Δ cells, those lacking *ATG2* exhibit a resistance to rapamycin that is attenuated when WT or mutant α-arrestins that are unable to be mono-ubiquitinated are over-expressed (Figure 6A, 6B column 9, 6C, and 5B-C; R.W.B, S.D., and K.C.). Similarly, the loss of Atg2's partner Atg18, which is a member of the PROPPIN family and binds both PI3P and PI(3,5)P_2, also confers rapamycin resistance that is diminished when WT α-arrestins or their K-R mutants are over-expressed (Figure 6B-C and 5B-C; R.W.B, S.D., and K.C.) [326–328]. The negative genetic interactions between Atg2, Atg6 and Atg18 and the α-arrestins suggests that these trafficking adapters may be tied to the lipid-related processes of autophagy.

In addition to macro-autophagy, we examined the effect of α-arrestins on the cytoplasm-to-vacuole targeting (Cvt) pathway, a selective form of autophagy that uses APs to traffic precursors of vacuolar proteases to the vacuole utilizing cargo receptors, including Atg11, Atg19, and Atg34 [165,172–180]. Similar to what we observed in *atg17*Δ cells, the loss of *ATG11* or

ATG34 results in strong rapamycin sensitivity that fails to be improved by the over-expression of α-arrestins (Figure 6B, columns 15-17 and 5C; R.W.B, S.D., and K.C.).

Though a significant portion of the autophagy-related genes we assessed possess genetic interactions with the α-arrestins, no discernable change in α-arrestin-induced rapamycin resistant arose with deletion of: 1) Atg9, the sole transmembrane protein among the autophagic machinery which is thought to serve as a seed for isolation membrane nucleation [130,220,245]; 2) Atg9's trafficking regulator Atg41 [329]; 3) the ubiquitin-like protein Atg8 that is integrated into AP membranes and helps to regulate their size and formation [232,330–332]; 4) the Atg5 and Atg12 proteins that control the activation and conjugation of Atg8 to phosphatidylethanolamine (PE) [232,237]; or 5) Atg22, the amino acid permease found in the vacuolar membrane which serves to transport the degradative products of autophagic degradation into the cytosol (Figure 6B-C; R.W.B, S.D., and K.C.) [276]. Collectively, these screens demonstrate extensive genetic connections between autophagy-related genes and the α-arrestins, with many ATG gene deletions altering α-arrestin induced resistance to rapamycin, the most notable of which are the lipid-related components Atg6, Atg2, and Atg18.

While the over-expression of select α-arrestins conferred resistance to rapamycin, their loss resulted in increased sensitivity to this drug. Indeed, the loss of either *ART1* or the combined loss of the paralogous *BUL1* and *BUL2* resulted in sensitivity to rapamycin, while *rim8*Δ and *aly1*Δ *aly2*Δ backgrounds displayed more modest degrees of sensitivity (Figure 5D). 9arrΔ cells further exhibited a near complete inability to grow on rapamycin-containing media, an effect likely tied to the absence of *ART1*, *ALY1*, and *ALY2* as the Buls are intact in this strain (Figure 5D) [59].

Given these results, as well as the findings of our genetic screen, I chose to further pursue the influence of *aly1*Δ *aly2*Δ, *art1*Δ, and 9arrΔ backgrounds on the cell's ability to generate and

traffic APs to the vacuole via electron microscopy. In order to preserve the autophagic bodies (ABs) normally rapidly degraded upon vacuolar entry, I further removed the gene *PEP4*, a master vacuolar protease whose loss prevents the maturation of many proteases and inhibits the degradative capacity of the vacuole [333,334]. This genetic modification thus allows for the evaluation of both autophagic flux, represented by the quantity of ABs found in the vacuoles of cells undergoing autophagy, and AP production, represented by the size of those same ABs [309]. Using this approach, I found that the absence of multiple α-arrestins in 9arrΔ cells strongly reduced both the size and abundance of ABs compared to the WT control (Figure 8A-C and 9A). Furthermore, I observed *art1*Δ and *aly1*Δ *aly2*Δ cells exhibited reduced AB size and a trend toward a lower number of ABs as well. Control cells lacking the essential AP component *ATG8* did not produce any detectable ABs (Figure 8A-C and 9A) [241]. A reduction in AB accumulation can be driven by defects in AP fusion to the vacuole, so I also assessed cells lacking the syntaxin-like t-SNARE Vam3, which is required AP fusion [263]. The cells lacking α-arrestins did not display any accumulation of APs in the cytosol, unlike what is observed in the *vam3*Δ control cells (Figure 8). We therefore thought it unlikely that the absence of α-arrestins caused a defect in AP-vacuolar fusion, favoring instead a model wherein α-arrestins influence an earlier stage of autophagy, such as initiation, nucleation, or phagophore expansion (Figure 8A compared to 9B-C). Notably, I observed the formation of low-electron density structures emanating from the cortical ER in *art1*Δ and 9arrΔ cells treated with rapamycin (Figure 8A, yellow arrows). We propose that, given their similarity in electron density to lipids, these structures likely represent the aberrant accumulation of lipids, but their identity requires further investigation to fully define. It is, however, tempting to speculate that the formation of these low electron-dense structures is linked to the phospholipid-related defects described later in this Chapter.

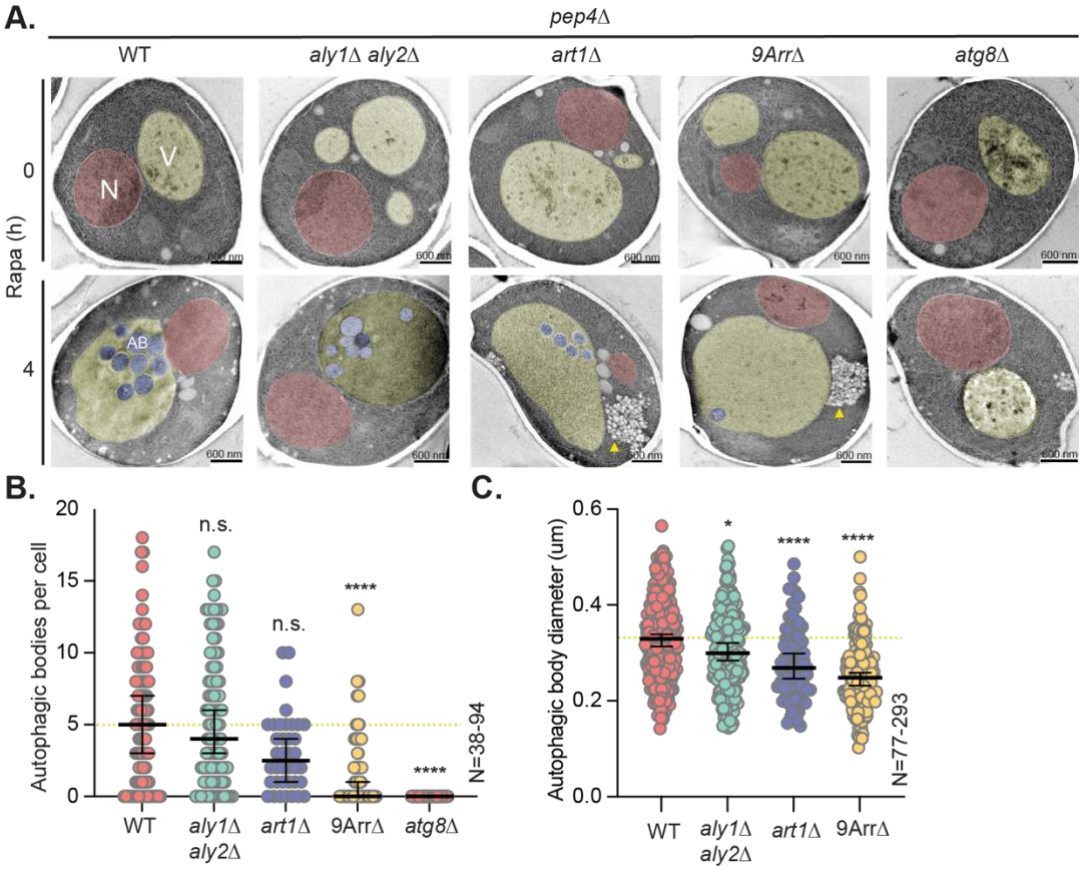

Figure 8. α-Arrestins help promote AP formation and are needed for accumulation of vacuolar autophagic bodies.

(A) Electron micrographs of cells lacking *PEP4* and the indicated α-arrestins were obtained. Cells are either untreated or treated for 4 h with 200ng/mL rapamycin. Cellular compartments are false colored (N = nucleus in red; V = vacuole in yellow; AB = autophagic body in blue). Yellow arrows mark aberrant structures with low electron density. Scale bars are equal to 600nm. (B-C) The number of autophagic bodies (B) accumulating in the vacuole and diameter of each autophagic body (C) was determined from the EM images in (A) and is plotted. The median number is shown as a black line for each group and error bars represent the 95% confidence interval. For reference, a yellow dashed line represents the median ratio value for WT prior to rapamycin treatment. Kruskal-Wallis statistical analysis with Dunn's post hoc test was performed to compare each distribution to that of the *pep4*Δ cells) (n.s. = not significant; **** = p-value <0.0001).

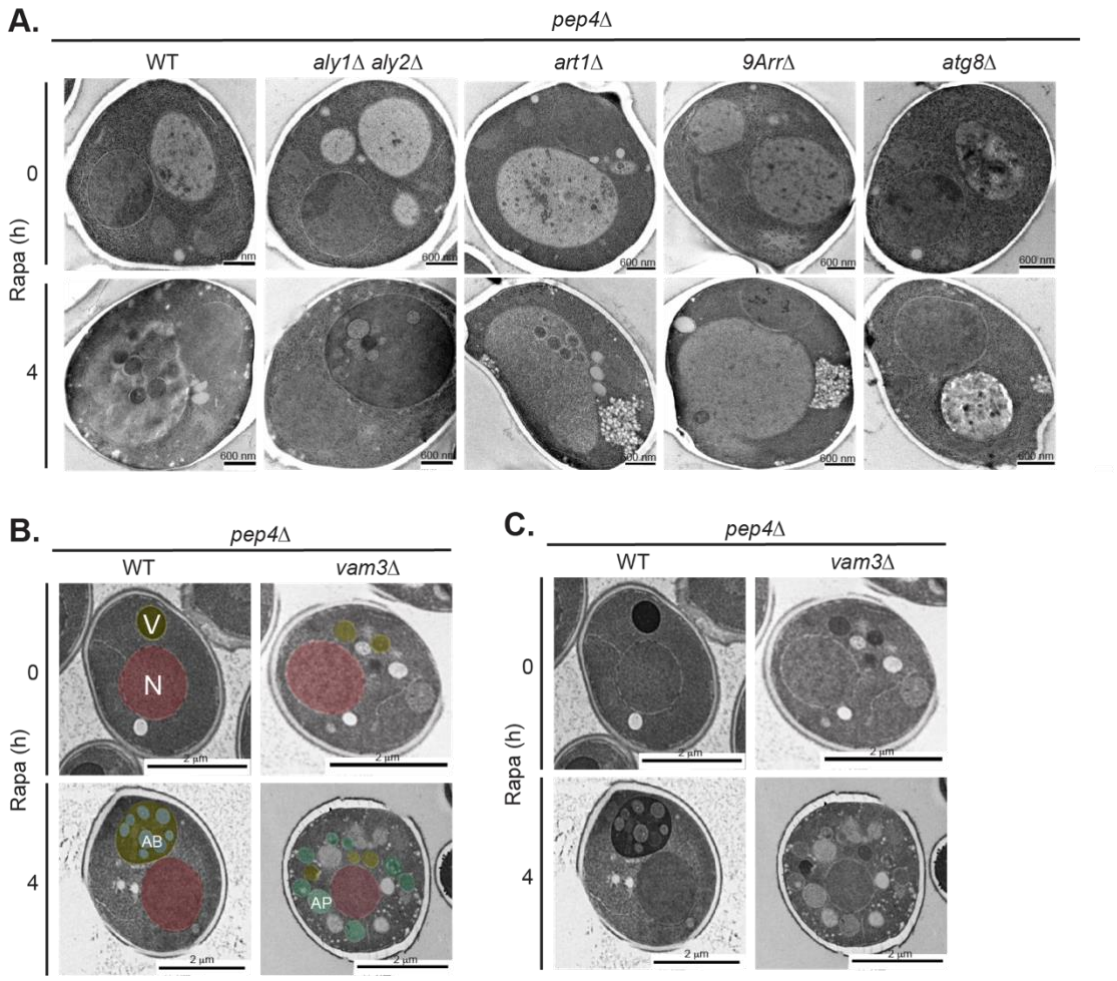

Figure 9. Loss of *VAM3* results in an accumulation of APs in the cytosol.

(**A**) Electron micrographs for the data shown in Figure 8A are provided without false coloring to allow readers to better gauge the density of organelles in the cells. (**B**-**C**) Electron micrographs of WT or *vam3*Δ cells lacking *PEP4* were obtained. Cells are either untreated or treated for 4 h with 200ng/mL rapamycin. In (**B**), the cellular compartments are false colored (N = nucleus in red; V = vacuole in yellow; AB = autophagic body in blue; AP = AP in green); however in (**C**) the unmodified cells shown in (**B**) are also shown. Scale bars are equal to 2 μm.

In order to further evaluate the potential α-arrestin-driven effects on AP formation and vacuolar delivery, I utilized time-lapse confocal microscopy to rapidly (30s intervals) capture images of cells expressing *ATG8pr*-GFP-*ATG8*, an established reporter of AP formation and trafficking that is directly conjugated to autophagosomal membranes (Figure 6C) [309]. Using

these data, I then measured the period of time between GFP-Atg8 puncta appearance and its vacuolar entry to evaluate the efficiency of AP production and trafficking, and found that these structures persist for longer in cells lacking α-arrestins (Figure 10A-B, S1-4 movies, available in 'Chapter 2' folder at OneDrive link: Supplemental Thesis Documents - Bowman). These results align with the EM observations and further suggest a requirement for the α-arrestins in the efficient formation of APs.

2.3.3 α-Arrestins are required for efficient GFP-Atg8 autophagic flux

To further evaluate GFP-Atg8, I used confocal microscopy to assess its vacuolar transport in WT and α-arrestin mutant cells. At steady state, prior to the inhibition of TORC1, I found GFP-Atg8 localized largely to the cytosol and formed occasional puncta that likely represent AP formation as part of the CVT pathway (Figure 11A). Following TORC1 inactivation by rapamycin, Atg8 is recruited to the PAS to assist in AP formation, exhibited by the frequent formation of puncta close to the limiting membrane of the vacuole (Figure 11A) [169,203,206,335]. Prior to the fusion of completed APs to the vacuole, Atg8 conjugated to their outer membrane is released from its PE anchor and released into the cytosol. The portion of Atg8 present on the inner membrane, however, travels with the AB into the vacuolar lumen for degradation [236,239,241]. Here, free GFP cleaved from GFP-Atg8 accumulates, due to the fact that GFP is somewhat resistant to protease digestion, in proportion with AP delivery thereby providing a quantitative readout of autophagic flux. These data are often interpreted by the ratio of vacuolar-to-whole cell GFP signal [236]. While the steady-state vacuolar:whole cell ratio was no different in α-arrestin mutants than WT cells, the induction of autophagy by rapamycin treatment resulted in a significant reduction of

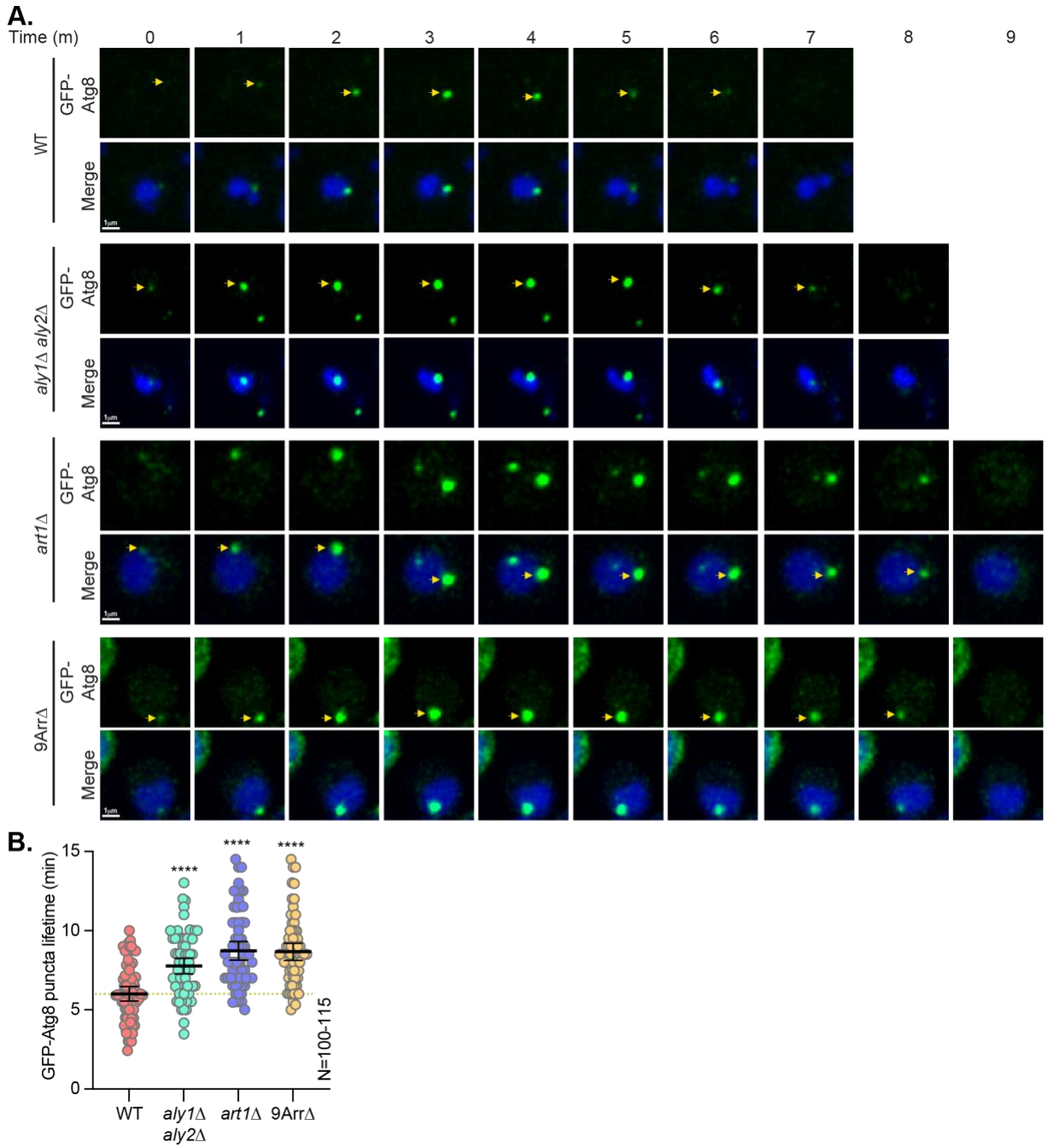

Figure 10. α-Arrestins are required for efficient AP delivery to the vacuole.

(A) Cells expressing *ATG8pr*-GFP-Atg8 in either WT or α-arrestin mutant cells were imaged by confocal microscopy at 1min intervals following 1h treatment with 200ng/mL rapamycin. CMAC is used to stain the vacuoles (shown in blue). Yellow arrows indicate the GFP-Atg8 puncta, representing APs. 3D projection videos of these cells over the same time periods are available in S1-4 Movies. (B) Quantification of lifetimes for the GFP-Atg8 puncta shown in (A), measured from appearance to merging with the vacuole, is shown as a graph. The lifetime of each puncta is

plotted as a circle. The median lifetime is shown as a black line and error bars represent the 95% confidence interval. For reference, a yellow dashed line represents the median lifetime for WT. Kruskal-Wallis statistical analysis with Dunn's post hoc test was performed to compare the lifetime distributions. Statistical comparisons between mutant and WT cells at that same time point are displayed in black asterisks (n.s. = not significant; four symbols has a p-value <0.0001).

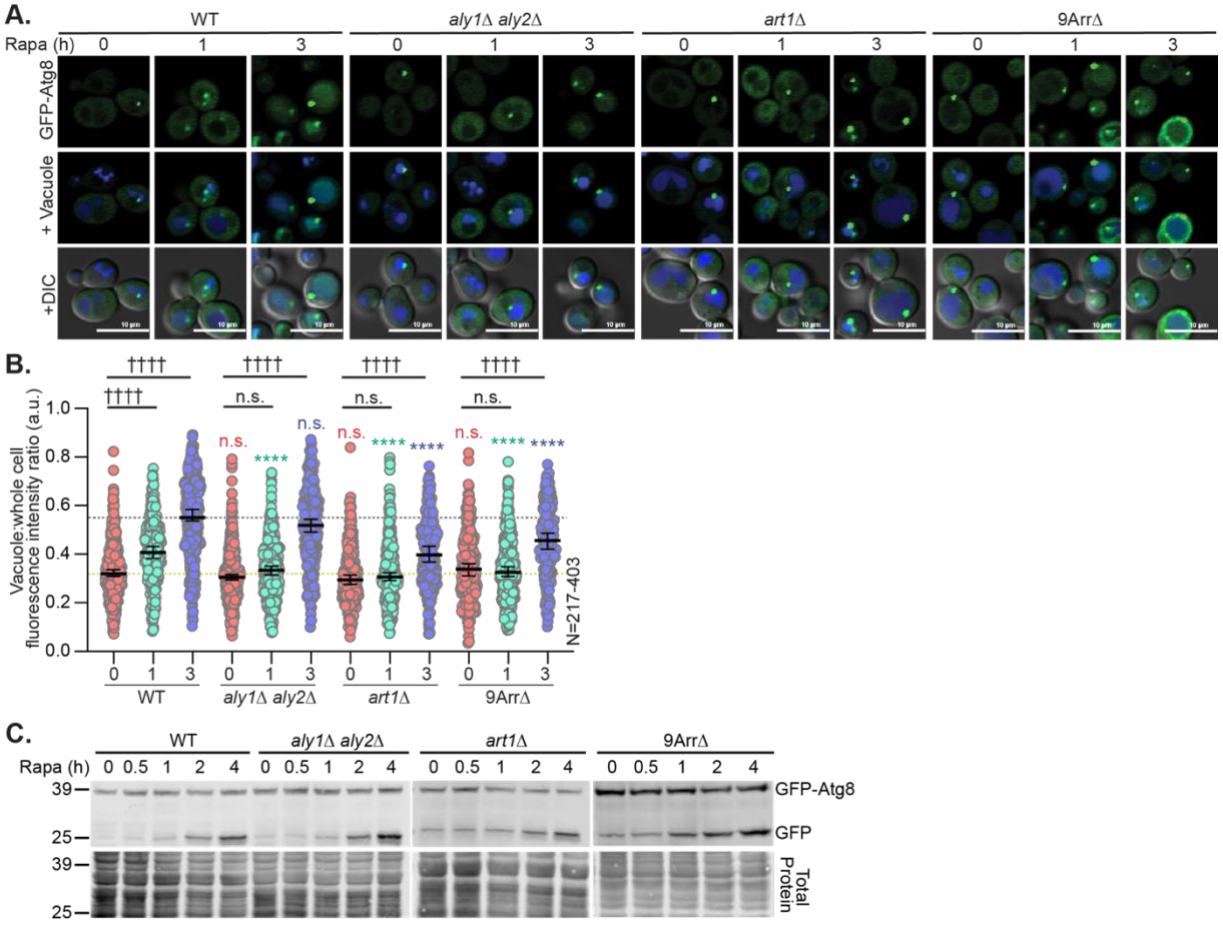

Figure 11. α-Arrestins are required for optimal autophagic flux.

(A) Cells expressing pRS416-*ATG8pr*-GFP-Atg8 in either WT or α-arrestin mutant cells were imaged by confocal microscopy at the indicated time post-treatment with 200ng/mL rapamycin. CMAC is used to stain the vacuoles (shown in blue). The merge (+DIC) contains the bright field cell image for reference. (B) Quantification of vacuolar to whole-cell fluorescence intensity ratio using Nikon.*ai* software (see Section 2.2.11) for the cells imaged in panel (A) is shown as a scatter plot. The ratio of vacuolar to whole-cell GFP intensity is plotted for each cell as a circle. The

median ratio is shown as a black line and the error bars represent the 95% confidence interval. For reference, yellow and grey dashed lines represent the median ratio value for WT prior to and post rapamycin treatment, respectively. Kruskal-Wallis statistical analysis with Dunn's post hoc test was performed to compare the ratio distributions. Statistical comparisons between mutant and WT cells at that 0, 1, and 3 hours post rapamycin are shown as red, green, and blue asterisks respectively. Statistical comparisons of WT or mutant cells to their respective t=0 timepoints are shown as black daggers. (n.s. = not significant; four symbols has a p-value <0.0001). (C) Protein extracts from cells as described in (A) were immunoblotted and probed with anti-GFP antibody. The REVERT total protein stain of the membrane is the loading control. Molecular weights are shown on the left side in kDa.

this value in the absence of the trafficking adapters (Figure 11A-B). In support of a defect in the efficiency of AP delivery to the vacuole, I found mutants lacking α-arrestins exhibited reduced ratios of vacuolar:whole cell fluorescence (Figure 11B). By 3h post-rapamycin treatment, both *art1*Δ and 9arrΔ cells still had reduced ratios of GFP signal, while in aly1Δ aly2Δ cells the GFP signal was comparable to that of WT.

A complementary biochemical assessment of GFP-Atg8 and autophagic flux can be accomplished via SDS-PAGE and immunoblotting to examine the abundance of free GFP breakdown product, produced in the vacuole, to that of full-length GFP-Atg8 [273,309]. When employing this method, 9arrΔ mutant cells exhibited higher levels of both free GFP and GFP-Atg8 prior to autophagy induction, indicating a potential increase in the expression of Atg8 due to the altered nutrient and metabolic landscape in this background (Figure 11C; N.O.). While the ratio of free GFP:GFP-Atg8 rose rapidly in WT and *aly1*Δ *aly2*Δ following the addition of rapamycin, this progression was noticeably altered in *art1*Δ and, especially, 9arrΔ cells where the levels of full length GFP-Atg8 abundance appeared to increase more rapidly than their corresponding GFP breakdown products (Figure 11C; N.O.). Together with the microscopy, these results further corroborate a defect in flux of APs to the vacuole in cells lacking α-arrestins.

2.3.4 α-Arrestins are important for phagophore expansion but are not required for Atg9 recruitment to the PAS

The nucleation of the isolation membrane at the PAS is thought to be initiated by the arrival of Atg9, embedded in small membrane-bound vesicles that represent a membrane 'seed' to produce APs. Atg9 also helps to anchor the Atg2/Atg18 lipid transfer complex to the tips of growing isolation membranes, while helping to distribute the components being transported by that complex via its lipid scramblase activity (Figure 6C) [211,214,220,336,337]. Atg9 abundance and recruitment to the PAS is critical for the progression of autophagy, with defects resulting in impaired AP production [130]. Using live-cell confocal microscopy of cells expressing endogenously tagged Atg9-mNG, there was no significant difference in the sum of whole-cell abundance of Atg9 between α-arrestin mutants and the WT control prior to rapamycin treatment, with each exhibiting a similar increase in abundance following autophagy induction (Figure 12A-C). While the mean intensity of Atg9 displayed some changes from the WT in 9arrΔ cells, this is likely attributable to their larger cell size (compare Figure 12B-C). Though the sum of Atg9's whole-cell fluorescence remained unchanged, we were curious whether there may be a defect in its intracellular trafficking, as has been linked to impaired autophagy initiation [211,219]. Atg9 is not only recruited to the PAS to seed AP formation, but also subsequently removed and recycled back to its cytosolic pools following AP completion, a process that utilizes the clathrin adapter complex AP-3 and retromer to control Atg9's trafficking regulator Atg27 [214,215]. However, evaluation of the AP-3-dependent cargoes Ypq2 and Yck3 by live-cell fluorescence microscopy revealed similar vacuolar membrane localization in both α-arrestin mutants and WT cells, suggesting this trafficking pathway is not disrupted by the loss of α-arrestins (Figure 13A-B; A.C.)

[338,339] Likewise, I found that the localization of retromer subunit, Vps17, and retromer cargo, Vps10, to be similarly unaffected (Figure 13C-D) [305,340]. Taken together, these results suggest that, as with Atg9's whole-cell abundance, the loss of α-arrestins does not disrupt the trafficking pathways controlling Atg9.

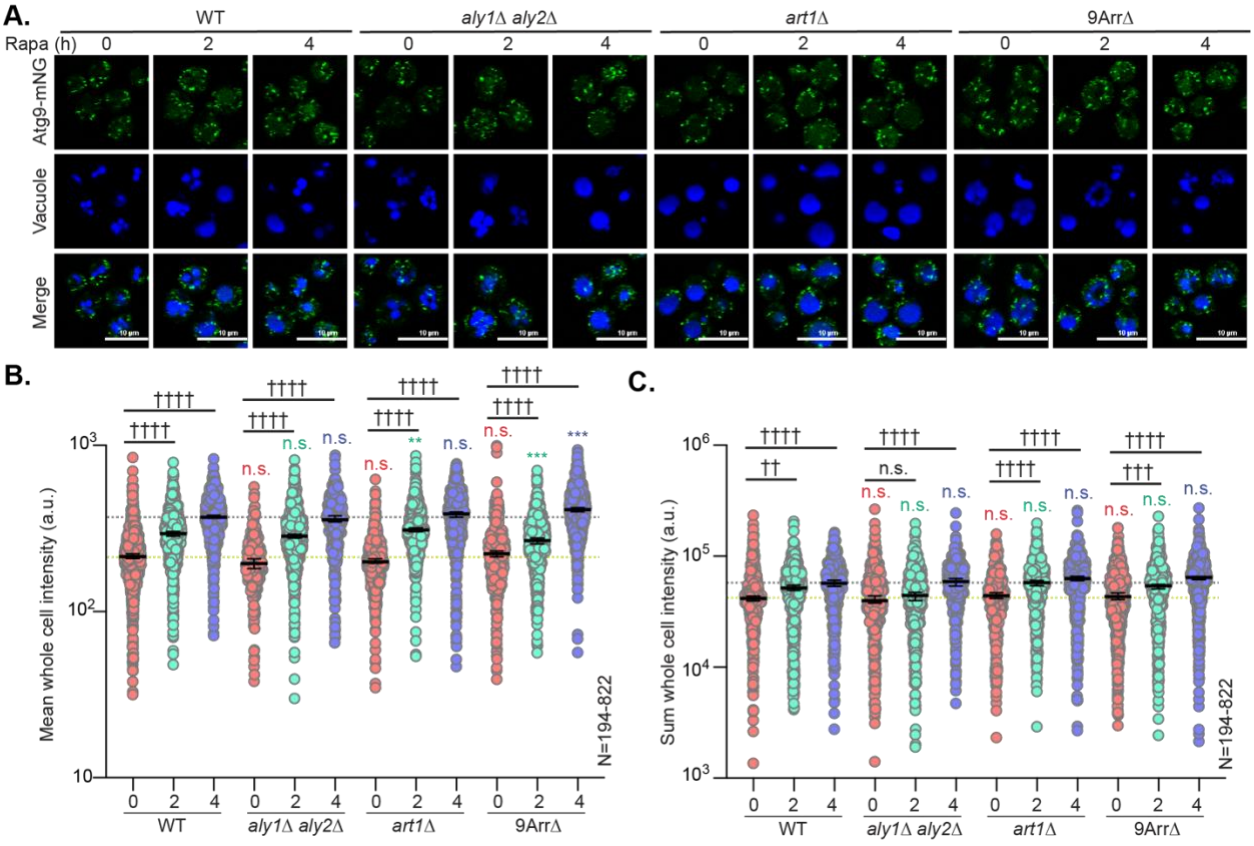

Figure 12. Atg9 abundance is not disrupted in the absence of α-arrestins.

(A) Either WT or α-arrestin mutant cells expressing Atg9-mNG from its chromosomal locus were imaged by confocal microscopy at the indicated times post-treatment with 200ng/ml rapamycin. CMAC was used to stain the vacuolar lumen (shown in blue). (B) Quantification of the mean whole cell mNG intensity using Nikon.*ai* software (see Section 2.2.11) for the cells in (A) is plotted for each cell as a circle. The median value is shown as a black line and the error bars represent the 95% confidence interval. For reference, a yellow or grey dashed line represents the median intensity value for WT prior to or following 4h of rapamycin treatment, respectively. Kruskal-Wallis statistical analysis with Dunn's post hoc test was performed to compare the intensity distributions. Statistical comparisons between mutant

and WT cells at that 0, 2, and 4 hours post rapamycin are shown as red, green, and blue asterisks respectively. Statistical comparisons of WT or mutant cells to their respective t=0 timepoints are shown as black daggers. (n.s. = not significant; four symbols has a p-value <0.0001). (C) Quantification of the sum whole cell mNG intensity using Nikon.*ai* software for the cells in (A) is plotted for each cell as a circle. The median value is shown as a black line and the error bars represent the 95% confidence interval. For reference, a yellow or grey dashed line represents the median intensity value for WT prior to or following 4h of rapamycin treatment, respectively. Statistical analyses and comparisons are as in (B).

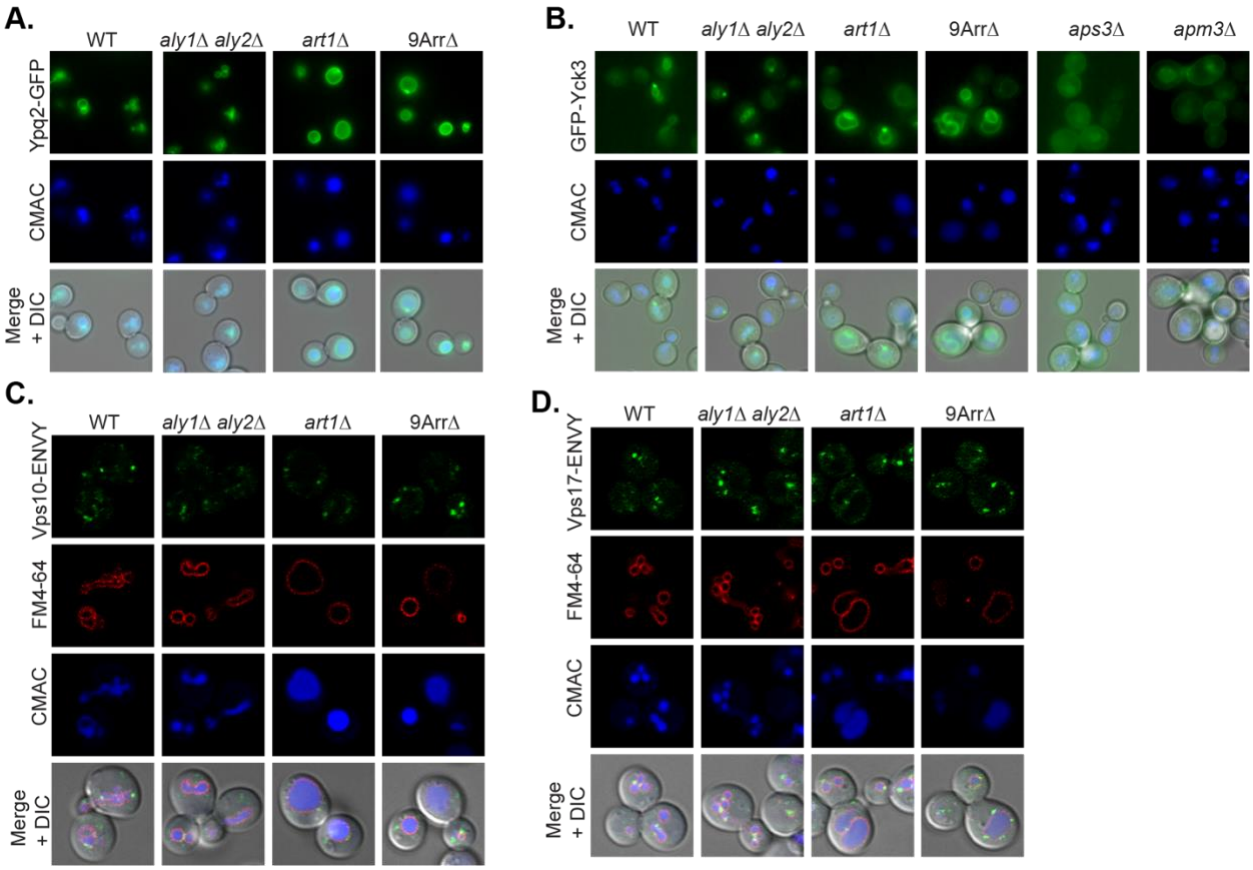

Figure 13. Retromer- and AP-3-dependent trafficking are not impaired in the absence of α-arrestins.

(A) Either WT or α-arrestin mutant cells expressing pRS415-*TEF1pr*-Ypq2-GFP were imaged by epifluorescent microscopy. CMAC was used to stain the vacuolar lumen (shown in blue). (B) Either WT or α-arrestin mutant cells expressing pRS416-GFP-Yck3 (gift from Weisman lab, Univ. of Michigan) were imaged by epifluorescent microscopy. CMAC was used to stain the vacuolar lumen (shown in blue). (C) Either WT or α-arrestin mutant cells

expressing Vps10-ENVY from its chromosomal locus were imaged by epifluorescent microscopy. CMAC and FM4-64 was used to stain the vacuolar lumen (shown in blue) or membrane (shown in red), respectively. (D) Either WT or α-arrestin mutant cells expressing Vps17-ENVY from its chromosomal locus were imaged by epifluorescent microscopy. CMAC and FM4-64 was used to stain the vacuolar lumen (shown in blue) or membrane (shown in red), respectively.

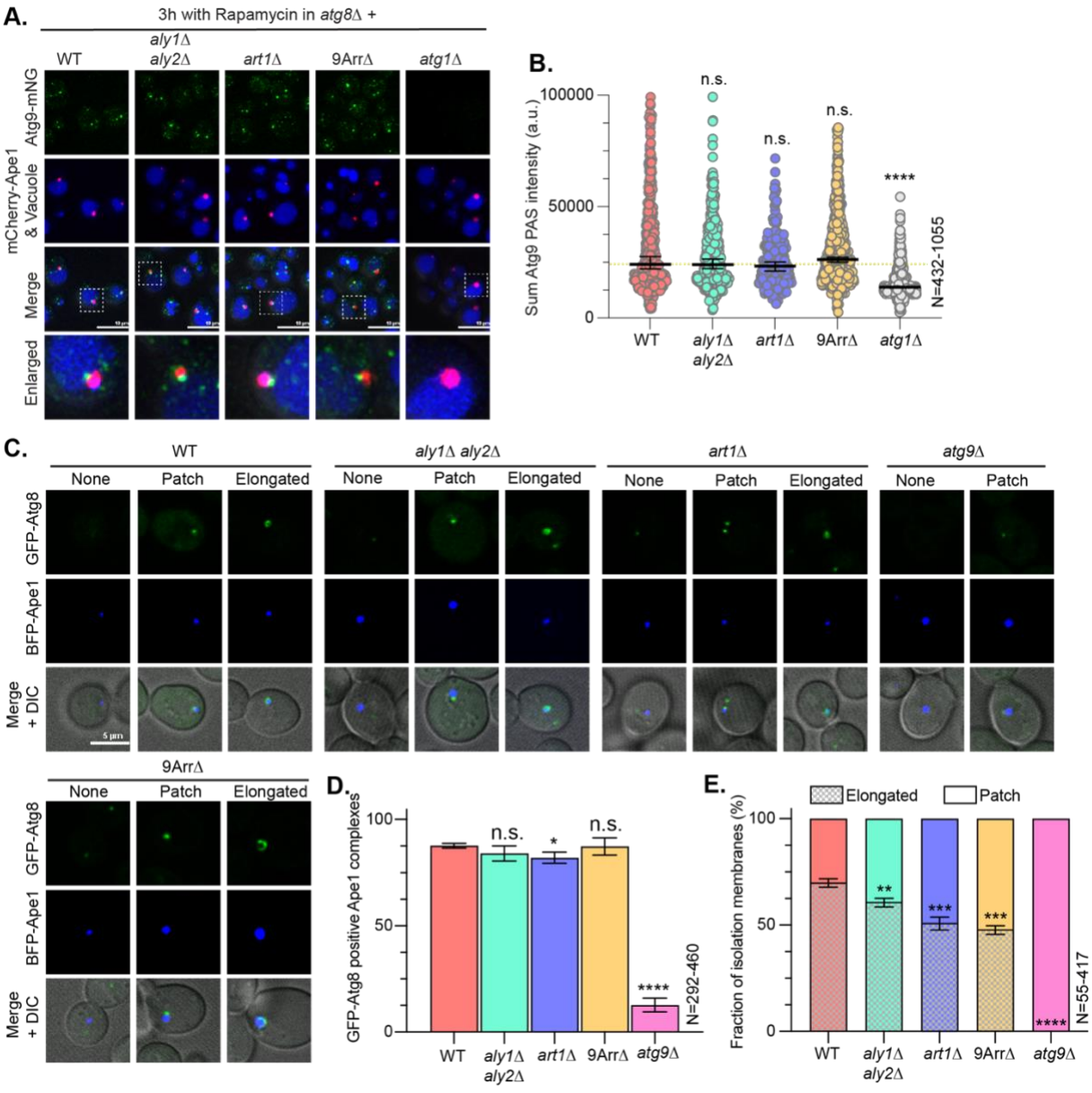

Figure 14. α-Arrestins are required for proper phagophore expansion.

(**A**) Cells lacking *ATG8*, which stalls AP production, and expressing chromosomally integrated Atg9-mNG from its endogenous locus in either WT, *atg1*Δ, or α-arrestin mutant, were imaged by confocal microscopy after 3h treatment

with 200ng/mL rapamycin. pRS416-*ADH1pr*-mCherry-Ape1 (gift from Segev lab, Univ. of Illinois at Chicago) was used to mark the PAS, while CMAC and FM4-64 were used to stain the vacuolar lumen (shown in blue) or membrane (shown in red), respectively. (**B**) The sum of the Atg9-mNG intensity at mCherry-Ape1-marked puncta, which represents the PAS, using Nikon.*ai* software (see Section 2.2.11) for the cells imaged as in (**A**) was plotted for each cell as a circle. The median value is shown as a black line and the error bars represent the 95% confidence interval. For reference, a yellow dashed line represents the median intensity value for WT. Kruskal- Wallis statistical analysis with Dunn's post hoc test was performed to compare the intensity distributions. Statistical comparisons between mutant and WT cells are displayed in black asterisks (n.s. = not significant; **** = p-value <0.0001). (C) Representative images displaying Atg8-positive structures from cells expressing *ATG8pr*-GFP-Atg8 [302] under the control of its own promoter and *CUP1pr*-BFP-Ape1 (gift from Kraft Lab, Univ. of Freiburg) were imaged by confocal microscopy 1h post-treatment with 200ng/mL rapamycin. The merge (+DIC) contains the bright field cell image for reference. (D) The mean percentage of cells with GFP-Atg8 positive Ape1 puncta, indicative of nucleated APs, from the images in (C) were plotted. Error bars represent the standard deviation. Unpaired t tests were performed to compare the percentages of GFP-Atg8 positive Ape1 puncta. Statistical comparisons between mutant and WT cells are displayed in black asterisks (n.s. = not significant; **** = p-value <0.0001). (E) The mean percentage of cells with either elongated GFP-Atg8 (colored bar), indicative of AP membrane expansion, or patched GFP-Atg8 (colored and hatched bar), indicative of initiated but not expanded APs, from the images in (C) were plotted. Error bars represent the standard deviation. Unpaired t tests were performed to compare the percentages of elongated structures. Statistical comparisons between mutant and WT cells are displayed in black asterisks (n.s. = not significant; **** = p-value <0.0001).

Finally, in order to assess the ability of cells to recruit Atg9 to the PAS, I utilized a background lacking *ATG8* that stalls AP formation but permits recruitment of other autophagy factors, like Atg9 and the classical CVT cargo Ape1 [341]. I expressed mCherry-Ape1 in this background as a marker of the PAS and measured the abundance of endogenously tagged Atg9-mNG at this structure after 3h of rapamycin treatment using live-cell confocal microscopy. Unlike cells lacking *ATG1*, the kinase responsible for the activation of Atg9 during autophagy, where I

observed no detectable Atg9 signal at the PAS, α-arrestin-mutants were nearly indistinguishable from the WT control (Figure 14A-B) [130]. As a result, our collective evaluation of Atg9 and the pathways that control its trafficking suggest that the impairment of autophagic flux observed in cells lacking α-arrestins is not driven by defects associated with Atg9 or this protein's involvement in the seeding of AP formation.

Having sufficiently ruled out isolation membrane nucleation as the source of the autophagy impairment observed in the absence of α-arrestins, I decided to next evaluate phagophore expansion using the 'giant Ape1' assay (Figure 14C-E) [130]. In this approach a massive complex of Ape1, driven by its over-expression (thus, 'giant' Ape1), is formed in cells and this allows us to monitor its encapsulation via isolation membrane expansion at the PAS [130]. These efforts by the cell result in the formation of a distinctive cup-shaped membrane, marked with Atg8, that wraps around the giant Ape1 complex. In contrast, when isolation membrane expansion is impaired, a smaller patch of membrane associates with the Ape1 structure but fails to elongate. By employing GFP-Atg8 to mark the isolation membrane, and over-expressing BFP-tagged Ape1, I thus evaluated the ability of WT and α-arrestin mutants to properly recruit Atg8 and undergo phagophore membrane expansion following rapamycin treatment using live-cell confocal microscopy. Further supporting our conclusions regarding Atg9 recruitment, α-arrestin mutants displayed no strong changes in their ability to recruit and form Atg8 puncta to the giant Ape1-marked PAS, while those lacking *ATG9* were severely impaired in this function (Figure 14D) [130]. Critically, however, a significantly reduced fraction of *aly1*Δ *aly2*Δ cells were found to produce elongated cup-like structures, and *art1*Δ and 9arrΔ cells were even further impaired (Figure 14E). These findings thus support a requirement for the α-arrestins in allowing the proper

expansion of the phagophore membrane, consistent with the reduced AB accumulation and prolonged GFP-Atg8 puncta lifetimes displayed in previous assays (Figures 8 and 10).

2.3.5 α-Arrestins do not alter TORC1 distribution or regulation of Atg13

Autophagy is inhibited under nutrient replete conditions by TORC1's phosphorylation of Atg13, thereby preventing the subsequent activation of the Atg1 kinase that controls further portions of the autophagy machinery (Figure 6C) [205,281]. Given the rich genetic connections between components involved in autophagy initiation and the α-arrestins, and the impaired AB delivery in cells lacking α-arrestins, we further evaluated the impact of α-arrestin mutants on the phospho-status of Atg13 using SDS-PAGE and immunoblotting before and after rapamycin treatment (Figure 15A; S.D.). We found Atg13 exhibited a similar electrophoretic mobility in WT and α-arrestin mutants prior to the addition of rapamycin, indicating TORC1 is active and able to phospho-inhibit Atg13 and autophagy (Figure 15A; S.D.). Similarly, we found the electrophoretic profile of Atg13 post-rapamycin addition to be nearly identical in WT and α-arrestin mutant cell extracts, with both displaying evidence of Atg13's dephosphorylation (Figure 15A; S.D.). Together, these results suggest that the absence of α-arrestins does not result in any defect in TORC1's control of Atg13.

While the majority of the TORC1 complex resides on the limiting membrane of the vacuole, Atg13's phospho-inhibition is accomplished by a second TORC1 population found in endosomes [287,342]. In order to determine the effect of α-arrestin loss on the distribution of this complex, we assessed the localization of plasmid-borne GFP-tagged Tor1, the kinase subunit that defines TORC1, via live-cell confocal microscopy (Figure 15B-E; R.W.B. and E.J.). Tor1's

vacuolar localization was quantified using both manual (Figure 15C; E.J.) and automated (Figure 15D) methods (see Section 2.2.11). This served to validate my automated approach using the

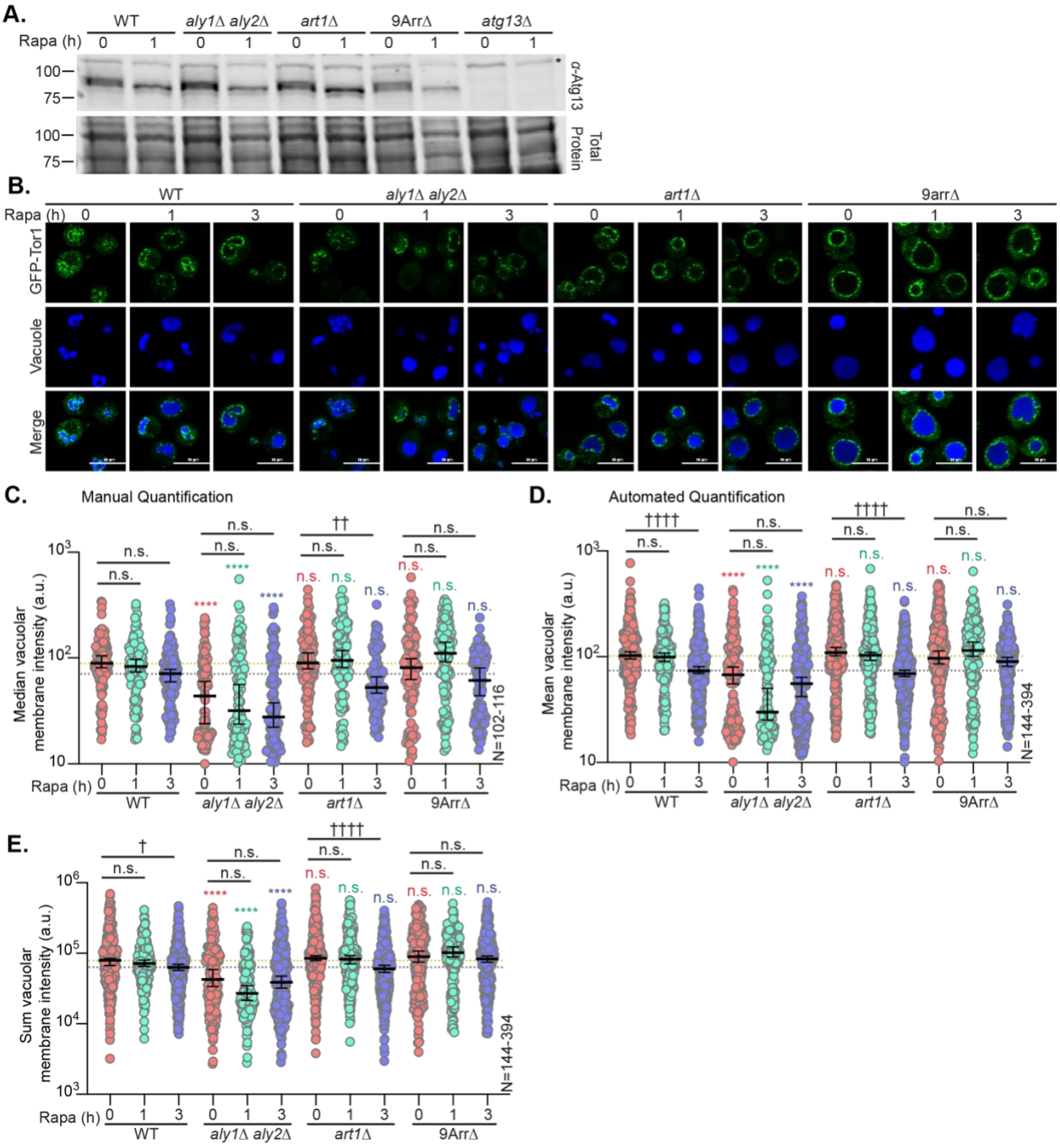

Figure 15. Tor1 signaling and localization are not affected by the loss of α-arrestins.

(**A**) WT cells or cells lacking the indicated α-arrestin were harvested at the indicated time points post-treatment with 200ng/mL rapamycin. Whole-cell protein extracts were made, analyzed by SDS-PAGE, immunoblotted and probed

with anti-Atg13 antibody (gift Kraft lab, Univ. of Freiburg). REVERT total protein stain of the membrane is the loading control and molecular weights are shown on the left in kDa. A non-specific band is marked with an asterisk (*). (**B**) Cells expressing *TOR1pr*-Tor1-GFP (gift from Ford lab, Univ. of Pittsburgh) in either WT or α-arrestin mutant cells were imaged by confocal microscopy at the indicated times post-treatment with 200ng/mL rapamycin. CMAC is used to stain the vacuoles (shown in blue). (**C**) Manual quantification of the median GFP intensity at the vacuolar membrane using ImageJ software (see Section 2.2.11) for the cells in panel (**B**) is shown as a graph. The median GFP intensity is plotted for each cell as a circle. The median value of each population is shown as a black line and the error bars represent the 95% confidence interval. For reference, a yellow or grey dashed line represents the median value for WT prior to or after 3h of rapamycin treatment, respectively. Kruskal-Wallis statistical analysis with Dunn's post hoc test was performed to compare the intensity distributions. Statistical comparisons between mutant and WT cells at that 0, 1, and 3 hours post rapamycin are shown as red, green, and blue asterisks, respectively. Statistical comparisons of WT or mutant cells to their respective t=0 timepoints are shown as black at the vacuolar membrane using Nikon.*ai* software (see methods) for the cells in panel (**B**) is shown as a graph. The mean GFP intensity is plotted for each cell as a circle. The median value is shown as a black line and the error bars represent the 95% confidence interval. For reference, a yellow or grey dashed line represents the median value for WT prior to or after 3h of rapamycin treatment, respectively. Statistical analyses and comparisons are as in (**C**). (**E**) Quantification of the sum GFP intensity at the vacuolar membrane using Nikon.*ai* software for the cells in panel (**A**) is shown as a graph. The sum GFP intensity is plotted for each cell as a circle. The median value is shown as a black line and the error bars represent the 95% confidence interval. For reference, a yellow or grey dashed line represents the median value for WT prior to or after 3h of rapamycin treatment, respectively. Statistical analyses and comparisons are as in (**C**). daggers/text. (n.s. = not significant; four symbols has a p-value <0.0001). (D) Quantification of the mean GFP intensity

machine learning platform NIS.*ai*, as each conveyed similar results (compare Figure 15C and D; R.W.B. and E.J.). Indeed, neither method found any significant difference in the median/mean level of GFP-Tor1 at the vacuolar membrane prior to rapamycin treatment for WT and *art1*Δ or 9arrΔ cells (Figure 15B-D; R.W.B. and E.J.). We did, however, notice a stark difference in the vacuolar morphology of WT and α-arrestin mutants, finding *aly1*Δ *aly2*Δ to possess hyper-

fragmented vacuoles, while those in *art1*Δ and 9arrΔ were most often enlarged and uni-lobed (Figure16A). Further manual and automated quantification of the lengths of the vacuolar membranes showed that they were significantly larger in the absence of *ART1* and the 9arrΔ cells than in WT cells (Figure 16B-C; R.W.B. and E.J.). As a consequence of these differences, I chose to assess both the concentration of the fluorescent signal, expressed by the mean pixel intensity (Figure 15D), and their total abundance, expressed by the sum pixel intensity (Figure 15E). In WT cells, I found the concentration of Tor1 at the vacuolar membrane to be significantly reduced after treatment with rapamycin (Figure 15C-D; R.W.B. and E.J.), likely driven by a concomitant increase in vacuolar membrane length that thins the largely stable total abundance of Tor1 at this structure (Figure 15E and 16B-C; R.W.B. and E.J.). A similar decrease in Tor1 concentration at the vacuolar surface and increase in vacuolar size post-rapamycin was observed in *art1*Δ cells (Figures 15C-D and 16B-C; R.W.B. and E.J.). In rapamycin treated 9arrΔ cells, however, I found no significant changes in the concentration or total abundance of vacuolar Tor1, with the sizes of the vacuole undergoing more modest changes as well (Figures 15C-D and 16B-C; R.W.B. and E.J.). Despite similar changes in vacuolar size to WT cells, I was surprised to find two populations of Tor1 in cells lacking *ALY1* and *ALY2*, with one displaying a stark reduction in both the concentration and abundance of Tor1 pre- and post-rapamycin addition (Figures 15C-E and 16B-C; R.W.B. and E.J.). While these changes I observed in Tor1 may be tied to the autophagy defects described for *aly1*Δ *aly2*Δ, it does not appear to be associated with TORC1's control of Atg13 (Figure 15A; S.D.).

As the over-expression of select α-arrestins confers resistance to the TORC1-inhibiting drug rapamycin, I further compared Tor1's localization in WT cells to those over-expressing Aly1, Aly2, or Art1 (Figure 17A-C). Since we found no significant changes in the concentration or

abundance of Tor1 at the vacuolar membrane of WT and α-arrestin-overexpressing cells, we concluded that changes in TORC1 localization are unlikely to be responsible for the latter's ability to resist rapamycin-induced growth inhibition (Figure 17A-C). Collectively, these evaluations lead us to suggest that the defect in autophagy found in cells lacking α-arrestins is not being driven by changes in TORC1 localization or its control of Atg13 phosphorylation.

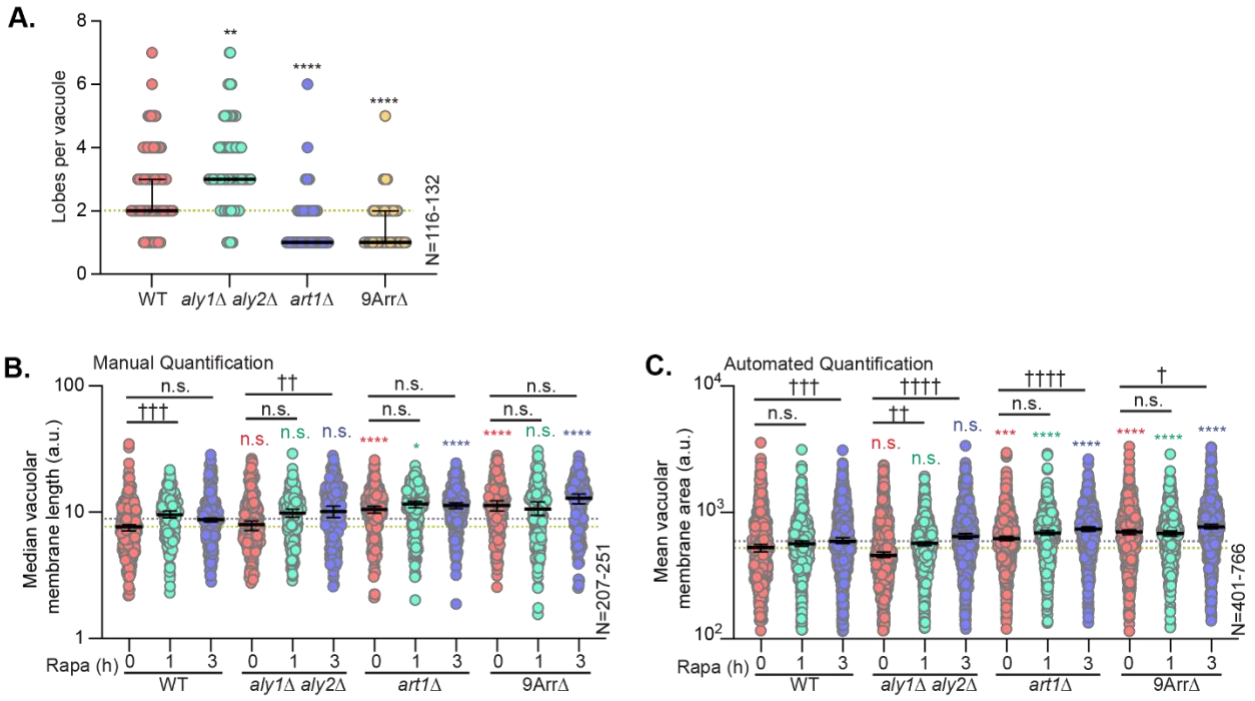

Figure 16. Vacuole morphologies are altered in the absence of α-arrestins.

(A) Manual quantification of the vacuolar membrane length as defined using Image J for the cells in Figures 15B and 18B is plotted for each cell as a circle. The median value is shown as a black line and the error bars represent the 95% confidence interval. For reference, a yellow or grey dashed line represents the median intensity value for WT prior to or following 3h of rapamycin treatment, respectively. Kruskal-Wallis statistical analysis with Dunn's post hoc test was performed to compare the intensity distributions. Statistical comparisons between mutant and WT cells at that 0, 1, and 3 hours post rapamycin are shown as red, green, and blue asterisks respectively. Statistical comparisons of WT or mutant cells to their respective t=0 timepoints are shown as black daggers. (n.s. = not significant; four symbols has a p-value <0.0001). (B) Automated quantification using Nikon.*ai* and the FM4-64 segmented vacuoles for the cells in Figures 15B and 18B is plotted for each cell as a circle. The median value is shown as a black line and the error bars

represent the 95% confidence interval. For reference, a yellow or grey dashed line represents the median intensity value for WT prior to or following 3h of rapamycin treatment, respectively. Statistical analyses and comparisons are as in (B). (C) The number of vacuole lobes for cells in Figure 19A was counted for the number of cells indicated. The median value is shown as a black line and the error bars represent the 95% confidence interval. A yellow line represents the median value for the WT population and is added for reference. Kruskal-Wallis statistical analysis with Dunn's post hoc test was performed to compare the populations of lobe numbers. Statistical comparisons between mutant and WT cells are shown as black asterisks. (n.s. = not significant; four symbols has a p-value <0.0001).

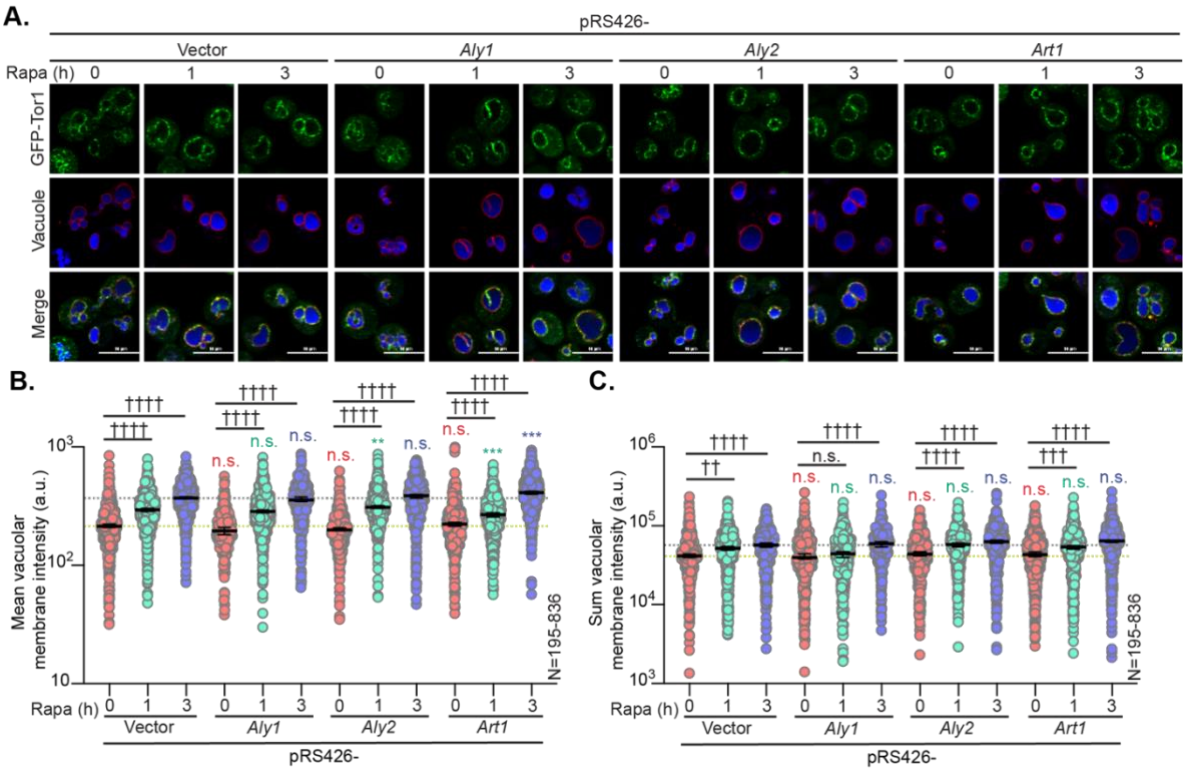

Figure 17. Tor1 localization is not affected by the overexpression of α-arrestins.

(A) WT cells expressing *TOR1pr*-GFP-TOR1 (gift from Ford lab, Univ. of Pittsburgh) and containing a pRS426-derived plasmid expressing either nothing (vector) or the indicated α-arrestin (under the control of its own promoter) were imaged by confocal microscopy at the indicated times post-treatment with 200ng/mL rapamycin. CMAC and FM4-64 was used to stain the vacuolar lumen (shown in blue) or membrane (shown in red), respectively. (B) Quantification of the mean GFP intensity at the vacuolar membrane using Nikon.*ai* software (see Section 2.2.11) for the cells in (A) is plotted for each cell as a circle. The median value is shown as a black line and the error bars represent

the 95% confidence interval. For reference, a yellow or grey dashed line represents the median intensity value for WT prior to or following 3h of rapamycin treatment, respectively. Kruskal-Wallis statistical analysis with Dunn's post hoc test was performed to compare the intensity distributions. Statistical comparisons between mutant and WT cells at that 0, 1, and 3 hours post rapamycin are shown as red, green, and blue asterisks respectively. Statistical comparisons of WT or mutant cells to their respective t=0 timepoints are shown as black daggers. (n.s. = not significant; four symbols has a p-value <0.0001). (C) Quantification of the sum GFP intensity at the vacuolar membrane using Nikon.*ai* software for the cells in (A) is plotted for each cell as a circle. The median value is shown as a black line and the error bars represent the 95% confidence interval. For reference, a yellow or grey dashed line represents the median intensity value for WT prior to or following 3h of rapamycin treatment, respectively. Statistical analyses and comparisons are as in (B).

2.3.6 α-Arrestins are needed to prevent aberrant Atg2-Atg18 accumulation on the limiting membrane of the vacuole

Following its nucleation, isolation membranes undergo rapid expansion facilitated in part through the transport of lipids from the ER mediated by the Atg2-Atg18 lipid transfer complex (Figure 6C) [242,244,246]. Given the genetic interactions between the α-arrestins and these lipid transfer proteins, as well as the α-arrestin-associated defect in phagophore expansion, I next assessed the localization and abundance of Atg2 and Atg18 (Figures 5-7; R.W.B, S.D., and K.C.). When expressing plasmid-borne GFP-Atg18, we found no clear abundance changes between WT and α-arrestin mutant cells by immunoblot analysis (Figure 18A; S.D.). Notably, Atg18 appeared to be destabilized and, potentially, undergo a shift in electrophoretic mobility after rapamycin treatment in these backgrounds (Figure 18A; S.D.). While this facet of Atg18's regulation has not, to our knowledge, been previously reported, since this alteration was not dependent upon α-arrestins we did not pursue it further.

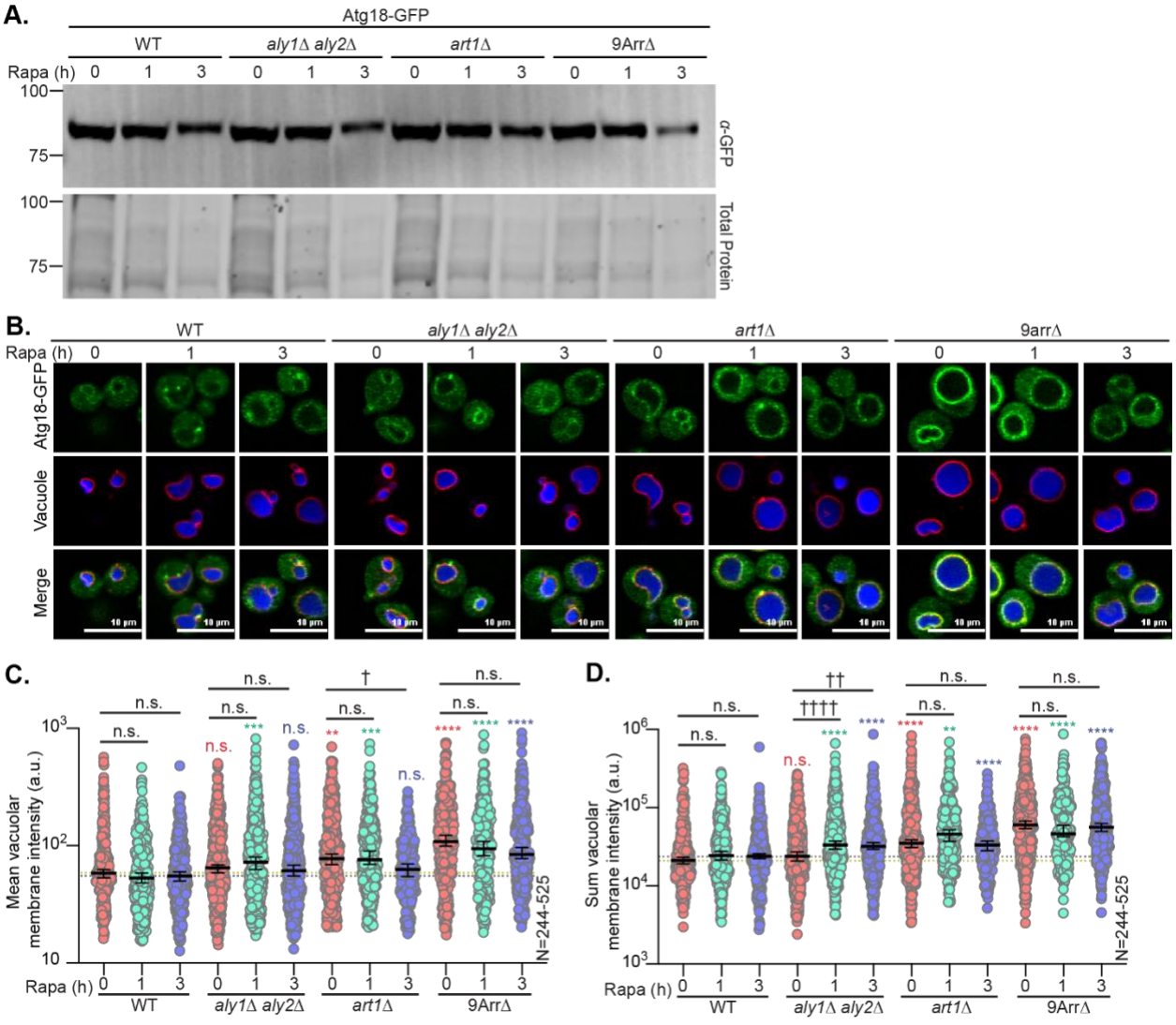

Figure 18. Lipid transfer protein Atg18, required for phagophore expansion, is mislocalized in the absence of α-arrestins.

(A) Cells expressing *ATG18pr*-Atg18-GFP in either WT or α-arrestin mutant cells were harvested at the indicated time points post-treatment with 200ng/mL rapamycin. Whole-cell protein extracts were made, analyzed by SDS-PAGE, immunoblotted and probed with anti-GFP antibody (Santa Cruz Biotechnology, Santa Cruz, CA). REVERT total protein stain of the membrane is the loading control and molecular weights are shown on the left in kDa. (B) Cells expressing *ATG18pr*-Atg18-GFP (gift from Kraft Lab, Univ. of Freiburg) in either WT or α-arrestin mutant cells were imaged by confocal microscopy at the indicated time post-treatment with 200ng/mL rapamycin. CMAC

and FM4-64 is used to stain the vacuolar lumen (shown in blue) and membrane (shown in red), respectively. (C) The mean GFP intensity at the vacuolar membrane using Nikon.*ai* software (see Section 2.2.11) is plotted for each cell as a circle. The median value is shown as a black line and the error bars represent the 95% confidence interval. A yellow or grey dashed line represents the median intensity value for WT prior to or following 3h of rapamycin treatment, respectively. Kruskal-Wallis statistical analysis with Dunn's post hoc test was performed to compare the intensity distributions. Statistical comparisons between mutant and WT cells at that 0, 1, and 3 hours post rapamycin are shown as red, green, and blue asterisks respectively. Statistical comparisons of WT or mutant cells to their respective t=0 timepoints are shown as black daggers. (n.s. = not significant; four symbols has a p-value <0.0001). (D) The sum GFP intensity at the vacuolar membrane using Nikon.*ai* software for the cells in (A) is plotted for each cell as a circle. The median value is shown as a black line and the error bars represent the 95% confidence interval. A yellow or grey dashed line represents the median intensity value for WT prior to or following 3h of rapamycin treatment, respectively. Statistical analyses and comparisons are as in (C).

Despite the fact that Atg18 abundance is unchanged in immunoblot analyses, by live-cell confocal microscopy there was a striking increase in both the concentration and abundance of Atg18 at the vacuolar membrane in *art1*Δ cells before and after rapamycin addition, and this is further increased in 9arrΔ cells (Figure 18B-D). Though Atg18's vacuolar residence was no different in WT and *aly1*Δ *aly2*Δ cells prior to rapamycin treatment, cells lacking the Alys had significantly elevated Atg18 concentration and total abundance at the vacuole within 1h of rapamycin treatment (Figure 18B-D). These results suggest Atg18 is being improperly retained at the vacuolar membrane in the absence of α-arrestins.

Similarly, I further observed α-arrestin-linked defects in the localization of endogenously expressed Atg2-mNG, a Vps13-family protein that directly facilitates the transfer of lipids and is normally found to localize, prior to rapamycin addition, to ER-associated puncta and is recruited to isolation membranes at the vacuole-anchored PAS once autophagy has been activated (Figure

6C and 19) [244,245]. As the binding of Atg18 to Atg2 impacts the ability of the latter to properly reach the PAS, I was unsurprised to find an increased abundance of Atg2 at the vacuolar membrane in cells lacking α-arrestins prior to rapamycin treatment (Figure 19A-C) [243,244,247]. While the concentration of Atg2 in the absence of α-arrestins is returned to WT levels post-rapamycin addition, its total abundance remains elevated in these backgrounds (compare Figure 19B and C). These findings indicate that, while Atg2's localization is not affected to the degree I observed for Atg18, both members of the lipid-transfer complex are improperly retained at the vacuolar surface in the absence of α-arrestins. As this complex's primary role lies in facilitating expansion of the isolation membrane, we propose this aberrant localization may represent a mechanism by which the lack of α-arrestins is linked to reduced AB size/abundance, AP lifetime, and phagophore expansion (Figures 8, 10, and 14C-D).

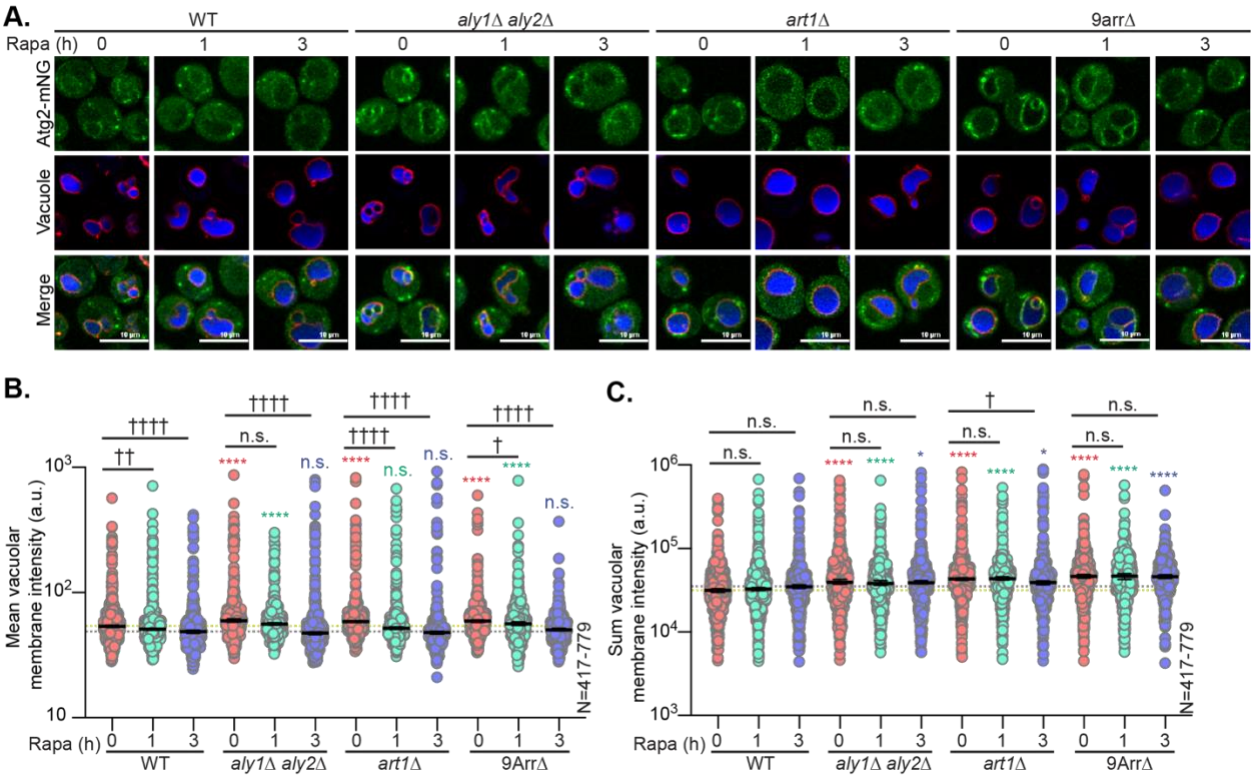

Figure 19. Lipid transfer proteins Atg2, required for phagophore expansion, is mislocalized in the absence of α-arrestins.

(A) Cells expressing chromosomally integrated Atg2-mNeonGreen (mNG) from its endogenous locus in either WT or α-arrestin mutant cells were imaged by confocal microscopy at the indicated time post-treatment with 200ng/mL rapamycin. CMAC and FM4-64 is used to stain the vacuolar lumen (shown in blue) and membrane (shown in red), respectively (B) The mean mNG intensity at the vacuolar membrane using Nikon.*ai* software (see Section 2.2.11) for the cells in (A) is plotted for each cell as a circle. The median value is shown as a black line and the error bars represent the 95% confidence interval. A yellow or grey dashed line represents the median intensity value for WT prior to or following 3h of rapamycin treatment, respectively. Kruskal-Wallis statistical analysis with Dunn's post hoc test was performed to compare the intensity distributions. Statistical comparisons between mutant and WT cells at that 0, 1, and 3 hours post rapamycin are shown as red, green, and blue asterisks respectively. Statistical comparisons of WT or mutant cells to their respective t=0 timepoints are shown as black daggers. (n.s. = not significant; four symbols has a p-value <0.0001). (C) The sum mNG intensity at the vacuolar membrane using Nikon.*ai* software for the cells in (A) is plotted for each cell as a circle. The median value is shown as a black line and the error bars represent the 95%

confidence interval. A yellow or grey dashed line represents the median intensity value for WT prior to or following 3h of rapamycin treatment, respectively. Statistical analyses and comparisons are as in (B).

2.3.7 α-Arrestins are needed to maintain the appropriate balance of Fab1, Vps34, and PI3P at the vacuolar membrane

Both Atg2 and Atg18 are recruited to isolation membranes by the presence of PI3P, with the latter also having a strong affinity to $PI(3,5)P_2$ [299,306,327,328,343,344]. Atg18, itself, regulates the activity of Fab1, the sole enzyme responsible for the conversion of PI3P to $PI(3,5)P_2$ in yeast [343,345,346]. Given that the absence of α-arrestins resulted in a strong retention of Atg18 at the vacuolar membrane, I decided to next assess the localization of the phospholipid kinases Vps34 and Fab1, as well as the distribution of PI3P itself, in WT and α-arrestin mutant cells by live-cell confocal microscopy. Similar to what I observed for its regulator Atg18, I found *art1*Δ and 9arrΔ cells expressing plasmid-borne Fab1-ENVY [262] to display both an elevated concentration and abundance of the $PI(3,5)P_2$ kinase at the vacuolar membrane pre- and post-rapamycin addition, though these measures were not statistically different from WT in the absence of *ALY1* and *ALY2* (Figure 20A-C). This finding supports the idea that the increased vacuolar retention of Atg18 may be linked to the similar retention of Fab1 in these backgrounds due to elevated production of $PI(3,5)P_2$ at this structure. To date, there is no established live-cell reporter for $PI(3,5)P_2$ localization and abundance, so we were unable to directly assess $PI(3,5)P_2$ distribution in cells.

PI3P, the direct precursor of $PI(3,5)P_2$, plays an important role in autophagy through its recruitment of proteins like Atg2 and Atg18 to the isolation membrane [223,227,229,230,346]. The production of PI3P is accomplished by the catalytic subunit Vps34 as part of either the

autophagy-dedicated PI3K Complex I, containing Atg14 and Atg38, or vacuolar protein sorting-related Complex II, instead containing Vps38. [223,322,323]. Though Vps34 is essential for autophagy, hyper-active mutants of this protein impede autophagy and prevent the release of PI3P-binding autophagic machinery prior to AP-vacuolar fusion [262]. Given this prominent role in autophagy, the genetic links to PI3K Complex I and II component Atg6 to the α-arrestins, as well as the mis-localization of the PI3P-binding Atg2 and Atg18 and the PI3P-modifying Fab1 in α-arrestin mutants, I focused next on assessing the localization and abundance of plasmid-borne GFP-Vps34 via live-cell confocal microscopy (Figure 20D-F). In both WT and *aly1*Δ *aly2*Δ cells, Vps34 was predominantly localized to the vacuolar membrane, with its concentration and abundance progressively decreasing after the addition of rapamycin (Figure 20D-F). While the total abundance of Vps34 in *art1*Δ and 9arrΔ cells was not significantly different from WT

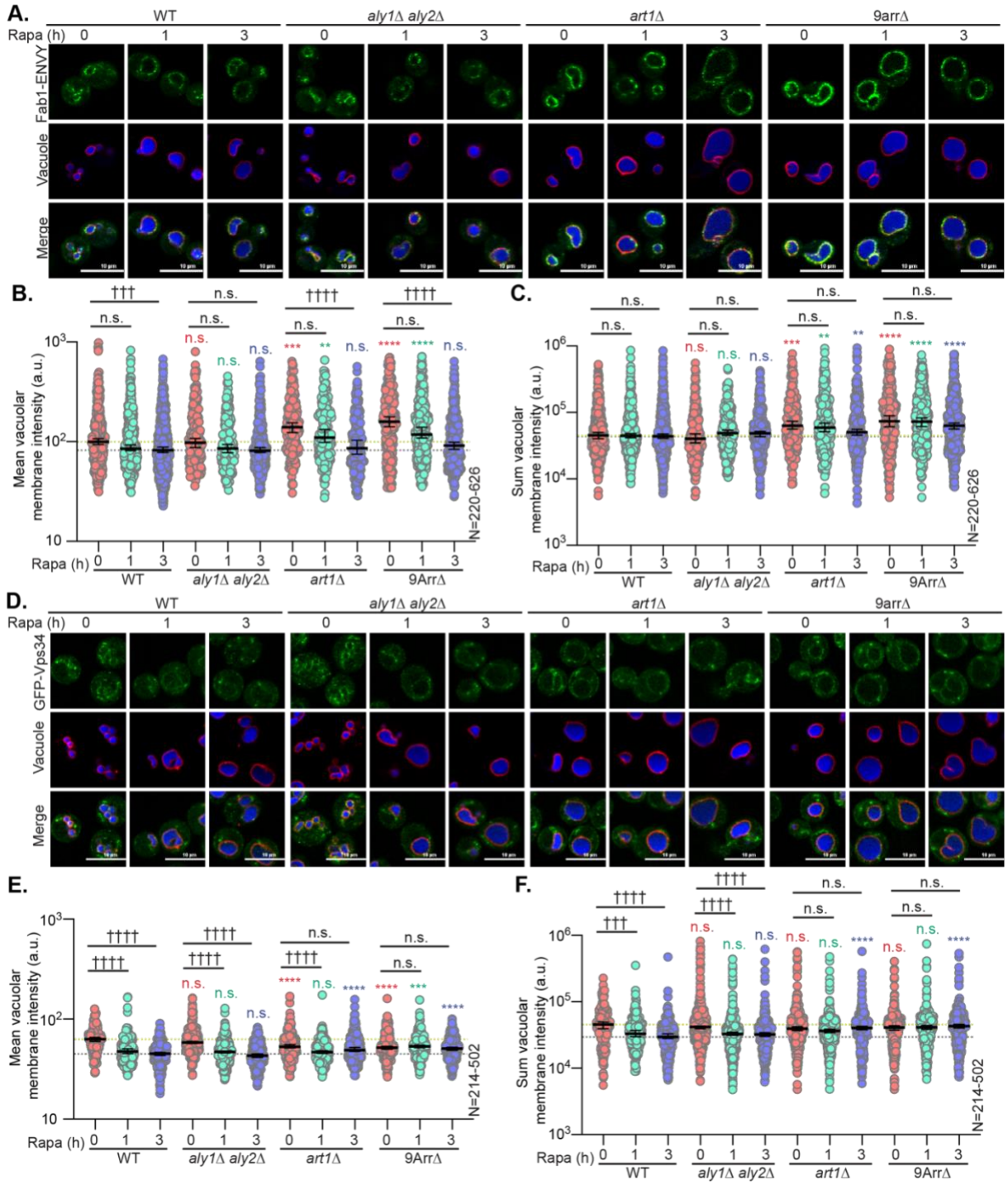

Figure 20. α-Arrestins are required for the proper localization of the phospholipid-modifying enzymes Fab1 and Vps34.

(A) Cells expressing *FAB1pr*-Fab1-ENVY (gift from Weisman lab, Univ. of Michigan) in either WT or α-arrestin

mutant cells were imaged by confocal microscopy at the indicated time post-treatment with 200ng/mL rapamycin. CMAC and FM4-64 was used to stain the vacuolar lumen (shown in blue) or membrane (shown in red), respectively. (B) Quantification of the mean ENVY intensity at the vacuolar membrane using Nikon.*ai* software (see Section 2.2.11) for the cells in (A) is plotted for each cell as a circle. The median value is shown as a black line and the error bars represent the 95% confidence interval. For reference, a yellow or grey dashed line represents the median intensity value for WT prior to or following 3h of rapamycin treatment, respectively. Kruskal-Wallis statistical analysis with Dunn's post hoc test was performed to compare the intensity distributions. Statistical comparisons between mutant and WT cells at that 0, 1, and 3 hours post rapamycin are shown as red, green, and blue asterisks respectively. Statistical comparisons of WT or mutant cells to their respective t=0 timepoints are shown as black daggers. (n.s. = not significant; four symbols has a p-value <0.0001). (C) Quantification of the sum of ENVY fluorescence intensity at the vacuolar membrane using Nikon.*ai* software for the cells in (A) is plotted for each cell as a circle. The median value is shown as a black line and the error bars represent the 95% confidence interval. For reference, a yellow or grey dashed line represents the median intensity value for WT prior to or following 3h of rapamycin treatment, respectively. Statistical analyses and comparisons are as in (B). (D) Cells expressing *VPS34pr*-GFP-Vps34 (gift from Weisman lab, Univ. of Michigan) were imaged by confocal microscopy as in (A). (E) Quantification of the mean GFP intensity at the vacuolar membrane using Nikon.*ai* software (see Section 2.2.11) for the cells in (D) is plotted for each cell as a circle. The description of features is the plot are the same as those indicated in (B). (F) Quantification of the sum GFP intensity at the vacuolar membrane using Nikon.*ai* software for the cells in (D) is plotted for each cell as a circle. Statistical analyses and comparisons are the same as those described in (B).

prior rapamycin treatment, the concentration of this protein was markedly lower, likely due their enlarged vacuolar sizes (Figure 20D-F and 21; R.W.B., A.C., and E.J.). Unlike the WT, Vps34 abundance at the vacuolar membrane failed to decrease, however, resulting instead in a significantly higher concentration after 3h post-rapamycin addition (Figure 17D-F). As aberrant retention may further result in an over-accumulation of PI3P, I next employed a plasmid expressing the PI3P-binding FYVE domain from the protein EEA1 tagged with GFP, GFP-FYVE(Eea1), using live-cell confocal microscopy (Figure 21A-B; A.C. and E.J.) [347]. While PI3P is normally

found predominantly in endosomes, as I observed in WT cells, those lacking α-arrestins more commonly exhibited strong vacuolar membrane localization of this reporter (Figure 21A-B; A.C. and E.J.). Given this support for an imbalance of PI3P in α-arrestin mutants, we propose a model wherein this mis-regulation of the phospholipid content in the vacuolar membrane results in the aberrant retention of Atg2 and Atg18, potentially preventing their proper recruitment to the PAS and resulting in impaired phagophore expansion and, thus, vacuolar flux to the vacuole (Figure 21C).

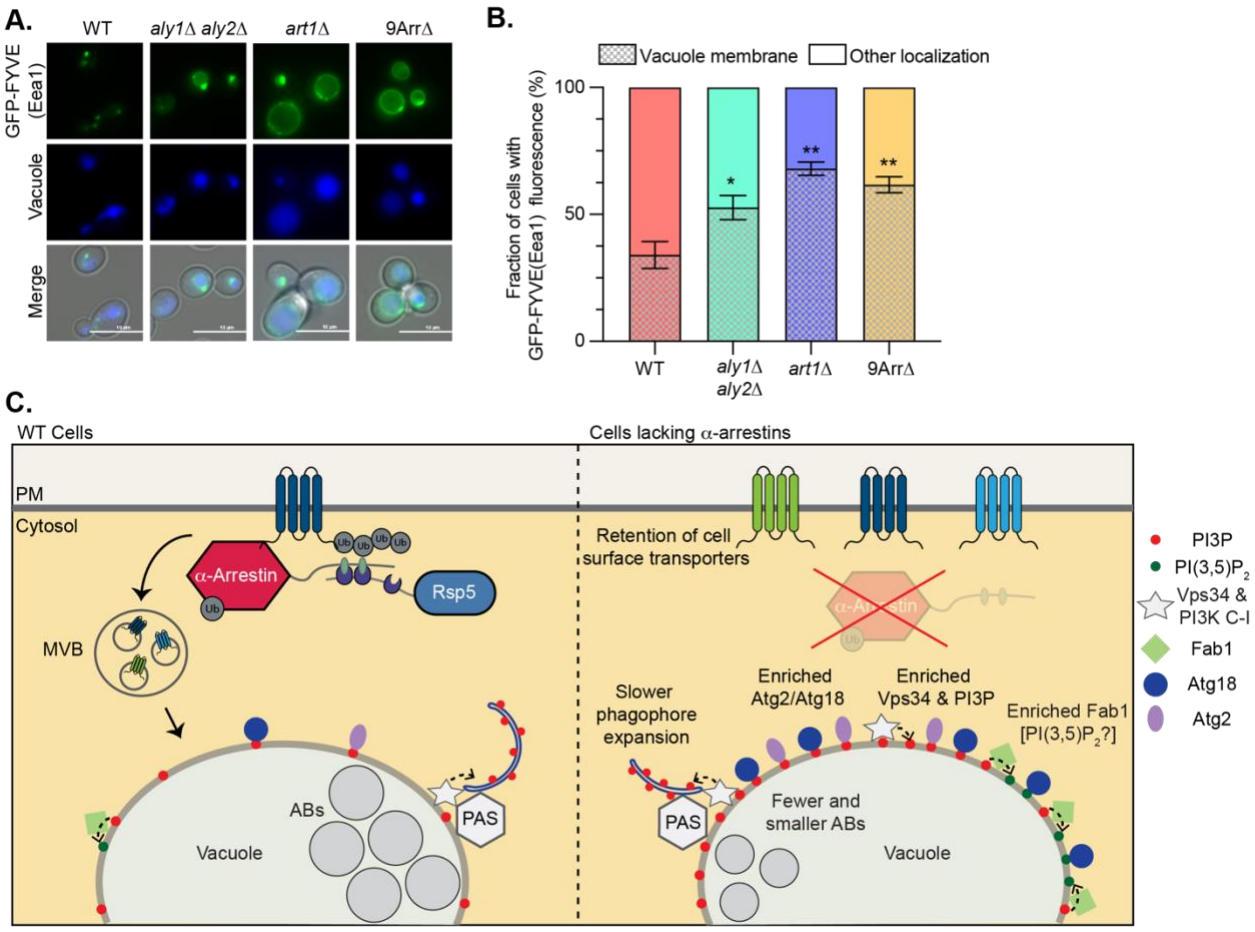

Figure 21. α-Arrestins are required for the proper distribution and abundance of PI3P.

(A) Cells expressing pRS426-GFP-Eea1-FYVE [3] in either WT or α-arrestin mutant cells were imaged by fluorescence microscopy. The vacuole lumen was stained with CMAC. (B) The fraction of cells displaying GFP-Eea1-FYVE localization (as imaged in A) to the limiting membrane of the vacuole or to endosomes/other localizations was

quantified for 3 replicate experiments using Image J. The median value is shown as a black line in the stacked bar graph and the error bars represent the 95% confidence interval. Unpaired Student's t-test with Welch's correction was used to assess statistical significance (* = p-value <0.05; ** = p-value <0.005). (C) Model of α-arrestin's influence on autophagy. When WT cells are treated with rapamycin, α-arrestins bind Rsp5 to control trafficking of membrane proteins to the vacuole. TORC1 signaling is impaired and autophagy is induced. Atg18-Atg2 bind to the vacuole membrane and are recruited to the PAS where AP expansion and subsequent fusion to the vacuole delivers autophagic bodies (AB) to the lumen of the vacuole for degradation. When cells lacking α-arrestins are treated with rapamycin, membrane transporters are aberrantly retained at the PM, resulting in loss of materials delivered to the vacuole. We find accumulation of PI3P and its kinase, Vps34, as well as Fab1, the kinase that generates $PI(3,5)P_2$, at the vacuole membrane. Atg18 and its binding partner Atg2, each of which binds PIPs, is also enriched at the limiting membrane of the vacuole. This may interfere with their activity at the PAS, as we observe slower phagophore expansion and delivery of fewer and smaller ABs to the vacuole lumen.

2.4 Discussion

The collective efforts herein establish a multi-level connection between the α-arrestins and autophagy, including a wide range of genetic interactions. While the over-expression of select α-arrestins confers resistance to the growth inhibition resulting from treatment with the TORC1-inhibiting drug rapamycin, the loss of many *ATG* family genes has a strong impact on this function. While mutants lacking components involved in the initiation of autophagy weakened α-arrestin-conferred rapamycin resistance, deletion of genes connected to the PI3P-producing PI3K complex and expansion of isolation membranes exhibited potent rapamycin resistance that was instead weakened by α-arrestin over-expression (Figures 5B-C, 6-7; R.W.B, S.D., and K.C.) [204,223,242,244,246,348,349]. These results align well with our further description of α-arrestin

mutant-associated rapamycin sensitivity, as well as defects in autophagic flux and isolation membrane expansion. Among these findings, we describe cells lacking *ALY1* and *ALY2*, *ART1*, or a group of 9 arrestins (9arrΔ) to exhibit an elevated abundance of the phospholipid PI3P at the vacuolar membrane, along with a coinciding over-enrichment of the PI3P- and PI(3,5)P_2-producing enzymes Vps34 and Fab1, respectively (Figures 21 and 21A-B; R.W.B., A.C., and E.J.) [223,350]. We propose that this defective regulation of PI3P and, potentially, PI(3,5)P_2 may be driving the aberrant retention of Atg2 and Atg18 to the vacuolar surface, further resulting in the impaired progression of autophagy itself (Figures 18-19) [231,306,327,343,344]. Among these impairments of autophagy, I found GFP-Atg8-marked APs to persist for longer periods of time in the cytosol, which is consistent with effects reported to be driven by the hyper-activity of Vps34 (Figure 10) [262]. Additionally, I observed α-arrestin-mutants to produce smaller ABs, consistent with their further inability to efficiently expand isolation membranes, as well as the mislocalization of Atg2 and Atg18 which directly support this aspect of the autophagic program (Figures 8, 14C-E, 18B-D, and 19) [242,244,246].

In contrast to these defects, and despite genetic links to the early stages of autophagy, I observed no significant impairment in the ability of α-arrestin mutants to regulate the abundance of the isolation membrane-seeding Atg9, nor its recruitment to the PAS in these backgrounds (Figures 12, 14A-B) [219,220,336]. This negative result is further supported by an absence of defects in the AP-3 and retromer pathways that control Atg9's trafficking (Figure 13; R.W.B. and A.C.) [215]. Atg9 is recycled away from completed APs through a mechanism involving PI3P, the Atg2-Atg18 complex, retromer, and the SNX-BAR protein family member Snx4 [175]. The Snx4 sorting nexin is thought to influence autophagy in multiple ways, including to endosome-to-Golgi trafficking of Atg9 and the vacuole-to-endosome recycling of the Atg9-regulator Atg27 [212,213].

The consistent absence of Atg9-associated defects in α-arrestin mutants led us to choose against further investigation into the potential involvement of Snx4, though connections between α-arrestins and protein recycling, as well as PI3P in the activity of Atg27, represent a notable aspect for future investigations [67,87–89,262].

The involvement of α-arrestins in permitting the proper regulation of autophagy, PI3P, and Vps34 draw striking parallels to recent work detailing the influence of hyperactive Vps34 on downstream membrane trafficking and autophagy [262]. Vps34 composes the catalytic core of both the autophagy-dedicated PI3K Complex I and the vacuolar protein sorting-related Complex II that represent the sole source of PI3P production [323,350,351]. The individual roles of these two PI3K complexes in the connection between α-arrestins and autophagy remains somewhat unclear. Though *VPS34* was not included in our autophagy-focused genetic screening, the loss of *ATG6*, a component of both PI3K complex forms required for their activity, results in strong rapamycin resistance that is weakened by the over-expression of the same α-arrestins whose increased abundance usually serves to bypass this treatments growth inhibition in WT cells (Figures 5-7; R.W.B, S.D., and K.C.). In contrast, the loss of *ATG14*, present in only the autophagy-dedicated PI3K Complex II, results in an exquisite sensitivity to rapamycin that is still moderately improved by the over-expression of Aly1, Aly2, Art1, or Art5 (Figures 5-7; R.W.B, S.D., and K.C.). These distinct outcomes seemingly support a more prominent role for the PI3K Complex I in the cellular response to rapamycin and its relationship to the α-arrestins, but the exact nature of that interplay will require the additional investigation.

Both the catalytic subunit of the PI3K complex, Vps34, and the product of its activity, PI3P, possess a broad set of cellular functions, including: 1) the rescue of membrane-bound cargo from late to early endosomes by retromer, 2) the generation of $PI(3,5)P_2$, 3) the function of

ESCRTs in the fusion of multi-vesicular bodies (MVBs) to the vacuole, and 4) the retrieval of membrane-bound proteins from the surface of the vacuole mediated by Snx4 [262,304,305,345,346,352,353]. The hyperactivity of Vps34 catalyzes increased production of PI3P and a subsequent increase in $PI(3,5)P_2$ [262]. Though we have not directly assessed this phospholipid's abundance in α-arrestin mutants, we did observe an increased vacuolar membrane abundance of Vps34, PI3P, the $PI(3,5)P_2$-producing kinase Fab1, and the $PI(3,5)P_2$-binding Atg18, strongly suggesting that it too is improperly regulated in these backgrounds (Figures 18, 20, 21A-B; R.W.B., A.C., and E.J.). Vps34 hyperactivity, like we observed in the absence of α-arrestins, increases the lifetime of GFP-Atg8 puncta and impairs autophagic flux, yet was not found to cause the same retention of Fab1 or Atg18 at the vacuolar surface (Figures 10-11 and 18-19; R.W.B. and N.O.) [262]. Similarly, while hyperactive Vps34 was found to disrupt the recycling of the Atg9-regulating Atg27 from the vacuolar membrane by Snx4 and retromer, we found no such shift in our assessment of the retromer pathway in α-arrestin mutants (Figure 13; R.W.B and A.C.) [262]. Therefore, while α-arrestin mutants do display an increased abundance of Vps34 and PI3P at the vacuolar membrane, despite exhibiting many similar effects on autophagy as hyperactive Vps34 isoforms, such inconsistencies in their relative effects prevent us from fully linking the two.

The effects of Vps34 hyperactivity on autophagy are attributed to the increased retention of PI3P-binding autophagic machinery to APs that impairs their fusion to the vacuole [262]. PI3P is normally removed from the outer AP membrane by the yeast myotubulinar-related PI3P phosphatase Ymr1, which, along with and the synaptojanin-like phosphatases, Sjl2 and Sjl3, also play a broader cellular role in mediating the conversion of PI3P to PI [354,355].While the loss of all three PI3P-phosphatases is synthetically lethal, cells lacking *YMR1* and *SJL2* exhibit a similar over-accumulation of PI3P at the vacuolar membrane [356]. This background results in the hyper-

fragmentation of the vacuole, similar to that seen in *aly1*Δ *aly2*Δ and hyperactive Vps34 mutants yet strikingly different from the *art1*Δ and 9arrΔ that exhibit the strongest PI3P misregulation [356]. It is, therefore, also unlikely that the regulation of PI3P is solely responsible for the vacuolar size defects I describe for α-arrestin mutants.

In addition to its essential role in autophagy, Atg18 further regulates both Fab1 activity and vacuolar morphology, having recently been demonstrated to control this latter aspect as part of a novel form of a Vps35-containing retromer complex [299,301,343,357]. Furthermore, *atg18*Δ cells exhibit both elevated $PI(3,5)P_2$ and enlarged vacuoles, though the role of this phospholipid in affecting the morphology of the vacuole is unclear given that its depletion in cells lacking proper Fab1 activity similarly results in enlarged vacuoles [358,359]. Instead, the regulation of vacuolar morphology by phospholipids is more likely driven by their recruitment of vacuolar fission and fusion machinery. In further support of this idea, Atg18 is not only capable of driving membrane scission events *in vitro* but is also required for the vacuole fragmentation resulting from hyperosmotic shock, and in regulating vacuolar inheritance [306]. Atg18's newly described binding of Vps35 to form a second variety of the retromer complex, an occurrence which competes with Vps35's association to the sorting nexins Vps5 and Vps17 as part of the more widely recognized retromer complex, is similarly required for hyperosmotic shock-induced vacuolar fragmentation [301]. Notably, *vps35*Δ cells exhibit both enlarged vacuoles and an elevated retention of Atg18 at the surface of this compartment, strikingly similar to the phenotypes I observed in *art1*Δ and 9arrΔ backgrounds [301]. As the retromer complex also contains the arrestin-like protein Vps26, it remains conceivable that other α-arrestins may also participate in the Atg18-containing retromer variant [30]. Given the previously described requirement for the α-arrestins in regulating Atg18, Vps34, and Fab1, as well as the vacuolar morphology defects found

in their absence, investigations into the role of this trafficking adaptor family in the regulation of vacuole inheritance and fission/fusion represent exciting avenues of future work.

Another facet of α-arrestin influence that remains to be fully described is the imbalance of phospholipids associated with their absence. One possible source of this misregulation is the metabolite changes that likely occur as a result of cell surface nutrient transporter retention when α-arrestins are not available to mediate their endocytic trafficking. We previously demonstrated this effect in the control of the glycerophosphoinositol (GPI) transporter Git1 by Aly1 and Aly2 [91]. Git1 accumulates at the plasma membrane in *aly1*Δ *aly2*Δ cells, leading to a marked sensitivity to exogenous GPI addition that likely results from its toxic intracellular over-accumulation [91]. Cellular biosynthetic pathways convert GPI to glycerol-3-phosphate and inositol, a critical precursor to phospholipid production [360,361]. Indeed, we also showed that the aberrant build-up of PI3P at the vacuolar membrane in *aly1*Δ *aly2*Δ cells is further exacerbated by the addition of excess GPI, representing a direct link between α-arrestin trafficking and phospholipid regulation [91]. The import of inositol occurs via the transporters Itr1 and Itr2, which undergo Art5-dependent internalization following inositol stimulation [59,362]. Given what occurs with GPI and Git1 in the absence of α-arrestin control, as well as the shifts in phospholipid flippase-associated phenotypes when Itr1 regulation is changed, it is likely that inositol levels are impacted by the absence of *ART5* [362–364]. Importantly, Art5, along with Aly1, Aly2, and Art1, represent the only α-arrestins to confer rapamycin resistance when over-expressed. The connections existing between this sub-group and the import of phospholipid precursors lends credence to the idea that transporter regulation by these α-arrestins may be linked to changes in the distribution and/or abundance of phospholipids like PI3P and PI(3,5)P_2, Atg18 and Atg2 retention at the vacuolar membrane, and vacuolar morphology. A similar connection between

metabolite balance and vacuole regulation has also been established for cells treated with methylglyoxal (MG), a byproduct of glycolysis. The treatment of cells with toxic levels of MG results in the over-accumulation of Atg18 to enlarged vacuoles that are resistance to hyperosmotic-stress induced fragmentation and drive defects in nuclear inheritance [365,366]. Though this is strikingly similar to what we observe in *art1*Δ and 9arrΔ cells, we have yet to investigate the potential role of MG or the possibility of nuclear inheritance defects in these backgrounds. Collectively, these connections between the α-arrestin regulation of nutrient transporters, vacuole morphology, and metabolic/phospholipid balance underscore the importance of further work in deciphering the complex interplay that likely exists.

Lastly, the model presented in Figure 21C assigns an indirect role for the α-arrestins in regulating the morphology of the vacuole, as well as the proteins that associate with this structure, instead attributing these affects to changes in the trafficking of nutrient transporters like those discussed above. It remains possible, however, that α-arrestins may also possess an as-yet undescribed function as direct regulators of vacuolar membrane composition, similar to other Rsp5-adapter proteins like Ear1 and Ssh4 [367–370]. The results discussed herein thus not only expand our understanding of how the α-arrestins influence the regulation of organelles and degradative pathways like endocytosis and autophagy, but further raise exciting questions about the trafficking adapter family's broader role in cellular metabolism.

3.0 α-Arrestins Aly1 and Aly2 are regulated by the TORC1 signaling complex and its downstream effectors

The contents of this chapter are adapted from a published article in the journal *Biomolecules (Ray W. Bowman II, Eric M. Jordahl, Sydnie Davis, Stefanie Hedayati, Hannah Barsouk, Nejla Ozbaki-Yagan, Annette Chiang, Yang Li, and Allyson F. O'Donnell, 2022).* R.W.B completed figures 24A-B, 25A-B, 26A-B, 28A-D, 29, 33A-D, 34A-D, 35, and 36A-B. Further contributions to figures include:

- Eric Jordahl: Table 5, 23A, 24C, 25C, 27C-D, 28E-H, 30-32, 33E-F, 34E-J,
- Sydnie Davis: 22A, Table 5, 23A-B, 24C, 25C, 30A-D
- Stefanie Hedayati: 31-32
- Hannah Barsouk: strain preparation for 27-29
- Nejla Ozbaki-Yagan: strain preparation for 27-29, 31 and 34-35
- Annette Chiang: 26C-D, 36C
- Yang Li: 26C-D
- Allyson F. O'Donnell: 22B-D, 27A, 36D

3.1 Introduction

Cells react to environmental stimuli, including changes in nutrient availability, by reorganizing the complement of proteins present at the cell surface. How, then, is this selective redistribution of plasma membrane-embedded proteins accomplished in response to changes in

stress or nutrient levels? In *Saccharomyces cerevisiae*, a model system which has been extensively utilized in the characterization of protein trafficking [371,372], the α-arrestins (or arrestin-related trafficking adaptors (ARTs)) play a prominent role [58,59,67,373,374]. Heavily regulated by multiple signaling networks, including the target of rapamycin complex 1 (TORC1) and the AMPK/Snf1 kinase, the α-arrestins respond to environmental cues by selectively binding to a broad set of membrane proteins, including amino acid, glucose, metal ion, and inositol transporters, as well as G-protein coupled receptors (GPCRs) [59,62,66,67,73,77,79,94,374]. In order to trigger the removal of these membrane proteins from the cell surface, the α-arrestins recruit the E3 ubiquitin ligase Rsp5. α-Arrestins act as protein trafficking adapters, mediating the interaction of their membrane-bound cargo with Rsp5, which ubiquitinates transporters to recruit additional components of the endocytic machinery to induce their internalization [295–298]. This model of α-arrestin endocytic regulation is reminiscent of the well-characterized control of GPCRs and other membrane proteins by the related β-arrestins in mammals [375–377]. Similarly, the mammalian arrestin-domain containing (ARRDC) α-arrestin family, and their better-studied orthologs in yeast, also serve to control the activity and trafficking of GPCRs and nutrient transporters [39,41,44,378,379].

α-Arrestin-mediated endocytosis is kept under tight regulation in order to maintain the appropriate plasma membrane proteome. One primary mechanism underpinning this control lies in the phospho-regulation of α-arrestins, which, while often serving to inhibit their endocytic activity, may also support their activities in intracellular sorting [66–68,76,77,90,129,293,294]. A second mechanism of α-arrestin control is achieved by α-arrestin degradation under cellular conditions where their activity is not required [90,93,156]. Finally, α-arrestin activity is also controlled through their condition-specific transcription, as occurs during carbon- or nitrogen-

starvation for Ecm21 and Csr2 [73,74]. Here, I focus on the identification of phospho-regulatory mechanisms for Aly1 and Aly2, finding them to be tightly linked to the stability of these α-arrestins. This type of relationship has already been described for the α-arrestin Rog3, which is destabilized following phosphorylation by the Snf1 kinase, though the full molecular details of this mechanism remain undefined [90].

α-Arrestins undergo extensive phospho-regulation, with as many as 87 α-arrestin phospho-sites having been identified by proteomic studies, implicating a diverse set of protein kinases and phosphatases in the control of the trafficking adaptor family [66,68,74,76,380,381]. Given the prominence and complexity of α-arrestin phospho-regulation, I utilized a targeted genetic screen of non-essential kinases and phosphatase deletion mutants to identify potential Aly1 and Aly2 regulators. The effect of each deletion mutant on colony growth when overexpressing either Aly1, Aly2, or empty vector was assessed on media containing either: 1) the drug rapamycin, a direct inhibitor of the TORC1 complex, or 2) high salt, a condition which induces the activity of many kinases and phosphatases, including the calcineurin phosphatase and the high osmolarity glycerol response kinase, Hog1 [382–385]. These two conditions were chosen due to the regulation of both Aly proteins by TORC1 and calcineurin. Furthermore, the Aly proteins control the trafficking of membrane cargo like the glutamic and aspartic acid permease Dip5, as well as the P-type ATPase sodium pump Ena1, both of which are internalized under high salt conditions [386]. My initial screen identified an extensive network of over 60 phospho-regulators that alter Aly-dependent phenotypes, from which we chose 18 kinases and phosphatases to further pursue. Satisfyingly, nearly all of these secondary candidates influence the abundance of Aly1 and/or Aly2, supporting a model wherein the stability of the Aly proteins is broadly controlled by phospho-regulation.

α-Arrestins, including the Alys, mediate the trafficking of the yeast mating pathway GPCRs Ste2 and Ste3, with additional components of this pathway being identified among my screen candidates [62,79]. However, due to the prominence of the TORC1 signaling network and its extensive connections to the regulation of α-arrestins, we chose to focus on two members of its downstream effectors: Sit4 and Npr1. Already possessing rich ties to α-arrestin regulation, the ceramide-activated type2A-related protein phosphatase Sit4 was chosen as one of my strongest candidates for its ability to improve Aly-mediated growth in the presence of rapamycin [77,93,94]. When TORC1 activity is suppressed, as during nitrogen starvation or treatment with rapamycin, Sit4 is released from its inhibition and binding to the TORC-regulating essential protein Tap42 [387,388]. Tap42 is itself inhibited by the binding of Tip41, also identified as a candidate in my screen, allowing for Sit4 to interact with Sit4-associated proteins (SAPs) and its activity toward other cellular targets like the nitrogen permease reactivator kinase Npr1 [77,94,388]. Npr1, another of my screen candidates and a known regulator of multiple α-arrestins, becomes active following Sit4-dependent dephosphorylation [66,67,388,389]. However, under the nutrient replete conditions that activate TORC1, Npr1 becomes hyper-phosphorylated and is considered to be inactive, demonstrating the balance of its phospho-regulation by TORC1, Sit4, and other regulators [66,137]. While Npr1 undergoes this inhibitory hyper-phosphorylation in the absence of *SIT4*, more recent studies suggest a more nuanced relationship between the TORC1-Sit4-Npr1 network [390,391]. For example, both Npr1 and Sit4 continues to have activity against some of their targets even when TORC1 is active [77,94,104,390,391]. Notably, Sit4 may further selectively target the dephosphorylation of α-arrestins when still bound to the TORC1 complex [77,94].

As mentioned previously, both Npr1 and Sit4 are known regulators of α-arrestins. Npr1 has direct activity against Aly2 and is required for its role in trafficking the general amino acid

permease Gap1 to the cell surface, while its inhibition drives changes in the phospho-status of Aly1 [67,104]. Npr1 can also inhibit Gap1 internalization through its phosphorylation of the α-arrestins Bul1 and Bul2 [77,94]. This mechanism is antagonized by Sit4-dependent dephosphorylation to promote the endocytosis of both Gap1 and the high affinity lactate transporter Jen1 [77,94,141,294]. Similarly, Npr1-dependent phosphorylation of Art1 prevents the rapamycin-induced removal of the arginine permease Can1 from the cell surface [66]. This trafficking event is prevented, however, in the absence of Npr1, underscoring the need for further study of Art1-Can1 regulation [64]. Yet another example lies in the cycloheximide (CHX)-induced endocytic trafficking of the thiamine transporter Thi7 by α-arrestin Art2, an event that is supported by Sit4 but considered independent of Npr1 [93].

In the course of this work, we found that the loss of *SIT4* leads to the hyper-phosphorylation of both Aly1 and Aly2 in cells grown in nutrient replete media. This suggests that, despite conditions supporting active TORC1, Sit4 is responsible for maintaining the dephosphorylation of these α-arrestins or a kinase normally inhibited by Sit4 is contributing to their hyper-phosphorylation. Notably, hyper-phosphorylated Aly1 and Aly2 are destabilized in the absence of *SIT4*, tying their phospho-regulation to the control of their abundance, a mechanism that has been previously demonstrated for other members of the α-arrestins [90]. Surprisingly, our pursuit of the mechanism underlying this destabilization of the Alys revealed a role for the vacuole. Furthermore, in the absence of both *SIT4* and *NPR1*, we observed not only the loss of Aly hyper-phosphorylation, but also an increase in their stability. These conditions further restored the ability of Aly1 and Aly2 to facilitate the trafficking of the Git1 glycerophosphoinositol transporter to the vacuole, linking this previously reported cargo-relationship to the TORC1-Sit4-Npr1 signaling network [91]. We offer forward a model for this signaling network wherein Npr1 is required to

induce the degradation of Aly1 and Aly2 via their hyper-phosphorylation, a modification which is antagonized by Sit4 either through direct dephosphorylation or its control of Npr1. We further posit that, while Npr1 is generally considered to be inhibited by active TORC1 when available nutrients are abundant, it maintains at least some activity toward the α-arrestins that is antagonized by Sit4 to prevent their degradation and preserve their stability and trafficking functions. This balanced relationship may thus provide a tunable system for α-arrestin-regulated endocytic activity in the presence of abundant nutrients.

3.2 Materials and Methods

3.2.1 Yeast Strains and Growth Conditions

The yeast strains used in this study are described in Table 3 and are derived from the BY4741 or BY4742 genetic backgrounds of *S. cerevisiae* (S288C in origin). Yeast cells were grown in either synthetic complete (SC) medium lacking the appropriate amino acid for plasmid selection, prepared as described in [310] and using ammonium sulfate as a nitrogen source, or YPD medium where indicated. Unless otherwise indicated, yeast cells were grown at 30 °C. Liquid medium was filter-sterilized and solid medium for agar plates had 2% agar *w*/*v* added before autoclaving.

Table 3. Strains used in Chapter 3

The *MAT* **a** deletion collection [311] was used for the strains in the KinDel library and the mini-library information can be found at odonnelllab.com. For simplicity, only strains used for experiments other than the initial screens are listed in the table below.

Strain	Genotype	Source
BY4741	MAT **a** *his3Δ1 leu2Δ0 ura3Δ0 met15Δ0*	[311]
*bub1*Δ	MAT **a** *bub1Δ*::KanMX *his3Δ1 leu2Δ0 ura3Δ0 met15Δ0*	[311]
*ctk1*Δ	MAT **a** *ctk1Δ*::KanMX *his3Δ1 leu2Δ0 ura3Δ0 met15Δ0*	[311]
*fus3*Δ	MAT **a** *fus3Δ*::KanMX *his3Δ1 leu2Δ0 ura3Δ0 met15Δ0*	[311]
*gip2*Δ	MAT **a** *gip2Δ*::KanMX *his3Δ1 leu2Δ0 ura3Δ0 met15Δ0*	[311]
*kin82*Δ	MAT **a** *kin82Δ*::KanMX *his3Δ1 leu2Δ0 ura3Δ0 met15Δ0*	[311]
*nem1*Δ	MAT **a** *nem1Δ*::KanMX *his3Δ1 leu2Δ0 ura3Δ0 met15Δ0*	[311]
*ptc4*Δ	MAT **a** *ptc4Δ*::KanMX *his3Δ1 leu2Δ0 ura3Δ0 met15Δ0*	[311]
*rck2*Δ	MAT **a** *rck2Δ*::KanMX *his3Δ1 leu2Δ0 ura3Δ0 met15Δ0*	[311]
*sip2*Δ	MAT **a** *sip2Δ*::KanMX *his3Δ1 leu2Δ0 ura3Δ0 met15Δ0*	[311]
*sit4*Δ	MAT **a** *sit4Δ*::KanMX *his3Δ1 leu2Δ0 ura3Δ0 met15Δ0*	[311]
*slt2*Δ	MAT **a** *slt2Δ*::KanMX *his3Δ1 leu2Δ0 ura3Δ0 met15Δ0*	[311]
*spo7*Δ	MAT **a** *spo7Δ*::KanMX *his3Δ1 leu2Δ0 ura3Δ0 met15Δ0*	[311]
*ste20*Δ	MAT **a** *ste20Δ*::KanMX *his3Δ1 leu2Δ0 ura3Δ0 met15Δ0*	[311]
*ste7*Δ	MAT **a** *ste7Δ*::KanMX *his3Δ1 leu2Δ0 ura3Δ0 met15Δ0*	[311]
*tip41*Δ	MAT **a** *tip41Δ*::KanMX *his3Δ1 leu2Δ0 ura3Δ0 met15Δ0*	[311]
*tor1*Δ	MAT **a** *tor1Δ*::KanMX *his3Δ1 leu2Δ0 ura3Δ0 met15Δ0*	[311]
*ymr1*Δ	MAT **a** *ymr1Δ*::KanMX *his3Δ1 leu2Δ0 ura3Δ0 met15Δ0*	[311]
*yvh1*Δ	MAT **a** *yvh1Δ*::KanMX *his3Δ1 leu2Δ0 ura3Δ0 met15Δ0*	[311]
*npr1*Δ	MAT **a** *npr1Δ*::KanMX *his3Δ1 leu2Δ0 ura3Δ0 met15Δ0*	[311]
*sit4*Δ *npr1*Δ	MAT **a** *sit4Δ*::KanMX *npr1*Δ::HphMX *his3Δ1 leu2Δ0 ura3Δ0 met15Δ0*	This study Using the sit4Δ::KanMX strain from the deletion collection, we PCR amplified the HphMX cassette [57] using primers with homology to the regions up- and downstream of the Npr1 coding sequence. We then validated that Npr1 was deleted using a PCR-based approach.
BY4742	MAT **α** *his3Δ1 leu2Δ0 ura3Δ0 lys2Δ0*	[311]
*pdr5*Δ	MAT **α** *pdr5Δ*::KanMX *his3Δ1 leu2Δ0 ura3Δ0 lys2Δ0*	[311]
*pep4*Δ	MAT **a** *pep4Δ*::KanMX *his3Δ1 leu2Δ0 ura3Δ0 met15Δ0*	This study We PCR amplified the KanMX cassette [58] using primers with homology to the regions up- and downstream of the Pep4 coding sequence. We then validated that Pep4 was deleted using a PCR-based approach.
*sit4*Δ *pdr5*Δ	MAT **a** *sit4Δ*::KanMX *pdr5*Δ::HphMX *his3Δ1 leu2Δ0 ura3Δ0 met15Δ0*	This study Using the sit4Δ::KanMX strain from the deletion collection, we PCR amplified the HphMX cassette [57] using primers with homology to the regions up- and

		downstream of the Pdr5 coding sequence. We then validated that Pdr5 was deleted using a PCR-based approach.
*sit4*Δ *pep4*Δ	MAT **a** *sit4Δ*::KanMX *pep4*Δ::HphMX *his3Δ1 leu2Δ0 ura3Δ0 met15Δ0*	This study Using the sit4Δ::KanMX strain from the deletion collection, we PCR amplified the HphMX cassette [57] using primers with homology to the regions up- and downstream of the Pep4 coding sequence. We then validated that Pep4 was deleted using a PCR-based approach.
*aly1*Δ *aly2*Δ (aka D2-6a)	MAT **a** *aly1Δ*::KanMX *aly2Δ*::KanMX *his3Δ1 leu2Δ0 ura3Δ0 met15Δ0 lys2Δ0*	[67]
9ArrΔ (EN60)	*ecm21*Δ::KanMX *csr2*Δ::KanMX *bsd2*Δ *rog3*Δ::NatMX *rod1*Δ *ygr068c*Δ *aly1*Δ *aly2*Δ *ylr392c*Δ*::*HIS3 *his3*Δ*0 ura3*Δ*0 leu2*Δ*0*	[59]

3.2.2 Serial Dilution Growth Assays

For the serial dilution growth assays on solid medium, cells were grown to saturation in liquid SC medium overnight, and the A_{600} was determined. Starting with an A_{600} of 1.0 (approximately 1.0×10^7 cells/mL), serial dilutions of either 3-fold or 5-fold (as in Figure 22A,B) were then generated and transferred to solid medium using a sterile replica-pinning tool. Cells were then grown at 30 °C for 3–6 days and images were captured using a Chemidoc XRS+ imager (BioRad, Hercules, CA, USA) and all were evenly modified in Photoshop (Adobe Systems Incorporated, San Jose, CA, USA). For rapamycin-containing plates, the rapamycin was obtained from LC Laboratories (Woburn, MA, USA), and a stock solution of 0.5 mg/mL in ethanol was made and then diluted to the final concentration indicated in the medium in each figure panel (typically 50 ng/mL). For salt-containing medium, sodium chloride was dissolved in the SC medium prior to autoclaving to generate the final concentrations indicated in each figure.

3.2.3 Plasmids and DNA Manipulations

Plasmids used in this work are described in Table 4. PCR amplifications for generating plasmid constructs were performed using Phusion High Fidelity DNA polymerase (ThermoFisher Scientific, Waltham, MA, USA) and confirmed by DNA sequencing. Plasmids were transformed into yeast cells using the lithium acetate method [312] and transformants were selected for use on SC mediums lacking specific nutrients.

Table 4. Plasmids used in Chapter 3

Plasmid	Genotype	Description (Reference)
pRS415	*TEF1prom*, CEN, *LEU2*	[313]
pRS415-*TEF1pr*-GFP	*TEF1prom*-GFP, CEN, *LEU2*	[91]
pRS415-Aly1-GFP	*TEF1prom-ALY1*-GFP, CEN, *LEU2*	This study The coding region of Aly1 lacking its stop codon was PCR amplified using pRS426-Aly1 as a template and primers with SpeI and PstI restriction site adaptors. These were then subcloned into pRS415-TEF1pr-GFP at the SpeI and PstI sites.
pRS415-Aly2-GFP	*TEF1prom-ALY2*-GFP, CEN, *LEU2*	This study The coding region of Aly2 lacking its stop codon was PCR amplified using pRS426-Aly2 as a template and primers with SpeI and PstI restriction site adaptors. These were then subcloned into pRS415-TEF1pr-GFP at the SpeI and PstI sites.
pRS415-Aly1^{PPxYless}-GFP	*TEF1prom-aly1^{PPxYless}*-GFP, CEN, *LEU2*	This study The coding region of Aly1PPxYless lacking its stop codon was PCR amplified using pRS426-Aly1PPxYless as a template and primers with SpeI and PstI restriction site adaptors. These were then subcloned into pRS415-TEF1pr-GFP at the SpeI and PstI sites.
pRS415-Aly2^{PPxYless}-GFP	*TEF1prom-aly2^{PPxYless}*-GFP, CEN, *LEU2*	This study The coding region of Aly2PPxYless lacking its stop codon was PCR amplified using pRS426-Aly2PPxYless as a template and primers with SpeI and PstI restriction site adaptors. These were then

		subcloned into pRS415-TEF1pr-GFP at the SpeI and PstI sites.
pRS415-Git1-GFP	*TEF1prom-GIT1*-GFP, 2µ, *LEU2*	[91]
pRS426	2µ, *URA3*	[313]
pRS426-Aly1	*ALY1prom-ALY1*, 2µ, *URA3*	[67]
pRS426-Aly2	*ALY2prom-ALY2*, 2µ, *URA3*	[67]
pRS426-Aly1^{PPxYless}	*ALY1prom-ALY1^{PPxYless}*, 2µ, *URA3*	[79]
pRS426-Aly2^{PPxYless}	*ALY2prom-ALY2^{PPxYless}*, 2µ, *URA3*	[79]
pCG04	ste6-166NBD2-3HA, 2µ, *URA3*	[392]

3.2.4 KinDel Library Screen

The kinase and phosphatase deletion (KinDel) library contains 187 unique non-essential gene deletions, each of which is annotated as being non-essential in the *Saccharomyces* Genome Database (SGD). This library initiated with a collection generated by Dr. J. Patterson (Patterson and Thorner, unpublished). We then used YeastMine, populated by SGD and powered by InterMine, and searched for 'protein kinase' or 'protein phosphatase'. These searches returned nearly 3000 candidates before duplicates and essential genes were removed. SGD annotations of the remaining genes were then further assessed for protein kinase and phosphatase function, resulting in a final list of 187 gene deletion mutants, which were then arrayed over two 96-well plates. The library is available upon request and is further documented at **https://www.odonnelllab.com/yeast-libraries** (accessed on 23 February 2022).

To screen for modifiers of α-arrestins' Aly1 and Aly2 function, the KinDel library was transformed with either pRS426-vector or pRS426-Aly1 or -Aly2 plasmids, each of which expressed Aly1 or Aly2 from their endogenous promoter but on a 2-micron plasmid backbone. Transformations were performed as described in [312] and were done with the aid of the Benchtop RoToR HAD robotic plate handler (Singer Instruments Co. Ltd., Roadwater, UK) and the Multidrop Combi (ThermoFisher) in the laboratory of Dr. Anne-Ruxandra Carvunis (Univ. of

Pittsburgh). Each transformed version of the library was stamped in technical triplicate to SC medium lacking uracil (as a control), SC-Ura- medium containing 0.8M NaCl, 1.5M NaCl, or 50 ng/mL rapamycin. Plates were grown at 30 °C for 2–4 days, and white light images were captured using the BioRad ChemiDoc XRS+ imager (Hercules, CA, USA) on days 1–4 of incubation. Images were converted to .jpg file format, and the pixel size of colonies was measured using the DissectionReader macro (generously provided by Dr. Kara Bernstein's laboratory (Univ. of Pittsburgh) and developed by John C. Dittmar and Robert J.D. Reid in Dr. Rodney Rothstein's laboratory (Columbia Univ.)) in Image J (National Institutes of Health, Bethesda, MA, USA). More information on this plugin can be found at: https://github.com/RothsteinLabCUMC/dissectionReader (accessed on 23 February 2022). Colony sizes from technical replicates were averaged and the standard deviation was determined (Supplemental Table S2, available in 'Chapter 3' folder at OneDrive link: Supplemental Thesis Documents - Bowman). The average sizes were then converted into individual sets of Z-scores for each plate in the library, based on the average colony size for each plate (this allowed for comparisons between pRS426 and pRS426-Aly1 or -Aly2 colony sizes). The average colony sizes for each gene deletion strain containing pRS426 were subtracted from the colony size for that gene deletion when over-expressing Aly1 or Aly2 to produce the 'change from vector' or ΔV value (Supplemental Table S2, available in 'Chapter 3' folder at OneDrive link: Supplemental Thesis Documents - Bowman). These ΔV values were then converted to Z-scores for each plasmid transformant, growth condition, and plate within the library. A Z-score cutoff of +/−1.2 was arbitrarily used to identify gene deletion candidates for further study. To be clear, there are likely other candidates from these screens that significantly affect Aly1 and/or Aly2 function; however, in the interest of having a manageable target set, we chose this cutoff for candidates. From the

conditions used (SC-Ura-, 0.8M and 1.5M NaCl, or rapamycin), the Aly1 and Aly2 candidates were combined into a single aggregate candidate list. Gene deletions that altered Aly1- or Aly2-dependent growth substantially in 2 of the 3 medium conditions listed were used to generate the secondary screening candidates list. We initially chose 62 candidates here; however, colony PCR used to verify the location of the KANMX4 cassette in the *cla4*Δ and *hog1*Δ isolates from our library revealed that these mutations were not correct and so they were discarded from the screen. These results were in contrast with many other colony PCR validations for strains used in this study. The 60 candidates were assessed for their ability to alter phenotypes using serial dilution growth assays, and, from this secondary screen, 18 candidates were chosen for further study. For these 18 final candidates, we assessed their ability to alter Aly1/Aly2-associated phenotypes (serial dilution growth assays), abundance (immunoblotting and microscopy), electrophoretic mobility (immunoblotting), or localization (microscopy), using the methods described herein.

3.2.5 Yeast Protein Extraction, CIP Treatments, and Immunoblot Analyses

Whole-cell extracts of yeast proteins were prepared using the trichloroacetic acid (TCA) extraction method as previously described [152] and as modified from [316]. In brief, cells were grown in SC medium to mid-exponential log phase at 30 °C (A_{600} = 0.6–1.0) and an equal density of cells was harvested by centrifugation. Cell pellets were flash-frozen in liquid nitrogen and stored at −80 °C until processing. Cells were lysed using sodium hydroxide and proteins were precipitated using 50% TCA. Precipitated proteins were solubilized in SDS/Urea sample buffer [8 M Urea, 200 mM Tris-HCl (pH 6.8), 0.1mM EDTA (pH 8), 100 mM DTT, Tris 100 mM (not pH adjusted)] and heated to 37 °C for 15 min. In some instances (Figure 26C,D), 15 µL of cell lysate was subsequently treated for 1 h at 37 °C with 40 units of Quick calf intestinal alkaline phosphatase

(CIP, New England Biolabs, Ipswitch, MA, USA) as per the manufacturer's recommendations, or mock-treated in CIP buffer without enzyme. Samples were then precipitated using 50% TCA and solubilized in SDS/Urea sample buffer as above. Proteins were resolved by SDS-PAGE and identified by immunoblotting with a mouse anti-green fluorescent protein (GFP) antibody (Santa Cruz Biotechnology, Santa Cruz, CA, USA) to detect GFP fused α-arrestins. As a protein-loading control, immunoblot membranes were stained after transfer with Revert™ (Li-Cor Biosciences, Lincoln, NE, USA) total protein stain and were detected using the Odyssey™ FC infrared imaging system (Li-Cor Biosciences). Anti-mouse, anti-rat, or anti-rabbit secondary antibodies, conjugated to IRDye-800 or IRDye-680 (Li-Cor Biosciences), were used to detect primary antibodies on the Odyssey™ FC infrared imaging system (Li-Cor Biosciences). Quantification of band intensities on immunoblot scans was performed using Image J software (NIH, Bethesda, MD, USA). In brief, bands were boxed, and the mean pixel intensity measured. Background fluorescence was subtracted from each measurement and band pixel intensities were compared across replicates.

3.2.6 Protein Stability Assays

The stability of GFP-tagged α-arrestins expressed from the pRS415-*TEF1* promoter plasmids (see Table 4) was assessed by immunoblotting. Cells were grown to mid-exponential growth phase (A_{600} 0.8–1.0) at 30 °C and cells were treated with 0.1 mg/mL CHX (Gold Bio, St. Louis, MD, USA) to block new protein synthesis; equal densities of cells were harvested over time. Cell pellets were treated as indicated above in Section 3.2.5, and TCA whole-cell protein extracts were made, resolved by SDS-PAGE, and the GFP-tagged proteins were detected by immunoblotting. To determine the impact of proteasomal inhibition on α-arrestin protein stability, similar assays were performed in cells where the multi-drug resistance pump, Pdr5, was deleted.

Cells were then treated with 100 μM MG132, a proteasomal inhibitor (APExBIO, Houston, TX, USA), for 1 h prior to the addition of 0.1 mg/mL CHX. Once again, equal densities of cells were harvested at time points post-treatment with MG132 and cycloheximide. TCA extracts were generated, proteins were resolved by SDS-PAGE and identified via immunoblotting. Quantification of proteins on membrane blots was performed using Image J software, as described in Section 3.2.5 above.

3.2.7 Fluorescence Microscopy

Fluorescent protein localization was assessed using high-content confocal microscopy. For high-content confocal microscopy, which was done to assess Aly1-, Aly2-, Aly1^{PPXYless}, or Aly2^{PPXYless}-GFP or Git1-GFP localization across kinase and phosphatase gene deletions, we grew cells overnight in SC medium in either 96-well dishes or culture tubes with orbital shaking or on a rotating drum, respectively, at 30 °C. We then diluted cells and regrew them in 96-well format for 4 h with shaking on a 30 °C platform shaker. Cells were then inoculated to low density (~A_{600} = 0.15) into Cell Carrier 96-ultra microwell plates (Perkin Elmer, Waltham, MA), where each well had been treated with 50 μL of 0.2 μg/μL concanavalin A (MP Biomedicals, Solon, OH, USA) and the bottom of the optical plastic surface that contacts the objective had been coated with RainEx (to allow water to glide along with the objective during imaging). Each well contained 15 μM Cell Tracker Blue CMAC (7-amino-4-chloromethylcoumarin) dye (Life Technologies, Carlsbad, CA, USA) and, for Git1 localization, 10 μM trypan blue (Gibco, Dublin, Ireland), to mark the vacuoles and the cell wall/cell surface, respectively. Cells were imaged using a Nikon Eclipse Ti2-E A1R inverted microscope outfitted with a water immersion 40× LWD objective (NA 1.15), and images were detected using GaAsP or multi-alkali photomultiplier tube detectors.

Acquisition was controlled using NIS-Elements software (Nikon) and all images within an experiment were captured using identical settings. Images were cropped and adjusted evenly using NIS-Elements.

3.2.8 Image Quantification and Statistical Analyses

Image quantification was done using the Nikon NIS-Elements, NIS.*ai* (Artificial Intelligence) and Nikon General Analysis 3 (GA3) software package. For quantification of Aly1-, Aly2-, Aly1^{PPXYless}, or Aly2^{PPXYless}-GFP signal, the NIS.*ai* software was trained on a ground truth set of samples, where cells had been segmented using the images acquired in the DIC channel. Next, the NIS.*ai* software performed iterative training until it achieved a training loss threshold of <0.02, which is indicative of a high degree of agreement between the initial ground truth provided and the output generated by the NIS.*ai* software. Then, fields of images captured via the high-content imaging were processed, so that the cells in a field of view were segmented using the DIC. Any partial cells at the edges of the image were removed. Then, the mean fluorescence intensity for each cell was defined in the GFP channel.

To measure the cell surface fluorescence in comparison to the vacuolar fluorescence for Git1-GFP, a transporter found at the cell surface whose trafficking to the vacuole is regulated by Aly1 and Aly2, we relied on the fiducial markers of trypan blue (TB), which marks the cell wall, and CMAC, which marks the vacuoles. We then trained the NIS.*ai* software to identify the yeast cell surface using the TB-stained cells. TB stains the cell wall, and its fluorescence can be captured using 561 nm laser excitation and 595–650 nm emission. However, it should be noted that TB maximal fluorescence is at 620 nm excitation and 627–720 nm detection, where it effectively marks bud scars and the cell surface. For our approach, it was better to use a very modest portion

of fluorescent signal, captured with the 561 nm excitation, so that bud scars were not observed and only faint cell surface fluorescence could be seen. While TB marks the cell wall, the cell wall cannot be distinguished from the plasma membrane at this resolution by fluorescence microscopy, therefore this serves as a marker for the cell surface in our machine learning software [393]. The NIS.*ai* software was trained using a manually defined 'ground truth' set of cell surfaces until it achieved a training loss threshold of <0.02, indicating strong agreement between the initial ground truth provided and the output generated by the NIS.*ai* software. In parallel with this, the CMAC staining was used to define the vacuole. A General Analyses 3 (Nikon) workflow was built in Nikon NIS-Elements software to pair the cell surface, as defined by TB staining with the internal vacuolar mask generated by the CMAC staining. This combined mask was used to measure the GFP fluorescence intensity at the cell surface and in the vacuole for all the cells in at least 6 fields of view for Git1-GFP (as shown in Figure 31B).

Fluorescent quantification was then assessed statistically using Prism (GraphPad Software, San Diego, CA, USA). Unless otherwise indicated, we performed the Kruskal–Wallis statistical test with Dunn's post hoc correction for multiple comparisons. In all cases, significant p-values from these tests are represented as: *, p value < 0.1; ** p value < 0.01; ***, p value < 0.001; ns, p value > 0.1. In some instances where multiple comparisons are made, the † symbol may additionally be used in place of the * with the same p value meanings, though indicating comparisons to a different reference sample.

3.2.9 RNA Extraction and Relative Quantitative Reverse Transcription Polymerase Chain Reaction (qRT-PCR) Analysis

RNA was extracted from wild-type, *sit4*Δ, *npr1*Δ, *tor1*Δ, *sit4*Δ *npr1*Δ, *pep4*Δ, or *sit4*Δ *pep4*Δ cells expressing one of three different plasmids: (1) pRS415-*TEF1pr*-GFP, (2) pRS415-*TEF1pr*-Aly1-GFP, or (3) pRS415-*TEF1pr*-Aly2-GFP using a hot phenol/chloroform extraction method, as described in [394]. In brief, 6 mL of midlog phase cells were harvested (OD_{600} = 1.0), washed in water, and flash-frozen in liquid nitrogen. Cell pellets were resuspended in AE buffer (50 mM sodium acetate [pH 5.3], 10 mM EDTA), and SDS was added to a final concentration of 1% (*w*/*v*). This mixture was vortexed, an equal volume of buffer-saturated phenol was added, and it was then incubated at 65 °C for 4 min. The mixture was then rapidly cooled in a dry ice/ethanol bath for 1 min, and microfuge tubes spun at 14,000 RPM for 8 min to separate phases. The top, aqueous layer was transferred to a new microfuge tube, and an equal volume of buffer-saturated phenol/chloroform was mixed into the sample by vortexing before the phases were separated by repeating the spin. The top, aqueous layer was again transferred to a new microfuge tube, and the RNA was precipitated using sodium acetate/ethanol, incubation at −20 °C overnight, and microcentrifugation at 14,000 RPM for 15 min at 4 °C. The supernatant was removed, and RNA pellets were washed with 80% ethanol, followed by microcentrifugation at 14,000 RPM for 15 mins at 4 °C. The supernatant was removed and RNA pellets were dried for 10 min. RNA pellets were resuspended in 75 μL of RNase-free water and the concentration was determined using a Nanodrop One Microvolume UV-Vis spectrophotometer (ThermoFisher Sci., Waltham, MA, USA); the quality of the RNA was determined by resolving 1 μg on a 1% agarose gel containing bleach.

For each sample, 1.5 µg of total RNA was converted to cDNA using a High Capacity RNA-to-cDNA kit (Applied Biosystems™, Waltham, MA, USA). The cDNA was then diluted 5-fold, and 0.5 µL was used in each real-time PCR reaction. Primers used for the PCR were: (1) *GFP* forward (5′CATTACCTGTCCACACAATCT3′) and *GFP* reverse (5′ATCCATGCCATGTGTAATCC3′) to detect all transcripts expressing GFP, (2) *TEF1* forward (5′CTCAAGCTGACTGTGCTATC3′) and *TEF1* reverse (5′CAAGGTGAAAGCCAACAAAG3′) to detect the expression of chromosomal *TEF1*, (3) YEP3 forward (5′CCAGCAATCCATTAAGGTTC3′) and *YEP3* reverse (5′CAGCGGTCTTCTTGTCCTTG3′) to detect expression of chromosomal *YEP3* as a control for cDNA abundance, and (4) *ADH1* forward (5′ATCTTCTACGAATCCCACGG3′) and *ADH1* reverse (5′CCACCGACTAATGGTAGCTT3′). PowerSYBR® Green PCR Master Mix (Applied Biosystems™, Waltham, MA, USA) was used for real-time PCR reactions in a 96-well PCR plate (Millipore Sigma, Burlington, MA, USA). Two replicate wells were assigned for each unique cDNA-primer combination, and cDNAs were prepared from two biological replicates for a total of 4 replicates (2 biological replicates with 2 technical replicates on each) for every cDNA-primer pairing. Platemax® UltraClear sealing films (Millipore Sigma, Burlington, MA) were used to seal the tops of PCR plates. Real-time PCR was performed on a 7900HT Fast Real-Time PCR System (Applied Biosystems™, Waltham, MA, USA) using the default program and the disassociation curve stage. The results were analyzed using the $2^{-\Delta\Delta CT}$ method [395]. Relative quantification (RQ) values to the WT were normalized to the *YEP3* gene as a control for expression. For each set of samples (pRS415-*TEF1pr*-GFP, pRS415-*TEF1pr*-Aly1-GFP, pRS415-*TEF1pr*-Aly2-GFP), expression in mutant strains is presented as relative to expression in wild-type cells. qRT-PCR results are presented as the mean of four replicates ± S.D. from two independent biological

experiments. We performed the Kruskal–Wallis statistical test with Dunn's post hoc correction for multiple comparisons. In all cases, significant *p*-values from these tests are represented as: *, *p* value < 0.1; ** *p* value < 0.01; ns, *p* value > 0.1.

3.3 Results

3.3.1 Identifying Kinases and Phosphatases that Influence Aly1- or Aly2-Mediated Growth in Response to Rapamycin or High-Salt Stress

We aimed to determine the kinases and phosphatases which control α-arrestins Aly1 and Aly2, which possess 40 and 87 phosphorylation sites, respectively, following treatment with rapamycin, a drug which mimics nitrogen starvation by directly inhibiting TORC1, or under high salt-driven osmotic stress. These conditions were chosen due to the resistance to rapamycin conferred by the over-expression of Aly1 or Aly2, as well as the fact that, not only are multiple membrane proteins controlled by the Alys internalized following salt stress, but regulators of the Alys are also activated under this condition (Figure 22A; S.D.) [67,68,385,386]. In order to enable the identification of Aly phospho-regulators, I built the kinase and phosphatase deletion (KinDel) library, a sub-library of the deletion collection containing mutants for all protein kinases and phosphatases annotated as being non-essential. Notably, I performed these screens as part of the Introduction to Molecular Genetics lab course (BIOSC0352) at the University of Pittsburgh (Spring of 2020 and '21). These screens of the KinDel library established the foundation of a course-based undergraduate research experience (CURE), participated in by 48 undergraduate students who contributed to our initial observations. To perform my screen, I transformed high

copy plasmids expressing either nothing (empty vector), or either Aly1 or Aly2 from their own promoters into each KinDel library strain. After measuring the size of each colony, I compared the growth of cells expressing empty-vector to those over-expressing an α-arrestin in the same deletion background on each media condition to identify synthetic genetic interactions (see section 3.2.4). We chose to further pursue those candidates that deviated both from the mean colony size (Z score > or < 1.25) on a given media condition and from its vector-expressing control (see section 3.2.4 and Supplemental Table S3, available in 'Chapter 3' folder at OneDrive link: Supplemental Thesis Documents - Bowman). This latter comparison, expressed as ΔV (see section 3.2.4) served to account for any sensitivity or resistance associated with the loss of a particular gene rather than the over-expression of either Aly1 or Aly2 alone.

Using this initial screen, we isolated the gene candidates listed in Supplemental Table S3 (further detail in Supplemental Table S4, both available in 'Chapter 3' folder at OneDrive link: Supplemental Thesis Documents - Bowman), and summarized in Figure 22B-D (A.F.O.). Notably, we identified nearly half of the genes present in the KinDel library as altering the Aly1- or Aly2-dependent phenotypes, respectively. We further performed extensive secondary screening in an effort to validate and refine our candidate groups, choosing to focus on the 60 candidates present in both Aly screens, as these α-arrestins are not only paralogous, but often share overlapping functional roles. We performed this secondary screening using serial dilution growth assays, a more sensitive measure than single-colony analysis, finding that all 60 gene deletion mutants altered the Aly-dependent growth phenotype when grown in the presence of either rapamycin or high-salt stress (Figure 22 and summarized in Table 5; S.D., E.J., and A.F.O.). The breadth of these effects further supports a wide-reaching network of α-arrestin phospho-regulators that likely act to improve their function, as the loss of many of these candidates reduced the resistance to

rapamycin normally conferred by Aly over-expression. Based on these results, we further refined our candidate group to a set of 18 genes found to impact those rapamycin phenotypes (Table 5; S.D and E.J.).

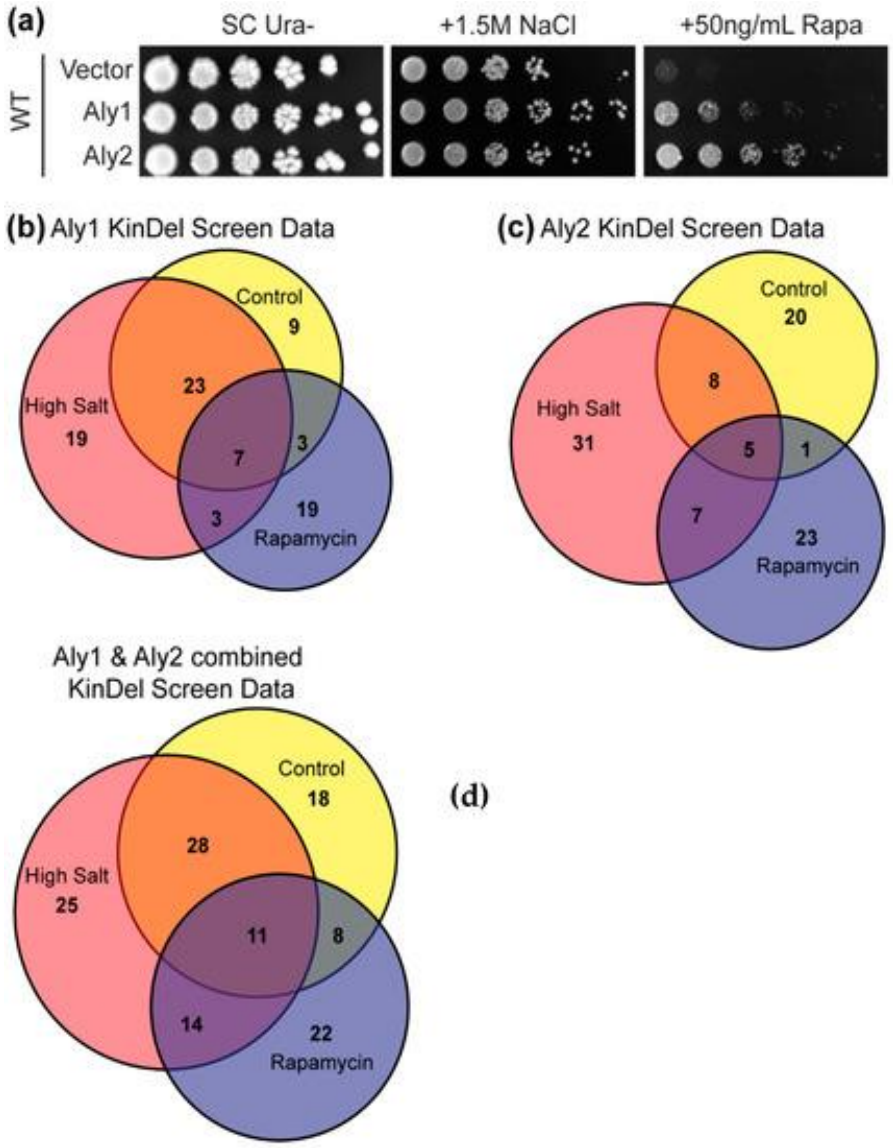

Figure 22. KinDel candidates that influence α-arrestin-dependent phenotypes.

(A) Growth of serial dilutions of WT cells containing the indicated pRS426-derived plasmids expressing either nothing (vector) or the indicated α-arrestin on SC medium lacking uracil and containing 1.5M NaCl or 50 ng/mL rapamycin. (B-D) Venn diagrams indicating the number of KinDel library gen deletions found to alter the sensitivity of (B) Aly1 or (C) Aly2 on control (yellow), high-salt (red), or rapamycin (blue) medium. The sum of the numbers in

each circle identifies the number of gene deletions in each class. Panel (D) shows the overlapping candidates identified in both the Aly1 and Aly2 screens for each medium condition.

Table 5. Summary of screening 18 gene deletion candidates from KinDel library with over-expression of Aly1 or Aly2

	pRS415-TEF1pr-Aly1-GFP				pRS415-TEF1pr-Aly2-GFP			
Gene	**NaCl**	**Rapa**	**Protein levels**	**Mobility shift?**	**NaCl**	**Rapa**	**Protein levels**	**Mobility shift?**
BUB1	**Sens**	**Sens**	**Equal**	**No**	**Sens**	**Sens**	**Equal**	**No**
CTK1	**Sens**	**Sens**	**Lower**	**No**	**Sens**	**Sens**	**Lower**	**Maybe**
FUS3	**Sens**	**Res**	**Hi/Equal**	**No**	**Sens**	**Equal**	**Equal**	**No**
GIP2	**Sens**	**Res**	**Equal**	**No**	**Sens**	**Res**	**Equal**	**Yes**
KIN82	**Equal**	**Equal**	**Equal**	**No**	**Equal**	**Res**	**Equal**	**No**
NEM1	**Equal**	**Sens**	**Lower**	**No**	**Equal**	**Sens**	**Lower**	**No**
PTC4	**Equal**	**Equal**	**Equal/Lower**	**No**	**Equal**	**Equal**	**Equal/Lower**	**No**
RCK2	**Equal**	**Equal**	**Equal/Lower**	**No**	**Equal**	**Equal**	**Equal/Lower**	**No**
SIP2	**Res**	**Sens**	**Lower**	**Yes**	**Res**	**Sens**	**Lower**	**No**
SIT4	**Sens**	**Sens**	**Lower**	**Yes**	**Sens**	**Res**	**Lower**	**Yes**
SLT2	**Sens**	**Sens**	**Equal**	**No**	**Equal**	**Sens**	**Lower**	**No**
SPO7	**Equal**	**Sens**	**Lower**	**No**	**Res**	**Sens**	**Equal/Lower**	**No**
STE7	**Res**	**Res**	**Equal/Lower**	**No**	**Res**	**Res**	**Equal/Lower**	**No**
STE20	**Sens**	**Sens**	**Lower**	**No**	**Sens**	**Sens**	**Equal/Lower**	**Yes**
TIP41	**Equal**	**Res**	**Lower**	**No**	**Equal**	**Res**	**Equal/Lower**	**No**
TOR1	**Equal**	**Sens**	**Equal/Lower**	**No**	**Equal**	**Sens**	**Equal/Lower**	**No**
YMR1	**Equal**	**Res**	**Equal/Lower**	**No**	**Equal**	**Equal**	**Equal**	**No**
YVH1	**Sens**	**Sens**	**Lower**	**Yes**	**Sens**	**Sens**	**Lower**	**Yes**

3.3.2 Some of the Kinases and Phosphatases That Impact Aly1- or Aly2-Mediated Growth Phenotypes Alter Aly Protein Abundance

To account for possible phenotypic changes driven by changes in their expression, a mode of regulation known to impact other α-arrestins like Ecm21 or Csr2, we transitioned to the use of plasmids expressing Aly1 or Aly2 from the strong, constitutive *TEF1* promoter and containing a C-terminal GFP tag (plasmid details in Table 4) [73,74]. This increased expression of Aly1 and Aly2 further improved their ability to confer resistance to rapamycin, supporting the idea that the strength of this phenotype is directly linked to the abundance of the α-arrestins (Figure 23; S.D. and E.J.). Over half of these secondary candidates affected the Aly-dependent growth on high salt, though these candidates were not further pursued, while over 60% affected the growth on rapamycin (Figure 23 and Table 5; S.D. and E.J.). Of note, many of the changes we observed in the Aly-dependent phenotypes were affected by the ability of the α-arrestin to interact with Rsp5, as the over-expression of mutants lacking their Rsp5-binding $^{L}/_{P}$PXY binding motifs (Aly1^{PPXYless} or Aly2^{PPXYless}) grew similarly to those expressing empty-vector (Figure 23B; S.D.). As the loss of Rsp5 binding severely affects α-arrestin trafficking function, these results suggest a prominent role for this interaction in the Aly-mediated response to salt stress or, more commonly, rapamycin [62,79,91]. While the $^{L}/_{P}$PXY motif-dependent changes in growth on rapamycin was clear for many candidates (*fus3*Δ, *gip2*Δ, *kin82*Δ, *ptc4*Δ, *rck2*Δ, *sip2*Δ, *spo7*Δ, *ste7*Δ, *tip41*Δ, and *ymr1*Δ), other gene deletion mutants were themselves highly sensitive to rapamycin (*ctk1*Δ, *nem1*Δ, *slt2*Δ, *ste20*Δ, *tor1*Δ, and *yvh1*Δ), preventing any robust Aly-driven growth and thus our ability to assess the role of Rsp5 binding. Surprisingly, we found Aly-over-expression in the absence of some gene candidates instead conferred sensitivity to rapamycin, a notable example of which occurs for Aly1, but not Aly2, in *sit4*Δ cells (Figure 23B, S.D. and E.J.). This dichotomy between the Alys also

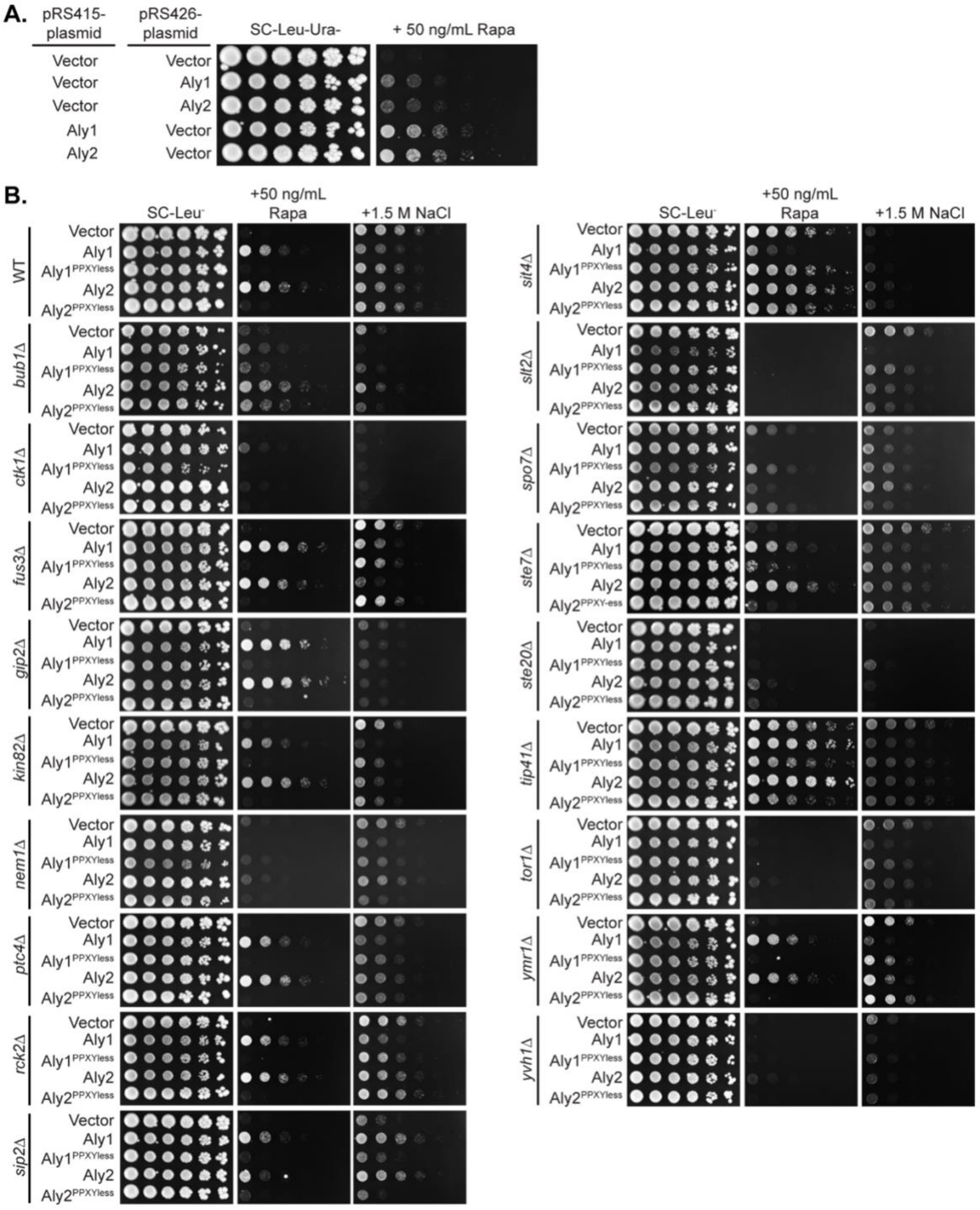

Figure 23. Secondary screening of KinDel candidates for growth phenotypes linked to Aly1- or Aly2-overexpression.

(A) Serial dilution growth assay to compare the pRS426-*ALY* promoter-expressed α-arrestins to the pRS415-*TEF1* promoter-expressed α-arrestins. Growth of serial dilutions of WT cells containing the indicated pRS426 or

pRS415-derived plasmid expressing either nothing (vector) or the indicated α-arrestin. (B) Serial dilution growth assays of WT cells or those lacking the gene indicated (from the KinDel library) and containing the indicated pRS415-*TEF1pr*-derived plasmid on the medium indicated.

occurred under salt stress, as we found multiple mutants (*kin82*Δ, *ptc4*Δ, *rck2*Δ, *slt2*Δ, *ste7*Δ, *tip41*Δ, and *tor1*Δ) displayed a similar Aly1-driven sensitivity that did not occur when over-expressing Aly2. While the lack of an Aly2-dependent phenotypic change during salt stress prevented our ability to assess the role of Rsp5-binding, the Aly1-dependent sensitivity consistently required the presence of its $^{L}/_{P}$PXY motif. A notable exception to these divergent roles was observed in the absence of *SIP2*, a subunit of the α-arrestin-regulating Snf1 kinase complex, where the over-expression of either Aly1 or Aly2 conferred strong resistance to salt stress that was completely dependent on their ability to bind Rsp5, representing a promising topic for future pursuits (Figure 23B; S.D.).

In order to further assess these 18 gene candidates, we utilized high-content fluorescence microscopy and immunoblotting to assess the electrophoretic mobility and abundance of GFP-tagged Aly1, Aly2, and their respective PPXYless mutants in these backgrounds (Figure 24-25, and summarized in Table 5; R.W.B, S.D. and E.J.). We observed a shift in Aly protein abundance for more than 70% of these delete mutants relative to the WT control (Figure 24, Figure 25, and summarized in Table 5. R.W.B., S.D., and E.J.). The use of high-content microscopy, coupled with automated image quantification using NIS.*ai* software (see Section 3.2.8), I was able to measure the fluorescence of 100s to 1000s of individual cells and assess their distribution across the population (Figure 24A-B, Figure 25A-B, and 26A-B). I found the Alys to localize mostly in the cytoplasm, as well a limited presence in the nucleus, exclusion from the vacuole, and occasional concentrated puncta likely residing at the Golgi or endosomes, largely consistent with previous

reports of their locale [58,66,67]. As such, while many of our candidates were found to impact Aly abundance, I did not observe any associated shifts in their subcellular localization as compared to the WT control (Figure 24A-B and Figure 25A-B).

TEF1-driven expression of free GFP in these backgrounds did reveal some variations in abundance, leading us to wonder if some of the effects we observed for the Alys might be influenced by changes in the expression of this promoter (Figure 26A-B). To our satisfaction, we rarely observed any change in transcript abundance as determined by qRT-PCR analysis targeted to the GFP region of *ALY1*-, *ALY2*-, and free-GFP transcripts, with the notable exception of an approximately 2-fold reduction for Aly1-GFP in *sit4*Δ cells (Figure 26C; A.C. and Y.L.). Further evaluation targeting chromosomal *TEF1* gene expression in some of these gene deletion backgrounds also revealed only small changes in transcript abundance compared to the WT control (Figure 26C-D; A.C. and Y.L.). Collectively, these findings support changes in protein stability, rather than transcriptional alterations, as the driver of the observed shifts in α-arrestin and GFP abundance. While transcriptional changes likely contributed to the reduced abundance of Aly1-GFP in *sit4*Δ cells, this is further considered below (see Section 3.3.3). Importantly, the shifts in abundance observed by microscopy were confirmed via immunoblot analyses, while additionally revealing changes in the electrophoretic mobility of Aly1- or Aly2-GFP in some deletion backgrounds, possibly due to altered degrees of phosphorylation (Figure 24C, Figure 25C, and Table 5; S.D. and E.J.). Our screens identified multiple components of two signaling pathways which affect Aly function, including members of the GPCR-controlled yeast mating pathway (Ste20, Ste7, and Fus3 kinases) [396,397], and the nutrient-responsive TORC1 signaling network (Tor1, Sit4, and Tip41) [137,388,389,391,398]. While the connection between the yeast mating

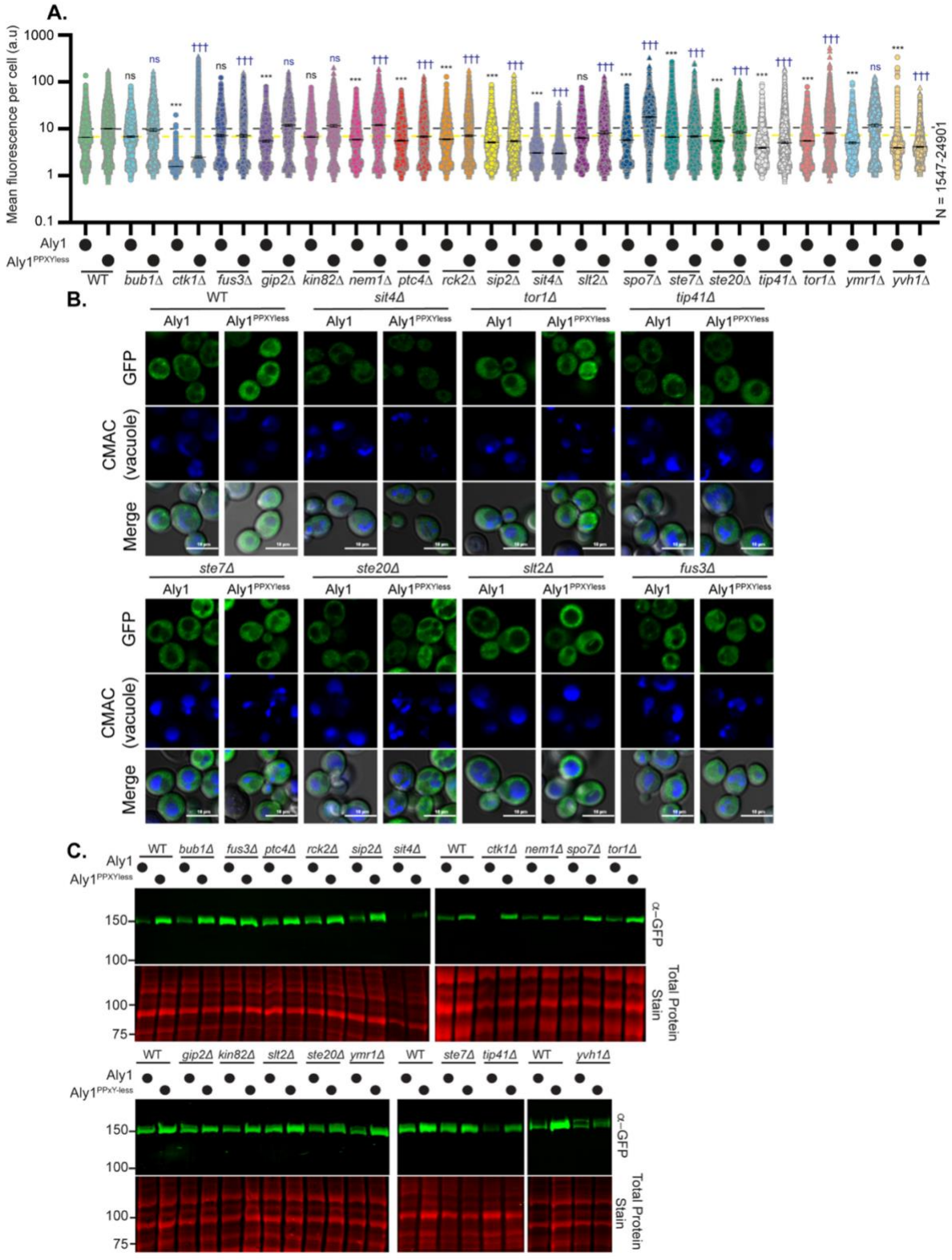

Figure 24. Kinases and phosphatases from the KinDel screen alter the abundance and electrophoretic mobility of Aly1.

(A) Cells expressing the indicated Aly1 protein fused to GFP (pRS415-*TEF1pr* plasmids) in either WT or the noted gene deletion backgrounds were imaged by high-content confocal microscopy and whole-cell fluorescence of the cells was quantified using NIS.*ai* and Nikon GA3 software. The mean fluorescence intensity from whole-cell measurements (in arbitrary units, au) is plotted for each cell as a circle. The median fluorescence intensity is shown as a black line for each group and the error bars represent the 95% confidence interval. A yellow or black dashed line represents the median fluorescence intensity for Aly1 or Aly1^{PPXYless} expressed in WT cells, respectively. Kruskal–Wallis statistical analysis with Dunn's post hoc test was performed to compare the fluorescence distributions to the cognate WT. In black asterisks (*) or blue daggers (†), comparisons are made to Aly1 or Aly1^{PPXYless} in WT cells, respectively (ns = not significant; three symbols have a p-value < 0.0005). (B) A subset of the fluorescent microscopy images acquired for the data presented in (A) are shown. CMAC is used to stain the vacuoles (shown in blue). Merge is overlaid with the transmitted light cell image as well as the fluorescence images. (C) Whole-cell extracts from the cells described in (A) were made, analyzed by SDS-PAGE and immunoblotting, and detected using an anti-GFP antibody. The REVERT total protein stain of the membrane is shown as a loading control. Molecular weights are shown on the left side in kDa.

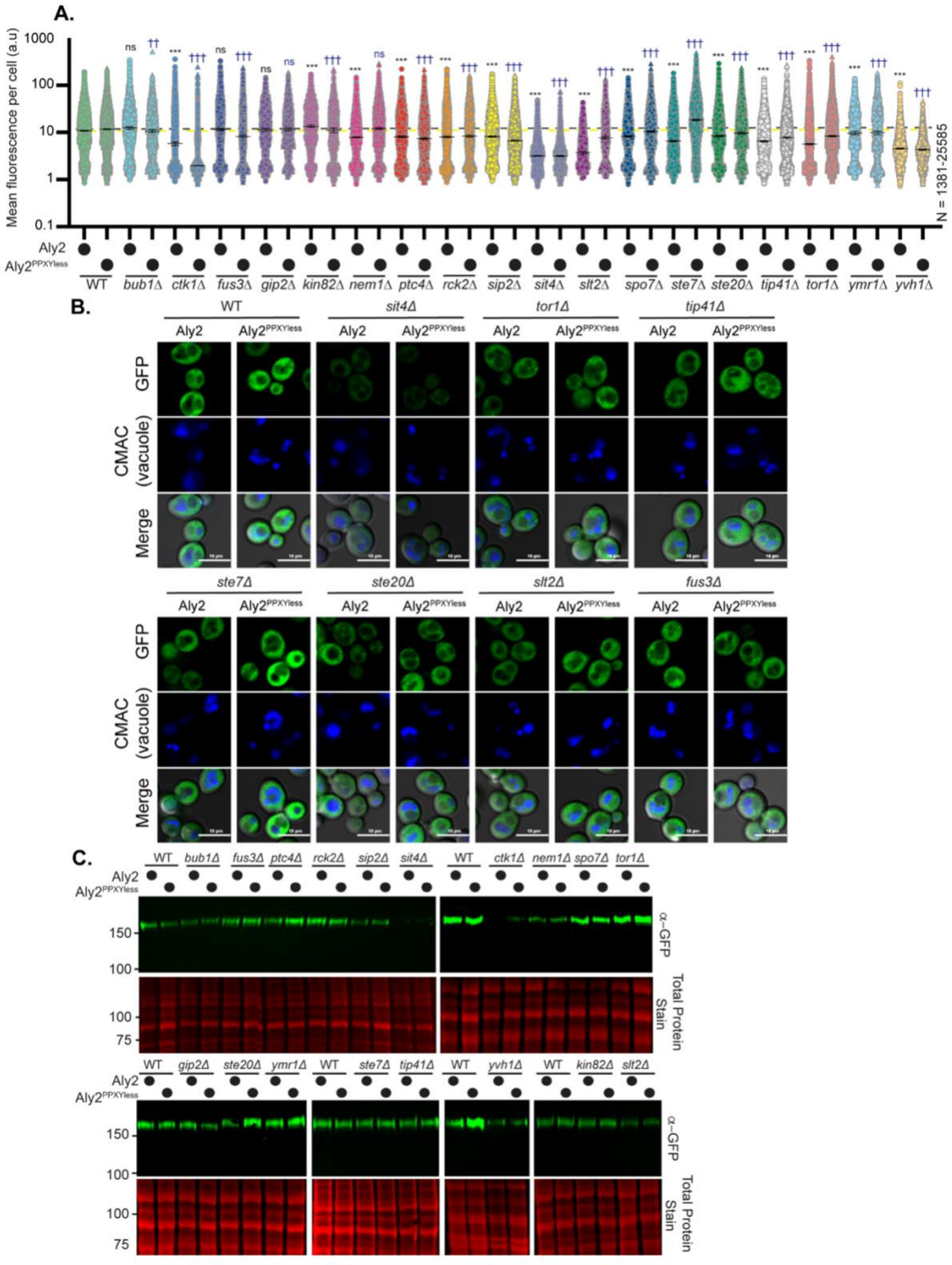

Figure 25. Kinases and phosphatases from the KinDel screen alter the abundance and electrophoretic mobility of Aly2.

(**A**) Cells expressing the indicated Aly2 protein fused to GFP (pRS415-*TEF1pr* plasmids) in either WT or the noted gene deletion backgrounds were imaged by high-content confocal microscopy, and whole-cell fluorescence of the cells was quantified using NIS.*ai* and Nikon GA3 software. The mean fluorescence intensity from whole-cell measurements (in arbitrary units, au) is plotted for each cell as a circle. The median fluorescence intensity is shown as a black line for each group and the error bars represent the 95% confidence interval. A yellow or black dashed line represents the median fluorescence intensity for Aly2 or Aly2^{PPXYless} expressed in WT cells, respectively. Kruskal–Wallis statistical analysis with Dunn's post hoc test was performed to compare the fluorescence distributions to the cognate WT. In black asterisks (*) or blue daggers (†), comparisons are made to Aly2 or Aly2^{PPXYless} in WT cells, respectively (ns = not significant; three symbols have a *p*-value < 0.0005). (**B**) A subset of the fluorescent microscopy images acquired for the data presented in (**A**) are shown. CMAC is used to stain the vacuoles (shown in blue). Merge is overlaid with the transmitted light cell image as well as the fluorescence images. (**C**) Whole-cell extracts from the cells described in (**A**) were made, analyzed by SDS-PAGE and immunoblotting, and detected using an anti-GFP antibody. The REVERT total protein stain of the membrane is shown as a loading control. Molecular weights are shown on the left side in kDa.

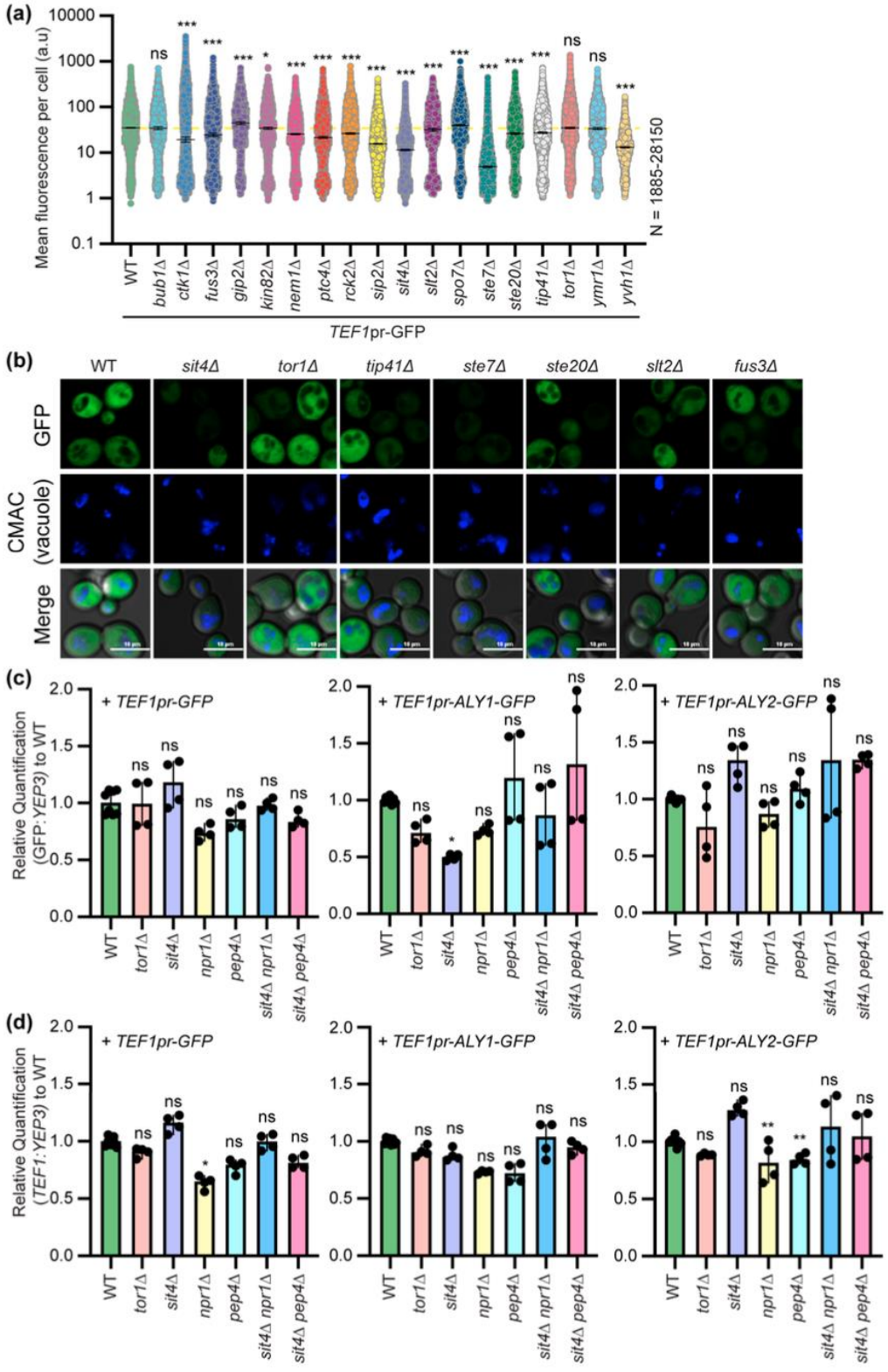

Figure 26. Assessing TEF1pr-GFP abundance in KinDel gene deletion candidates.

(A) Cells expressing the pRS415-*TEFpr*-GFP were imaged by high-content confocal microscopy and the whole cell fluorescence was quantified using Nikon.*ai* software. The mean fluorescence intensity from whoce cell measurements (in arbitrary units, au) is plotted for each cell as a circle. The median fluorescence intensity is shown as a black line for each group and the error bars represent the 95% confidence intercal. A yellow dashed line respresents the median fluorescence intensity for GFP expressed in WT cells. Kruskal-Wallis statistical analysis with Dunn's post hoc test was performed to compare the GFP fluorescence distributions to that of WT cells. In black asterisks, statistical comparisons are made to GFP in WT cells. (ns = not significant; one symbol has a p-value <0.05; three symbols have a p-value<0.0005). (B) A subset of the fluorescent microscopy images acquired for the data presented in (a) are shown. CMAC is used to stain the vacuoles (shown in blue). While in some instances the abundance changes for free GFP mirrors that of the Alys fused to GFP, the fluorescence is much higher for free GFP than any of the Aly-GFP fusions (~ an order of magnitude higher for GFP than the Alys). (C-D) Relative quantifications of qRT-PCR analyses of (C) GFP or (D) chromosomal *TEF1* transcripts to the *YEP3* control transcripts are presented for four replicate experiments. Transcript abundances in cells bearing gene deletions and expressing the indicated *TEF1pr*-X-GFP plasmid are presented relative to the transcript abundance in the WT controls. Kruskal-Wallis statistical analysis with Dunn's post hoc test was performed to compare the transcript abundances to the cognate WT (ns = not significant; one symbol has a p-value <0.05; three symbols have a p-value<0.0005).

pathway and Aly regulation warrants further study, given that Aly1 and Aly2 are already known to play a role in the trafficking of the GPCR heading this pathway in *MAT***a** yeast [62,79], we instead chose to focus on *SIT4* and the TORC1 signaling network, components tied to our strongest-observed effects on the Alys. Indeed, we not only observed the over-expression of Aly1 to confer sensitivity in the already rapamycin-resistant *sit4*Δ background, but also a decrease in the abundance and electrophoretic mobility of Aly1 and Aly2 proteins in this background (Figure 23B, Figure 24, Figure 25, and Figure 27B; R.W.B., S.D., E.J., H.B., and N.O.).

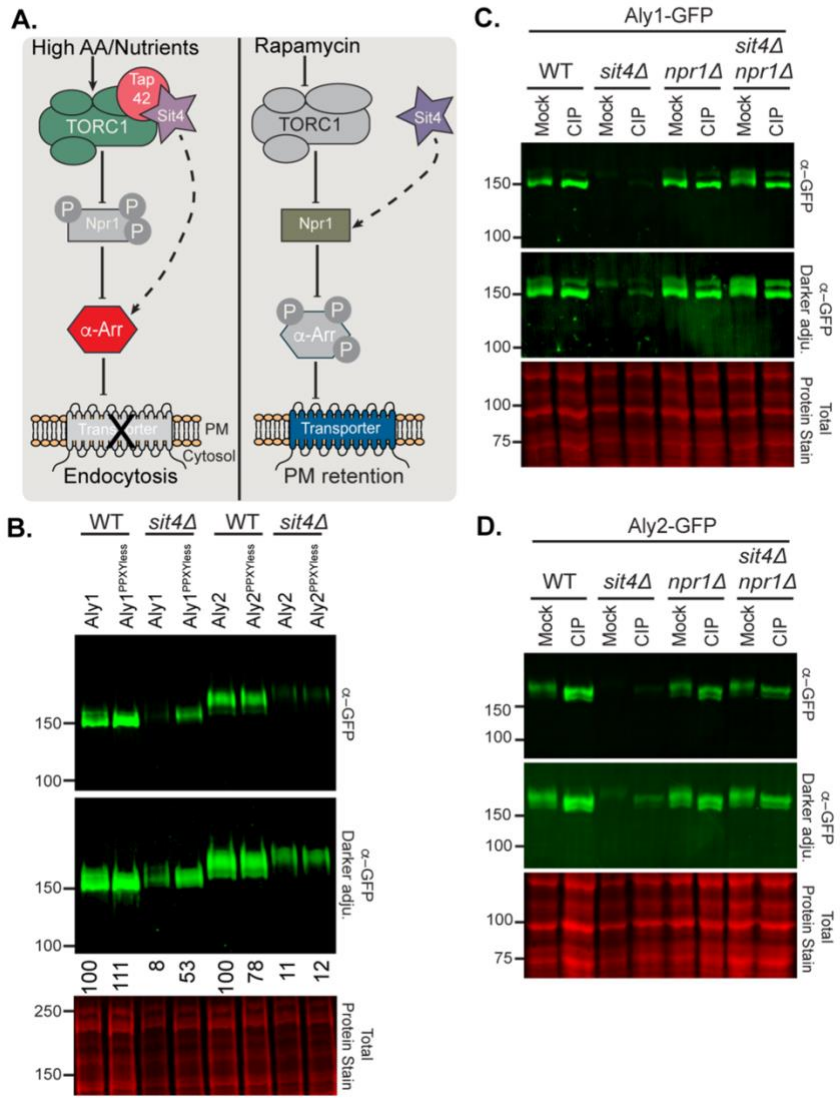

Figure 27. Sit4 and Npr1 regulate Aly abundance and phosphorylation.

(A) Model of TORC1 regulation of Sit4 and Npr1 based on studies of Bul regulation of Gap1. In robust nutrients, TORC1 is active and Tap42-Sit4 are thought to be bound. This may direct Sit4 activity towards α-arrestins, as indicated by a dashed line. α-Arrestins are active and can remove nutrient transporters from the PM. In response to rapamycin or poor nutrient conditions, TORC1 is inhibited, and the Tap42-Sit4 complex dissociates. Sit4 phosphatase activity is now thought to be directed to Npr1 (dashed-line with arrow), which becomes active. Active Npr1 can phosphorylate and inhibit α-arrestins, preventing the removal of nutrient transporters from the PM. Activation or inhibition are indicated by lines that end in arrowheads or blunt lines, respectively. Complexes whose activity is lost in the condition indicated are shown in grey. (B) Whole-cell extracts were made from the indicated strains expressing

Alys as GFP-tagged proteins from the *TEF1pr* and then resolved by SDS-PAGE. Immunoblots were probed with anti-GFP antibody to examine Aly abundance and mobility. REVERT total protein stain is shown for each blot as a loading control (red). The percent of Aly protein, corrected for the loading control, for each lane is calculated relative to WT Aly in WT cells. (C,D) Whole-cell extracts were made from the indicated strains expressing Aly-GFP from the *TEF1pr* and then were either treated with calf intestinal alkaline phosphatase (CIP) or incubated in the same conditions without enzyme (mock). Extracts were then resolved by SDS-PAGE and probed with anti-GFP antibody. REVERT total protein stain is shown for each blot as a loading control (red). For all panels, molecular weights are shown on the left side in kDa. Alys as GFP-tagged proteins from the *TEF1pr* and then resolved by SDS-PAGE. Immunoblots were probed with anti-GFP antibody to examine Aly abundance and mobility. REVERT total protein stain is shown for each blot as a loading control (red). The percent of Aly protein, corrected for the loading control, for each lane is calculated relative to WT Aly in WT cells. (C,D) Whole-cell extracts were made from the indicated strains expressing Aly-GFP from the *TEF1pr* and then were either treated with calf intestinal alkaline phosphatase (CIP) or incubated in the same conditions without enzyme (mock). Extracts were then resolved by SDS-PAGE and probed with anti-GFP antibody. REVERT total protein stain is shown for each blot as a loading control (red). For all panels, molecular weights are shown on the left side in kDa.

3.3.3 Sit4 and Npr1 Regulate Aly1 and Aly2 Phosphorylation and Abundance

α-Arrestin-mediated trafficking is regulated by the TORC1-Sit4-Npr1 signaling network, summarized in Figure 27A (A.F.O) based on work centered on the α-arrestins Bul1 and Bul2 and further discussed in Section 3.4 [66,67,77,94,104]. Briefly, under nutrient replete conditions, active TORC1 is bound to Sit4-Tap42, preventing Sit4 from dephosphorylating and activating the kinase Npr1, but potentially maintaining its ability to selectively dephosphorylate α-arrestins to allow for their control of nutrient transporter internalization [77,94]. Conversely, when TORC1 is inhibited, as occurs during nutrient starvation or following treatment with rapamycin, it is no longer able to drive the phospho-inhibition of Npr1. Sit4, now released from its own inhibition by

Tap42, acts to further dephosphorylate Npr1, activating its ability to drive α-arrestin phosphorylation and inhibit their endocytic functions. Active Npr1 may also promote the recycling of the general amino acid permease Gap1 to the cell surface by Aly2 to aid in cell survival during starvation [67]. While Aly2 is a direct substrate of Npr1, with Aly1 having also been found to undergo Npr1-dependent phosphorylation, neither α-arrestin has been linked to regulation by Sit4 [67,104]. In an effort to discern molecular details underlying the relationship between Sit4 and the Alys, we further assessed the mobility and abundance of these α-arrestins and their PPXYless mutants in a *sit4*Δ background (Figure 27B; E.J.). While all forms of Aly1 and Aly2 have decreased abundance and electrophoretic mobility in *sit4*Δ cells, their mobility returns to WT levels following treatment with calf intestinal phosphatase (CIP), confirming both Alys as hyper-phosphorylated in the absence of *SIT4* (Figure 27C-D; E.J.). As the coordinated regulation of other α-arrestins by Sit4 and Npr1 has been previously demonstrated, we expanded our assessment to further include this associated kinase despite its exclusion from our previously mentioned group of 18 candidates due to having only affected Aly1-, and not Aly2-, mediated growth on rapamycin [77,94].

While not surprising, given that Npr1 is largely inactive under the rich growth conditions used, we observed no change in the electrophoretic mobility of Aly1 or Aly2 in *npr1*Δ cells. In a notable contrast to what we observed in a *sit4*Δ, however, cells lacking both *SIT4* and *NPR1* also exhibited similar mobility profiles to WT cells (Figure 27C-D; E.J.). This leads us to suggest that, under these rich growth conditions, Sit4 acts to prevent the hyper-phosphorylation of Aly1 and Aly2 by Npr1.

When examined by fluorescence microscopy, I found that the localization of either Aly1- or Aly2-GFP is similar to WT controls in *tor1*Δ, *sit4*Δ, *npr1*Δ, and *sit4*Δ *npr1*Δ cells (Figure 28A-

D). The abundance of Aly2-GFP, however, was modestly reduced in the absence of *NPR1* or *TOR1*, and, as observed previously, even further depleted in cells lacking *SIT4* (Figure 28C-D; R.W.B., H.B., and N.O.). Remarkably, the combined absence of *SIT4* and *NPR1* restored Aly2-GFP abundance from those seen in a *sit4*Δ, a shift we found to not be connected to changes in *TEF1pr*-Aly2-GFP transcript levels (Figure 26C; A.C. and Y.L.). These findings were further corroborated by immunoblot analysis, where we observed similar trends in Aly2-GFP abundance (Figure 28G-H; S.D., E.J.).

I was surprised to find that, unlike Aly2, Aly1-GFP displayed two distinct sub-populations in *sit4*Δ *npr1*Δ cells (Figure 29 shows distributions for 10 replicate experiments). The first, comprising ~42% of cells, displayed an increased abundance of Aly1-GFP compared to *sit4*Δ cells, while the remaining second population contained almost no detectable Aly1-GFP (Figure 28A-B, compare Pop. 1 to Pop. 2, Figure 29). Furthermore, when transformed with Aly1-GFP, *sit4*Δ *npr1*Δ cells produce both small and large colonies on solid media, representing slow- and fast-growing populations, respectively, and either of these colony types produced populations of Aly1-GFP abundance (Figure 28A-B and Figure 29). As mentioned previously, *TEF1pr-ALY1*-GFP transcripts, unlike those for Aly2, were found to have an approximately 2-fold lower abundance in *sit4*Δ cells than the WT control. While these transcript levels were largely restored in a *sit4*Δ *npr1*Δ background, we again observed two distinct populations (Figure 26C; A.C. and Y.L.). Critically, these changes in transcript abundance were not present for the endogenous *TEF1* locus in either background, suggesting the changes observed for *ALY1* correspond to a shift in transcript stability rather than *TEF1* promoter expression, though we did not investigate this mechanism further in these studies (Figure 26D; A.C. and Y.L). While immunoblot analyses of Aly1 or Aly1^{PPXYless}-GFP largely reproduced what we observed by microscopy in *tor1*Δ, *sit4*Δ, *npr1*Δ, and

*sit4*Δ *npr1*Δ cells, we once again observed variability across 7 replicate experiments (Figure 28E-F; S.D. and E.J.). While we observed a return of Aly1-GFP electrophoretic mobility to WT levels in *sit4*Δ *npr1*Δ cells, the stability of this protein was improved in only some of these experiments (Figure 28C-D,F, R.W.B., S.D., and E.J.). We suggest that these two approaches describe the same variability of Aly1-GFP abundance, with microscopy able to discern the mixed populations at single-cell resolution rather than the whole-population data obtained via immunoblotting.

The abundance of Aly1-GFP present in a given protein extract depends upon the proportion of *sit4*Δ *npr1*Δ cells that have reduced rather than restored levels of the α-arrestin, leading to the variability we observed using this method and our subsequent preference for the higher degree of cell-to-cell resolution achievable via microscopy (compare Figure 27C and 28F; S.D. and E.J.). Of note, we found Aly1^{PPXYless}-GFP abundance to be improved in *sit4*Δ *npr1*Δ compared to *sit4*Δ cells via immunoblotting and lacking the variability between experiments observed for Aly1-GFP (Figure 28F; S.D. and E.J.). As this PPXYless mutant also found to be dephosphorylated, we suggest that the α-arrestin's interaction with the Rsp5 ubiquitin ligase is at partially responsible for promoting Aly1-GFP instability in the absence of both *SIT4* and *NPR1*.

Together, these observations lead us to further suggest that the over-expression of functional Aly1 is detrimental to *sit4*Δ *npr1*Δ cells, leading to the involvement of secondary genetic mechanisms which reduce *ALY1* transcript and protein abundance to allow for improved cell growth. We observed a similar effect in *sit4*Δ *pep4*Δ cells (see Figure 32 and 26C; R.W.B., S.D., E.J., A.C., and Y.L) where the abundance of *ALY1* transcripts and protein levels were destabilized in a sub-population of the cells. Collectively, these results support a role for Npr1 in the hyperphosphorylation and destabilization of the Alys when Sit4 is not present, with a secondary mechanism operating to additionally limit the abundance of Aly1 in this background. It is possible

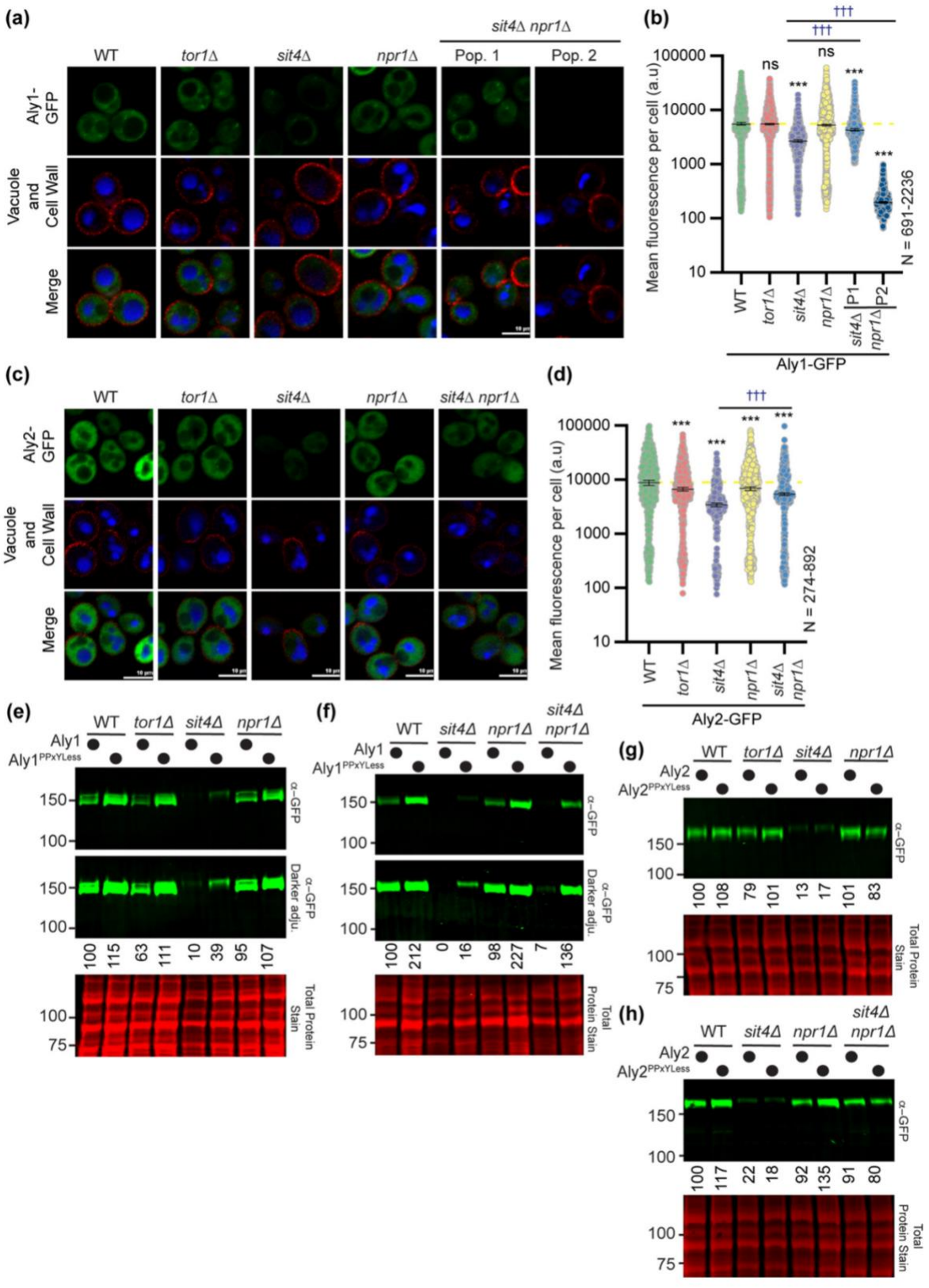

Figure 28. Sit4 and Npr1 regulate Aly abundance but do not affect localization.

(A) Aly1-GFP or (C) Aly2-GFP was expressed from the *TEF1pr* in either WT cells or those lacking the gene indicated and imaged by high-content fluorescence microscopy. CMAC is used to stain the vacuoles (shown in blue) and trypan blue (shown in red) is used to mark the cell wall. All images are shown as equally adjusted from a single experiment. (B) or (D) The whole-cell fluorescence of cells imaged in (A) or (C), respectively, was determined using NIS.*ai* and Nikon GA3 software, and the fluorescence for each cell is plotted as a circle. The median fluorescence intensity is shown as a black line for each group and the error bars represent the 95% confidence interval. A yellow dashed line represents the median fluorescence intensity for Aly1 or Aly2, expressed in WT cells in panels (B) and (D), respectively. Kruskal–Wallis statistical analysis with Dunn's post hoc test was performed to compare the fluorescence distributions to the cognate WT. In black asterisks (*), statistical comparisons are made to Aly1 or Aly2 in WT cells for panels (B) and (D), respectively. In blue daggers (†), the indicated statistical comparisons are made (ns = not significant; three symbols = p-value < 0.0005). (E-H) Whole-cell extracts were made from the indicated strains expressing Alys as GFP-tagged proteins from the *TEF1pr* and then resolved by SDS-PAGE. Immunoblots were probed with anti-GFP antibody to examine Aly abundance and mobility. REVERT total protein stain is shown for each blot as a loading control (red). The percent of Aly protein, corrected for the loading control, for each lane is calculated relative to WT Aly in WT cells.

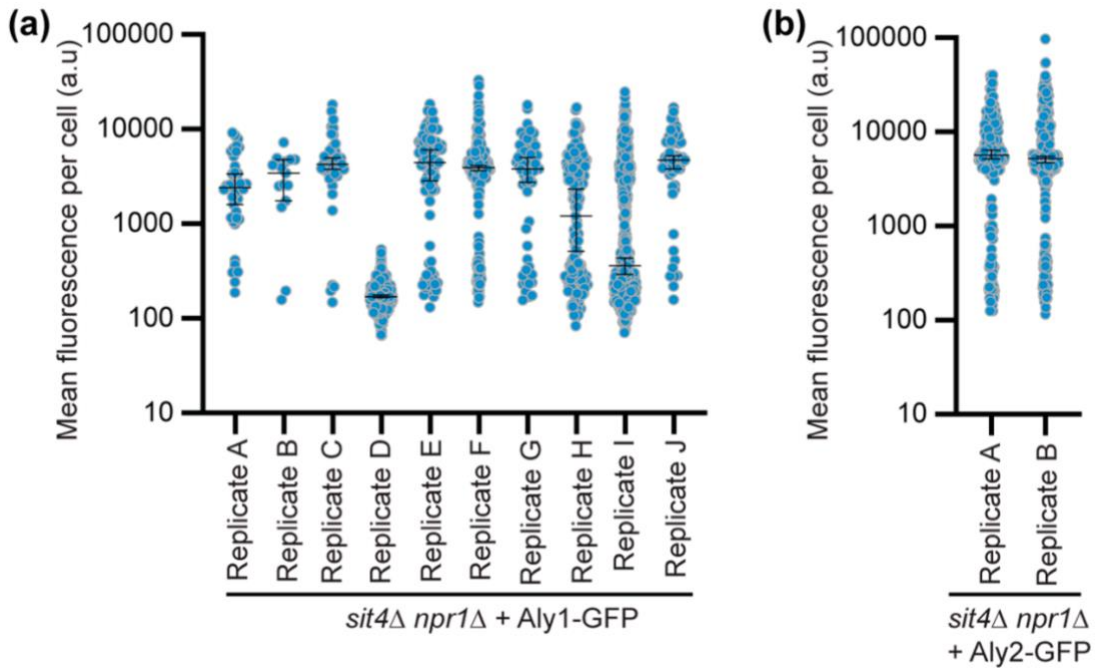

Figure 29. Fluorescence distributions for Aly1- or Aly2-GFP in *sit4*Δ *npr1*Δ replicate experiments.

Whole cell fluorescence was quantified for *sit4*Δ *npr1*Δ cells expressing (**A**) Aly1-GFP or (**B**) Aly2-GFP across the biological replicate experiments indicated (A-J for Aly1 and A-B for Aly2) using Nikon.*ai* software. The mean fluorescence intensity from whole cell measurements (in arbitrary units, a.u.) is plotted for each cell as a circle. The median fluorescence intensity is shown as a black line for each group and the error bars represent the 95% confidence interval. This figure demonstrates the high degree of variability in the Aly1-GFP abundance across 10 replicate experiments in the *sit4*Δ *npr1*Δ background.

that the Sit4 phosphatase is acting directly to dephosphorylate the Alys. Given that Npr1 is likely inactive under the rich growth conditions we employed, however, it is also possible that the absence of Sit4 results in increased activity of Npr1 toward these α-arrestins [388]. Therefore, we propose that without Sit4-dependent dephosphorylation to antagonize the Npr1's phosphorylation of the Alys, these α-arrestins become hyperphosphorylated and subsequently destabilized.

3.3.4 TORC1 inhibition or Loss of Sit4 Induces Aly1 and Aly2 Instability and Defective Vacuole Function Restores Aly Levels

Despite the results presented in Section 3.3.2, α-arrestin stability is not known to be controlled by the TORC1 signaling complex. We therefore sought to further evaluate the role of this key signaling hub in the control of Aly1 and Aly2 stability by assessing their stability in cells treated with either the TORC1-inhibiting drug rapamycin, or the protein synthesis-inhibiting drug CHX compared to untreated cells. Despite the routine use of both drugs, secondary effects of their use on cell signaling networks have often been under-appreciated. Rapamycin not only directly inhibits TORC1, but also indirectly represses the protein synthesis supported by the signaling complex [104,118,399]. Conversely, the block in protein synthesis achieved by CHX treatment also activates the TORC1 complex, likely due to the subsequent rise in free amino acid levels [399–401]. In light of these additional effects, data obtained with their use requires careful consideration. The addition of rapamycin results in a rapid reduction of Aly1 and Aly2 protein levels, with a near complete loss after 4 hours of treatment (Figure 30A-D; E.J.). Similarly, the Alys are also degraded after the

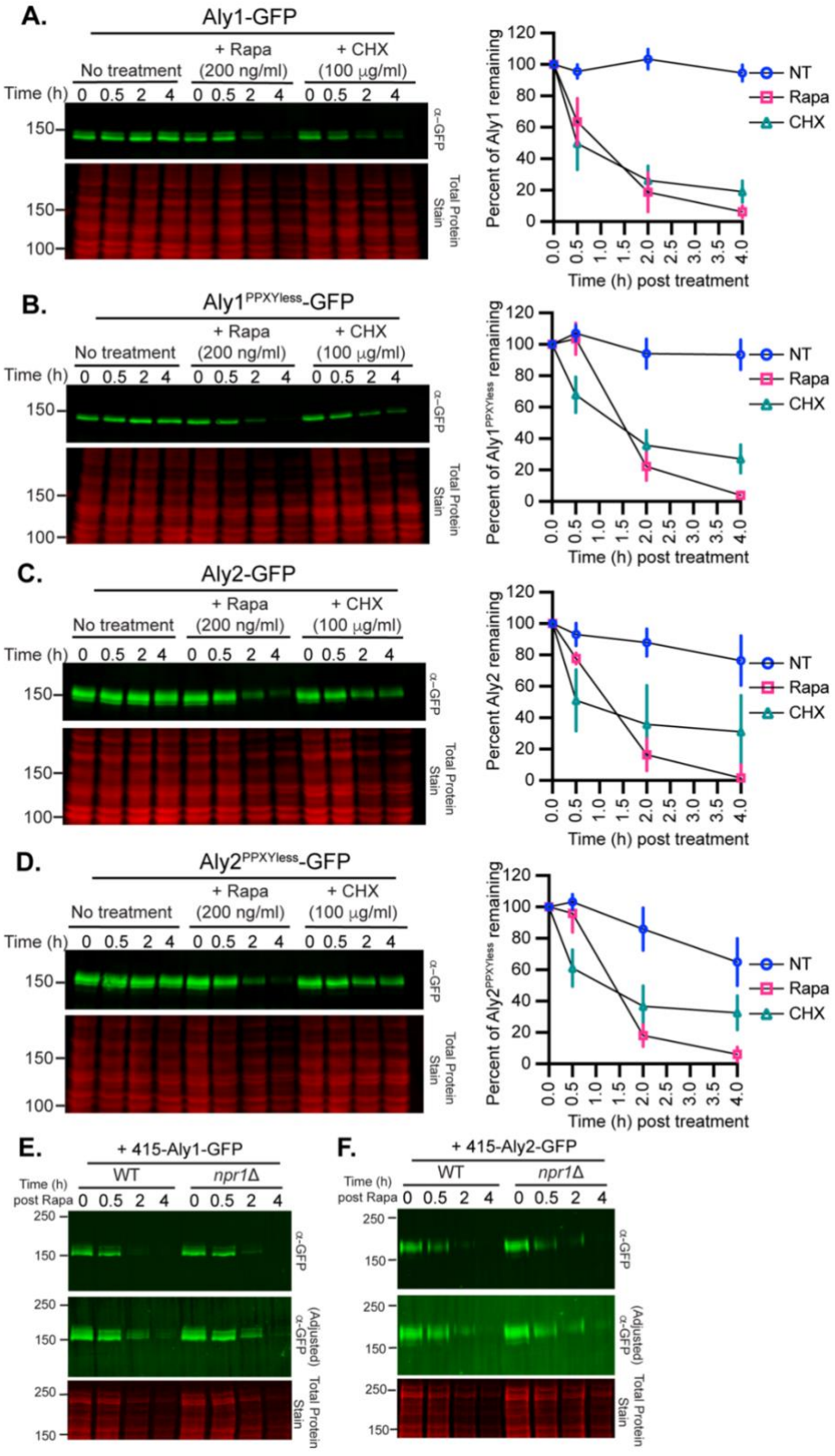

Figure 30. Rapamycin treatment destabilizes Aly1 and Aly2, irrespective of Rsp5 binding

(A–D) Whole-cell extracts from WT cells treated with nothing (no treatment; NT), rapamycin (rapa 200 ng/mL), or cycloheximide (CHX 100 μg/mL) for the times indicated, and expressing (A) Aly1-GFP, (B) Aly1^{PPXYless}-GFP, (C) Aly2-GFP, or (D) Aly2^{PPXYless}-GFP, or from *npr1*Δ cells expressing (E) Aly1-GFP or (F) Aly2-GFP, were resolved by SDS-PAGE. Anti-GFP antibody was used to detect tagged α-arrestins and REVERT total protein stain was used as a loading control. Blots shown are one representative from 4 replicate experiments. Molecular weights are shown on the left side in kDa. For blots in panels (A–D), the pixel intensities for the GFP-detected band and the lane in the loading control were measured using Image J. A correction factor based on the loading control was applied to each pixel intensity measurement. The t = 0 point was set to 100%, and all abundances are presented relative to that point. The error bars represent the SEM.

addition of CHX, though this occurs more slowly as 20-40% of the initial protein levels remain after 4 hours of treatment (Figure 30A-D; E.J.). In untreated cells, however, Aly1 remains highly stable over this time period, while Aly2 undergoes only a minor reduction in abundance, likely due to the progression of cell culture density towards saturation. From this we can conclude that the Alys are more effectively destabilized by rapamycin than CHX treatment. Though both treatments result in a reduction of the α-arrestin's abundance, it is difficult to discern how much of this effect derives from changes TORC1 signaling as opposed to those in protein synthesis.

The electrophoretic mobility of Aly2 and Aly2^{PPXYless} were also both reduced following rapamycin treatment, supporting a role for protein modification prior to degradation (Figure 30C-D; E.J.). As this mobility shift occurred even in the absence of Rsp5 binding, we suggest that phosphorylation is likely responsible for these changes. Rapamycin-driven TORC1 inhibition results in the partial dephosphorylation of Npr1, though to a lesser extent than occurs during nitrogen starvation, a shift associated with activation of this kinase [66,77,93,137]. While we anticipated that Npr1 may thus be playing in a role in driving the phosphorylation and degradation of Aly1 and Aly2, we observed no difference in either their stability or mobility between WT and

*npr1*Δ cells (Figure 30E-F; E.J.). As a result, we conclude that Npr1 is not responsible for these rapamycin-induced changes.

As TORC1 also directly controls the function of Sit4, we decided to further assess Aly degradation in the absence of this phosphatase. In an effort to discern between the role of the proteasome and the vacuole in Aly stability, we utilized the proteasome-inhibiting drug MG132 in cells lacking the multidrug-resistant transporter Pdr5 [402]. After incubating cells for 1 hour with either DMSO or MG132, we further added CHX and monitored protein stability via immunoblotting. While proteosome inhibition with MG132 moderately increased the abundance of Aly1 and Aly1^{PPXYless} prior to the addition of CHX, their stability was not noticeably different from DMSO-treated control cells in the timepoints following (Figure 31A; E.J.). Both Aly2 and Aly2^{PPXYless} did exhibit a modest increase in abundance following proteasome inhibition, but, as with Aly1, neither protein's stability profile was altered post-CHX treatment (Figure 31C; E.J.). Furthermore, inhibition of the proteasome had very little impact on the instability of the Alys in the absence of *SIT4* (Figure 31B,D; E.J.). We validated the ability of our MG132 treatments to inhibit the proteasome utilizing a substrate, called NBD2*, known to undergo proteasome-dependent degradation (graciously provided by Jeff Brodsky, Univ. of Pittsburgh) [403]. To our satisfaction, in contrast to what we observed with Aly1 and Aly2, treatment with MG132 resulted in a strong stabilization of Ndb2* abundance (Figure 32; E.J.). As proteasomal degradation is often triggered by ubiquitination, we further assessed the stability of the Alys in the absence of various E3 ubiquitin ligases, finding none of those tested to significantly influence either α-arrestin's steady-state abundance (Figure 33A-F; R.W.B. and E.J.). Of note, we did observe an electrophoretic mobility shift for Aly1 in cells lacking *ASI1*, an E3 involved in protein quality control at the inner nuclear membrane, though this connection was not pursued further (Figure

33A,C,E; R.W.B and E.J.). Taken together, these results do not support a significant role for the proteasome in controlling Aly1 or Aly2 protein stability, in stark contrast to what has been previously reported for the proteasomal degradation of fellow α-arrestin Art1 [156].

We next assessed the role of the vacuole in controlling Aly1 and Aly2's stability, employing strains lacking *PEP4*, a vacuolar aspartyl protease that is required for the proteolytic activation of most other proteases in this compartment [334]. Utilizing fluorescent microscopy, I observed a modest increase in the abundance of Aly1, but not Aly2, when comparing *pep4*Δ cells to the WT control (Figure 34A-D). Similar results were obtained via immunoblotting, with only small changes in Aly abundance occurring prior to the addition of CHX (Figure 34E,F,I; E.J.). Vacuolar inhibition did, however, significantly improve the stability of Aly2, with higher fluorescence observed in *sit4*Δ *pep4*Δ cells than when lacking *SIT4* alone (Figure 34B,D). As occurred in a *sit4*Δ *npr1*Δ, I observed two distinct sub-populations in cells expressing Aly1-GFP, with the first restoring the α-arrestin's abundance to near WT levels, while the second exhibited almost no detectable fluorescence (Figure 34A,C). Furthermore, this split population again corresponded to the formation of large and small colonies when grown on solid media. We additionally found that the combined absence of *SIT4* and *PEP4* did increase the abundance of *ALY1*-GFP transcripts compared to *sit4*Δ cells, representing another possible mechanism by which the mode of vacuolar inhibition may be impacting protein levels (Figure 26; A.C. and Y.L.). Together, these findings further support the existence of a secondary mechanism to prevent the toxic over-accumulation of Aly1.

Indeed, as with *sit4*Δ *npr1*Δ cells, immunoblot analyses did not reveal any increase in Aly1 stability with the additional loss of *PEP4* to *sit4*Δ cells, a result we again attribute to the population-

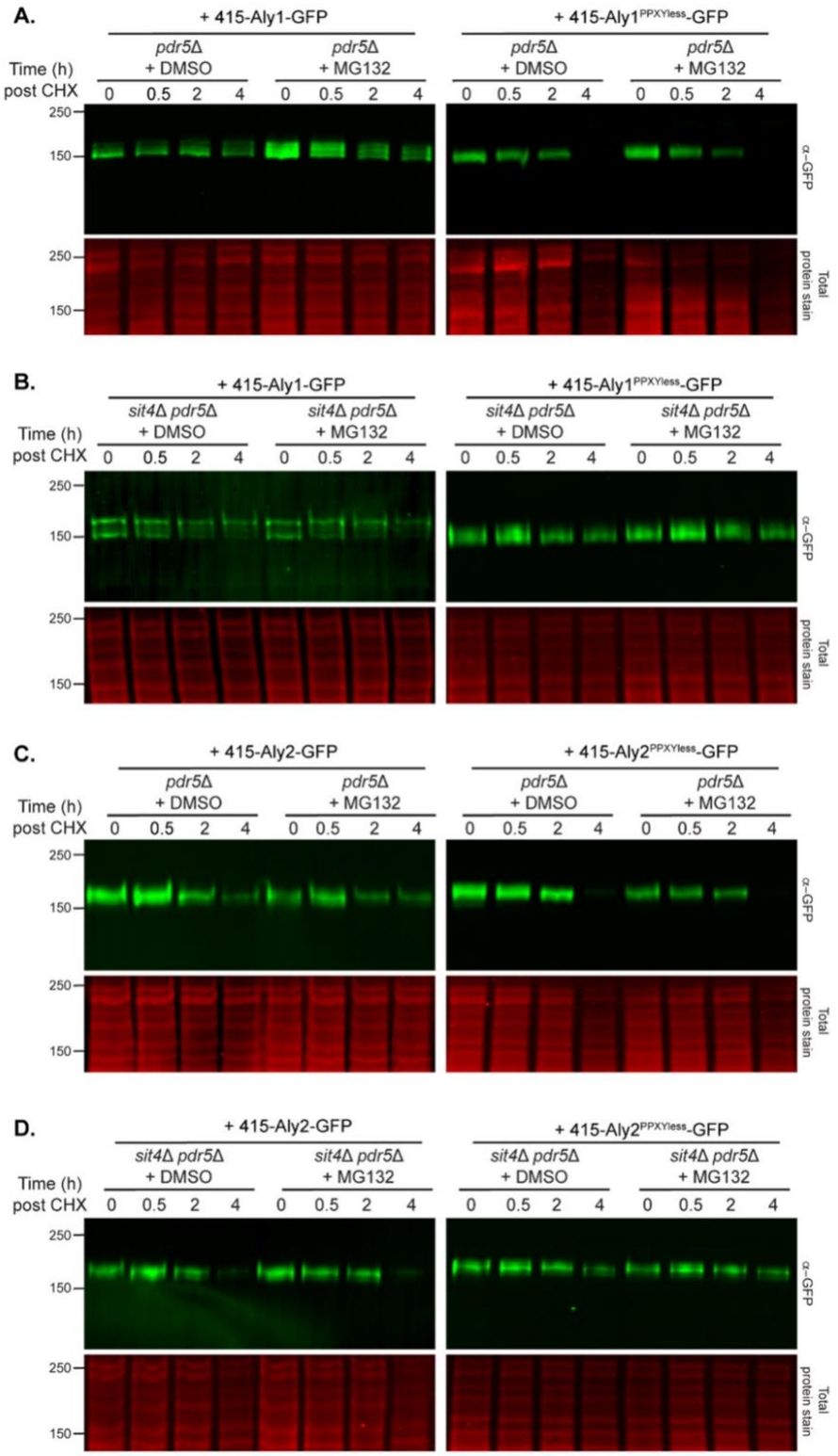

Figure 31. Inhibition of the proteasome does not lead to stabilization of Alys.

(A–D) Whole-cell extracts from cells expressing (A) Aly1-GFP, (B) Aly1^{PPXYless}-GFP, (C) Aly2-GFP, or (D) Aly2^{PPXYless}-GFP were treated with either vehicle control (DMSO) or MG132 for 60 min and then cycloheximide (CHX) for the time indicated (hours); proteins were resolved by SDS-PAGE. Anti-GFP antibody was used to detect tagged α-arrestins and REVERT total protein stain was used as a loading control. Blots shown are one representative from 2–3 replicate experiments. Molecular weights are shown on the left side in kDa.

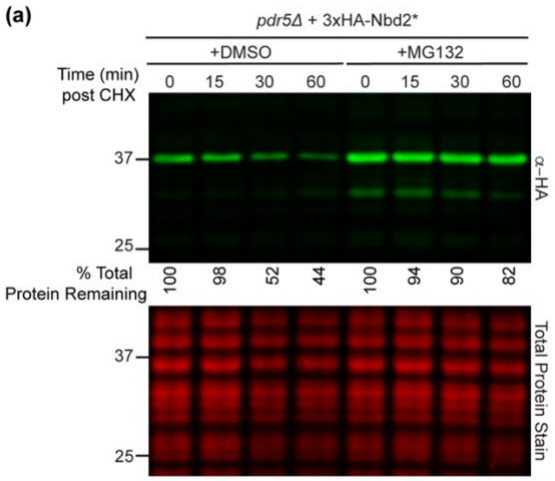

Figure 32. NBD2* as a control for MG132 proteasome degradation assays.

(**A**) Whole-cell extracts from cells expressing 3xHA-Nbd2* were treated with either vehicle control (DMSO) or MG132 for 60 minutes and then cycloheximide (CHX) for the time indicated (hours) and were resolved by SDS-PAGE. Anti-HA antibody was used to detect tagged Nbd2* and REVERT total protein stain was used as a loading control. Blots shown are one representative of 2 replicate experiments. Molecular weights are shown on the left side in kDa. For each lane, the pixel intensities for the HA-detected band and the loading control were measured using ImageJ. A correction factor based on the loading control was applied to each pixel intensity measurement. The t=0 point was set to 100% and the % of protein remaining is indicated for each time point. Based on these assays we find significant stabilization of Nbd2*. Nbd2* serves as a positive control for our MG132-dependent proteasome degradation assays with Aly-GFP.

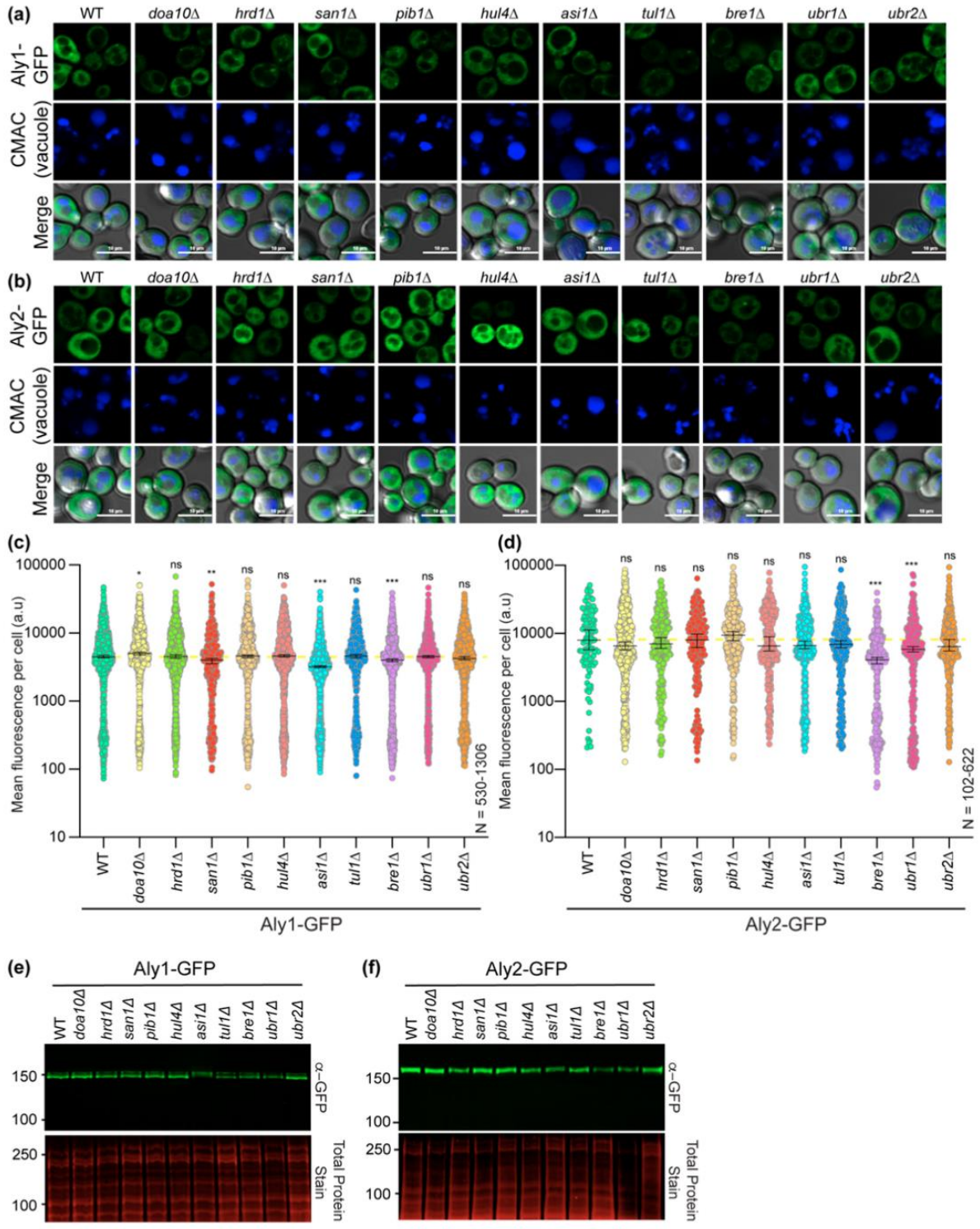

Figure 33. Loss of E3 ubiquitin ligases does not increase Aly1 protein abundance.

(**A**) Aly1-GFP or (**B**) Aly2-GFP was expressed from the *TEF1pr* in either WT cells or those lacking the gene indicated and imaged by high-content fluorescence microscopy. CMAC is used to stain the vacuoles (shown in blue). All images

are shown as equally adjusted from a single experiment. (**C-D**) The whole cell fluorescence of cells imaged in (**A**) or (**B**), respectively, was determined using Nikon.*ai* software and the fluorescence for each cell is plotted as a circle. The median fluorescence intensity is shown as a black line for each group and the error bars represent the 95% confidence interval. A yellow dashed line represents the median fluorescence intensity for Aly1 or Aly2 expressed in WT cells in panels (**A**) and (**B**), respectively. (**E-F**) Whole-cell extracts from the cells imaged in (**A**) and (**B**), respectively, were analyzed by SDS-PAGE and detected using an anti-GFP antibody. The REVERT total protein stain of the membrane is shown as a loading control. Molecular weights are shown on the left side in kDa.

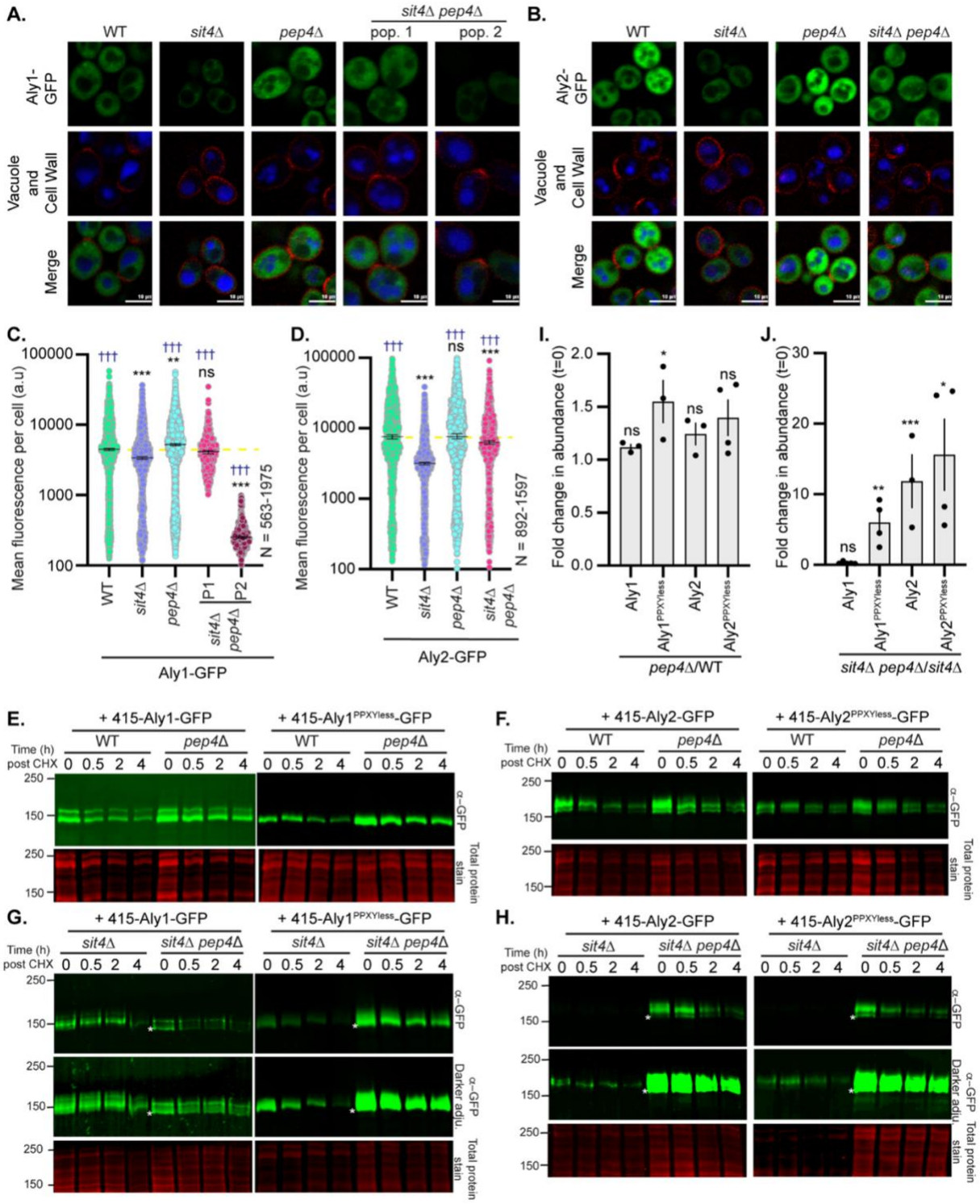

Figure 34. Impaired vacuole protease function increases Aly protein abundance.

(**A**) Aly1-GFP or (**B**) Aly2-GFP was expressed from the *TEF1pr* in either WT cells or those lacking the gene indicated and imaged by high-content fluorescence microscopy. CMAC is used to stain the vacuoles (shown in blue), and trypan

blue (shown in red) is used to mark the cell wall. (C) or (D) The whole-cell fluorescence of cells imaged in (A) or (B), respectively, was determined using NIS.*ai* software, and the fluorescence for each cell is plotted as a circle. The median fluorescence intensity is shown as a black line for each group, and the error bars represent the 95% confidence interval. A yellow dashed line represents the median fluorescence intensity for Aly1 or Aly2, expressed in WT cells in panels (G) and (H), respectively. Kruskal–Wallis statistical analysis with Dunn's post hoc test was performed to compare the fluorescence distributions to the cognate WT. In black asterisks (*), statistical comparisons are made to Aly1 or Aly2 in WT cells for panels (C,D), respectively. In blue daggers (†), statistical comparisons are made to Aly1 or Aly2 in *sit4*Δ cells for panels (C,D), respectively (ns = not significant; two symbols = *p*-value < 0.005; three symbols = *p*-value < 0.0005). (E–H) Whole-cell extracts expressing the α-arrestin indicated in WT, *pep4*Δ, *sit4*Δ, or *sit4*Δ *pep4*Δ cells were made from cells treated with cycloheximide (CHX) for the time indicated (hours) and resolved by SDS-PAGE. Anti-GFP antibody was used to detect tagged α-arrestins and REVERT total protein stain was used as a loading control. Blots shown are one representative from 2–3 replicate experiments. Molecular weights are shown on the left side in kDa. For panels (G,H), a white asterisk marks the faster migrating species observed in the *sit4*Δ *pep4*Δ extracts that are not found in the *sit4*Δ alone. (I,J) A plot of the fold change in the t = 0 absolute pixel intensities for the Aly-GFP bands shown in (E,F) or (G,H), respectively, is presented so that the influence of Pep4 on steady-state Aly abundances can be considered relative to WT (E,F,I) or *sit4*Δ (G,H,J) cells. Each fold change data point is presented as a circle, and the mean is represented by the height of the bar graph. Error bars represent the SEM. Student's *t*-test with Welch's correction was performed on the pixel intensity values for each (i.e., comparing Aly1 t = 0 band intensities for WT vs. *pep4*Δ), and results are presented over each column. ns = not significant; * = $p < 0.05$; ** = $p < 0.005$; *** = *p*-value < 0.0005).

level resolution of cell extracts and immunoblotting compared to the cell-to-cell resolution of microscopy.

Of note, these mixed populations and colony size differences were not observed when expressing non-Rsp5 binding Aly1^{PPXYless} in *sit4*Δ *pep4*Δ cells, while showing a strongly improved level of abundance by immunoblotting (Figure 34G and 35; R.W.B. and E.J.). These results implicate the role of Aly1 as an adapter for Rsp5 as a driver of the toxicity resulting from its

overexpression. Though not always significant, the loss of *PEP4* did tend to improve the stability of both Alys and their PPXYless mutants at steady-state (Figure 34C-F, 34I, 35; R.W.B. and E.J.). Similarly, the additional loss of *PEP4* to *sit4*Δ cells rescued much of the reduced abundance, though not for Aly1 when evaluated via immunoblotting (Figure 34G-H,J; E.J.). Additionally, there was a notable appearance of a faster-migrating species for all Alys in *sit4*Δ *pep4*Δ cell extracts not seen in the absence of *SIT4* alone (Figure 34G-H, marked with white asterisks; E.J.). We suggest that, as with *sit4*Δ *npr1*Δ cells, the combined loss of *SIT4* and *PEP4* results in a population of stable, non-phosphorylated Aly proteins. Blocking protein synthesis with CHX treatment further revealed an increase in the stability profile in both *pep4*Δ and *sit4*Δ *pep4*Δ cells for both PPXYless mutants and Aly2, though not Aly1, compared to those where *PEP4* was still intact (Figure 34; R.W.B. and E.J.).

We were surprised to find that, in both *sit4*Δ and *sit4*Δ *pep4*Δ cells, there was a notable lack of GFP signal accumulating in the vacuolar compartment. GFP's highly stable folding is known to be resistant to vacuolar proteases, with free GFP capable of continuing to produce fluorescent signal in their presence [59,404]. We would therefore expect to observe such signal if the GFP-tagged Alys were being degraded by the vacuole in the absence of *SIT4*, while we instead observed a reduction in cytoplasmic signal (Figure 28A,C). Similarly, we would have expected to observe an increase in vacuolar fluorescence following the loss of active vacuolar proteolysis in *pep4*Δ cells if the vacuole was degrading GFP-tagged Alys, yet we again observed increased cytosolic signal (Figure 35A-B). While this result is confounding, it may be explained by changes in the balance of cellular nutrients (like the free amino acids produced by and stored in the vacuole) in the absence of active vacuolar proteolysis, and subsequent shifts in the α-arrestin's stability and

modification status. Such changes may help explain the altered mobility profile of both Aly1 and Aly2 seen in *sit4*Δ *pep4*Δ cells (Figure 34G-H; E.J.).

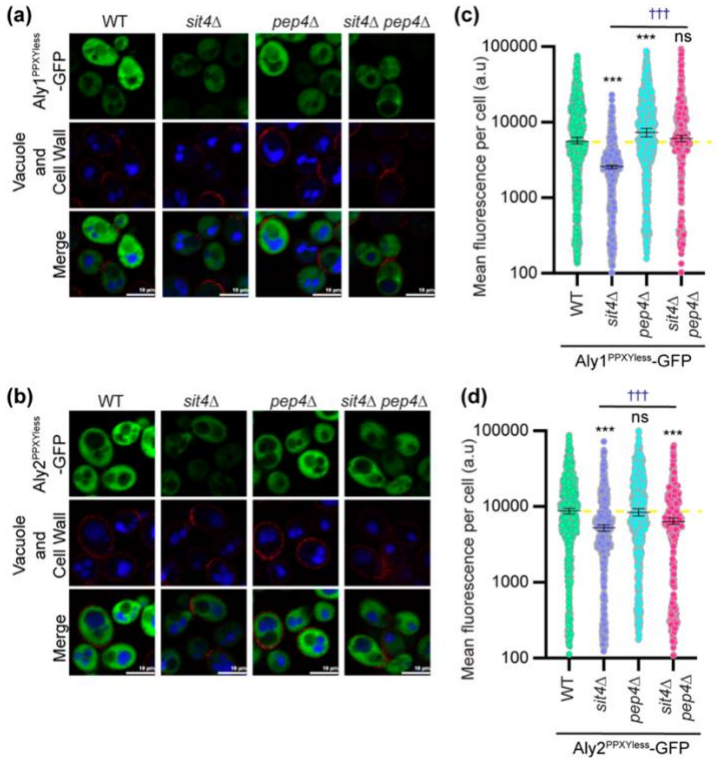

Figure 35. Impaired vacuole protease function increases Aly1^{PPXYless} protein abundance.

(**A**) Aly1^{PPXYless}-GFP or (**B**) Aly2^{PPXYless}-GFP was expressed from the *TEF1pr* in either WT cells or those lacking the gene indicated and imaged by high-content fluorescence microscopy. CMAC was used to stain the vacuoles (shown in blue) and trypan blue (shown in red) is used to mark the cell wall. (**C**-**D**) The whole cell fluorescence of cells imaged in (**A**) or (**B**), respectively, was determined using Nikon.*ai* software and the fluorescence for each cell is plotted as a circle. The median fluorescence intensity is shown as a black line for each group and the error bars represent the 95% confidence interval. A yellow dashed line represents the median fluorescence intensity for Aly1 or Aly2 expressed in WT cells in panels (**A**) or (**B**), respectively. Kruskal-Wallis statistical analysis with Dunn's post hoc test was performed to compare the fluorescence distributions to the cognate WT. In black asterisks, statistical comparisons are made to Aly1^{PPXYless} or Aly2^{PPXYless} in WT cells for panels (**C**) or (**D**), respectively. In blue daggers,

statistical comparisons are made to Aly1^{PPXYless} or Aly2^{PPXYless} in *sit4*Δ cells for panels (**C**) or (**D**), respectively. (ns=not significant; three symbols = p-value <0.0005).

Collectively, these results provide a link between the loss of Aly protein abundance in the absence of *SIT4* and the proteolytic activity of the vacuole. The notable loss of Aly protein abundance after CHX treatment in *pep4*Δ cells suggests that, when vacuolar degradation is impaired, these α-arrestins are instead degraded by the proteasome. While these results support the exciting possibility that the Alys may access both routes of degradation, as has been described for other substrates, this remains a prominent point requiring further investigation [392].

3.3.5 Sit4 and Npr1 Regulate Aly-Mediated Trafficking of the Git1 Transporter

Given our new-found appreciation for the impact of Sit4 and Npr1 on Aly1 and Aly2's regulation, we were curious about what potential role this signaling pathway might have in α-arrestin-mediated protein trafficking. We recently reported that the endocytic trafficking of the glycerophosphoinositol transporter Git1 is controlled by Aly1 and Aly2 [91]. Thus, we sought to assess the role of the TORC1-Sit4-Npr1 network in affecting Git-GFP abundance and localization by microscopy and immunoblotting. As anticipated, Git1 was found at the cell surface and vacuole in WT control cells. This result was validated via immunoblotting, where extracts from WT cells displayed a balance of both intact Git1-GFP and free GFP, the latter reflecting a degradation-resistant fragment cleaved from Git1-GFP in the vacuole (Figure 36A-C; R.W.B. and E.J.). In the absence of either *ALY1* and *ALY2* (*aly1*Δ *aly2*Δ), or 9 of the 14 yeast α-arrestins (9arrΔ), I found Git1 to be retained at the plasma membrane, with little to no signal in the vacuolar compartment (Figure 36A-B) [59]. In agreement, the same cells assessed via immunoblotting exhibited a much

higher proportion of full-length Git1-GFP (Figure 36C; E.J.). While *tor1*Δ cells retained a slightly higher fraction of Git1 at the plasma membrane compared to WT, the lack of corroboration by immunoblot analysis makes the biological significance of this result unclear (Figure 36A-C; R.W.B. and E.J.). Notably, however, the loss of *NPR1* resulted in a strong increase of both cell surface retention and full-length protein abundance, supporting a role for this kinase as a prominent regulator of Git1 trafficking. Furthermore, in the absence of *SIT4*, we found a dramatically higher proportion of Git1 at the plasma membrane compared to WT cells, nearly equal to that in 9arrΔ cells, and to exhibit almost no detectable GFP breakdown product. This result was not surprising, given the extremely low abundance of Aly1 and Aly2, the α-arrestins primarily responsible for controlling Git1 endocytosis, in *sit4*Δ cells (Figure 27B, E.J.). Importantly, the combined loss of both *SIT4* and *NPR1* partially restored Git1's ability to reach the vacuole compared to *sit4*Δ cells, further demonstrating the intertwined relationship these regulators have on α-arrestin trafficking (Figure 36A-C; R.W.B. and E.J.). In addition, Aly2 abundance is largely restored when *NPR1* is further removed from *sit4*Δ cells, with both Aly1 and Aly2 losing their *sit4*Δ-associated hyper-phosphorylation (Figure 27C-D; E.J.). This phospho-shift thus likely reflects an improved state of

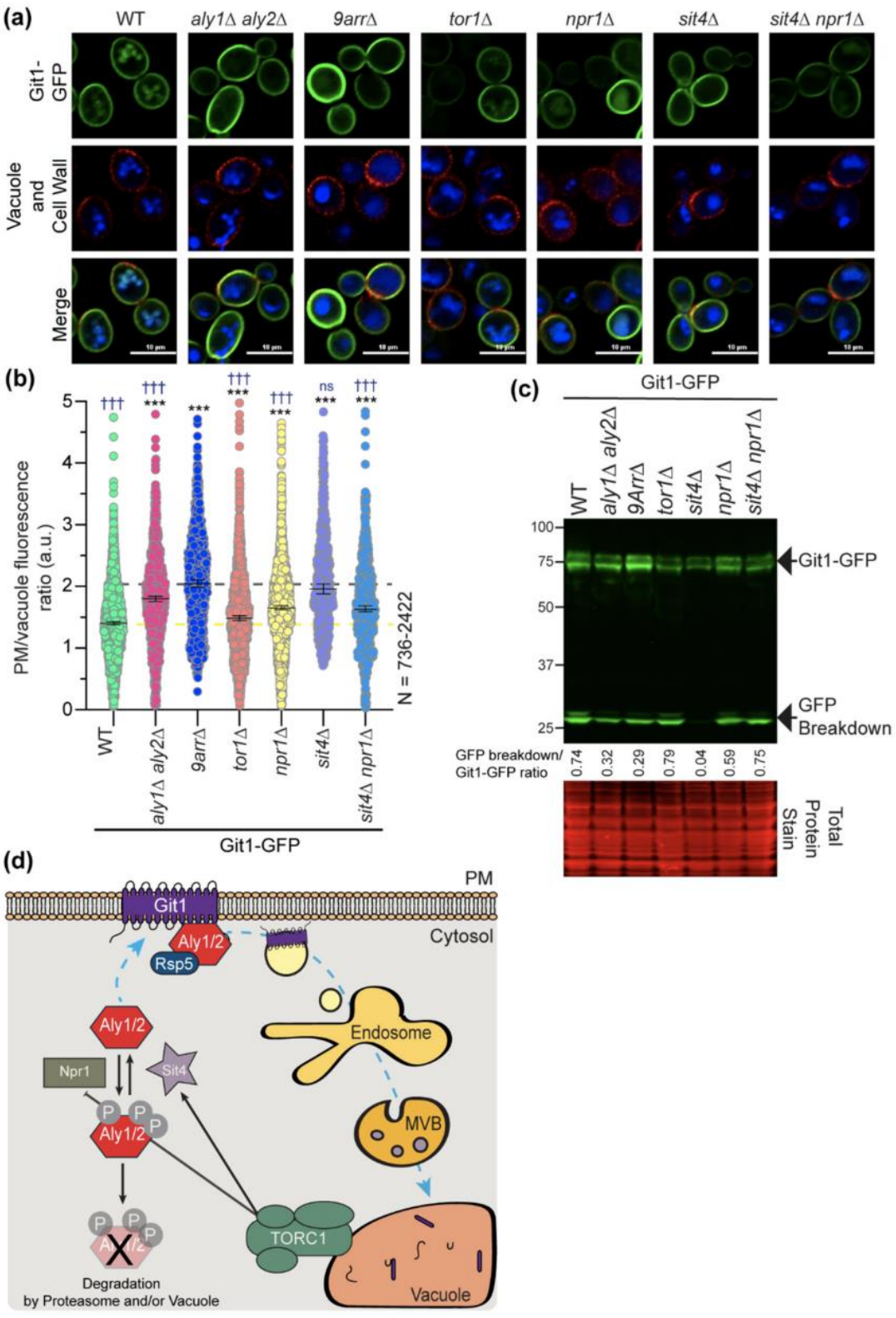

Figure 36. TORC1-Sit4-Npr1 regulation of Aly-mediated trafficking of Git1

(A) Git1-GFP was expressed from the *TEF1pr* in either WT cells or those lacking the gene indicated and imaged by high-content fluorescence microscopy. CMAC is used to stain the vacuoles (shown in blue) and trypan blue (shown in red) is used to mark the cell wall. (B) The PM and vacuolar fluorescence intensities from the cells depicted in (a) were quantified using NIS.*ai* and Nikon GA3 software and the distributions of the PM/vacuole fluorescence ratios in arbitrary units (a.u.) were plotted as scatter plots. The horizonal midline in black represents the median and the 95% confidence interval is represented by the error bars. Yellow and grey dashed lines are used as references to indicate the median ratio for WT or 9ArrΔ cells, respectively. Kruskal–Wallis statistical analysis with Dunn's post hoc test was performed to compare the fluorescence distributions to either WT or 9ArrΔ cells. In black asterisks (*), statistical comparisons are made to WT cells. In blue daggers (†), statistical comparisons are made to 9ArrΔ cells. (ns = not significant; three symbols = *p*-value < 0.0005). (C) Whole-cell extracts from cells expressing Git1-GFP from the *TEF1* promoter were resolved by SDS-PAGE and immunoblotted. Anti-GFP antibody was used to detect Git1-GFP and REVERT total protein stain was used as a loading control. Blot shown is representative of 2 replicate experiments. Molecular weights are shown on the left side in kDa. The ratio of GFP breakdown product (represents the vacuolar pool of GFP) over Git1-GFP (represents the pool of Git1 outside of the vacuole) for each lane is presented. (D) Model of TORC1-Sit4-Npr1 regulation of Aly-mediated trafficking of Git1.

function for these α-arrestins, which, together with our other findings, supports a new model for the TORC1-Sit4-Npr1 signaling network's role in α-arrestin regulation (Figure 36D; A.F.O). The proper maintenance of Aly1 and Aly2's phospho-status relies upon the presence of Sit4, whose absence not only results in their hyper-phosphorylation, but also a drastic decrease in stability and, subsequently, an inability to mediate the endocytic trafficking of membrane-bound transporter cargo like Git1 [91]. These outcomes rely on the presence of Npr1, as the combined loss of *SIT4* and *NPR1* reverses Aly hyper-phosphorylation, resulting in their restored stability and ability to support Git1 trafficking.

3.4 Discussion

In the work described above, we identify a range of kinases and phosphatases that influence the electrophoretic mobility and/or stability of α-arrestins Aly1 and Aly2, underscoring the complexity of the trafficking adapter family's phospho-regulation. While these efforts uncovered many promising leads for Aly regulation, we chose to focus here on the role of the TORC1-Sit4-Npr1 signaling axis. Among the rich collection of previous work linking TORC1 to α-arrestin regulation, one model suggests that, while α-arrestins are maintained in a dephosphorylated state that allows for their endocytic control of nutrient transporters when TORC1 is active, impairment of this complex instead leads to a block in α-arrestin trafficking due to Npr1-driven phospho-inhibition. Phospho-sites for many α-arrestins – including Art1, Art2, Bul1, Bul2, Aly1, and Aly2 – have been linked to TORC1 and Npr1 via mass spectroscopy [66,104]. Our efforts serve to further support a role for TORC1 and Npr1 as regulators of Aly1 and Aly2, while additionally implicating the related phosphatase Sit4 and its associated regulators Tip41 and Slt2. Our results indicate Npr1 is capable of regulating the phospho-status of these α-arrestins even under conditions where TORC1 is likely active, as Aly1 and Aly2 undergo Npr1-dependent hyper-phosphorylation in the absence of *SIT4* when grown under nutrient replete conditions. Similar results have been described by the André lab for the hyper-phosphorylation of fellow α-arrestins Bul1 and Bul2 in *sit4*Δ cells, in this case occurring in both nitrogen-rich (TORC1 activating) and -poor (TORC1 inhibiting) conditions [77]. We, however, demonstrate that, unlike the Buls, Aly1 and Aly2 exhibit Npr1-dependent hyperphosphorylation and instability in the absence of *SIT4*. In a divergence of Aly regulation, Sit4 appears capable of regulating *ALY1* transcript abundance, while the levels of *ALY2* transcripts are largely unaffected. We further conclude that Npr1 and the

degradative capacity of the vacuole are both tied to Aly1 and Aly2's destabilization in *sit4*Δ cells, as their phospho-status and abundance were similarly returned towards that seen in WT cells in *sit4*Δ *npr1*Δ and *sit4*Δ *pep4*Δ backgrounds.

Given the shift in electrophoretic mobility for the Alys in *sit4*Δ *pep4*Δ cells, as well as the surprising absence of vacuolar Aly-GFP signal in this background, we propose that this impairment of vacuolar protease activity may have further influences on cell signaling which inhibit the ability of Npr1 to regulate the phospho-status of these α-arrestins. For example, changes in the abundance of free amino acids resulting from vacuolar impairment may be altering the activity of the nutrient sensing TORC1 complex, which resides mainly on the vacuolar surface, and thus its downstream effectors. The effects resulting from the loss of *SIT4* further extends to protein trafficking, as the Aly-controlled Git1 transporter exhibits similar cell-surface retention in *sit4*Δ cells as those in which these α-arrestins have been lost entirely (*aly1*Δ *aly2*Δ and 9arrΔ), while its trafficking is restored in the absence of both *SIT4* and *NPR1*. Below, I further discuss these collective findings in the broader context of TORC1-Sit4-Npr1 regulation of other α-arrestins, with a focus on regulatory facets that are either conserved or unique in comparison to the Alys.

The α-arrestin Art1 is itself a direct substrate of Npr1, possessing both Npr1- and rapamycin-dependent phospho-sites [66]. Though Npr1 kinase activity is reduced when TORC1 is inactive, this effect is less dramatic when triggered by rapamycin treatment than occurs during nitrogen starvation [66,77,137]. Rapamycin is reported to induce the Npr1-dependent hyper-phosphorylation of Art1, which possesses both N-terminal residues directly phosphorylated by Npr1 and C-terminal sites which rely on those Npr1-targeted sites to permit their own modification by other regulators [66]. This study further showed that, while CHX-induced TORC1 activation

results in Art1 dephosphorylation and recruitment to the cell surface to mediate the internalization of the arginine permease Can1, the further addition of the direct TORC1-inhibiting rapamycin is sufficient to prevent these outcomes. While these collective results are highly suggestive of a role for Npr1 in the TORC1-driven phospho-regulation of α-arrestins, a subsequent study found Can1 to be retained at the plasma membrane in rapamycin-treated cells lacking *NPR1* [64]. This runs counter to the previous group's model wherein the loss of Npr1-inhibition should result in strong Can1 internalization driven by hyper-activation of Art1, underscoring the complexity and nuance present in α-arrestin phospho-regulation. In contrast to what we observed for Aly1 and Aly2, neither TORC1 activation by CHX nor inhibition by rapamycin induces Art1 degradation. Furthermore, while the protein phosphatase Z proteins Ppz1 and Ppz2 are linked to the methionine-induced dephosphorylation of Art1, which activates its ability to internalize the methionine permease Mup1, this occurs at residues distinct from those connected to Npr1 [66,129].

While the involvement of Sit4 in the regulation of Art1 is yet to be investigated, work from the André lab has directly linked the phosphatase to α-arrestins Bul1 and Bul2 [77,94,294]. Under nitrogen-limiting conditions, Sit4 is thought to be inhibited by the binding of Tap42 and the TORC1 complex, though recent work has shown may still retain some selective activity under these conditions [390,391]. In support of this model, Npr1 undergoes Sit4-dependent dephosphorylation and activation during nitrogen limitation, allowing the kinase to phosphorylate Bul1 and Bul2, promoting their binding to inhibitory 14-3-3 proteins and, in turn, inhibiting their ability to remove the general amino acid permease Gap1 from the cell surface [77,94]. Upon nitrogen stimulation, activated TORC1 now directs Sit4's activity away from Npr1 and toward the Buls, leading to their dephosphorylation and Gap1's removal. While both the Buls and Alys are hyper-phosphorylated in the absence of *SIT4*, the Buls do not undergo the same destabilization as

their fellow α-arrestins. While Sit4-dependent dephosphorylation promotes the release of Bul1 and Bul2's inhibition by 14-3-3 proteins, its effect on the previously reported 14-3-3 inhibition of Aly1 and Aly2 remains a subject of future studies [68,77,94].

TORC1 regulation of the α-arrestins is far from consistent, however, as demonstrated by its regulation of another α-arrestin, Ecm21 [73,93]. Efforts to identify new α-arrestin cargo proteins via quantitative mass spectroscopy revealed that Ecm21 controls the internalization of B-vitamin transporter Thi7 following the addition of its substrate (thiamine) or TORC1 inhibition by rapamycin [93]. This lies in stark contrast to the regulation of Bul1 and Bul2 when TORC1 is inhibited, where activated Npr1 inhibits the Buls and prevents their internalization of Gap1. In this case, the loss of *NPR1* actually resulted in reduced internalization of Thi7, similar to what we observed for the trafficking of Git1 by the Alys in this background, suggesting Npr1 may possess condition-specific roles in both the positive and negative regulation of α-arrestins. In yet another similarity between Ecm21's control of Thi7 and our study of the Alys, the loss of *SIT4* results in the retention of Thi7 at the cell surface, further highlighting the importance of this phosphatase in regulating the α-arrestins [93].

Though not pursued herein, my genetic screen further identified additional candidates related to the TORC1-Sit4-Npr1 network, namely the Tip41 and Slt2. The Tap42-interacting protein Tip41 is a negative regulator of TORC1 that binds to Tap42, thereby serving to prevent its inhibition of Sit4 while also potentially altering its substrate specificity [77,94,388]. Notably, we found the abundance of Aly1 and Aly2 to be severely diminished in *tip41*Δ cells, similar to what occurs in the absence of *SIT4* and a supporting a model wherein Tip41 may help promote Aly dephosphorylation and stabilization. The role of Tip41 and Sit4 in regulating Npr1's phospho-status will also be an interesting avenue of future pursuit, as their loss results in a state of hyper-

phosphorylation often considered to be inhibitory [388]. Npr1 undergoes variable degrees of phosphorylation, with a near-complete dephosphorylation during amino acid or nitrogen starvation and an intermediary phospho-state in cells treated with rapamycin. As TORC1 is directly inhibited by this drug, Npr1's phosphorylation under this condition is driven by a different upstream regulator. Recent proteomic work identified Npr1 phospho-inhibition driven by Slt2, a MAP kinase controlled in part by the rapamycin-insensitive TORC2 complex whose absence we found destabilizes Aly2, but not Aly1 [104,405]. This, again, represents a remaining thread for future work, as Slt2 may aid in the hyper-phosphorylation and inhibition of Npr1 to stabilize the Aly2, as well as the potential convergent regulation of α-arrestins by TORC1 and TORC2.

There yet remain many aspects of TORC1 regulation of the α-arrestins that have yet to be detailed, including the distinction between mechanisms which are specific to individual α-arrestins and those which more broadly affects multiple members of the trafficking adapter family. For example, the endocytic trafficking of nutrient transporters by the Alys, Buls, and Art1 can either be stimulated by active TORC1 or impeded by rapamycin-driven TORC inhibition and Npr1 activity. In contrast stands the regulatory circuit in which Npr1 directly phosphorylated Aly2 to stimulate the trafficking of Gap1 to the cell surface in cells undergoing nitrogen starvation, as well as the rapamycin-induced endocytic activity of Ecm21 [67,93]. Our work here further demonstrates the complexity and nuance of the α-arrestins by this regulatory network, as Sit4 was required to antagonize Npr1-driven phosphorylation and destabilization of Aly1 and Aly2 under rich growth conditions where Npr1 is thought to be inhibited by active TORC1. Collectively, these findings support a model wherein kinase activity can be finely tuned to achieve distinct substrate specificities in response to a common stimulus, while underscoring the remaining gaps in our understanding of the TORC1-Sit4-Npr1 signaling network's control of the α-arrestins.

4.0 Conclusions and future directions

In the following section I have summarized how my research advances the understanding of α-arrestins' role in autophagy and the maintenance of phospholipid balance and describe the phospho-regulation of this family of protein trafficking adapters. Furthermore, I discuss a variety of questions this work raises and possible directions for future research in these areas.

4.1 Significance of this study

4.1.1 Major conclusions

Previously, an unclear link between α-arrestins and autophagy was established in the rice fungus *Magnaporthe oryzae*, based predominantly on colocalization of an α-arrestin with Atg8 [286]. My studies thus represent the first connection between autophagy and the α-arrestins in yeast and set the stage for future work investigating this connection in human cells, where autophagy has an ever-expanding relevance to health and disease [406–410]. Indeed, the closely related β-arrestins, which are not present in yeast, influence autophagy. This connection includes the enhancement of liver fibrosis in autophagy-mediated Snail signaling, coordinating autophagy, and mediating neuroprotection under ischemic stress, and the modulation of autophagy in hepatocellular carcinogenesis [411–413].

Using a high-throughput screen of the ScUbI library collection, we identified several autophagy-related genes that disrupted the rapamycin resistance conferred by the over-expression

of α-arrestins Aly1 and Aly2 (Figure 4) [152] I further found that of the 14 yeast α-arrestins, only four (Aly1, Aly2, Art1, and Art5) confer rapamycin resistance when over-expressed (Figure 5A). For at least Aly1 and Aly2, this phenotype is directly tied to their increased abundance, as driving high expression using the *TEF1pr* further improves their rapamycin resistance (Figure 22A). The Alys also must bind the Rsp5 ubiquitin ligase to stimulate growth on rapamycin, as the PPXYless mutants of both α-arrestins failed to change the rapamycin sensitivity of cells relative to the vector controls (Figures 6 and 7). The cellular response to TORC1 inhibition involves a wide-ranging internalization of cell surface transporters, including multiple α-arrestin cargo, and dramatic changes in the phospho-regulation of α-arrestins and other Rsp5-related proteins [84,285]. As a result, α-arrestin-conferred rapamycin resistance may indicate an change in the cell's ability to regulate the functions of more abundant populations of these specific α-arrestins due to a lack of a similar increase in the abundance of their regulators. Furthermore, since only a few α-arrestins confer resistance to rapamycin when over expressed, it seems likely that some specific functional aspect of these α-arrestins gives rise to this phenotype. Additional results support the idea that these functions may be tied to lipid-related roles, as the strongest genetic ties between the α-arrestins and autophagy include genes involved in autophagy initiation and lipid production/transfer (Figures 5-7). This, along with the defects I observed in the distribution and abundance of phospholipid modifiers (Vps34 and Fab1), binding factors (Atg2 and Atg18), and of the phospholipid PI3P itself, further strengthen the reported ties between this family of protein trafficking adapters and the regulation of lipid homeostasis and transporters of phospholipid precursors (Figures 18-21) [59,362]. The involvement of Vps34 and PI3P alongside the autophagy-related defects I describe is also notably reminiscent of those reported to be driven by hyperactive Vps34 [262]. As a result, we propose a model, herein, where these changes to the

phospholipid landscape result from the mis-regulation of cell surface transporters in the absence of α-arrestin, driving mislocalization of autophagic machinery that support the expansion of isolation membranes at the PAS, and further results in a decrease in AB size and an impairment of autophagic flux (Figures 8, 10-11, 18-19 and 21).

Further targeted screening efforts, instead using a subset of the yeast deletion collection containing mutants of non-essential kinases and phosphatases on both rapamycin- and high salt-containing media, identified various regulators of α-arrestin function (Figure 22). We found the loss of any member of the Tor1-Sit4-Npr1 signaling network disrupted the rapamycin resistance conferred by the over-expression of Aly1 or Aly2, with a dramatic destabilization of these α-arrestins in *sit4*Δ cells (Figures 23-25, Supplemental Tables S3 and S4, available in 'Chapter 3' folder at OneDrive link: Supplemental Thesis Documents - Bowman). As both Sit4 and Npr1 are well-connected to α-arrestin regulation, it was somewhat unsurprising to find the Alys are hyper-phosphorylated in the absence of *SIT4* and that this hyperphosphorylation is dependent on the presence of the *NPR1* kinase (Figure 27) [66,67,77,94,104]. What was surprising, however, was the discovery that the destabilization of the Alys was not dependent on the proteasome, which has been reported to control the stability fellow α-arrestin Art1 (Figure 31) [156]. Instead, we found vacuolar inhibition to increase the steady-state abundance of Aly1 and mutants of the Alys that fail to bind Rsp5, though not Aly2 (Figure 34-35). While vacuolar inhibition did not fully stabilize any of these α-arrestin forms, this does represent the first reported instance of the vacuole playing a role in the stability and degradation of an α-arrestin. We further expand our understanding of how these TORC1-related phospho-regulators affect α-arrestin-mediated protein trafficking by demonstrating that the loss of Aly-mediated trafficking of Git1 to the vacuole in *sit4*Δ cells is significantly restored by the further loss of *NPR1* (Figure 36A-C) [91]. Together, these data lead

us to a new model for the TORC1-Sit4-Npr1 regulation of α-arrestin phosphorylation and stability. Finally, this work further establishes an exciting and novel link between α-arrestin degradation and the proteolytic activity of the vacuole.

4.1.2 Limitations of this study

Though the experimental results I discuss here represent significant steps in our understanding of α-arrestin regulation and the family's role in broader cellular processes like autophagy and the maintenance of phospholipid balance, there remain limitations to the scope and specificity of these conclusions which must be considered. From a broad perspective, the investigations described in both Chapters 2 and 3 rely upon targeted genetic screens of libraries derived from the yeast deletion collection [311]. The use of a targeted screen is in fact, itself, a limitation. While the ScUbI and KinDel libraries were constructed to include the most likely candidates for ubiquitin- and phospho-regulation of the α-arrestins, a screen of the entire deletion collection represents a significant broadening of scope that would likely reveal additional groups of regulators. Along that same vein, though the yeast deletion collection covers a vast majority of the organism's genome, it, by nature, lacks essential gene mutations. To help fill this gap, we could make use of temperature-sensitive mutants in essential genes during similar analyses with the a-arretins, thus helping to define their activities in these pathways [414].

Furthermore, while the most prominent candidates from each screen were extensively evaluated, there are many candidate genes that were not pursued further. For example, while we chose to focus on autophagy-related genes, which represented the most enriched group of mutants to negatively impact α-arrestin-conferred rapamycin resistance, we did not investigate any of the

screen candidates which strengthened the rapamycin-resistance phenotype. Among these, Gene Ontology analysis of the ScUbI screen results found an enrichment for genes related to ERAD, a process by which misfolded proteins are extracted from the ER and targeted for proteasome-dependent degradation (Figure 4) [415]. Similarly, despite our assessment of a broad range of ATG mutants for potential genetic connections to the α-arrestins, we only analyzed less than half of the more than 40 members of this gene family [200,416].

Another limitation lies in the fact that genes involved in AP fusion to the vacuole were not analyzed in our genetic screens. These were omitted in part due to the fact that they play a broader role in the fusion of non-autophagic vesicles (Figure 6), which would likely confound their intepretation. Still, while the results of my EM analyses did not support any defect in AP fusion to the vacuole in the absence of α-arrestins, alterations in vacuole fusion in cells with altered α-arrestin function remains unstudied. Furthermore, our investigation of how α-arrestin mutants affect autophagy did not include the analyses of the paralogous α-arrestins Bul1 and Bul2. Despite the strong rapamycin sensitivity of *bul1*Δ *bul2*Δ cells, this mutant was not included in any of our autophagy-focused experiments as their over-expression did not confer resistance to rapamycin (Figure 5D). These α-arrestins remain intact in the 9arrΔ background, further preventing us from assessing their role in supporting the self-degradative program. As such, despite our efforts to cast a wide net in our evaluation of the α-arrestin's links to autophagy, there remain significant gaps in the scope of these studies.

Further limitations in these studies derive from the techniques we chose to employ. For example, we chose to use plasmid-based reporters to assess the localization and abundance of proteins of interest like Vps34, Atg18, and even the autophagy reporter GFP-Atg8. Despite our careful assessments and the routine use of these plasmids in the literature, the use of such plasmid-

expressed tools in the presence of their endogenous chromosomal forms results in an increase in expression for these proteins above their normal levels. It thus remains possible that some of the effects we observed may be at least partially driven by these, even modest, elevations in protein levels. In addition, though we carefully quantified all imaging data in Chapter 2, we did not quantify all of the biochemical data presented that chapter. While I went to great lengths to develop methods that allowed for extensive measurement and statistical analysis of the microscopy-derived data, this same level of interrogation is at times absent from the immunoblot experiments. One confounding element for quantification of the immunoblots is the fact that the protein abundances on blots in the *sit4*Δ background were so low as to be barely detectible via immunoblotting. This very low abundance of the Aly-GFP products meant that assessments of fold-change in protein levels using this approach had a high degree of variability. For this reason, the microscopy quantification, which is presented throughout Chapter 2, was viewed as the more robust and reproducible approach.

Moreover, our connections of α-arrestins to autophagy still lacks a direct mechanistic link. Our model in Figure 21C proposes that the lack of α-arrestin-mediated control of cell surface transporter endocytosis results in an imbalance of key phospholipids and, subsequently, the improper retention of autophagic machinery on the vacuole membrane. However, we have not identified a specific set of transporters associated with these phenotypes and, instead we rely on previously reported relationships like those between α-arrestin-mediated trafficking and changes in the uptake of phospholipid precursors, as well as the membrane trafficking- and autophagy-related defects shown to be driven by changes to phospholipid regulation [91,262].

Additional limitations are also present in our assessment of Aly1 and Aly2's phospho-regulation. Like our ubiquitin-focused screens, the KinDel screen produced more candidates than

we were able to further pursue (Figure 22 and Supplemental Tables S3 and S4, available at OneDrive link: Supplemental Thesis Documents - Bowman). For example, a notable group of such candidates belong to the yeast mating pathway, including *STE20*, *STE7*, and *FUS3*. Similarly, we were unable to fully assess other members of the TORC1-related pathway that constituted the focus of our efforts, including *TIP41* and *SLT2*. However, the link between TORC1 and Slt2 was only very recently identified and that precluded its inclusion in our studies. While these two groups represent the most promising candidates for further investigations, we conducted secondary screening of 60 deletion mutants that were each confirmed to affect Aly-mediated growth on at least one of the media conditions we used. This constitutes a rather large group of potential regulators that received no further assessment, but these data are published to assist in studies by the larger field and in future studies from the O'Donnell lab. Our investigations to define Npr1 and Sit4 in regulation of Alys could have been further strengthened by additional biochemical analyses to demonstrate direct phosphorylation/dephosphoryation by these enzymes. While work from Dr. O'Donnell has previously demonstrated Npr1's ability to directly phosphorylate the Alys, we utilized genetic manipulations and assessment of phospho-mobility changes on immunoblots to demonstrate Aly1 and Aly2's *NPR1*-dependent hyperphosphorylation in the absence of *SIT4* [67]. As a result, this relationship lacks the further support of such experiments to assess the direct binding or activity between either Npr1 or Sit4 and these α-arrestins, raising the possibility that other intermediate regulators could also be involved. Similarly, while we demonstrate that proteasomal inhibition by MG132 does not stabilize either Aly protein, finding instead a stabilizing effect driven by the vacuolar inhibition in *pep4*Δ cells, another notable limitation is represented by the absence of investigating their combined effect.

4.2 Future directions

Because of the limitations discussed in Section 4.1.2, as well as the new questions raised by the results discussed in these studies, there are many avenues by which this research can be furthered. Below, I discuss some of these possible future directions.

4.2.1 Short Term

The most obvious route of study to further pursue the results described herein lies in the further evaluation of the results obtained in our ubiquitin- and phosphorylation-focused ScUbI and KinDel screens. As our studies of each screen's most prominent candidates revealed novel connections to the α-arrestins, it is highly likely that some of the unstudied candidates are also important regulators of the Alys ((Figure 4, 22, and Supplemental Tables S1-S4, available at OneDrive link: Supplemental Thesis Documents - Bowman)). As demonstrated, for example, by the ERAD- or mating pathway-related genes mentioned above in Section 4.1.2, several prominent pathways are connected to α-arrestins by our screens, and these could form the basis for future studies. Such characterizations could likely follow a similar path of experimentation, utilizing biochemical analyses and live-cell microscopy to assess the downstream effects of these regulators on the α-arrestins. It would be interesting to determine if any of these remaining candidates act as direct regulators of the Alys. Additional in vitro studies using purified kinases or phosphatases in combination with the Alys could allow us to determine if any of them can directly control α-arrestin phosphorylation. Mass spectroscopy analyses could also be used to help define the specific phosphorylated residues in these α-arrestins and the functional impact of mutations in these sites

could then be defined, as has been done previously in the O'Donnell lab for regulation of α-arrestins by calcineurin [68].

Beyond a more complete interrogation of our screen results, the connections between the α-arrestins, autophagy, and phospholipid balance described in Chapter 2 also carry rich potential for immediate future work. One important question that could be addressed is whether, as proposed in our model (Figure 21C), alterations in nutrient import due to aberrant cell-surface retention of lipid-related transporters is truly the driver of the autophagy defects we identify. To address these possibilities, the PI3P distribution, autophagic flux, or Atg2/Atg18 localization in α-arrestin mutants that further lack lipid-related transporters, including the GPI transporter *GIT1* or the inositol-transporting *ITR1* and *ITR2*, could be assessed [91,362]. If uptake of GPI or inositol is a driver of the autophagic defect, then loss of these transporters could phenotypically suppress that defect. Assays like these would be a significant step towards more firmly establishing a mechanistic connection between the α-arrestins and the efficient progression of autophagy.

In addition, we hypothesize that the aberrant vacuolar retention of the lipid transfer complex members Atg2 and Atg18 causes the defective phagophore expansion [90,361]. To directly assess this possibility, we could attempt to restore their localization, either by reducing PI3P on the vacuole membrane (as could be done by over-expressing PI3P phosphatases) or by artificially correcting their association (as could be done by expressing them as a single fusion [247]) to improve autophagic flux in α-arrestin mutants. Another method that could help restore autophagic flux in the α-arrestin mutants is by over-expressing other ATG proteins that could potentially provide a sufficient population of active molecules to restore function to the PAS. In addition**,** as Atg2 functions directly to transport lipids from the ER to the growing phagophore, and it's localization to these membranes is influenced by its ability to bind Atg18 [244], the

artificial targeting of Atg2 to the PAS via fusion to Atg8 in α-arrestin mutants would allow us to determine if the strong retention of Atg18 to the vacuolar membrane is playing a role the phagophore expansion and autophagic flux defects observed in these backgrounds [247]. We could also attempt to free Atg18 from its aberrant vacuolar retention by over-expressing a phosphatidylinositol phosphatase like Ymr1 [356]. The increased abundance of such a phospholipid modifier should reduce the overall abundance of PI3P, and subsequently $PI(3,5)P_2$, thereby allowing the PI3P generated on the growing phagophore to properly recruit Atg18 to the PAS. A similar conceptual approach may lie in selectively disrupting non-autophagic PI3P production by deleting the PI3K Complex II-component *VPS38* in α-arrestin mutants, leaving the autophagy-dedicated PI3K Complex I as the only remaining functional isoform [223]. Such a loss should drastically reduce the abundance of PI3P away from the PAS, thereby allowing us to determine if the elevated abundance of this phospholipid at the vacuolar membrane we report to occur in the absence of α-arrestins is truly responsible for the lipid transfer protein retention and autophagic flux defects seen in these same backgrounds [366–369].

Finally, as my work with the Knop lab screening tFT-tagged membrane proteins for stability changes in the absence of α-arrestins was interrupted by the COVID-19 pandemic, the completion of these efforts further represents another clear course of future investigations (Appendix A) [417]. Though the initial high-throughput screens have been completed for several pairs of α-arrestin mutants, the candidates these efforts uncovered have yet to be validated. This could be accomplished by evaluating the most promising tFT-tagged candidates via FACS, live-cell microscopy, as well as SDS-PAGE and immunoblotting, to confirm any stability changes indicated by the colony-based screening (Figures 37-38). Additionally, reconstruction of such tFT-tagged constructs with other fluorophores, like GFP, would enable similar approaches to further

determine if any stability changes were being impacted by the presence of the tFT tag or defects that may have occurred during the construction of the tFT library itself. The tFT tag itself represents another powerful tool for use in future experiments. Providing a readout of stability, as well the localization and abundance feedback offered by more traditional fluorescent epitope tags, this novel fluorophore could be further appended to any protein of interest to offer this additional insight via live-cell microscopy.

4.2.2 Long Term

While the strategies discussed above in section 4.2.1 represent additional work that could be accomplished soon, the results described herein also raise more long-term questions. For example, it would be interesting to ask whether further regulatory connections to the α-arrestins could be gleaned from adapted screens of the ScUbI and/or KinDel deletion libraries. Our previous screens relied upon growth phenotypes driven by the over-expression of Aly1 or Aly2 on media containing either rapamycin or high salt, yet the α-arrestins are well-known to possess distinct responses to a variety of stimuli (Figures 4 and 22). These same libraries could also be screened using other stimuli, like the toxic proline analog azetidine-2-carboxylic acid (AzC) to which Aly-over-expressing cells are more sensitive than WT controls [68]. Similarly, as we only investigated the effects of deletion mutants on Aly1- and Aly2-dependent phenotypes, these libraries could be used to screen for effectors of other members of the α-arrestin family. Such screening efforts, though requiring significant degrees of follow up experiments like those described in Chapter 3, could serve to further expand the known repertoire of ubiquitin- and phosphorylation-related α-

arrestin regulators by expanding the scope to include other arrestin family members, as well as diversifying the range of external factors stimulating their activity.

Along similar lines, the connections already established following our existing screens could be further strengthened by more careful interrogation. One such avenue could lie in the characterization of the α-arrestins' connection to the TORC1-Sit4-Npr1 signaling axis described in Chapter 3. Most deletion strains used in these experiments were, as with the initial KinDel screen itself, derived from the yeast deletion collection library [311]. While this resource represents a widely used and powerful tool for identifying genetic interactions, it is also known to further contain a wide array of off-target mutations that often go undetected. Despite confirming the absence of the target gene that we were focused on in these strains, other additional genetic perturbations in these genetic backgrounds could have influenced our results. This is a caveat in many genetic studies unless multiple isolates of newly constructed gene deletions are also assessed. This contingency could be accounted for in future work by reproducing key mutant strains like *sit4*Δ, *npr1*Δ, or *tor1*Δ for inclusion in similar experiments to those already conducted, allowing for more confident validation of the results we describe. Similarly, regulatory relationships identified using even perfectly constructed deletion mutants could be problematically obscured by unidentified epistatic compensations to the prolonged absence of those genetic elements in the strains themselves. The loss of *SIT4*, for instance, results in a wide array of unintended phenotypes including altered cellular, vacuolar, and mitochondrial morphology [418–420]. Though we established a clear mechanistic explanation for the α-arrestin-associated changes we observed, the potential influence of such epistatic factors present in those null mutants cannot be ruled out. This possibility could be accounted for in future experiments by either substituting endogenous Sit4 proteins for a catalytically dead mutant, and thus preserving its ability to act as a

scaffold for other protein interactions, or by using an inducible degradation system to limit the span of time during which Sit4 would be absent.

A further topic worthy of future pursuits centers around our identification of a novel role for the vacuole in the degradation of Aly1 and Aly2 (Figures 34-35). While previous studies have tied α-arrestin degradation to the proteasome (see Section 1.1.3.2.3), our results demonstrate a stabilization of the Alys when vacuolar degradation is impaired, though the mechanism by which this could occur remains undefined. It would be interesting to determine if this pair of α-arrestins is somehow being trafficked along with their membrane-bound cargo for degradation in the vacuole, or if another route to this compartment, like autophagy, is responsible. This line of questioning pairs well with the possibility, raised by our observations presented in Chapter 3, that suggest the α-arrestins may be playing a role in regulating the composition of the vacuolar membrane itself. Not only do we demonstrate changes in the phospholipid content and peripheral protein retention to the vacuolar surface in the absence of α-arrestins, but this structure also contains many possible candidates for α-arrestin-controlled cargo like the nucleoside transporter Fun26 or the ABC transporter Adp1 [421]. α-Arrestin-mediated trafficking of such cargo into the vacuolar lumen, either through intra-luminal budding or microautophagy, may not only represent an additional regulatory role for the trafficking adaptors, but also prove key in unveiling their own route to the vacuole.

As another possible avenue, the misregulation of Atg18's localization in the absence of α-arrestins may be affecting its ability to function in a newly reported variant of the retromer complex [301]. It would therefore be of interest to determine if the α-arrestins are capable of binding Atg18 in place of the arrestin-like Vps26 as part of this complex, an outcome that could be assessed via co-immunoprecipitation or proximity proteomics experiments like those used to uncover this new

form of Atg18-retromer [301]. Such a role for the α-arrestins could thus provide a link to a more direct role in regulation of vacuolar membrane proteins, as well as another possible route to their own degradation. As has been used to characterize other Rsp5 adapters that help control the composition of the vacuolar membrane and the compartment's morphology, the potential for α-arrestins to perform a similar role could also evaluated by monitoring the trafficking of α-arrestin cargo proteins mistargeted to this locale [367–370].

Another intriguing option for future work lies in uncovering the identity of the aberrant low-electron density structures we observed in rapamycin-treated *art1*Δ and 9arrΔ cells via EM (Figure 8A, yellow arrows). Given their similarity in electron density to lipid droplets, as well as their proximity to the cortical ER, it is tempting to posit that these structures may represent either excess accumulations of lipids or failed autophagosomes [422,423]. The activation of free fatty acids in the ER by the acyl-CoA synthetase Faa1 is reported to support the *de novo* production of phospholipids for transport by the Atg2-Atg18 complex to the growing phagophore [424]. If, as we suggest, the Atg2-Atg18 complex is failing to properly localize in α-arrestin mutants, these newly formed phospholipids may be accumulating in the ER and driving the formation of the aberrant lipid-like structures. This possibility could be evaluated in the future by using EM to determine if these structures are still produced in the absence of *FAA1*.

Finally, the role of α-arrestins in the cellular response to, and recovery from, nitrogen starvation represents yet another course of future investigations. The inhibition of TORC1 by nitrogen starvation results in the wide-spread endocytosis of cell surface nutrient transporters that are degraded in the vacuole to help support cell survival in coordination with autophagy, while further inducing cell signaling cascades which transition cells to a state of quiescence [104,285]. This plasma membrane remodeling includes many α-arrestin cargo and their transit via the α-

arrestin-related MVB pathway, while the subsequent quiescence-inducing signaling includes targeting of Art1 via the Npr1 kinase [104,285]. These facts, along with the notable lack of ability for 9arrΔ cells to resume proliferation after even short periods of nitrogen starvation, heavily implicate the α-arrestins in supporting the proper cellular response to this stimulus (Figure 41). Indeed, as discussed in Appendix C, our preliminary results suggest 9arrΔ cells are even more sensitive to nitrogen starvation than the MVB-defective *vps4*Δ or vacuolar fusion-defective *vrp1*Δ (Figure 41) [64,137,425]. This increased sensitivity suggests that the α-arrestins are likely helping cells respond to nitrogen starvation via roles beyond nutrient transporter trafficking, representing an enticing topic of future studies. Given the preliminary nature of our assessments, the ability of α-arrestin mutants to resume proliferation after periods of nitrogen starvation would first need to be reproduced, efforts which could be further aided by the inclusion of additional backgrounds like those lacking other α-arrestins like Art1. In the absence of changes specific to individual α-arrestins, the defects present in 9arrΔ cells could be further assessed by complementing this strain with plasmid-expressed versions of the missing α-arrestins to discern which members of the protein trafficking adapter family are having the greatest effect. Once validated, these relationships could be further detailed by using proximity proteomics and/or mass spectroscopy targeting the pertinent α-arrestins after transition to media lacking nitrogen sources to identify both changes in α-arrestin regulation and binding partners which may be important for their role in this response.

Appendix A : Identification of α-arrestin cargo through screening with a tandem-fluorescent protein timer (tFT)

This project was developed in collaboration with Dr. Michael Knop at the University of Heidelberg in Heidelberg, Germany. These experiments represent work conducted at the University of Heidelberg that was interrupted by the COVID-19 pandemic, resulting in my inability to remain in Germany for the completion of this project. Screen data was produced by R.W.B with subsequent data analyses by Matthias Meurer (Univ. of Heidelberg), Daniel Kirrmaier (Univ. of Heidelberg), and Amanda Kowalczyk (Univ. of Pittsburgh).

Appendix A.1 Introduction

The α-arrestins' best described function lies in mediating the endocytic trafficking of membrane-bound proteins at the cells surface, with at least 28 such proteins having been identified as α-arrestin cargo to date [58,59,62,66,67,73,74,77,79,87–97]. While broadly focused mass spectroscopy-based efforts have hinted at a wide range of proteins under such control, a targeted screen of the membrane-bound proteome has yet to be published [64,83]. In collaboration with the Knop lab at the Univ. of Heidelberg, I therefore examined how the combined loss of paired α-arrestin paralogs (*aly1*Δ *aly2*Δ, *bul1*Δ *bul2*Δ, *art5*Δ *rim8*Δ, and *ecm21*Δ *csr2*Δ) affects the abundance and turnover of the membrane-bound proteome using a tandem fluorescent protein timer (tFTs). This tFT tag is composed of two fluorescent proteins with different kinetics of fluorophore maturation, namely mCherry and superfolder GFP (sfGFP) (Figure 37A). The ratio of

mCherry:sfGFP fluorescence intensities subsequently serves as a metric for protein turnover and stability, whereas sfGFP signal represents measure of protein abundance (Figure 37A) [426]. These screens were conducted using a targeted sub-set of the genome-wide endogenously tagged tFT collection, produced by the Knop lab, containing strains expressing tFT-tagged proteins known or predicted to contain transmembrane domains (membrane sub-library) [426]. As the remodeling of the cell surface proteome occurs differentially under various stress conditions, I conducted these screens on SC control media, as well as a broad range of media conditions. Together, we found a significant number of membrane proteins whose stability was altered in the absence of α-arrestins compared to the WT controls. To our satisfaction, each mutant pair induced changes to distinct sub-sets of these proteins, with further condition-specific groupings being found within each α-arrestin mutant background. These exciting findings thus represent a powerful starting point for future investigations with the potential to greatly broaden our understanding of the breadth of α-arrestin influence in mediating the trafficking of membrane-bound proteins under specific cellular stressors.

Appendix A.2 Materials and methods

The tFT membrane sub-library was constructed by the Knop lab as described in [427]. Similarly, screening of the tFT membrane sub-library was adapted from the method described in [427]. In short, haploid array strains carrying deletions of pairs of α-arrestin paralogs were generated as described in Table 6. Screens were conducted in 1536-colony format on solid media containing 1% agarose. Using a RoToR pinning robot (Singer), tFT query strains (prior to marker excision), dummy colonies on the outer rows and columns to minimize the influence of nutrient

access on colony size and fluorescence and, on each plate, a set of reference strains spanning the full range of protein abundances and stabilities in the tFT library were mated with α-arrestin and BY4741 array mutants on YPD media. Selection of diploids was achieved by pinning of mated strains to YPD media containing standard concentrations of hygromycin and NAT and grown at 30˚C overnight. Sporulation of diploid colonies was achieved by pinning to media containing 2% agar and 2% potassium acetate and grown at 23˚C for 5 days. Initial selection of haploids was accomplished by pinning sporulated colonies to SC media lacking histidine, arginine, and lysine containing 50mg/L canavanine and thialysine and grown at 30˚C for 2 days. These initial haploids underwent a second round of haploid selection by pinning to SC media lacking histidine, arginine, and lysine containing 50mg/L canavanine and thialysine plus hygromycin and NAT and grown at 30˚C overnight. Next, marker excision was achieved by pinning secondary haploids to SC media lacking histidine with 2% galactose and raffinose and grown at 30˚C overnight. The isolation of cells that had successfully undergone marker excision was achieved by pinning of marker excised colonies to SC media lacking histidine with 50mg/L additional uracil and 1g/L 5-FOA and grown at 30˚C for 1-2 days. Finally, the completed screening plates were pinned to each of 13 media screening conditions composed of SC media lacking histidine with: 1) 10ng/ml rapamycin, 2) 50ng/ml rapamycin, 3) 10 mM urea in place of ammonium sulfate, 4) twice the normal concentration of amino acids, 5) 0.2% 2-deoxyglucose, 6) 5% glucose, 7) 3% glycerol in place of glucose, 8) 1M NaCl, 9) 1M sorbitol, 10) adjustment of pH to 3.5 with HCl, 11) adjust of pH to 8.0 with Tris-HCl, 12) 0.1% oleic acid and 0.5% Tween, and 13) no additional manipulations (standard control media). These plates were then grown overnight at 30˚C. In each screen, a single tFT strain was crossed with one BY4741 strain, and three biological replicates of the relevant α-arrestin mutant in 384 colony format. These arrays were condensed into 1536 format to produce 3

technical replicates of each biological replicate pinned next to each other. Fluorescence intensities of the final colonies were measured 24h after pinning to each screen condition using an Infinite M1000 plate reader equipped with stackers for automated plate loading (Tecan) in custom temperature control chambers set to 30˚C. Measurements in mCherry (587/10 nm excitation, 610/10 nm emission, optimal detector gain) and sfGFP (488/10 nm excitation, 510/10 nm emission, optimal detector gain) channels were performed at 400 Hz frequency of the flash lamp, with 10 flashes averaged for each measurement. Additional statistical analyses of these screen results were conducted with the help of Amanda Kowalczyk at the University of Pittsburgh. These analyses first removed all border colonies and any plates where replicates exhibited high standard deviations. Then, the values of remaining colonies were normalized for variation in signal due to plate position. A regression was fitted across control colony values based on position. Those values were then predicted for the corresponding test colonies and the corrected value generated by subtracting the predicted test value from the observed test value. Values from reference colonies were then subtracted on a linear scale, with negative and zero values set to NA. Next, ratios were calculated as mCherry minus sfGFP corrected values, with pairwise t-tests (Welch t-test) performed between wild type and α-arrestin knockouts per gene. Additionally, mean values (sfGFP and mCherry for both wild type and control), ratio values (difference between sfGFP and mCherry for both wild type and control), and differences in ratios (wild type ratio minus knockout ratio) were reported. Finally, p-values were Benjamini-Hochberg corrected and a p-value cutoff of <0.1, rank by effect size (difference in ratios), was applied.

Table 6. Strains used in Appendix A

Strain	Genotype	Source
tFT library: YMaM330	ORF-mCherry-SceIsite-SpCYC1term-ScURA3-SceIsite-mCherryΔN-sfGFP	[427]
BY4741-hph	*MAT* **a** *ura3*::*HPH his3Δ1 leu2Δ0 met15Δ0*	This study
*aly1*Δ *aly2*Δ	*MAT* **a** *aly1Δ::KanMX aly2Δ::HPH his3Δ1 leu2Δ0 ura3Δ0 met15Δ0*	This study
*bul1*Δ *bul2*Δ	*MAT* **a** *bul1Δ::KanMX bul2Δ::HPH his3Δ1 leu2Δ0 ura3Δ0 met15Δ0*	This study
*art5*Δ *rim8*Δ	*MAT* **a** *art5Δ::KanMX rim8Δ::HPH his3Δ1 leu2Δ0 ura3Δ0 met15Δ0*	This study
*ecm21*Δ *csr2*Δ	*MAT* **a** *ecm21Δ::KanMX csr2Δ::HPH his3Δ1 leu2Δ0 ura3Δ0 met15Δ0*	This study

Appendix A.3 Results and discussion

In collaboration with the Knop lab at the Univ. or Heidelberg, I conducted high-throughput screens of the tFT membrane sub-library, a collection of strains 567 expressing unique endogenously tFT-tagged proteins known or predicted to contain transmembrane domains, mated to either WT (BY4741) or one of four separate sets of double deletion mutants lacking paralogous pairs of α-arrestins (*aly1*Δ *aly2*Δ, *bul1*Δ *bul2*Δ, *art5*Δ *rim8*Δ, and *ecm21*Δ *csr2*Δ) [14,426,428]. These screens relied upon whole-colony fluorescent readouts of cells expressing distinct tFT-protein fusions, where the signal produced by the slow-maturing fluorophore mCherry and fast-maturing sfGFP contained within the tFT enabled the determination of each protein's abundance (sfGFP alone) and, importantly, stability (mCherry:sfGFP ratio) (Figure 37A). As the remodeling of the cell surface proteome occurs differentially under different stress conditions, I conducted these screens not only on SC control media (His-), but also a broad range of media that employed stressors we considered most likely to induce the trafficking of potential α-arrestin cargo, including the nitrogen-starvation mimicking drug rapamycin (rapa), an alternative nitrogen source

(urea), excess amino acid content (2xAA), a toxic analog of glucose (2-deoxyglucose), high glucose (5%), an alternative carbon source (glycerol), osmotic stress (NaCl and sorbitol), high pH (8.0), low pH (3.5), and lipid stress (oleic acid). These efforts produced initial data sets detailing the readouts of sfGFP and mCherry fluorescent intensity values for all WT, α-arrestin deletion mutant, and control strains that were further analyzed with the help of Amanda Kowalcyzk (Univ. of Pittsburgh) (data files available in 'Appendix A' folder at OneDrive link: Supplemental Thesis Documents - Bowman). This secondary analysis took into account the position of colonies on each plate and the intensities of control colonies to produce normalized values that were compared across replicates, using a p-value cutoff of <0.1 to remove candidates whose replicate variability was too high to be considered biologically relevant (see Section A.2). While many condition/mutant combinations produced hundreds of significant gene candidates, limited growth and high variability rendered some data sets nearly unusable, particularly those grown on glycerol or pH 8.0 (Figure 37B). The trafficking of specific membrane proteins is controlled by specific sub-sets of the α-arrestin family, and often induced under distinct conditions [373,374,429]. We were, therefore, reassured that the results of this screening were meaningful by our finding that, within a given condition, the groupings of significant genes were highly distinct when compared across α-arrestin mutant pairs (Figure 37C). Additionally, those genes found to change significantly within these mutant pairs were largely specific to only a handful of stress conditions (Figure 37D).

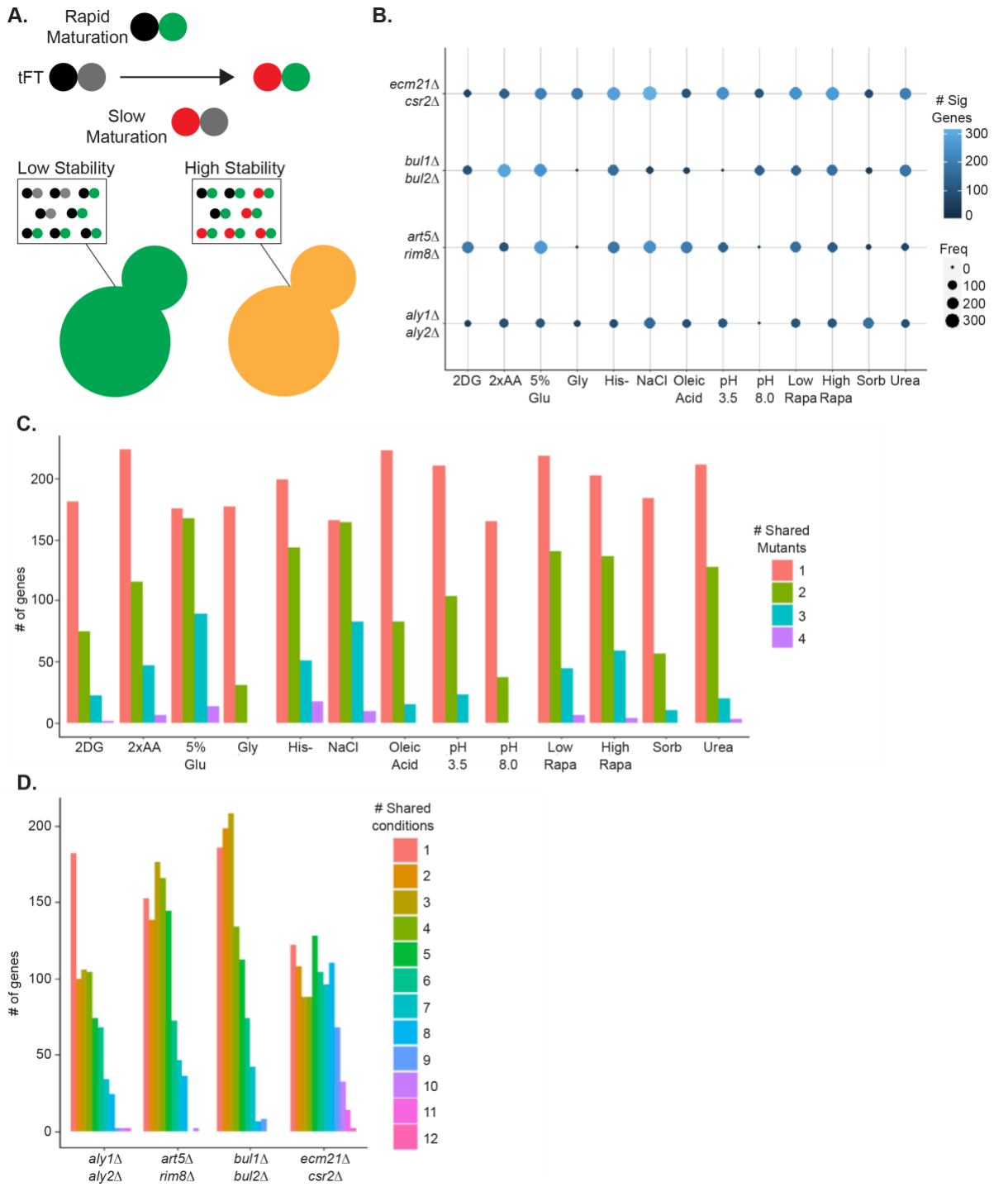

Figure 37. tFT screening of α-arrestin double mutants reveals mutant- and condition-specific candidate groups.

(**A**) Representation of the tFT timer containing mCherry (red) fused to sfGFP (green). After translation, the rapidly folding sfGFP matures more quickly than the slower folding mCherry, resulting in a dynamic change in the ratio of intensities produced by these tandem fluorophores that coincides with the age of the timer and a stability readout for

the protein to which it has been fused. These stability changes can be assessed at the cellular or colony level with low stability represented by mostly immature timers producing sfGFP signal and high stability represented by mostly mature timers producing both sfGFP and mCherry signal. Adapted from Figure 1A in [428] (**B**) The number of genes producing significant (p-value <0.1) fluorescent readouts across replicates is charted as a colored circle for each α-arrestin mutant pair (left) in each media condition (bottom) (see Section A.2 for full media condition description). The number of significant genes is expressed by circle color, with dark blue representing 0 and light blue representing 300 genes, respectively. The frequency of significant genes is expressed by circle size, with the smallest circles representing 0 and the largest circles representing 300. (**C**) The number of genes producing significant (p-value <0.1) fluorescent readouts across replicates (left) in each media condition (bottom) is charted as a function of the number of α-arrestin mutant pair screens in which each appeared (right). (**D**) The number of genes producing significant (p-value <0.1) fluorescent readouts across replicates (left) in each α-arrestin mutant pair (bottom) is charted as a function of the number of media conditions in which each appeared (right).

Though cells elicit extensive remodeling of the proteins present at the cell surface and other membrane-bound compartments to optimize their ability to survive various stress conditions, such actions are tightly controlled and highly unlikely to result in stability changes for the majority of transmembrane proteins. The reliability of these screen results was therefore further supported by our finding that most tFT-tagged proteins exhibited a mCherry:sfGFP ratio change close to zero in both WT and α-arrestin mutant backgrounds (Figure 38A-B). This specificity also strengthens the likelihood that those proteins whose tFT ratios was found to change most between WT and α-arrestin mutant colonies represent strong candidates for future experiments evaluating their potential as α-arrestin cargo (Figure 38C). Together, while these screen results represent only the beginning stages of a larger project due to the COVID-19 pandemic's interruption of our initial experimental plan, they represent a powerful starting point for future endeavors likely to offer deep

and extensive insight into the impact of the α-arrestins on the trafficking and stability control of the membrane-bound proteome.

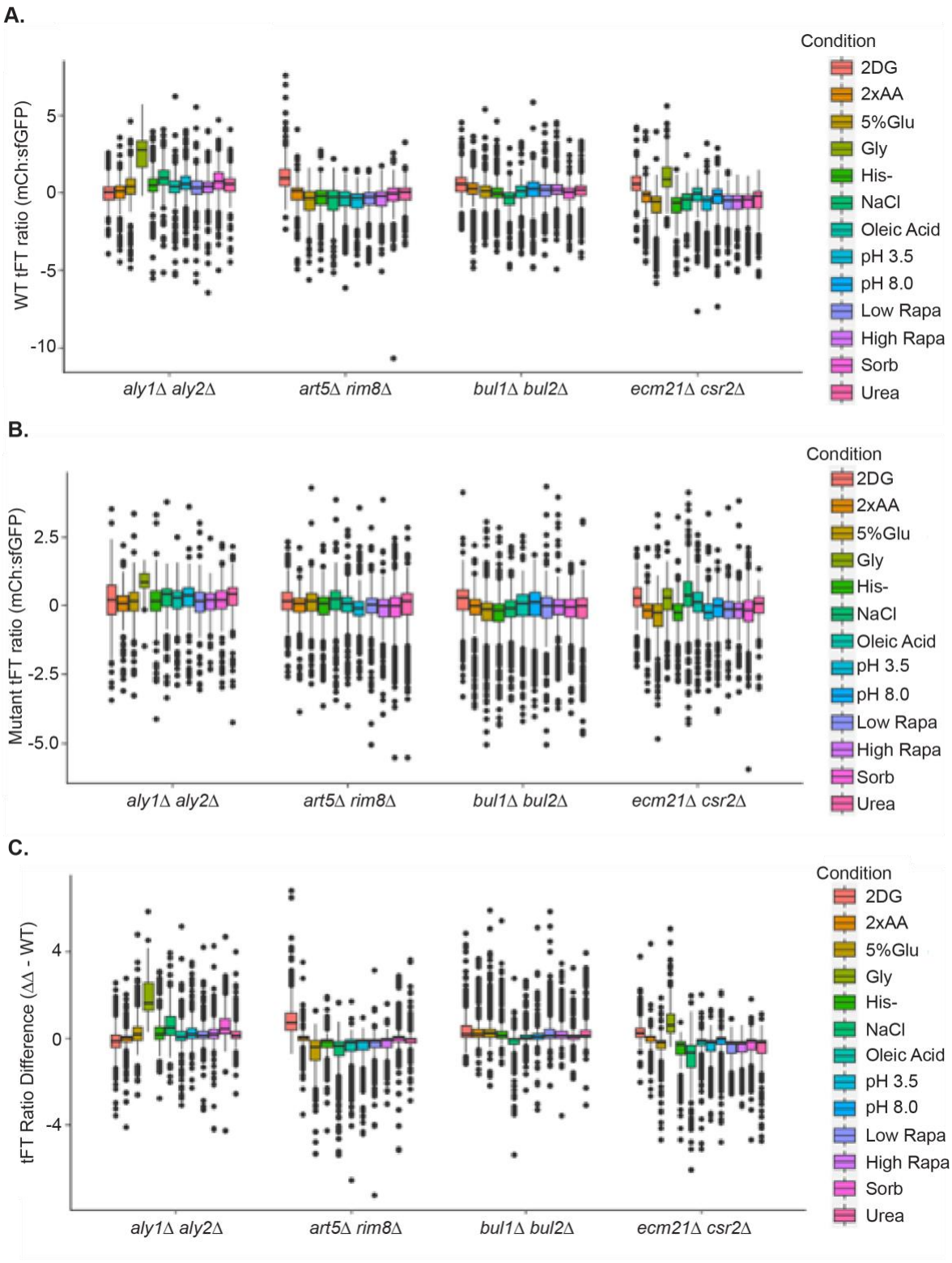

Figure 38. The majority of tFT-tagged proteins undergo minimal stability change in WT and α-arrestin mutant cells.

(**A**) The ratio of mCherry:sfGFP intensity (left) for each gene producing significant (p-value <0.1) fluorescent readouts in WT colonies across replicates is charted in each condition (right) and divided by the α-arrestin mutant pair present in each screen set that contained those WT colonies (bottom). Those values within +/- 1 standard deviation of the mean ratio (black line) are represented by a colored box, while those outside +/- 1 standard deviation of the mean appear as black circles. (**B**) The ratio of mCherry:sfGFP intensity (left) for each gene producing significant (p-value <0.1) fluorescent readouts in α-arrestin mutant colonies across replicates is charted in each condition (right) and divided by the α-arrestin mutant pair (bottom). Those values within +/- 1 standard deviation of the mean ratio (black line) are represented by a colored box, while those outside +/- 1 standard deviation of the mean appear as black circles. (**C**) The change in mCherry:sfGFP intensity ratio for a single gene between WT and α-arrestin mutant colonies (left) for each gene producing significant (p-value <0.1) fluorescent readouts across replicates is charted in each condition (right) and divided by the α-arrestin mutant pair present in each screen set (bottom). Those values within +/- 1 standard deviation of the mean ratio (black line) are represented by a colored box, while those outside +/- 1 standard deviation of the mean appear as black circles.

Appendix B : α-Arrestins are required to maintain normal nuclear-vacuolar junctions and lipid droplet abundance

In this section I will discuss experiments I conducted demonstrating the morphology of nuclear-vacuolar junctions and lipid droplet regulation that are disrupted in the absence of α-arrestins.

Appendix B.1 Introduction

Membrane contact sites (MCS) form at the junction of sub-cellular compartments through the direct binding of proteins embedded in each respective membrane, playing important roles in the regulation of ion homeostasis and lipid biosynthesis [430–432]. A prominent example of a MCS occurs at the nuclear-vacuolar junction (NVJ), formed by the interaction of the vacuolar-embedded Vac8 and nuclear-embedded Nvj1, and serving to regulate processes like piecemeal microautophagy of the nucleus (PMN) and lipid biosynthesis [423,433,434]. PMN is a site-specific type of autophagy wherein a portion of the nucleus adjacent to the NVJ invaginates into the vacuolar lumen where it can be degraded [433,434]. NVJs also regulate the biosynthesis of lipids like long-chain fatty acids that are incorporated into lipid droplets (LDs) derived from the peri-nuclear ER during nutrient starvation or rapamycin-induced TORC1 inhibition [423,435]. LDs serve as energy stores, increasing in size and abundance when nutrients become limiting, as well as a storage compartment for various lipid species, helping to regulate their abundance and biosynthesis that are important in the exit of cells from the quiescent G_0 cell cycle stage [435–

437]. In the work described in this section, I found that cells exhibit enlarged NVJs in the absence of α-arrestins, as well as a potential defect in PMN following treatment with rapamycin. Furthermore, α-arrestin mutants display an elevated abundance of lipid droplets, both before and after rapamycin-induced TORC1 inhibition. These results thus indicate a link between this family of protein trafficking adapters and the regulation of MCSs like the NVJ and lipid droplet abundance.

Appendix B.2 Materials and methods

Fluorescent protein localization was assessed using confocal microscopy. We grew cells overnight in SC medium in culture tubes on a rotating drum at 30°C. We then diluted cells (~A_{600} = 0.3) and regrew them in culture tubes for 4 h on a rotating drum at 30°C. For cells treated with rapamycin (LC Laboratories, Woburn, MA), 200 ng/ml rapamycin was added to 1ml of cells in an Eppendorf tube and incubated in an end-over-end rotator at 30˚C for indicated times. Prior to imaging, FM4-64, CMAC, or BODIPY stains were used to mark the vacuole membrane, the vacuole lumen or lipid droplets, respectively. For cells stained with FM4-64, 1 ml of cells treated with 100 μg/ml FM4-64 for 30 minutes at 30˚C. Cells were then washed, resuspended in 1 ml SC medium, and incubated at 30˚C for 1h. For cells stained with CMAC, 20 uM Cell Tracker Blue CMAC (7-amino-4-chloromethylcoumarin) dye (Life Technologies, Carlsbad, CA) was added to 1 ml of mid-log cells 1 hour just prior to imaging. Cells were then inoculated to low density (~A_{600} = 0.15) onto 35 mm glass bottom microwell dishes (MatTek Corporation, Ashland, MA) that were either poly-D-lysine coated or had been treated with 50 μl of 0.2 mg/ml concanavalin A (MP Biomedicals, Solon, OH) . For cells stained with BODIPY™, 1 μl of 50μg/ml BODIPY™ (4,4-

Difluoro-1,3,5,7,8-Pentamethyl-4-Bora-3a,4a,-Diaza-s-Indacene) dye (ThermoFisher Scientific, Waltham, MA) was added to 150 μl of low-density cells(~A_{600} = 0.3) in the microwell dishes 10 minutes prior to imaging. Cells were imaged using a Nikon Eclipse Ti2-E A1R inverted microscope (Nikon, Chiyoda, Tokyo, Japan) outfitted with a 100x objective (NA 1.49) and images were detected using GaAsP or multi-alkali photomultiplier tube detectors as single median planes. Acquisition was controlled using NIS-Elements software (Nikon, Chiyoda, Tokyo, Japan) and all images within an experiment were captured using identical settings. Images were deconvolved using the Richardson-Lucy algorithm, cropped, and adjusted evenly using NIS-Elements.

To determine the number of lipid droplets per cell, single median planes of cells stained with BODIPY (see Section B.2 above) obtained using confocal microscopy were first deconvolved using the Richardson-Lucy algorithm, then manually assessed for the number of stained puncta (488nm channel) present per cell. Each cell in the image field was defined based on its appearance in the DIC image. Fluorescent quantification was assessed statistically using Prism (GraphPad Software, San Diego, CA). Unless otherwise indicated, we performed the Kruskal-Wallis statistical test with Dunn's post hoc correction for multiple comparisons. In all cases, significant p-values from these tests are represented as: *, p value <0.1; ** p value <0.01; ***, p value <0.001; ns, p value >0.1. In some instances where multiple comparisons are made, the † symbol may additionally be used in place of the * with the same p value meanings but indicating comparisons to a different reference sample.

Table 7. Strains used in Appendix B

Strain	Genotype	Source
BY4741	*MAT* **a** *his3Δ1 leu2Δ0 ura3Δ0 met15Δ0*	[311]
aly1Δ aly2Δ (aka D2-6a)	*MAT* **a** *aly1Δ::KanMX aly2Δ::KanMX his3Δ1 leu2Δ0 ura3Δ0 met15Δ0 lys2Δ0*	[67]
*9Arr*Δ (EN60)	*MAT* **a** *ecm21Δ::KanMX csr2Δ::KanMX bsd2Δ rog3Δ::NatMX rod1Δ ygr068cΔ aly1Δ aly2Δ ldb19Δ ylr392cΔ::HIS3 his3Δ0 ura3Δ0 leu2Δ0*	[59]
art1Δ	*MAT* **a** *art1Δ::KanMX his3Δ1 leu2Δ0 ura3Δ0 met15Δ0*	[311]
BY4741 *NVJ1*-mNG	*MAT* **a** Nvj1-mNG::*HPH his3Δ1 leu2Δ0 ura3Δ0 met15Δ0*	This study
aly1Δ aly2Δ NVJ1-mNG	*MAT* **a** *aly1Δ*::*KanMX aly2Δ*::*KanMX* Nvj1-mNG::*HPH his3Δ1 leu2Δ0 ura3Δ0 met15Δ0 lys2Δ0*	This study
art1Δ NVJ1-mNG	*MAT* **a** *art1Δ::KanMX* Nvj1-mNG::*HPH his3Δ1 leu2Δ0 ura3Δ0 met15Δ0*	This study
9arrΔ *NVJ1*-mNG	*MAT* **a** *ecm21Δ::KanMX csr2Δ::KanMX bsd2Δ rog3Δ::NatMX rod1Δ ygr068cΔ aly1Δ aly2Δ ldb19Δ ylr392cΔ::HIS3* Nvj1-mNG::*HPH his3Δ0 ura3Δ0 leu2Δ0*	This study

Appendix B.3 Results and discussion

NVJs are formed at the MCS between the nucleus and the vacuole through the interaction of the vacuolar membrane embedded Vac8 with the nuclear periphery protein Nvj1 [423,433,434]. I thus assessed the morphology of NVJs in WT and α-arrestin mutant cells expressing Nvj1-mNG from its endogenous locus using live-cell confocal microscopy before and after treatment with rapamycin (Figure 39). At steady-state, cells lacking α-arrestins displayed elongated Nvj1-mNG patches compared to the WT control, as has been reported to occur in cells undergoing carbon source limitation or rapamycin-induced TORC1 inhibition (Figure 39) [423,430]. These results indicate that this MCS is misregulated in the absence of α-arrestins and raises the possibility that defective nutrient import normally controlled by α-arrestin cargo may be tied to this morphological shift. After treatment with rapamycin, α-arrestin mutants continued to display larger Nvj1-mNG patches than WT cells (Figure 39). As expected, I observed Nvj1-marked puncta in the lumen of the vacuole in WT cells once TORC1 was inhibited, likely corresponding to the induction of PMN

(Figure 39, white arrows) [433,434]. While *aly1*Δ *aly2*Δ cells similarly exhibited evidence of PMN induction, I found *art1*Δ cells to produce noticeably fewer intra-vacuolar Nvj1 puncta (Figure 39, white arrows). Furthermore, I found almost a near complete absence of such structures in 9arrΔ cells, indicating the α-arrestins may be required for the proper induction and function of PMN (Figure 39).

NVJs are important sites of lipid regulation in cells, representing the sites of lipid biosynthesis and the formation of LDs [423,432]. As a result of the aberrant NVJ morphology I observed in the absence of α-arrestins, I next assessed the localization and abundance of lipid droplets in both WT and α-arrestin mutants by live-cell confocal microscopy using the LD dye BODIPY (see Section B.2). As has been previously reported, I found WT cells to contain BODIPY-marked LDs at peri-vacuolar sites appearing to be adjacent to the nucleus that were noticeably larger following treatment with rapamycin (Figure 40A) [423]. Though *aly1*Δ *aly2*Δ cells displayed similar LD localization and abundance to the WT control at stead-state, I found a significantly higher number of these structures after the addition of rapamycin in this background (Figure 40A-B). Notably, *art1*Δ and 9arrΔ cells both exhibited a similarly elevated LD abundance even before rapamycin treatment, with this mode of TORC1 inhibition resulting in a further elevation of LD number in these backgrounds (Figure 40B). I further found this marked increase to coincide with the striking accumulation of LDs in tight formation around the limiting membrane of the vacuole, especially at what appear to be NVJs (Figure 40A). Together these results support a model wherein α-arrestin are required for the proper maintenance of NVJs, with their absence resulting in an elevation abundance of LDs that are produced at this MCS [423]. This connection is further strengthened by the fact that the α-arrestins control the endocytic trafficking of multiple lipid-related transporters, as well as the reported role of the α-arrestin-regulating Sit4 phosphatase

in LD formation, though further investigations will be required to detail the exact nature of this link [73,77,91,94,138,391,423,435].

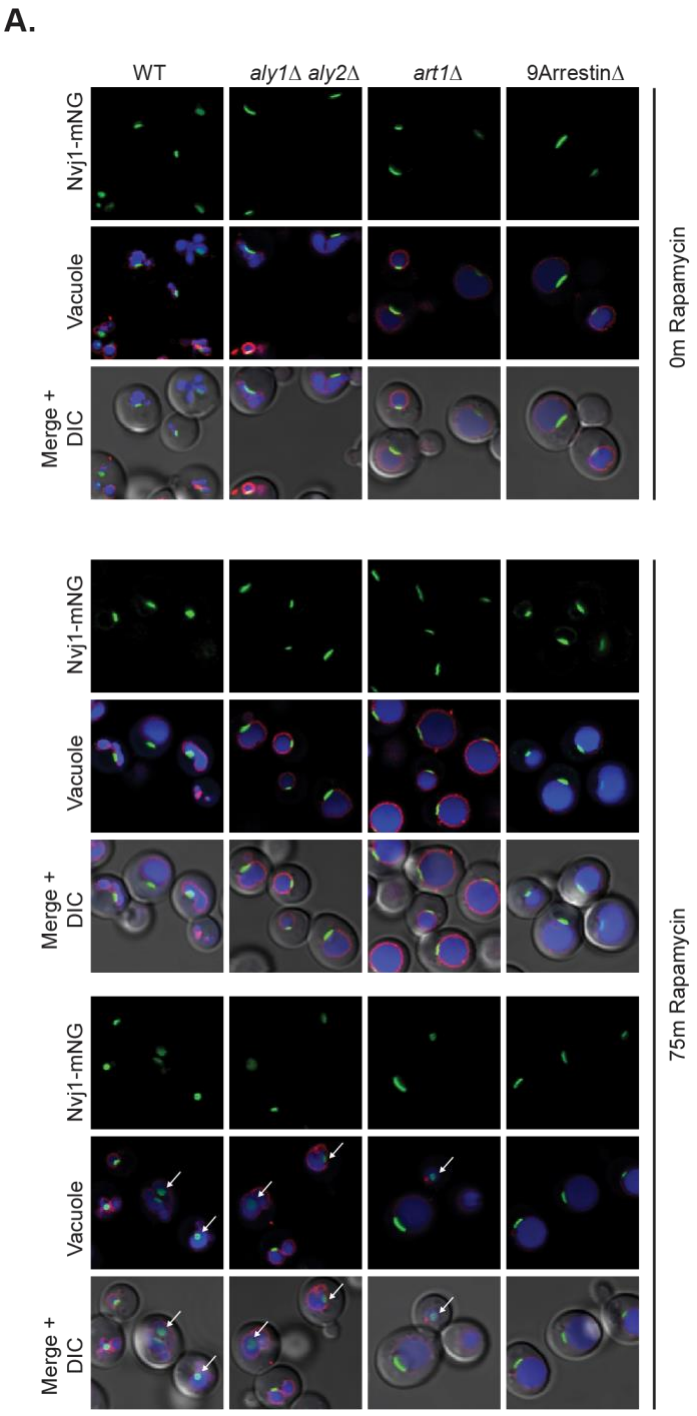

Figure 39. α-Arrestins are needed to maintain normal nuclear-vacuolar junction morphology

(**A**) Cells expressing endogenously tagged Nvj1-mNG (green) in either WT or α-arrestin mutant cells were imaged by confocal microscopy before and after treatment with 200ng/mL rapamycin. CMAC and FM4-64 is used to stain the vacuolar lumen (shown in blue) and membrane (shown in red), respectively. White arrows indicate intraluminal Nvj1-mNG structures likely produced by PMN.

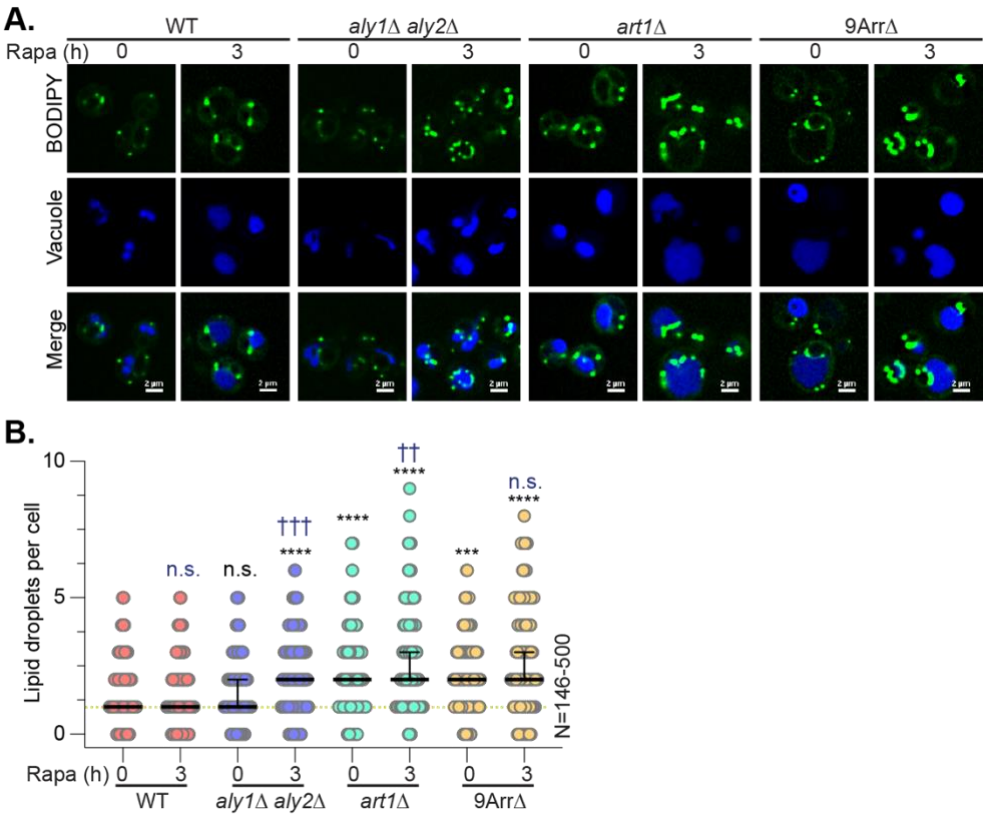

Figure 40. α-Arrestins are needed to maintain proper lipid droplet abundance.

(**A**) Either WT or α-arrestin mutant cells stained with BODIPY to mark lipid droplets (shown in green), and CMAC, to stain the vacuole (shown in blue), were imaged by confocal microscopy at the indicated times post-treatment with 200ng/ml rapamycin. (**B**) Quantification of the number of lipid droplets per cell for the cells imaged in panel (a) is shown as a graph. The median number is shown as a black line and the error bars represent the 95% confidence interval. For reference, a yellow dashed line represents the median value for WT. Kruskal-Wallis statistical analysis with Dunn's post hoc test was performed to compare the lipid droplet counts. Statistical comparisons between mutant and WT cells at that same time point are displayed in black asterisks. Statistical comparisons of WT or mutant cells to their respective t=0 timepoints are shown as blue daggers. (n.s. = not significant; four symbols has a p-value <0.0001).

Appendix C Starvation recovery

In this section, I describe experiments performed by Karandeep Chera, an undergraduate student at Duquesne University, and myself assessing the ability of cells to resume proliferation after periods of nitrogen starvation.

Appendix C.1 Introduction

Cells are capable of surviving periods of nutrient starvation by producing temporary pools of intracellular building blocks through the degradation of non-essential components at the cell surface and in the cytosol utilizing processes like autophagy and the MVB pathway [64,190,285]. These responses are largely controlled by the TORC1 signaling complex, whose inhibition by nutrient starvation or rapamycin treatment triggers the endocytic degradation of most cell surface proteins, with some high-affinity transporters like the general amino acid permease Gap1 being maintained at the plasma membrane to scavenge for whatever extra-cellular nutrients may still be available [84,285]. Prolonged exposure to such conditions further triggers cells to exit the cell cycle and enter a state of quiescence, where cell growth and division is halted, and catabolic processes are widely downregulated [104,436,438]. The nutrient supply provided combined efforts of autophagy and the endocytic trafficking of the MVB pathway is required for cells to survive these periods of nutrient limitation, as both the MVB-defective *vps4*Δ and autophagy-deficient *atg8*Δ backgrounds lack the ability to resume proliferation once returned to nutrient-rich conditions [285]. In the experiments described below, we find that 9arrΔ cells to be even more

sensitive to prolonged periods of nitrogen starvation than what has been reported for cells lacking *VPS4* or *ATG8*, suggesting this family of protein trafficking adapters possess an as-yet underappreciated role in the ability of cells to properly respond to such stress conditions.

Appendix C.2 Materials and methods

The ability of cells to resume proliferation after periods of nitrogen starvation was assessed by serial dilution growth assays similar to that described in [285]. In short, cell cultures were grown overnight in SC complete liquid media at 30˚C. These cultures were used in serial dilution growth assays (0 days starvation) where, starting with an OD_{600} of 1.0 (approximately 1.0 x 10^7 cells/ml), 5-fold serial dilutions were generated and transferred to solid SC complete solid media using a sterile replica-pinning tool. These cells were grown at 30°C for 1-2 days and images captured using a Chemidoc XRS+ imager (BioRad, Hercules, CA). Cells from these same cultures were reinoculated at low density (OD_{600}=1.0) in SD liquid media lacking the amino acids and ammonium sulfate and incubated at 30˚C for 1-13 days. Portions of these cultures were removed periodically (times indicated in Figure 34) and subjected to the same serial dilution growth assays described above.

Table 8. Strains used in Appendix C

Strain	Genotype	Source
BY4741	*MAT* **a** *his3Δ1 leu2Δ0 ura3Δ0 met15Δ0*	[311]
*aly1*Δ *aly2*Δ (aka D2-6a)	*MAT* **a** *aly1Δ::KanMX aly2Δ::KanMX his3Δ1 leu2Δ0 ura3Δ0 met15Δ0 lys2Δ0*	[67]
*9Arr*Δ (EN60)	*MAT* **a** *ecm21Δ::KanMX csr2Δ::KanMX bsd2Δ rog3Δ::NatMX rod1Δ ygr068cΔ aly1Δ aly2Δ ldb19Δ ylr392cΔ::HIS3 his3Δ0 ura3Δ0 leu2Δ0*	[59]
*art1*Δ	*MAT* **a** *art1Δ::KanMX his3Δ1 leu2Δ0 ura3Δ0 met15Δ0*	[311]
*vps4*Δ	*MAT* **a** *vps4Δ::KanMX his3Δ1 leu2Δ0 ura3Δ0 met15Δ0*	[311]
*vrp1*Δ	*MAT* **a** *vrp1Δ::KanMX his3Δ1 leu2Δ0 ura3Δ0 met15Δ0*	[311]
*atg1*Δ	*MAT* **a** *atg1Δ::KanMX his3Δ1 leu2Δ0 ura3Δ0 met15Δ0*	[311]
*atg8*Δ	*MAT* **a** *atg8Δ::KanMX his3Δ1 leu2Δ0 ura3Δ0 met15Δ0*	[311]

Appendix C.3 Results and discussion

As described above, cells rely upon the cooperative efforts of the MVB pathway and autophagy to survive prolonged periods of nutrient starvation by degrading much of the cell-surface proteome and non-selective portions of the cytosol, while increasing the abundance of high-affinity nutrient transporters like Gap1 at the plasma membrane [285]. These collective efforts provide a pool of nutrients that allow for cell survival and the resumption of cell growth when returned to nutrient-replete conditions. As the α-arrestins mediate the trafficking of many cell-surface nutrient transporters, including Gap1, and are required for the efficient action of autophagy, we assessed the ability of α-arrestin mutants to resume proliferation after exposure to varying periods of nitrogen starvation (Figure 41) [58,59,67,77,285]. We found that, prior to exposure to media lacking sources of nitrogen, α-arrestin mutants *aly1*Δ *aly2*Δ*, aly1*Δ *aly2*Δ *art5*Δ *ldb19*Δ (4ArrΔ), and 9arrΔ grew similarly to WT cells after both 1 and 2 days of growth on SC complete media (Figure 41). While cells lacking proper function of the MVB pathway (*vps4*Δ), autophagy (*atg8*Δ), or both (*vrp1*Δ) showed a reduced rate of growth after 1 day on SC complete media, each strain exhibited similar degrees of growth after 2 days on the same media (Figure 41)

[166,439,440]. Notably, after only 2 days in media lacking nitrogen, 9arrΔ displayed a severe impairment in their ability to resume proliferation compared to the WT control, similar what we observed in *vrp1*Δ cells (Figure 41). While 4ArrΔ cells displayed a modest reduction in growth after this period of starvation when returned to rich media for 1 day, *aly1*Δ *aly2*Δ cells behaved similar to the WT control, and both appeared to grow normally after 2 days on rich media (Figure 41). As expected, MVB- and/or autophagy-defective mutants each displayed increasingly impaired growth after 4, 7, and 13 days of nitrogen starvation, respectively (Figure 41) [285]. To our surprise, however, 9arrΔ cells were even more severely impaired, displaying a nearly complete lack of ability to resume proliferation on rich media after 7 days of starvation (Figure 41). While the most obvious cause of this effect can be attributed to the impaired endocytic trafficking of nutrient transporters in this α-arrestin mutant, the increased sensitivity to nitrogen starvation displayed compared to the MVB-defective *vps4*Δ further implicates the role of α-arrestins in supporting efficient autophagy (Chapter 2). Furthermore, 9arrΔ are also more sensitive to this stress condition than cells lacking *VRP1*, which is required for the fusion of both MVBs and APs to the vacuole, raising the additional possibility that the absence of multiple α-arrestins is having a further detrimental effect, potentially on cell cycle regulation [439]. It remains unclear, however, which α-arrestins are responsible for this effect, as both *aly1*Δ *aly2*Δ and 4arrΔ cells behaved similar to the WT control at all periods of nitrogen starvation assessed (Figure 41).

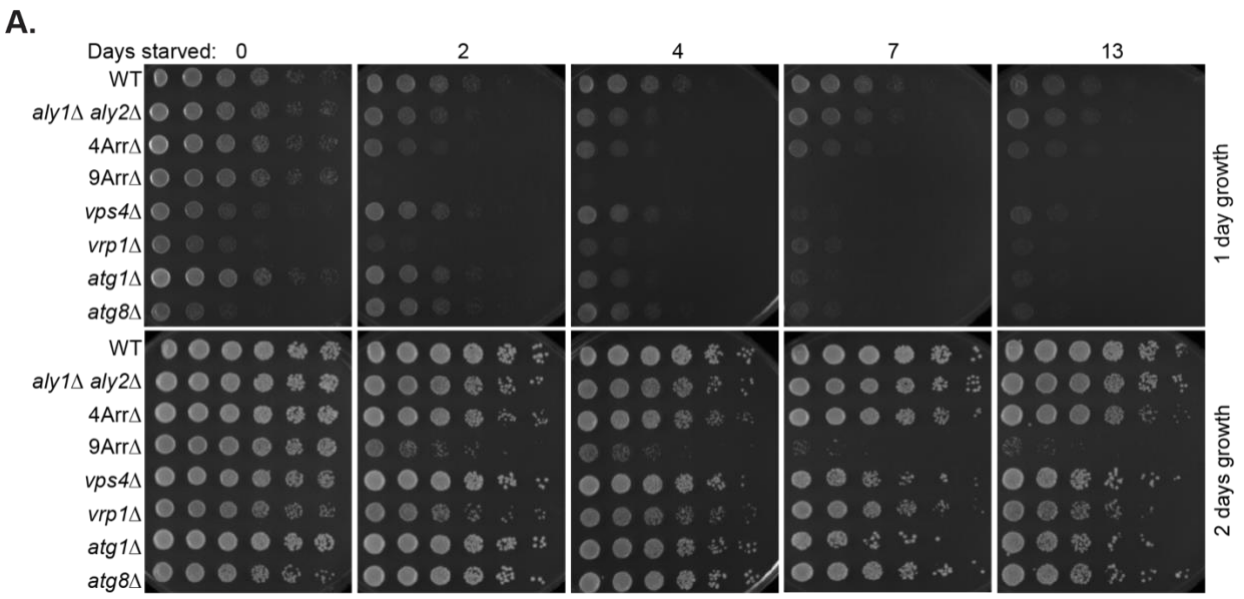

Figure 41. α-Arrestins are required for the the resumption of proliferation following nitrogen starvation.

(**A**) Serial dilution growth assays of WT and the indicated mutant cells (left) on SC complete media after 1 (top) or 2 (bottom) days of growth at 30˚C following the indicated periods of exposure to media lacking amino acids and ammonium sulfate.

Bibliography

1. Duina AA, Miller ME, Keeney JB. Budding yeast for budding geneticists: A primer on the Saccharomyces cerevisiae model system. Genetics. 2014;197. doi:10.1534/genetics.114.163188
2. Karathia H, Vilaprinyo E, Sorribas A, Alves R. Saccharomyces cerevisiae as a model organism: A comparative study. PLoS One. 2011;6. doi:10.1371/journal.pone.0016015
3. Botstein D, Chervitz SA, Cherry JM. Yeast as a model organism. Science. 1997. doi:10.1126/science.277.5330.1259
4. Schekman R. The secretory pathway in yeast. Trends Biochem Sci. 1982;7: 243–246. doi:10.1016/0968-0004(82)90034-2
5. Barlowe C, Orci L, Yeung T, Hosobuchi M, Hamamoto S, Salama N, et al. COPII: A membrane coat formed by Sec proteins that drive vesicle budding from the endoplasmic reticulum. Cell. 1994;77. doi:10.1016/0092-8674(94)90138-4
6. Novick P, Field C, Schekman R. Identification of 23 complementation groups required for post-translational events in the yeast secretory pathway. Cell. 1980;21. doi:10.1016/0092-8674(80)90128-2
7. Zierath JR, Lendahl U. Scientific Background: Machinery Regulating Vesicle Traffic, A Major Transport System in our Cells. Nobelförsamlingen The Nobel Assembly at Karolinska Institutet. 2013;14.
8. Muñiz M, Zurzolo C. Sorting of GPI-anchored proteins from yeast to mammals - Common pathways at different sites? Journal of Cell Science. 2014. doi:10.1242/jcs.148056

9. Dancourt J, Barlowe C. Protein sorting receptors in the early secretory pathway. Annual Review of Biochemistry. 2010. doi:10.1146/annurev-biochem-061608-091319

10. Conibear E. Converging views of endocytosis in yeast and mammals. Current Opinion in Cell Biology. 2010. doi:10.1016/j.ceb.2010.05.009

11. Bard F, Malhotra V. The formation of TGN-to-plasma-membrane transport carriers. Annual Review of Cell and Developmental Biology. 2006. doi:10.1146/annurev.cellbio.21.012704.133126

12. Bockaert J, Pin JP. Molecular tinkering of G protein-coupled receptors: An evolutionary success. EMBO Journal. 1999. doi:10.1093/emboj/18.7.1723

13. Wilden U, Hall SW, Kuhn H. Phosphodiesterase activation by photoexcited rhodopsin is quenched when rhodopsin is phosphorylated and binds the intrinsic 48-kDa protein of rod outer segments. Proc Natl Acad Sci U S A. 1986;83. doi:10.1073/pnas.83.5.1174

14. Alvarez CE. On the origins of arrestin and rhodopsin. BMC Evol Biol. 2008;8. doi:10.1186/1471-2148-8-222

15. Kim YM, Benovic JL. Differential roles of arrestin-2 interaction with clathrin and adaptor protein 2 in G protein-coupled receptor trafficking. Journal of Biological Chemistry. 2002;277. doi:10.1074/jbc.M204528200

16. Luttrell LM, Gesty-Palmer D. Beyond desensitization: Physiological relevance of arrestin-dependent signaling. Pharmacological Reviews. 2010. doi:10.1124/pr.109.002436

17. Smith JS, Rajagopal S. The β-Arrestins: Multifunctional regulators of G protein-coupled receptors. Journal of Biological Chemistry. 2016;291. doi:10.1074/jbc.R115.713313

18. Bouvier M, Hausdorff WP, de Blasi A, O'Dowd BF, Kobilka BK, Caron MG, et al. Removal of phosphorylation sites from the β2-adrenergic receptor delays onset of agonist-promoted desensitization. Nature. 1988;333. doi:10.1038/333370a0

19. Benovic JL, Kühn H, Weyand I, Codina J, Caron MG, Lefkowitz RJ. Functional desensitization of the isolated beta-adrenergic receptor by the beta-adrenergic receptor kinase: potential role of an analog of the retinal protein arrestin (48-kDa protein). Proc Natl Acad Sci U S A. 1987;84. doi:10.1073/pnas.84.24.8879

20. Wilden U, Wüst E, Weyand I, Kühn H. Rapid affinity purification of retinal arrestin (48 kDa protein) via its light-dependent binding to phosphorylated rhodopsin. FEBS Lett. 1986;207. doi:10.1016/0014-5793(86)81507-1

21. Degraff JL, Gurevich V., Benovic JL. The third intracellular loop of α2-adrenergic receptors determines subtype specificity of arrestin interaction. Journal of Biological Chemistry. 2002;277. doi:10.1074/jbc.M207495200

22. Marion S, Oakley RH, Kim KM, Caron MG, Barak LS. A β-arrestin binding determinant common to the second intracellular loops of rhodopsin family G protein-coupled receptors. Journal of Biological Chemistry. 2006;281. doi:10.1074/jbc.M508074200

23. Ferguson SSG, Downey WE, Colapietro AM, Barak LS, Ménard L, Caron MG. Role of β-arrestin in mediating agonist-promoted G protein-coupled receptor internalization. Science (1979). 1996;271. doi:10.1126/science.271.5247.363

24. Lee KB, Pals-Rylaarsdam R, Benovic JL, Hosey MM. Arrestin-independent internalization of the m1, m3, and m4 subtypes of muscarinic cholinergic receptors. Journal of Biological Chemistry. 1998;273. doi:10.1074/jbc.273.21.12967

25. Snyder JC, Rochelle LK, Lyerly HK, Caron MG, Barak LS. Constitutive internalization of the Leucine-rich g protein-coupled receptor-5 (LGR5) to the trans-Golgi network. Journal of Biological Chemistry. 2013;288. doi:10.1074/jbc.M112.447540

26. Tian X, Kang DS, Benovic JL. β-Arrestins and G protein-coupled receptor trafficking. Handbook of Experimental Pharmacology. 2014. doi:10.1007/978-3-642-41199-1_9

27. Vines CM, Revankar CM, Maestas DC, LaRusch LL, Cimino DF, Kohout TA, et al. N-Formyl Peptide Receptors Internalize but Do Not Recycle in the Absence of Arrestins. Journal of Biological Chemistry. 2003;278. doi:10.1074/jbc.C300291200

28. Shukla AK, Kim J, Ahn S, Xiao K, Shenoy SK, Liedtke W, et al. Arresting a transient receptor potential (TRP) channel: β-arrestin 1 mediates ubiquitination and functional down-regulation of TRPV4. Journal of Biological Chemistry. 2010;285. doi:10.1074/jbc.M110.141549

29. Simonin A, Fuster D. Nedd4-1 and β-arrestin-1 are key regulators of Na+/H + exchanger 1 ubiquitylation, endocytosis, and function. Journal of Biological Chemistry. 2010;285. doi:10.1074/jbc.M110.115089

30. Shi H, Rojas R, Bonifacino JS, Hurley JH. The retromer subunit Vps26 has an arrestin fold and binds Vps35 through its C-terminal domain. Nat Struct Mol Biol. 2006;13. doi:10.1038/nsmb1103

31. Granzin J, Cousin A, Weirauch M, Schlesinger R, Büldt G, Batra-Safferling R. Crystal structure of p44, a constitutively active splice variant of visual arrestin. J Mol Biol. 2012;416. doi:10.1016/j.jmb.2012.01.028

32. Han M, Gurevich V v., Vishnivetskiy SA, Sigler PB, Schubert C. Crystal structure of β-arrestin at 1.9 Å: Possible mechanism of receptor binding and membrane translocation. Structure. 2001;9. doi:10.1016/S0969-2126(01)00644-X

33. Hwang J, Suh HW, Jeon YH o., Hwang E, Nguyen LT, Yeom J, et al. The structural basis for the negative regulation of thioredoxin by thioredoxin-interacting protein. Nat Commun. 2014;5. doi:10.1038/ncomms3958

34. Aubry L, Klein G. True arrestins and arrestin-fold proteins: A structure-based appraisal. Progress in Molecular Biology and Translational Science. 2013. doi:10.1016/B978-0-12-394440-5.00002-4

35. Aubry L, Guetta D, Klein G. The Arrestin Fold: Variations on a Theme. Curr Genomics. 2009;10. doi:10.2174/138920209787847014

36. Staub O, Dho S, Henry PC, Correa J, Ishikawa T, McGlade J, et al. WW domains of Nedd4 bind to the proline-rich PY motifs in the epithelial Na+ channel deleted in Liddle's syndrome. EMBO Journal. 1996;15. doi:10.1002/j.1460-2075.1996.tb00593.x

37. Belgareh-Touzé N, Léon S, Erpapazoglou Z, Stawiecka-Mirota M, Urban-Grimal D, Haguenauer-Tsapis R. Versatile role of the yeast ubiquitin ligase Rsp5p in intracellular trafficking. Biochemical Society Transactions. 2008. doi:10.1042/BST0360791

38. Jumper J, Evans R, Pritzel A, Green T, Figurnov M, Ronneberger O, et al. Highly accurate protein structure prediction with AlphaFold. Nature. 2021;596. doi:10.1038/s41586-021-03819-2

39. Dores MR, Lin H, Grimsey NJ, Mendez F, Trejo J. The α-Arrestin ARRDC3 mediates ALIX ubiquitination and G protein-coupled receptor lysosomal sorting. Mol Biol Cell. 2015;26. doi:10.1091/mbc.E15-05-0284

40. Wu N, Zheng B, Shaywitz A, Dagon Y, Tower C, Bellinger G, et al. AMPK-Dependent Degradation of TXNIP upon Energy Stress Leads to Enhanced Glucose Uptake via GLUT1. Mol Cell. 2013;49. doi:10.1016/j.molcel.2013.01.035

41. Shea FF, Rowell JL, Li Y, Chang TH, Alvarez CE, Means RE. Mammalian Alpha Arrestins Link Activated Seven Transmembrane Receptors to Nedd4 Family E3 Ubiquitin Ligases and Interact with Beta Arrestins. PLoS One. 2012;7. doi:10.1371/journal.pone.0050557

42. Waldhart AN, Dykstra H, Peck AS, Boguslawski EA, Madaj ZB, Wen J, et al. Phosphorylation of TXNIP by AKT Mediates Acute Influx of Glucose in Response to Insulin. Cell Rep. 2017;19. doi:10.1016/j.celrep.2017.05.041

43. Parikh H, Carlsson E, Chutkow WA, Johansson LE, Storgaard H, Poulsen P, et al. TXNIP regulates peripheral glucose metabolism in humans. PLoS Med. 2007;4. doi:10.1371/journal.pmed.0040158

44. Patwari P, Emilsson V, Schadt EE, Chutkow WA, Lee S, Marsili A, et al. The arrestin domain-containing 3 protein regulates body mass and energy expenditure. Cell Metab. 2011;14. doi:10.1016/j.cmet.2011.08.011

45. Anand S, Foot N, Ang CS, Gembus KM, Keerthikumar S, Adda CG, et al. Arrestin-Domain Containing Protein 1 (Arrdc1) Regulates the Protein Cargo and Release of Extracellular Vesicles. Proteomics. 2018;18. doi:10.1002/pmic.201800266

46. Nabhan JF, Hu R, Oh RS, Cohen SN, Lu Q. Formation and release of arrestin domain-containing protein 1-mediated microvesicles (ARMMs) at plasma membrane by recruitment of TSG101 protein. Proc Natl Acad Sci U S A. 2012;109. doi:10.1073/pnas.1200448109

47. Mackenzie KD, Foot NJ, Anand S, Dalton HE, Chaudhary N, Collins BM, et al. Regulation of the divalent metal ion transporter via membrane budding. Cell Discov. 2016;2. doi:10.1038/celldisc.2016.11

48. Foot NJ, Gonzalez MB, Gembus K, Fonseka P, Sandow JJ, Nguyen TT, et al. Arrdc4-dependent extracellular vesicle biogenesis is required for sperm maturation. J Extracell Vesicles. 2021;10. doi:10.1002/jev2.12113

49. Chen Y, Ning J, Cao W, Wang S, Du T, Jiang J, et al. Research Progress of TXNIP as a Tumor Suppressor Gene Participating in the Metabolic Reprogramming and Oxidative Stress of Cancer Cells in Various Cancers. Frontiers in Oncology. 2020. doi:10.3389/fonc.2020.568574

50. Soung YH, Ford S, Yan C, Chung J. The role of arrestin domain-containing 3 in regulating endocytic recycling and extracellular vesicle sorting of integrin β4 in breast cancer. Cancers (Basel). 2018;10. doi:10.3390/cancers10120507

51. Hoshino A, Costa-Silva B, Shen TL, Rodrigues G, Hashimoto A, Tesic Mark M, et al. Tumour exosome integrins determine organotropic metastasis. Nature. 2015;527. doi:10.1038/nature15756

52. Draheim KM, Chen HB, Tao Q, Moore N, Roche M, Lyle S. ARRDC3 suppresses breast cancer progression by negatively regulating integrin B4. Oncogene. 2010;29. doi:10.1038/onc.2010.250

53. Oka SI, Masutani H, Liu W, Horita H, Wang D, Kizaka-Kondoh S, et al. Thioredoxin-binding protein-2-like inducible membrane protein is a novel vitamin D3 and peroxisome proliferator-activated receptor (PPAR)γ ligand target protein that regulates PPARγ signaling. Endocrinology. 2006;147. doi:10.1210/en.2005-0679

54. Arakaki AK, Pan W, Trejo J. The α-Arrestin ARRDC3 Suppresses Breast Carcinoma Invasion by Regulating GPCR Lysosomal Sorting and Signaling. The FASEB Journal. 2018;32. doi:10.1096/fasebj.2018.32.1_supplement.695.13

55. Arakaki AKS, Pan WA, Wedegaertner H, Roca-Mercado I, Chinn L, Gujral TS, et al. α-Arrestin ARRDC3 tumor suppressor function is linked to GPCR-induced TAZ activation and breast cancer metastasis. J Cell Sci. 2021;134. doi:10.1242/jcs.254888

56. Chen J, Saxena G, Mungrue IN, Lusis AJ, Shalev A. Thioredoxin-interacting protein A critical link between glucose toxicity and β-cell apoptosis. Diabetes. 2008;57. doi:10.2337/db07-0715

57. Saxena G, Chen J, Shalev A. Intracellular shuttling and mitochondrial function of thioredoxin- interacting protein. Journal of Biological Chemistry. 2010;285. doi:10.1074/jbc.M109.034421

58. Lin CH, MacGurn JA, Chu T, Stefan CJ, Emr SD. Arrestin-Related Ubiquitin-Ligase Adaptors Regulate Endocytosis and Protein Turnover at the Cell Surface. Cell. 2008;135. doi:10.1016/j.cell.2008.09.025

59. Nikko E, Pelham HRB. Arrestin-mediated endocytosis of yeast plasma membrane transporters. Traffic. 2009;10. doi:10.1111/j.1600-0854.2009.00990.x

60. Novoselova T v., Zahira K, Rose RS, Sullivan JA. Bul proteins, a nonredundant, antagonistic family of ubiquitin ligase regulatory proteins. Eukaryot Cell. 2012;11. doi:10.1128/EC.00009-12

61. Ghaddar K, Merhi A, Saliba E, Krammer E-M, Prévost M, André B. Substrate-Induced Ubiquitylation and Endocytosis of Yeast Amino Acid Permeases. Mol Cell Biol. 2014;34. doi:10.1128/mcb.00699-14

62. Alvaro CG, O'Donnell AF, Prosser DC, Augustine AA, Goldman A, Brodsky JL, et al. Specific α-Arrestins Negatively Regulate Saccharomyces cerevisiae Pheromone Response by Down-Modulating the G-Protein-Coupled Receptor Ste2. Mol Cell Biol. 2014;34. doi:10.1128/mcb.00230-14

63. Zhao Y, MacGurn JA, Liu M, Emr S. The ART-Rsp5 ubiquitin ligase network comprises a plasma membrane quality control system that protects yeast cells from proteotoxic stress. Elife. 2013;2013. doi:10.7554/eLife.00459

64. Jones CB, Ott EM, Keener JM, Curtiss M, Sandrin V, Babst M. Regulation of Membrane Protein Degradation by Starvation-Response Pathways. Traffic. 2012;13. doi:10.1111/j.1600-0854.2011.01314.x

65. Baile MG, Guiney EL, Sanford EJ, MacGurn JA, Smolka MB, Emra SD. Activity of a ubiquitin ligase adaptor is regulated by disordered insertions in its arrestin domain. Mol Biol Cell. 2019;30. doi:10.1091/MBC.E19-08-0451

66. MacGurn JA, Hsu PC, Smolka MB, Emr SD. TORC1 regulates endocytosis via npr1-mediated phosphoinhibition of a ubiquitin ligase adaptor. Cell. 2011;147. doi:10.1016/j.cell.2011.09.054

67. O'Donnell AF, Apffel A, Gardner RG, Cyert MS. α-arrestins Aly1 and Aly2 regulate intracellular trafficking in response to nutrient signaling. Mol Biol Cell. 2010;21. doi:10.1091/mbc.E10-07-0636

68. O'Donnell AF, Huang L, Thorner J, Cyert MS. A calcineurin-dependent switch controls the trafficking function of α-arrestin Aly1/Art6. Journal of Biological Chemistry. 2013;288. doi:10.1074/jbc.M113.478511

69. Khanday FA, Saha M, Bhat PJ. Molecular characterization of MRG19 of Saccharomyces cerevisiae: Implication in the regulation of galactose and nonfermentable carbon source utilization. Eur J Biochem. 2002;269. doi:10.1046/j.1432-1033.2002.03303.x

70. Herrador A, Herranz S, Lara D, Vincent O. Recruitment of the ESCRT Machinery to a Putative Seven-Transmembrane-Domain Receptor Is Mediated by an Arrestin-Related Protein. Mol Cell Biol. 2010;30. doi:10.1128/mcb.00132-09

71. Frattini C, Villa-Hernández S, Pellicanò G, Jossen R, Katou Y, Shirahige K, et al. Cohesin Ubiquitylation and Mobilization Facilitate Stalled Replication Fork Dynamics. Mol Cell. 2017;68. doi:10.1016/j.molcel.2017.10.012

72. Bilsland E, Hult M, Bell SD, Sunnerhagen P, Downs JA. The Bre5/Ubp3 ubiquitin protease complex from budding yeast contributes to the cellular response to DNA damage. DNA Repair (Amst). 2007;6. doi:10.1016/j.dnarep.2007.04.010

73. Ivashov V, Zimmer J, Schwabl S, Kahlhofer J, Weys S, Gstir R, et al. Complementary a-arrestin-ubiquitin ligase complexes control nutrient transporter endocytosis in response to amino acids. Elife. 2020;9. doi:10.7554/ELIFE.58246

74. Hovsepian J, Defenouillère Q, Albanèse V, Váchová L, Garcia C, Palková Z, et al. Multilevel regulation of an α-arrestin by glucose depletion controls hexose transporter endocytosis. Journal of Cell Biology. 2017;216. doi:10.1083/jcb.201610094

75. Bendrioua L, Smedh M, Almquist J, Cvijovic M, Jirstrand M, Goksör M, et al. Yeast AMP-activated protein kinase monitors glucose concentration changes and absolute glucose levels. Journal of Biological Chemistry. 2014;289. doi:10.1074/jbc.M114.547976

76. Becuwe M, Vieira N, Lara D, Gomes-Rezende J, Soares-Cunha C, Casal M, et al. A molecular switch on an arrestin-like protein relays glucose signaling to transporter endocytosis. Journal of Cell Biology. 2012;196. doi:10.1083/jcb.201109113

77. Merhi A, André B. Internal Amino Acids Promote Gap1 Permease Ubiquitylation via TORC1/Npr1/14-3-3-Dependent Control of the Bul Arrestin-Like Adaptors. Mol Cell Biol. 2012;32. doi:10.1128/mcb.00463-12

78. Hatakeyama R, Kamiya M, Takahara T, Maeda T. Endocytosis of the Aspartic Acid/Glutamic Acid Transporter Dip5 Is Triggered by Substrate-Dependent Recruitment of the Rsp5 Ubiquitin Ligase via the Arrestin-Like Protein Aly2. Mol Cell Biol. 2010;30. doi:10.1128/mcb.00464-10

79. Prosser DC, Pannunzio AE, Brodsky JL, Thorner J, Wendland B, O'Donnell AF. α-Arrestins participate in cargo selection for both clathrin-independentand clathrin-mediated endocytosis. J Cell Sci. 2015;128. doi:10.1242/jcs.175372

80. Prosser DC, Drivas TG, Maldonado-Báez L, Wendland B. Existence of a novel clathrin-independent endocytic pathway in yeast that depends on Rho1 and formin. Journal of Cell Biology. 2011;195. doi:10.1083/jcb.201104045

81. Levin DE. Cell Wall Integrity Signaling in Saccharomyces cerevisiae . Microbiology and Molecular Biology Reviews. 2005;69. doi:10.1128/mmbr.69.2.262-291.2005

82. Ozaki K, Tanaka K, Imamura H, Hihara T, Kameyama T, Nonaka H, et al. Rom1p and Rom2p are GDP/GTP exchange proteins (GEPs) for the Rho1p small GTP binding protein in Saccharomyces cerevisiae. EMBO Journal. 1996;15. doi:10.1002/j.1460-2075.1996.tb00573.x

83. Villers J, Savocco J, Szopinska A, Degand H, Nootens S, Morsomme P. Study of the plasma membrane proteome dynamics reveals novel targets of the nitrogen regulation in yeast. Molecular and Cellular Proteomics. 2017;16. doi:10.1074/mcp.M116.064923

84. Iesmantavicius V, Weinert BT, Choudhary C. Convergence of ubiquitylation and phosphorylation signaling in rapamycin-treated yeast cells. Molecular and Cellular Proteomics. 2014;13. doi:10.1074/mcp.O113.035683

85. Gupta R, Kus B, Fladd C, Wasmuth J, Tonikian R, Sidhu S, et al. Ubiquitination screen using protein microarrays for comprehensive identification of Rsp5 substrates in yeast. Mol Syst Biol. 2007;3. doi:10.1038/msb4100159

86. Swaney DL, Beltrao P, Starita L, Guo A, Rush J, Fields S, et al. Global analysis of phosphorylation and ubiquitylation cross-talk in protein degradation. Nat Methods. 2013;10. doi:10.1038/nmeth.2519

87. Soetens O, de Craene JO, André B. Ubiquitin Is Required for Sorting to the Vacuole of the Yeast General Amino Acid Permease, Gap1. Journal of Biological Chemistry. 2001;276. doi:10.1074/jbc.M102945200

88. de Craene JO, Soetens O, André B. The Npr1 Kinase Controls Biosynthetic and Endocytic Sorting of the Yeast Gap1 Permease. Journal of Biological Chemistry. 2001;276. doi:10.1074/jbc.M102944200

89. Becuwe M, Léon S. Integrated control of transporter endocytosis and recycling by the arrestin-related protein Rod1 and the ubiquitin ligase Rsp5. Elife. 2014;3. doi:10.7554/eLife.03307

90. O'Donnell AF, McCartney RR, Chandrashekarappa DG, Zhang BB, Thorner J, Schmidt MC. 2-Deoxyglucose Impairs Saccharomyces cerevisiae Growth by Stimulating Snf1-

Regulated and α-Arrestin-Mediated Trafficking of Hexose Transporters 1 and 3. Mol Cell Biol. 2015;35. doi:10.1128/mcb.01183-14

91. Robinson BP, Hawbaker S, Chiang A, Jordahl EM, Anaokar S, Nikiforov A, et al. Alpha-arrestins Aly1/Art6 and Aly2/Art3 regulate trafficking of the glycerophosphoinositol transporter Git1 and impact phospholipid homeostasis. Biol Cell. 2022;114. doi:10.1111/boc.202100007

92. Nikko E, Sullivan JA, Pelham HRB. Arrestin-like proteins mediate ubiquitination and endocytosis of the yeast metal transporter Smf1. EMBO Rep. 2008;9. doi:10.1038/embor.2008.199

93. Savocco J, Nootens S, Afokpa W, Bausart M, Chen X, Villers J, et al. Yeast α-arrestin Art2 is the key regulator of ubiquitylation-dependent endocytosis of plasma membrane vitamin B1 transporters. PLoS Biol. 2019;17. doi:10.1371/journal.pbio.3000512

94. Crapeau M, Merhi A, André B. Stress conditions promote yeast Gap1 permease ubiquitylation and down-regulation via the arrestin-like bul and aly proteins. Journal of Biological Chemistry. 2014;289. doi:10.1074/jbc.M114.582320

95. Sen A, Hsieh WC, Hanna CB, Hsu CC, Pearson M, Tao WA, et al. The Na+ pump Ena1 is a yeast epsin-specific cargo requiring its ubiquitylation and phosphorylation sites for internalization. J Cell Sci. 2020;133. doi:10.1242/jcs.245415

96. Wawrzycka D, Sadlak J, Maciaszczyk-Dziubinska E, Wysocki R. Rsp5-dependent endocytosis and degradation of the arsenite transporter Acr3 requires its N-terminal acidic tail as an endocytic sorting signal and arrestin-related ubiquitin-ligase adaptors. Biochim Biophys Acta Biomembr. 2019;1861. doi:10.1016/j.bbamem.2019.02.004

97. Suzuki A, Mochizuki T, Uemura S, Hiraki T, Abe F. Pressure-induced endocytic degradation of the Saccharomyces cerevisiae low-affinity tryptophan permease Tat1 is mediated by Rsp5 ubiquitin ligase and functionally redundant PPxy motif proteins. Eukaryot Cell. 2013;12. doi:10.1128/EC.00049-13

98. Gournas C, Saliba E, Krammer EM, Barthelemy C, Prévost M, André B. Transition of yeast Can1 transporter to the inward-facing state unveils an α-arrestin target sequence promoting its ubiquitylation and endocytosis. Mol Biol Cell. 2017;28. doi:10.1091/mbc.E17-02-0104

99. Guiney EL, Klecker T, Emr SD. Identification of the endocytic sorting signal recognized by the Art1-Rsp5 ubiquitin ligase complex. Mol Biol Cell. 2016;27. doi:10.1091/mbc.E16-08-0570

100. Keener JM, Babst M. Quality Control and Substrate-Dependent Downregulation of the Nutrient Transporter Fur4. Traffic. 2013;14. doi:10.1111/tra.12039

101. Gournas C, Gkionis S, Carquin M, Twyffels L, Tyteca D, André B. Conformation-dependent partitioning of yeast nutrient transporters into starvation-protective membrane domains. Proc Natl Acad Sci U S A. 2018;115. doi:10.1073/pnas.1719462115

102. Busto J v, Elting A, Haase D, Spira F, Kuhlman J, Schäfer-Herte M, et al. Lateral plasma membrane compartmentalization links protein function and turnover. EMBO J. 2018;37. doi:10.15252/embj.201899473

103. Fujita S, Sato D, Kasai H, Ohashi M, Tsukue S, Takekoshi Y, et al. The C-terminal region of the yeast monocarboxylate transporter Jen1 acts as a glucose signal–responding degron recognized by the α-arrestin Rod1. Journal of Biological Chemistry. 2018;293. doi:10.1074/jbc.RA117.001062

104. Dokládal L, Stumpe M, Hu Z, Jaquenoud M, Dengjel J, de Virgilio C. Phosphoproteomic responses of TORC1 target kinases reveal discrete and convergent mechanisms that orchestrate the quiescence program in yeast. Cell Rep. 2021;37. doi:10.1016/j.celrep.2021.110149

105. Braten O, Livneh I, Ziv T, Admon A, Kehat I, Caspi LH, et al. Numerous proteins with unique characteristics are degraded by the 26S proteasome following monoubiquitination. Proc Natl Acad Sci U S A. 2016;113. doi:10.1073/pnas.1608644113

106. Touati SA, Kataria M, Jones AW, Snijders AP, Uhlmann F. Phosphoproteome dynamics during mitotic exit in budding yeast. EMBO J. 2018;37. doi:10.15252/embj.201798745

107. Soulard A, Cremonesi A, Moes S, Schütz F, Jenö P, Hall MN. The rapamycin-sensitive phosphoproteome reveals that TOR controls protein kinase A toward some but not all substrates. Mol Biol Cell. 2010;21. doi:10.1091/mbc.E10-03-0182

108. Soufi B, Kelstrup CD, Stoehr G, Fröhlich F, Walther TC, Olsen J v. Global analysis of the yeast osmotic stress response by quantitative proteomics. Mol Biosyst. 2009;5. doi:10.1039/b902256b

109. Shively CA, Kweon HK, Norman KL, Mellacheruvu D, Xu T, Sheidy DT, et al. Large-Scale Analysis of Kinase Signaling in Yeast Pseudohyphal Development Identifies Regulation of Ribonucleoprotein Granules. PLoS Genet. 2015;11. doi:10.1371/journal.pgen.1005564

110. Saleem RA, Rogers RS, Ratushny A v., Dilworth DJ, Shannon PT, Shteynberg D, et al. Integrated phosphoproteomics analysis of a signaling network governing nutrient response and peroxisome induction. Molecular and Cellular Proteomics. 2010;9. doi:10.1074/mcp.M000116-MCP201

111. Romanov N, Hollenstein DM, Janschitz M, Ammerer G, Anrather D, Reiter W. Identifying protein kinase-specific effectors of the osmostress response in yeast. Sci Signal. 2017;10. doi:10.1126/scisignal.aag2435

112. Vlastaridis P, Papakyriakou A, Chaliotis A, Stratikos E, Oliver SG, Amoutzias GD. The pivotal role of protein phosphorylation in the control of yeast central metabolism. G3: Genes, Genomes, Genetics. 2017;7. doi:10.1534/g3.116.037218

113. Olson DK, Fröhlich F, Christiano R, Hannibal-Bach HK, Ejsing CS, Walther TC. Rom2-dependent phosphorylation of Elo2 controls the abundance of very long-chain fatty acids. Journal of Biological Chemistry. 2015;290. doi:10.1074/jbc.M114.629279

114. Oliveira AP, Ludwig C, Zampieri M, Weisser H, Aebersold R, Sauer U. Dynamic phosphoproteomics reveals TORC1-dependent regulation of yeast nucleotide and amino acid biosynthesis. Sci Signal. 2015;8. doi:10.1126/scisignal.2005768

115. Lebesgue N, Megyeri M, Cristobal A, Scholten A, Chuartzman SG, Voichek Y, et al. Combining Deep Sequencing, Proteomics, Phosphoproteomics, and Functional Screens to Discover Novel Regulators of Sphingolipid Homeostasis. J Proteome Res. 2017;16. doi:10.1021/acs.jproteome.6b00691

116. Kanshin E, Kubiniok P, Thattikota Y, D'Amours D, Thibault P. Phosphoproteome dynamics of Saccharomyces cerevisiae under heat shock and cold stress . Mol Syst Biol. 2015;11. doi:10.15252/msb.20156170

117. Kanshin E, Bergeron-Sandoval LP, Isik SS, Thibault P, Michnick SW. A Cell-Signaling Network Temporally Resolves Specific versus Promiscuous Phosphorylation. Cell Rep. 2015;10. doi:10.1016/j.celrep.2015.01.052

118. Huber A, Bodenmiller B, Uotila A, Stahl M, Wanka S, Gerrits B, et al. Characterization of the rapamycin-sensitive phosphoproteome reveals that Sch9 is a central coordinator of protein synthesis. Genes Dev. 2009;23. doi:10.1101/gad.532109

119. Holt LJ, Tuch BB, Villen J, Johnson AD, Gygi SP, Morgan DO. Global analysis of cdk1 substrate phosphorylation sites provides insiqhts into evolution. Science (1979). 2009;325. doi:10.1126/science.1172867

120. Hitchcock AL, Auld K, Gygi SP, Silver PA. A subset of membrane-associated proteins is ubiquitinated in response to mutations in the endoplasmic reticulum degradation machinery. Proc Natl Acad Sci U S A. 2003;100. doi:10.1073/pnas.2135500100

121. Guo X, Niemi NM, Hutchins PD, Condon SGF, Jochem A, Ulbrich A, et al. Ptc7p Dephosphorylates Select Mitochondrial Proteins to Enhance Metabolic Function. Cell Rep. 2017;18. doi:10.1016/j.celrep.2016.12.049

122. Gruhler A, Olsen J v., Mohammed S, Mortensen P, Færgeman NJ, Mann M, et al. Quantitative phosphoproteomics applied to the yeast pheromone signaling pathway. Molecular and Cellular Proteomics. 2005;4. doi:10.1074/mcp.M400219-MCP200

123. Fröhlich F, Olson DK, Christiano R, Farese R v., Walther TC. Proteomic and phosphoproteomic analyses of yeast reveal the global cellular response to sphingolipid depletion. Proteomics. 2016;16. doi:10.1002/pmic.201600269

124. Fang NN, Chan GT, Zhu M, Comyn SA, Persaud A, Deshaies RJ, et al. Rsp5/Nedd4 is the main ubiquitin ligase that targets cytosolic misfolded proteins following heat stress. Nat Cell Biol. 2014;16. doi:10.1038/ncb3054

125. Esteras M, Liu IC, Snijders AP, Jarmuz A, Aragon L. Identification of sumo conjugation sites in the budding yeast proteome. Microbial Cell. 2017;4. doi:10.15698/mic2017.10.593

126. Chen SH, Albuquerque CP, Liang J, Suhandynata RT, Zhou H. A proteome-wide analysis of kinase-substrate network in the DNA damage response. Journal of Biological Chemistry. 2010;285. doi:10.1074/jbc.M110.106989

127. Albuquerque CP, Smolka MB, Payne SH, Bafna V, Eng J, Zhou H. A multidimensional chromatography technology for in-depth phosphoproteome analysis. Molecular and Cellular Proteomics. 2008;7. doi:10.1074/mcp.M700468-MCP200

128. BastosdeOliveira FM, Kim D, Cussiol JR, Das J, Jeong MC, Doerfler L, et al. Phosphoproteomics Reveals Distinct Modes of Mec1/ATR Signaling during DNA Replication. Mol Cell. 2015;57. doi:10.1016/j.molcel.2015.01.043

129. Lee S, Ho HC, Tumolo JM, Hsu PC, MacGurn JA. Methionine triggers Ppz-mediated dephosphorylation of Art1 to promote cargo-specific endocytosis. Journal of Cell Biology. 2019;218. doi:10.1083/jcb.201712144

130. Papinski D, Schuschnig M, Reiter W, Wilhelm L, Barnes CA, Maiolica A, et al. Early Steps in Autophagy Depend on Direct Phosphorylation of Atg9 by the Atg1 Kinase. Mol Cell. 2014;53. doi:10.1016/j.molcel.2013.12.011

131. Paulo JA, Gygi SP. A comprehensive proteomic and phosphoproteomic analysis of yeast deletion mutants of 14-3-3 orthologs and associated effects of rapamycin. Proteomics. 2015;15. doi:10.1002/pmic.201400155

132. Peng J, Schwartz D, Elias JE, Thoreen CC, Cheng D, Marsischky G, et al. A proteomics approach to understanding protein ubiquitination. Nat Biotechnol. 2003;21. doi:10.1038/nbt849

133. Shinoda J, Kikuchi Y. Rod1, an arrestin-related protein, is phosphorylated by Snf1-kinase in Saccharomyces cerevisiae. Biochem Biophys Res Commun. 2007;364. doi:10.1016/j.bbrc.2007.09.134

134. Zhou C, Elia AEH, Naylor ML, Dephoure N, Ballif BA, Goel G, et al. Profiling DNA damage-induced phosphorylation in budding yeast reveals diverse signaling networks. Proc Natl Acad Sci U S A. 2016;113. doi:10.1073/pnas.1602827113

135. González A, Hall MN. Nutrient sensing and TOR signaling in yeast and mammals . EMBO J. 2017;36. doi:10.15252/embj.201696010

136. Galan JM, Moreau V, Andre B, Volland C, Haguenauer-Tsapis R. Ubiquitination mediated by the Npi1p/Rsp5p ubiquitin-protein ligase is required for endocytosis of the yeast uracil permease. Journal of Biological Chemistry. 1996;271. doi:10.1074/jbc.271.18.10946

137. Schmidt A, Beck T, Koller A, Kunz J, Hall MN. The TOR nutrient signalling pathway phosphorylates NPR1 and inhibits turnover of the tryptophan permease. EMBO Journal. 1998;17. doi:10.1093/emboj/17.23.6924

138. Bowman Ii RW, Jordahl EM, Davis S, Hedayati S, Barsouk H, Ozbaki-Yagan N, et al. TORC1 Signaling Controls the Stability and Function of α-Arrestins Aly1 and Aly2. 2022. doi:10.3390/biom12040533

139. Ptacek J, Devgan G, Michaud G, Zhu H, Zhu X, Fasolo J, et al. Global analysis of protein phosphorylation in yeast. Nature. 2005;438. doi:10.1038/nature04187

140. Llopis-Torregrosa V, Ferri-Blázquez A, Adam-Artigues A, Deffontaines E, van Paul H Heusden G, Yenush L. Regulation of the Yeast Hxt6 Hexose Transporter by the Rod1 α-Arrestin, the Snf1 Protein Kinase, and the Bmh2 14-3-3 Protein. Journal of Biological Chemistry. 2016;291. doi:10.1074/jbc.M116.733923

141. Hovsepian J, Albanèse V, Becuwe M, Ivashov V, Teis D, Léon S. The yeast arrestin-related protein Bul1 is a novel actor of glucose-induced endocytosis. Mol Biol Cell. 2018;29. doi:10.1091/mbc.E17-07-0466

142. Alvaro CG, Aindow A, Thorner J. Differential phosphorylation provides a switch to control how α-arrestin Rod1 down-regulates mating pheromone response in saccharomyces cerevisiae. Genetics. 2016;203. doi:10.1534/genetics.115.186122

143. Kee Y, Lyon N, Huibregtse JM. The Rsp5 ubiquitin ligase is coupled to and antagonized by the Ubp2 deubiquitinating enzyme. EMBO Journal. 2005;24. doi:10.1038/sj.emboj.7600710

144. Krogan NJ, Cagney G, Yu H, Zhong G, Guo X, Ignatchenko A, et al. Global landscape of protein complexes in the yeast Saccharomyces cerevisiae. Nature. 2006;440. doi:10.1038/nature04670

145. Hesselberth JR, Miller JP, Golob A, Stajich JE, Michaud GA, Fields S. Comparative analysis of Saccharomyces cerevisiae WW domains and their interacting proteins. Genome Biol. 2006;7. doi:10.1186/gb-2006-7-4-r30

146. Gavin AC, Aloy P, Grandi P, Krause R, Boesche M, Marzioch M, et al. Proteome survey reveals modularity of the yeast cell machinery. Nature. 2006;440. doi:10.1038/nature04532

147. Ho Y, Gruhler A, Heilbut A, Bader GD, Moore L, Adams SL, et al. Systematic identification of protein complexes in Saccharomyces cerevisiae by mass spectrometry. Nature. 2002. doi:10.1038/415180a

148. Andoh T, Hirata Y, Kikuchi A. PY motifs of Rod1 are required for binding to Rsp5 and for drug resistance. FEBS Lett. 2002;525. doi:10.1016/S0014-5793(02)03104-6

149. Talaia G, Gournas C, Saliba E, Barata-Antunes C, Casal M, André B, et al. The α-Arrestin Bul1p Mediates Lactate Transporter Endocytosis in Response to Alkalinization and Distinct Physiological Signals. J Mol Biol. 2017;429. doi:10.1016/j.jmb.2017.09.014

150. Ziv I, Matiuhin Y, Kirkpatrick DS, Erpapazoglou Z, Leon S, Pantazopoulou M, et al. A perturbed ubiquitin landscape distinguishes between ubiquitin in trafficking and in proteolysis. Molecular and Cellular Proteomics. 2011;10. doi:10.1074/mcp.M111.009753

151. Starita LM, Lo RS, Eng JK, von Haller PD, Fields S. Sites of ubiquitin attachment in Saccharomyces cerevisiae. Proteomics. 2012;12. doi:10.1002/pmic.201100166

152. Hager NA, Krasowski CJ, Mackie TD, Kolb AR, Needham PG, Augustine AA, et al. Select α-arrestins control cell-surface abundance of the mammalian Kir2.1 potassium channel in a yeast model. Journal of Biological Chemistry. 2018;293. doi:10.1074/jbc.RA117.001293

153. MacDonald C, Shields SB, Williams CA, Winistorfer S, Piper RC. A Cycle of Ubiquitination Regulates Adaptor Function of the Nedd4-Family Ubiquitin Ligase Rsp5. Current Biology. 2020;30. doi:10.1016/j.cub.2019.11.086

154. Herrador A, Léon S, Haguenauer-Tsapis R, Vincent O. A mechanism for protein monoubiquitination dependent on a trans-acting ubiquitin-binding domain. Journal of Biological Chemistry. 2013;288. doi:10.1074/jbc.C113.452250

155. Kee Y, Muñoz W, Lyon N, Huibregtse JM. The deubiquitinating enzyme Ubp2 modulates Rsp5-dependent Lys 63-linked polyubiquitin conjugates in Saccharomyces cerevisiae. Journal of Biological Chemistry. 2006;281. doi:10.1074/jbc.M608756200

156. Ho HC, MacGurn JA, Emr SD. Deubiquitinating enzymes Ubp2 and Ubp15 regulate endocytosis by limiting ubiquitination and degradation of ARTs. Mol Biol Cell. 2017;28. doi:10.1091/mbc.E17-01-0008

157. Fang NN, Zhu M, Rose A, Wu KP, Mayor T. Deubiquitinase activity is required for the proteasomal degradation of misfolded cytosolic proteins upon heat-stress. Nat Commun. 2016;7. doi:10.1038/ncomms12907

158. Amerik AY, Nowak J, Swaminathan S, Hochstrasser M. The Doa4 deubiquitinating enzyme is functionally linked to the vacuolar protein-sorting and endocytic pathways. Mol Biol Cell. 2000;11. doi:10.1091/mbc.11.10.3365

159. Swaminathan S, Amerik AY, Hochstrasser M. The Doa4 deubiquitinating enzyme is required for ubiquitin homeostasis in yeast. Mol Biol Cell. 1999;10. doi:10.1091/mbc.10.8.2583

160. Lee S, Tumolo JM, Ehlinger AC, Jernigan KK, Qualls-Histed SJ, Hsu PC, et al. Ubiquitin turnover and endocytic trafficking in yeast are regulated by ser57 phosphorylation of ubiquitin. Elife. 2017;6. doi:10.7554/eLife.29176

161. Yang Z, Klionsky DJ. Eaten alive: A history of macroautophagy. Nature Cell Biology. 2010. doi:10.1038/ncb0910-814

162. Matile P. Biochemistry and Function of Vacuoles. Annu Rev Plant Physiol. 1978;29. doi:10.1146/annurev.pp.29.060178.001205

163. Deter RL, Baudhuin P, de Duve C. Participation of lysosomes in cellular autophagy induced in rat liver by glucagon. J Cell Biol. 1967;35. doi:10.1083/jcb.35.2.c11

164. de DUVE C. The lysosome. Sci Am. 1963;208: 64–72. doi:10.1038/SCIENTIFICAMERICAN0563-64

165. Klionsky DJ, Cueva R, Yaver DS. Aminopeptidase I of Saccharomyces cerevisiae is localized to the vacuole independent of the secretory pathway. Journal of Cell Biology. 1992;119. doi:10.1083/jcb.119.2.287

166. Tsukada M, Ohsumi Y. Isolation and characterization of autophagy-defective mutants of Saccharomyces cerevisiae. FEBS Lett. 1993;333. doi:10.1016/0014-5793(93)80398-E

167. Harding TM, Morano KA, Scott S v., Klionsky DJ. Isolation and characterization of yeast mutants in the cytoplasm to vacuole protein targeting pathway. Journal of Cell Biology. 1995;131. doi:10.1083/jcb.131.3.591

168. Thumm M, Egner R, Koch B, Schlumpberger M, Straub M, Veenhuis M, et al. Isolation of autophagocytosis mutants of Saccharomyces cerevisiae. FEBS Lett. 1994;349. doi:10.1016/0014-5793(94)00672-5

169. Ichimura Y, Kirisako T, Takao T, Satomi Y, Shimonishi Y, Ishihara N, et al. A ubiquitin-like system mediates protein lipidation. Nature. 2000;408. doi:10.1038/35044114

170. Kametaka S, Matsuura A, Wada Y, Ohsumi Y. Structural and functional analyses of APG5, a gene involved in autophagy in yeast. Gene. 1996;178. doi:10.1016/0378-1119(96)00354-X

171. Takeshige K, Baba M, Tsuboi S, Noda T, Ohsumi Y. Autophagy in yeast demonstrated with proteinase-deficient mutants and conditions for its induction. Journal of Cell Biology. 1992;119. doi:10.1083/jcb.119.2.301

172. Kim J, Scott S v., Oda MN, Klionsky DJ. Transport of a large oligomeric protein by the cytoplasm to vacuole protein targeting pathway. Journal of Cell Biology. 1997. doi:10.1083/jcb.137.3.609

173. Leber R, Silles E, Sandoval I v., Mazón MJ. Yo1082p, a Novel CVT Protein Involved in the Selective Targeting of Aminopeptidase I to the Yeast Vacuole. Journal of Biological Chemistry. 2001;276. doi:10.1074/jbc.M101438200

174. Pfaffenwimmer T, Reiter W, Brach T, Nogellova V, Papinski D, Schuschnig M, et al. Hrr25 kinase promotes selective autophagy by phosphorylating the cargo receptor A tg19 . EMBO Rep. 2014;15. doi:10.15252/embr.201438932

175. Reggiori F, Wang CW, Nair U, Shintani T, Abeliovich H, Klionsky DJ. Early Stages of the Secretory Pathway, but Not Endosomes, Are Required for Cvt Vesicle and Autophagosome Assembly in Saccharomyces cerevisiae. Mol Biol Cell. 2004;15. doi:10.1091/mbc.E03-07-0479

176. Scott S v., Baba M, Ohsumi Y, Klionsky DJ. Aminopeptidase I is targeted to the vacuole by a nonclassical vesicular mechanism. Journal of Cell Biology. 1997;138. doi:10.1083/jcb.138.1.37

177. Kim J, Kamada Y, Stromhaug PE, Guan J, Hefner-Gravink A, Baba M, et al. Cvt9/Gsa9 functions in sequestering selective cytosolic cargo destined for the vacuole. Journal of Cell Biology. 2001;153. doi:10.1083/jcb.153.2.381

178. Shintani T, Huang WP, Stromhaug PE, Klionsky DJ. Mechanism of cargo selection in the cytoplasm to vacuole targeting pathway. Dev Cell. 2002;3. doi:10.1016/S1534-5807(02)00373-8

179. Watanabe Y, Noda NN, Kumeta H, Suzuki K, Ohsumi Y, Inagaki F. Selective transport of α-mannosidase by autophagic pathways: Structural basis for cargo recognition by Atg19 and Atg34. Journal of Biological Chemistry. 2010;285. doi:10.1074/jbc.M110.143545

180. Yorimitsu T, Klionsky DJ. Atg11 links cargo to the vesicle-forming machinery in the cytoplasm to vacuole targeting pathway. Mol Biol Cell. 2005;16. doi:10.1091/mbc.E04-11-1035

181. Mijaljica D, Prescott M, Devenish RJ. A late form of nucleophagy in Saccharomyces cerevisiae. PLoS One. 2012;7. doi:10.1371/journal.pone.0040013

182. Mochida K, Oikawa Y, Kimura Y, Kirisako H, Hirano H, Ohsumi Y, et al. Receptor-mediated selective autophagy degrades the endoplasmic reticulum and the nucleus. Nature. 2015;522. doi:10.1038/nature14506

183. Mochida K, Yamasaki A, Matoba K, Kirisako H, Noda NN, Nakatogawa H. Super-assembly of ER-phagy receptor Atg40 induces local ER remodeling at contacts with forming autophagosomal membranes. Nat Commun. 2020;11. doi:10.1038/s41467-020-17163-y

184. Yang Y, Klionsky DJ. A novel reticulophagy receptor, Epr1: a bridge between the phagophore protein Atg8 and ER transmembrane VAP proteins. Autophagy. 2021. doi:10.1080/15548627.2020.1837457

185. Kraft C, Deplazes A, Sohrmann M, Peter M. Mature ribosomes are selectively degraded upon starvation by an autophagy pathway requiring the Ubp3p/Bre5p ubiquitin protease. Nat Cell Biol. 2008;10. doi:10.1038/ncb1723

186. Motley AM, Nuttall JM, Hettema EH. Pex3-anchored Atg36 tags peroxisomes for degradation in Saccharomyces cerevisiae. EMBO Journal. 2012;31. doi:10.1038/emboj.2012.151

187. Kanki T, Wang K, Cao Y, Baba M, Klionsky DJ. Atg32 Is a Mitochondrial Protein that Confers Selectivity during Mitophagy. Dev Cell. 2009;17. doi:10.1016/j.devcel.2009.06.014

188. Okamoto K, Kondo-Okamoto N, Ohsumi Y. Mitochondria-Anchored Receptor Atg32 Mediates Degradation of Mitochondria via Selective Autophagy. Dev Cell. 2009;17. doi:10.1016/j.devcel.2009.06.013

189. Iwama R, Ohsumi Y. Analysis of autophagy activated during changes in carbon source availability in yeast cells. Journal of Biological Chemistry. 2019;294. doi:10.1074/jbc.RA118.005698

190. Onodera J, Ohsumi Y. Autophagy is required for maintenance of amino acid levels and protein synthesis under nitrogen starvation. Journal of Biological Chemistry. 2005;280. doi:10.1074/jbc.M506736200

191. Yokota H, Gomi K, Shintani T. Induction of autophagy by phosphate starvation in an Atg11-dependent manner in Saccharomyces cerevisiae. Biochem Biophys Res Commun. 2017;483. doi:10.1016/j.bbrc.2016.12.112

192. Kawamata T, Horie T, Matsunami M, Sasaki M, Ohsumi Y. Zinc starvation induces autophagy in yeast. Journal of Biological Chemistry. 2017;292. doi:10.1074/jbc.M116.762948

193. Horie T, Kawamata T, Matsunami M, Ohsumi Y. Recycling of iron via autophagy is critical for the transition from glycolytic to respiratory growth. Journal of Biological Chemistry. 2017;292. doi:10.1074/jbc.M116.762963

194. Lesmana R, Sinha RA, Singh BK, Zhou J, Ohba K, Wu Y, et al. Thyroid hormone stimulation of autophagy is essential for mitochondrial biogenesis and activity in skeletal muscle. Endocrinology. 2016;157. doi:10.1210/en.2015-1632

195. Galati S, Boni C, Gerra MC, Lazzaretti M, Buschini A. Autophagy: A Player in response to Oxidative Stress and DNA Damage. Oxid Med Cell Longev. 2019;2019. doi:10.1155/2019/5692958

196. Shapira KE, Shapira G, Schmukler E, Pasmanik-Chor M, Shomron N, Pinkas-Kramarski R, et al. Autophagy is induced and modulated by cholesterol depletion through transcription of autophagy-related genes and attenuation of flux. Cell Death Discov. 2021;7. doi:10.1038/s41420-021-00718-3

197. Wileman T. Autophagy as a defence against intracellular pathogens. Essays Biochem. 2013;55. doi:10.1042/BSE0550153

198. Yun HR, Jo YH, Kim J, Shin Y, Kim SS, Choi TG. Roles of autophagy in oxidative stress. Int J Mol Sci. 2020;21. doi:10.3390/ijms21093289

199. Kroemer G, Mariño G, Levine B. Autophagy and the Integrated Stress Response. Molecular Cell. 2010. doi:10.1016/j.molcel.2010.09.023

200. Klionsky DJ, Cregg JM, Dunn WA, Emr SD, Sakai Y, Sandoval I v., et al. A unified nomenclature for yeast autophagy-related genes. Developmental Cell. 2003. doi:10.1016/S1534-5807(03)00296-X

201. Nakatogawa H, Suzuki K, Kamada Y, Ohsumi Y. Dynamics and diversity in autophagy mechanisms: Lessons from yeast. Nature Reviews Molecular Cell Biology. 2009. doi:10.1038/nrm2708

202. Baba M, Ohsumi Y, Osumi M. Analysis of the Membrane Structures Involved in Autophagy in Yeast by Freeze-Replica Method. Cell Struct Funct. 1995;20. doi:10.1247/csf.20.465

203. Yeasmin AMST, Waliullah TM, Kondo A, Kaneko A, Koike N, Ushimaru T. Orchestrated action of PP2A antagonizes atg13 phosphorylation and promotes autophagy after the inactivation of TORC1. PLoS One. 2016;11. doi:10.1371/journal.pone.0166636

204. Kabeya Y, Kamada Y, Baba M, Takikawa H, Sasaki M, Ohsumi Y. Atg17 functions in cooperation with Atg1 and Atg13 in yeast autophagy. Mol Biol Cell. 2005;16. doi:10.1091/mbc.E04-08-0669

205. Kamada Y, Funakoshi T, Shintani T, Nagano K, Ohsumi M, Ohsumi Y. Tor-mediated induction of autophagy via an Apg1 protein kinase complex. Journal of Cell Biology. 2000;150. doi:10.1083/jcb.150.6.1507

206. Yorimitsu T, He C, Wang K, Klionsky DJ. Tap42-associated protein phosphatase type 2A negatively regulates induction of autophagy. Autophagy. 2009;5. doi:10.4161/auto.5.5.8091

207. Memisoglu G, Eapen V v., Yang Y, Klionsky DJ, Haber JE. PP2C phosphatases promote autophagy by dephosphorylation of the Atg1 complex. Proc Natl Acad Sci U S A. 2019;116. doi:10.1073/pnas.1817078116

208. Mizushima N. The role of the Atg1/ULK1 complex in autophagy regulation. Current Opinion in Cell Biology. 2010. doi:10.1016/j.ceb.2009.12.004

209. Scott S v., Nice DC, Nau JJ, Weisman LS, Kamada Y, Keizer-Gunnink I, et al. Apg13p and Vac8p are part of a complex of phosphoproteins that are required for Cytoplasm to vacuole targeting. Journal of Biological Chemistry. 2000;275. doi:10.1074/jbc.M002813200

210. Hollenstein DM, Gómez-Sánchez R, Ciftci A, Kriegenburg F, Mari M, Torggler R, et al. Vac8 spatially confines autophagosome formation at the vacuole in S. Cerevisiae. J Cell Sci. 2019;132. doi:10.1242/jcs.235002

211. Yamamoto H, Kakuta S, Watanabe TM, Kitamura A, Sekito T, Kondo-Kakuta C, et al. Atg9 vesicles are an important membrane source during early steps of autophagosome formation. Journal of Cell Biology. 2012;198. doi:10.1083/jcb.201202061

212. Shirahama-Noda K, Kira S, Yoshimori T, Noda T. TRAPPis responsible for vesicular transport from early endosomes to Golgi, facilitating Atg9 cycling in autophagy. J Cell Sci. 2013;126. doi:10.1242/jcs.131318

213. Ohashi Y, Munro S. Membrane delivery to the yeast autophagosome from the golgi-endosomal system. Mol Biol Cell. 2010;21. doi:10.1091/mbc.E10-05-0457

214. Backues SK, Orban DP, Bernard A, Singh K, Cao Y, Klionsky DJ. Atg23 and Atg27 Act at the Early Stages of Atg9 Trafficking in S. cerevisiae. Traffic. 2015;16. doi:10.1111/tra.12240

215. Segarra VA, Boettner DR, Lemmon SK. Atg27 tyrosine sorting motif is important for its trafficking and Atg9 localization. Traffic. 2015;16. doi:10.1111/tra.12253

216. Ma M, Burd CG, Chi RJ. Distinct complexes of yeast Snx4 family SNX-BARs mediate retrograde trafficking of Snc1 and Atg27. Traffic. 2017;18. doi:10.1111/tra.12462

217. Geng J, Nair U, Yasumura-Yorimitsu K, Klionsky DJ. Post-golgi sec proteins are required for autophagy in Saccharomyces cerevisiae. Mol Biol Cell. 2010;21. doi:10.1091/mbc.E09-11-0969

218. Kakuta S, Yamamoto H, Negishi L, Kondo-Kakuta C, Hayashi N, Ohsumi Y. Atg9 vesicles recruit vesicle-tethering proteins Trs85 and Ypt1 to the autophagosome formation site. Journal of Biological Chemistry. 2012;287. doi:10.1074/jbc.M112.411454

219. Mari M, Griffith J, Rieter E, Krishnappa L, Klionsky DJ, Reggiori F. An Atg9-containing compartment that functions in the early steps of autophagosome biogenesis. Journal of Cell Biology. 2010;190. doi:10.1083/jcb.200912089

220. Sawa-Makarska J, Baumann V, Coudevylle N, von Bülow S, Nogellova V, Abert C, et al. Reconstitution of autophagosome nucleation defines Atg9 vesicles as seeds for membrane formation. Science (1979). 2020;369. doi:10.1126/SCIENCE.AAZ7714

221. Suzuki SW, Yamamoto H, Oikawa Y, Kondo-Kakuta C, Kimurac Y, Hirano H, et al. Atg13 HORMA domain recruits Atg9 vesicles during autophagosome formation. Proc Natl Acad Sci U S A. 2015;112. doi:10.1073/pnas.1421092112

222. Shima T, Kirisako H, Nakatogawa H. COPII vesicles contribute to autophagosomal membranes. Journal of Cell Biology. 2019;218. doi:10.1083/jcb.201809032

223. Kihara A, Noda T, Ishihara N, Ohsumi Y. Two distinct Vps34 phosphatidylinositol 3-kinase complexes function in autophagy and carboxypeptidase y sorting in Saccharomyces cerevisiae. Journal of Cell Biology. 2001;153. doi:10.1083/jcb.152.3.519

224. Araki Y, Ku WC, Akioka M, May AI, Hayashi Y, Arisaka F, et al. Atg38 is required for autophagy-specific phosphatidylinositol 3-kinase complex integrity. Journal of Cell Biology. 2013;203. doi:10.1083/jcb.201304123

225. Burman C, Ktistakis NT. Regulation of autophagy by phosphatidylinositol 3-phosphate. FEBS Letters. 2010. doi:10.1016/j.febslet.2010.01.011

226. Suzuki K, Kubota Y, Sekito T, Ohsumi Y. Hierarchy of Atg proteins in pre-autophagosomal structure organization. Genes to Cells. 2007;12. doi:10.1111/j.1365-2443.2007.01050.x

227. Obara K, Noda T, Niimi K, Ohsumi Y. Transport of phosphatidylinositol 3-phosphate into the vacuole via autophagic membranes in Saccharomyces cerevisiae. Genes to Cells. 2008;13. doi:10.1111/j.1365-2443.2008.01188.x

228. Cheng J, Fujita A, Yamamoto H, Tatematsu T, Kakuta S, Obara K, et al. Yeast and mammalian autophagosomes exhibit distinct phosphatidylinositol 3-phosphate asymmetries. Nat Commun. 2014;5. doi:10.1038/ncomms4207

229. Axe EL, Walker SA, Manifava M, Chandra P, Roderick HL, Habermann A, et al. Autophagosome formation from membrane compartments enriched in phosphatidylinositol 3-phosphate and dynamically connected to the endoplasmic reticulum. Journal of Cell Biology. 2008;182. doi:10.1083/jcb.200803137

230. Juris L, Montino M, Rube P, Schlotterhose P, Thumm M, Krick R. PI 3P binding by Atg21 organises Atg8 lipidation . EMBO J. 2015;34. doi:10.15252/embj.201488957

231. Krick R, Henke S, Tolstrup J, Thumm M. Dissecting the localization and function of Atg18, Atg21 and Ygr223c. Autophagy. 2008;4. doi:10.4161/auto.6801

232. Mizushima N, Noda T, Yoshimori T, Tanaka Y, Ishii T, George MD, et al. A protein conjugation system essential for autophagy. Nature. 1998;395. doi:10.1038/26506

233. Fujioka Y, Noda NN, Nakatogawa H, Ohsumi Y, Inagaki F. Dimeric coiled-coil structure of saccharomyces cerevisiae Atg16 and its functional significance in autophagy. Journal of Biological Chemistry. 2010;285. doi:10.1074/jbc.M109.053520

234. Kuma A, Mizushima N, Ishihara N, Ohsumi Y. Formation of the ~350-kDa Apg12-Apg5·Apg16 multimeric complex, mediated by Apg16 oligomerization, is essential for autophagy in yeast. Journal of Biological Chemistry. 2002;277. doi:10.1074/jbc.M111889200

235. Tanida I, Mizushima N, Kiyooka M, Ohsumi M, Ueno T, Ohsumi Y, et al. Apg7p/Cvt2p: A novel protein-activating enzyme essential for autophagy. Mol Biol Cell. 1999;10. doi:10.1091/mbc.10.5.1367

236. Kirisako T, Ichimura Y, Okada H, Kabeya Y, Mizushima N, Yoshimori T, et al. The reversible modification regulates the membrane-binding state of Apg8/Aut7 essential for autophagy and the cytoplasm to vacuole targeting pathway. Journal of Cell Biology. 2000;151. doi:10.1083/jcb.151.2.263

237. Nakatogawa H. Two ubiquitin-like conjugation systems that mediate membrane formation during autophagy. Essays Biochem. 2013;55. doi:10.1042/BSE0550039

238. Ohsumi Y. Molecular dissection of autophagy: Two ubiquitin-like systems. Nature Reviews Molecular Cell Biology. 2001. doi:10.1038/35056522

239. Nakatogawa H, Ichimura Y, Ohsumi Y. Atg8, a Ubiquitin-like Protein Required for Autophagosome Formation, Mediates Membrane Tethering and Hemifusion. Cell. 2007;130. doi:10.1016/j.cell.2007.05.021

240. Harada K, Kotani T, Kirisako H, Sakoh-Nakatogawa M, Oikawa Y, Kimura Y, et al. Two distinct mechanisms target the autophagy-related e3 complex to the pre- autophagosomal structure. Elife. 2019;8. doi:10.7554/eLife.43088

241. Xie Z, Nair U, Klionsky DJ. Atg8 controls phagophore expansion during autophagosome formation. Mol Biol Cell. 2008;19. doi:10.1091/mbc.E07-12-1292

242. Obara K, Sekito T, Niimi K, Ohsumi Y. The Atg18-Atg2 complex is recruited to autophagic membranes via phosphatidylinositol 3-phosphate and exerts an essential function. Journal of Biological Chemistry. 2008;283. doi:10.1074/jbc.M803180200

243. Lei Y, Tang D, Liao G, Xu L, Liu S, Chen Q, et al. The crystal structure of Atg18 reveals a new binding site for Atg2 in Saccharomyces cerevisiae. Cellular and Molecular Life Sciences. 2021;78. doi:10.1007/s00018-020-03621-9

244. Kotani T, Kirisako H, Koizumi M, Ohsumi Y, Nakatogawa H. The Atg2-Atg18 complex tethers pre-autophagosomal membranes to the endoplasmic reticulum for autophagosome formation. Proc Natl Acad Sci U S A. 2018;115. doi:10.1073/pnas.1806727115

245. Gómez-Sánchez R, Rose J, Guimarães R, Mari M, Papinski D, Rieter E, et al. Atg9 establishes Atg2-dependent contact sites between the endoplasmic reticulum and phagophores. Journal of Cell Biology. 2018;217. doi:10.1083/jcb.201710116

246. Valverde DP, Yu S, Boggavarapu V, Kumar N, Lees JA, Walz T, et al. ATG2 transports lipids to promote autophagosome biogenesis. Journal of Cell Biology. 2019;218. doi:10.1083/JCB.201811139

247. Kobayashi T, Suzuki K, Ohsumi Y. Autophagosome formation can be achieved in the absence of Atg18 by expressing engineered PAS-targeted Atg2. FEBS Lett. 2012;586. doi:10.1016/j.febslet.2012.06.008

248. Suzuki K, Akioka M, Kondo-Kakuta C, Yamamoto H, Ohsumi Y. Fine mapping of autophagy-related proteins during autophagosome formation in Saccharomyces cerevisiae. J Cell Sci. 2013;126. doi:10.1242/jcs.122960

249. Graef M, Friedman JR, Graham C, Babu M, Nunnari J. ER exit sites are physical and functional core autophagosome biogenesis components. Mol Biol Cell. 2013;24. doi:10.1091/mbc.E13-07-0381

250. Schütter M, Giavalisco P, Brodesser S, Graef M. Local Fatty Acid Channeling into Phospholipid Synthesis Drives Phagophore Expansion during Autophagy. Cell. 2020;180. doi:10.1016/j.cell.2019.12.005

251. Shpilka T, Welter E, Borovsky N, Amar N, Mari M, Reggiori F, et al. Lipid droplets and their component triglycerides and steryl esters regulate autophagosome biogenesis. EMBO J. 2015;34. doi:10.15252/embj.201490315

252. Velázquez AP, Tatsuta T, Ghillebert R, Drescher I, Graef M. Lipid droplet-mediated ER homeostasis regulates autophagy and cell survival during starvation. Journal of Cell Biology. 2016;212. doi:10.1083/jcb.201508102

253. Biazik J, Ylä-Anttila P, Vihinen H, Jokitalo E, Eskelinen EL. Ultrastructural relationship of the phagophore with surrounding organelles. Autophagy. 2015;11. doi:10.1080/15548627.2015.1017178

254. Backues SK, Chen D, Ruan J, Xie Z, Klionsky DJ. Estimating the size and number of autophagic bodies by electron microscopy. Autophagy. 2014;10. doi:10.4161/auto.26856

255. Zhou F, Wu Z, Zhao M, Murtazina R, Cai J, Zhang A, et al. Rab5-dependent autophagosome closure by ESCRT. Journal of Cell Biology. 2019;218. doi:10.1083/JCB.201811173

256. Zhen Y, Spangenberg H, Munson MJ, Brech A, Schink KO, Tan KW, et al. ESCRT-mediated phagophore sealing during mitophagy. Autophagy. 2020;16. doi:10.1080/15548627.2019.1639301

257. Knorr RL, Lipowsky R, Dimova R. Autophagosome closure requires membrane scission. Autophagy. 2015;11. doi:10.1080/15548627.2015.1091552

258. Yu ZQ, Ni T, Hong B, Wang HY, Jiang FJ, Zou S, et al. Dual roles of Atg8 - PE deconjugation by Atg4 in autophagy. Autophagy. 2012;8. doi:10.4161/auto.19652

259. Nakatogawa H, Ishii J, Asai E, Ohsumi Y. Atg4 recycles inappropriately lipidated Atg8 to promote autophagosome biogenesis. Autophagy. 2012;8. doi:10.4161/auto.8.2.18373

260. Nair U, Yen WL, Mari M, Cao Y, Xie Z, Baba M, et al. A role for Atg8-PE deconjugation in autophagosome biogenesis. Autophagy. 2012;8. doi:10.4161/auto.19385

261. Cebollero E, van der Vaart A, Zhao M, Rieter E, Klionsky DJ, Helms JB, et al. Phosphatidylinositol-3-phosphate clearance plays a key role in autophagosome completion. Current Biology. 2012;22. doi:10.1016/j.cub.2012.06.029

262. Steinfeld N, Lahiri V, Morrison A, Metur SP, Klionsky DJ, Weisman LS. Elevating PI3P drives select downstream membrane trafficking pathways. Mol Biol Cell. 2021;32. doi:10.1091/MBC.E20-03-0191

263. Darsow T, Rieder SE, Emr SD. A multispecificity syntaxin homologue, Vam3p, essential for autophagic and biosynthetic protein transport to the vacuole. Journal of Cell Biology. 1997;138. doi:10.1083/jcb.138.3.517

264. Ishihara N, Hamasaki M, Yokota S, Suzuki K, Kamada Y, Kihara A, et al. Autophagosome requires specific early sec proteins for its formation and NSF/SNARE for vacuolar fusion. Mol Biol Cell. 2001;12. doi:10.1091/mbc.12.11.3690

265. Fischer Von Mollard G, Stevens TH. The Saccharomyces cerevisiae v-SNARE Vti1p is required for multiple membrane transport pathways to the vacuole. Mol Biol Cell. 1999;10. doi:10.1091/mbc.10.6.1719

266. Dilcher M, Köhler B, von Mollard GF. Genetic Interactions with the Yeast Q-SNARE VTI1 Reveal Novel Functions for the R-SNARE YKT6. Journal of Biological Chemistry. 2001;276. doi:10.1074/jbc.M101551200

267. Krämer L, Ungermann C. HOPS drives vacuole fusion by binding the vacuolar SNARE complex and the Vam7 PX domain via two distinct sites. Mol Biol Cell. 2011;22. doi:10.1091/mbc.E11-02-0104

268. Wurmser AE, Sato TK, Emr SD. New component of the vacuolar class C-Vps complex couples nucleotide exchange on the Ypt7 GTPase to SNARE-dependent docking and fusion. Journal of Cell Biology. 2000;151. doi:10.1083/jcb.151.3.551

269. Wang CW, Stromhaug PE, Shima J, Klionsky DJ. The Ccz1-Mon1 protein complex is required for the late step of multiple vacuole delivery pathways. Journal of Biological Chemistry. 2002;277. doi:10.1074/jbc.M208191200

270. Kümmel D, Ungermann C. Principles of membrane tethering and fusion in endosome and lysosome biogenesis. Current Opinion in Cell Biology. 2014. doi:10.1016/j.ceb.2014.04.007

271. Balderhaar HJ kleine, Ungermann C. CORVET and HOPS tethering complexes - coordinators of endosome and lysosome fusion. Journal of Cell Science. 2013. doi:10.1242/jcs.107805

272. Liu X, Mao K, Yu AYH, Omairi-Nasser A, Austin J, Glick BS, et al. The Atg17-Atg31-Atg29 Complex Coordinates with Atg11 to Recruit the Vam7 SNARE and Mediate Autophagosome-Vacuole Fusion. Current Biology. 2016;26. doi:10.1016/j.cub.2015.11.054

273. Torggler R, Papinski D, Kraft C. Assays to monitor autophagy in Saccharomyces cerevisiae. Cells. 2017. doi:10.3390/cells6030023

274. Teter SA, Eggerton KP, Scott S v., Kim J, Fischer AM, Klionsky DJ. Degradation of lipid vesicles in the yeast vacuole requires function of Cvt17, a putative lipase. Journal of Biological Chemistry. 2001;276. doi:10.1074/jbc.C000739200

275. Epple UD, Suriapranata I, Eskelinen EL, Thumm M. Aut5/Cvt17p, a putative lipase essential for disintegration of autophagic bodies inside the vacuole. J Bacteriol. 2001;183. doi:10.1128/JB.183.20.5942-5955.2001

276. Yang Z, Huang J, Geng J, Nair U, Klionsky DJ. Atg22 recycles amino acids to link the degradative and recycling functions of autophagy. Mol Biol Cell. 2006;17. doi:10.1091/mbc.E06-06-0479

277. Sekito T, Chardwiriyapreecha S, Sugimoto N, Ishimoto M, Kawano-Kawada M, Kakinuma Y. Vacuolar transporter Avt4 is involved in excretion of basic amino acids from the vacuoles of Saccharomyces cerevisiae. Biosci Biotechnol Biochem. 2014;78. doi:10.1080/09168451.2014.910095

278. Nishida I, Watanabe D, Tsolmonbaatar A, Kaino T, Ohtsu I, Takagi H. Vacuolar amino acid transporters upregulated by exogenous proline and involved in cellular localization of proline in Saccharomyces cerevisiae. Journal of General and Applied Microbiology. 2016;62. doi:10.2323/jgam.2016.01.005

279. Yang Z, Klionsky DJ. Permeases recycle amino acids resulting from autophagy. Autophagy. 2007;3. doi:10.4161/auto.3631

280. Noda T, Ohsumi Y. Tor, a phosphatidylinositol kinase homologue, controls autophagy in yeast. Journal of Biological Chemistry. 1998;273. doi:10.1074/jbc.273.7.3963

281. Kamada Y, Yoshino K, Kondo C, Kawamata T, Oshiro N, Yonezawa K, et al. Tor Directly Controls the Atg1 Kinase Complex To Regulate Autophagy. Mol Cell Biol. 2010;30. doi:10.1128/mcb.01344-09

282. Funakoshi T, Matsuura A, Noda T, Ohsumi Y. Analyses of APG13 gene involved in autophagy in yeast, Saccharomyces cerevisiae. Gene. 1997;192. doi:10.1016/S0378-1119(97)00031-0

283. Reggiori F, Ungermann C. Autophagosome Maturation and Fusion. Journal of Molecular Biology. 2017. doi:10.1016/j.jmb.2017.01.002

284. Bryant NJ, Stevens TH. Vacuole Biogenesis in Saccharomyces cerevisiae : Protein Transport Pathways to the Yeast Vacuole . Microbiology and Molecular Biology Reviews. 1998;62. doi:10.1128/mmbr.62.1.230-247.1998

285. Müller M, Schmidt O, Angelova M, Faserl K, Weys S, Kremser L, et al. The coordinated action of the MVB pathway and autophagy ensures cell survival during starvation. Elife. 2015;4. doi:10.7554/eLife.07736

286. Dong B, Xu X, Chen G, Zhang D, Tang M, Xu F, et al. Autophagy-associated alpha-arrestin signaling is required for conidiogenous cell development in Magnaporthe oryzae. Sci Rep. 2016;6. doi:10.1038/srep30963

287. Hatakeyama R, Péli-Gulli MP, Hu Z, Jaquenoud M, Garcia Osuna GM, Sardu A, et al. Spatially Distinct Pools of TORC1 Balance Protein Homeostasis. Mol Cell. 2019;73. doi:10.1016/j.molcel.2018.10.040

288. Boeckstaens M, Merhi A, Llinares E, van Vooren P, Springael JY, Wintjens R, et al. Identification of a Novel Regulatory Mechanism of Nutrient Transport Controlled by TORC1-Npr1-Amu1/Par32. PLoS Genet. 2015;11. doi:10.1371/journal.pgen.1005382

289. Haguenauer-Tsapis R, André B. Membrane trafficking of yeast transporters: mechanisms and physiological control of downregulation. 2004. doi:10.1007/b97215

290. Seglen PO, Gordon PB, Holen I. Non-selective autophagy. Seminars in cell biology. 1990.

291. Yorimitsu T, Klionsky DJ. Autophagy: Molecular machinery for self-eating. Cell Death and Differentiation. 2005. doi:10.1038/sj.cdd.4401765

292. Wen X, Klionsky DJ. An overview of macroautophagy in yeast. Journal of Molecular Biology. 2016. doi:10.1016/j.jmb.2016.02.021

293. Herrador A, Livas D, Soletto L, Becuwe M, Léon S, Vincent O. Casein kinase 1 controls the activation threshold of an α-arrestin by multisite phosphorylation of the interdomain hinge. Mol Biol Cell. 2015;26. doi:10.1091/mbc.E14-11-1552

294. O'Donnell AF. The Running of the Buls: Control of Permease Trafficking by α-Arrestins Bul1 and Bul2. Mol Cell Biol. 2012;32. doi:10.1128/mcb.01176-12

295. Piper RC, Dikic I, Lukacs GL. Ubiquitin-dependent sorting in endocytosis. Cold Spring Harb Perspect Biol. 2014;6. doi:10.1101/cshperspect.a016808

296. Hicke L, Zanolari B, Riezman H. Cytoplasmic tail phosphorylation of the α-factor receptor is required for its ubiquitination and internalization. Journal of Cell Biology. 1998;141. doi:10.1083/jcb.141.2.349

297. Marchese A, Raiborg C, Santini F, Keen JH, Stenmark H, Benovic JL. The E3 ubiquitin ligase AIP4 mediates ubiquitination and sorting of the G protein-coupled receptor CXCR4. Dev Cell. 2003;5. doi:10.1016/S1534-5807(03)00321-6

298. Vina-Vilaseca A, Sorkin A. Lysine 63-linked polyubiquitination of the dopamine transporter requires WW3 and WW4 domains of Nedd4-2 and UBE2D ubiquitin-

conjugating enzymes. Journal of Biological Chemistry. 2010;285. doi:10.1074/jbc.M109.058990

299. Dove SK, Piper RC, McEwen RK, Yu JW, King NC, Hughes DC, et al. Svp1p defines a family of phosphatidylinositol 3,5-bisphosphate effectors. EMBO Journal. 2004;23. doi:10.1038/sj.emboj.7600203

300. Rieter E, Vinke F, Bakula D, Cebollero E, Ungermann C, Proikas-Cezanne T, et al. Atg18 function in autophagy is regulated by specific sites within its β-propeller. J Cell Sci. 2013;126. doi:10.1242/jcs.115725

301. Marquardt L, Taylor M, Kramer F, Schmitt K, Braus GH, Valerius O, et al. Vacuole fragmentation depends on a novel Atg18-containing retromer-complex. Autophagy. 2022. doi:10.1080/15548627.2022.2072656

302. Guan J, Stromhaug PE, George MD, Habibzadegah-Tari P, Bevan A, Dunn J, et al. Cvt18/Gsa12 is required for cytoplasm-to-vacuole transport, pexophagy, and autophagy in Saccharomyces cerevisiae and Pichia pastoris. Mol Biol Cell. 2001;12. doi:10.1091/mbc.12.12.3821

303. Barth H, Meiling-Wesse K, Epple UD, Thumm M. Autophagy and the cytoplasm to vacuole targeting pathway both require Aut10p. FEBS Lett. 2001;508. doi:10.1016/S0014-5793(01)03016-2

304. Katzmann DJ, Stefan CJ, Babst M, Emr SD. Vps27 recruits ESCRT machinery to endosomes during MVB sorting. Journal of Cell Biology. 2003;162. doi:10.1083/jcb.200302136

305. Burda P, Padilla SM, Sarkar S, Emr SD. Retromer function in endosome-to-Golgi retrograde transport is regulated by the yeast Vps34 Ptdlns 3-kinase. J Cell Sci. 2002;115. doi:10.1242/jcs.00090

306. Zieger M, Mayer A. Yeast vacuoles fragment in an asymmetrical two-phase process with distinct protein requirements. Mol Biol Cell. 2012;23. doi:10.1091/mbc.E12-05-0347

307. Bas L, Papinski D, Kraft C. Ykt6 mediates autophagosome-vacuole fusion. Molecular and Cellular Oncology. 2018. doi:10.1080/23723556.2018.1526006

308. Yu JW, Lemmon MA. All Phox Homology (PX) Domains from Saccharomyces cerevisiae Specifically Recognize Phosphatidylinositol 3-Phosphate. Journal of Biological Chemistry. 2001;276. doi:10.1074/jbc.M108811200

309. Klionsky DJ, Abdel-Aziz AK, Abdelfatah S, Abdellatif M, Abdoli A, Abel S, et al. Guidelines for the use and interpretation of assays for monitoring autophagy (4th edition)1. Autophagy. 2021. doi:10.1080/15548627.2020.1797280

310. Johnston GC, Pringle JR, Hartwell LH. Coordination of growth with cell division in the yeast Saccharomyces cerevisiae. Exp Cell Res. 1977;105. doi:10.1016/0014-4827(77)90154-9

311. Brachmann CB, Davies A, Cost GJ, Caputo E, Li J, Hieter P, et al. Designer deletion strains derived from Saccharomyces cerevisiae S288C: A useful set of strains and plasmids for PCR-mediated gene disruption and other applications. Yeast. 1998;14. doi:10.1002/(SICI)1097-0061(19980130)14:2<115::AID-YEA204>3.0.CO;2-2

312. Gietz RD, Schiestl RH. High-efficiency yeast transformation using the LiAc/SS carrier DNA/PEG method. Nat Protoc. 2007;2. doi:10.1038/nprot.2007.13

313. Sikorski RS, Hieter P. A system of shuttle vectors and yeast host strains designed for efficient manipulation of DNA in Saccharomyces cerevisiae. Genetics. 1989;122. doi:10.1093/genetics/122.1.19

314. Varlakhanova N v., Mihalevic MJ, Bernstein KA, Ford MGJ. Pib2 and the EGO complex are both required for activation of TORC1. J Cell Sci. 2017;130. doi:10.1242/jcs.207910

315. Lipatova Z, Majumdar U, Segev N. Trs33-containing TRAPP IV: A novel autophagy-specific Ypt1 GEF. Genetics. 2016;204. doi:10.1534/genetics.116.194910

316. Volland C, Urban-Grimal D, Géraud G, Haguenauer-Tsapis R. Endocytosis and degradation of the yeast uracil permease under adverse conditions. Journal of Biological Chemistry. 1994;269. doi:10.1016/s0021-9258(17)36959-4

317. Xie Y, Rubenstein EM, Matt T, Hochstrasser M. SUMO-independent in vivo activity of a SUMO-targeted ubiquitin ligase toward a short-lived transcription factor. Genes Dev. 2010;24. doi:10.1101/gad.1906510

318. Maere S, Heymans K, Kuiper M. BiNGO: A Cytoscape plugin to assess overrepresentation of Gene Ontology categories in Biological Networks. Bioinformatics. 2005;21. doi:10.1093/bioinformatics/bti551

319. Shannon P, Markiel A, Ozier O, Baliga NS, Wang JT, Ramage D, et al. Cytoscape: A software Environment for integrated models of biomolecular interaction networks. Genome Res. 2003;13. doi:10.1101/gr.1239303

320. Wickham H. ggpolt2 Elegant Graphics for Data Analysis. Use R! series. 2016.

321. Frankl A, Mari M, Reggiori F. Electron microscopy for ultrastructural analysis and protein localization in saccharomyces cerevisiae. Microbial Cell. 2015. doi:10.15698/mic2015.11.237

322. Klionsky DJ. The molecular machinery of autophagy: Unanswered questions. J Cell Sci. 2005;118. doi:10.1242/jcs.01620

323. Obara K, Sekito T, Ohsumi Y. Assortment of phosphatidylinositol 3-kinase complexes-Atg14p directs association of complex I to the pre-autophagosomal structure in Saccharomyces cerevisiae. Mol Biol Cell. 2006;17. doi:10.1091/mbc.E05-09-0841

324. Shintani T, Suzuki K, Kamada Y, Noda T, Ohsumi Y. Apg2p Functions in Autophagosome Formation on the Perivacuolar Structure. Journal of Biological Chemistry. 2001;276. doi:10.1074/jbc.M102346200

325. Wang CW, Kim J, Huang WP, Abeliovich H, Stromhaug PE, Dunn WA, et al. Apg2 Is a Novel Protein Required for the Cytoplasm to Vacuole Targeting, Autophagy, and Pexophagy Pathways. Journal of Biological Chemistry. 2001;276. doi:10.1074/jbc.M102342200

326. Gopaldass N, Fauvet B, Lashuel H, Roux A, Mayer A. Membrane scission driven by the PROPPIN Atg18. EMBO J. 2017;36. doi:10.15252/embj.201796859

327. Baskaran S, Ragusa MJ, Boura E, Hurley JH. Two-Site Recognition of Phosphatidylinositol 3-Phosphate by PROPPINs in Autophagy. Mol Cell. 2012;47. doi:10.1016/j.molcel.2012.05.027

328. Krick R, Busse RA, Scacioc A, Stephan M, Janshoff A, Thumm M, et al. Structural and functional characterization of the two phosphoinositide binding sites of PROPPINs, a β-propeller protein family. Proc Natl Acad Sci U S A. 2012;109. doi:10.1073/pnas.1205128109

329. Yao Z, Delorme-Axford E, Backues SK, Klionsky DJ. Atg41/Icy2 regulates autophagosome formation. Autophagy. 2015;11. doi:10.1080/15548627.2015.1107692

330. Hanada T, Noda NN, Satomi Y, Ichimura Y, Fujioka Y, Takao T, et al. The Atg12-Atg5 conjugate has a novel E3-like activity for protein lipidation in autophagy. Journal of Biological Chemistry. 2007;282. doi:10.1074/jbc.C700195200

331. Romanov J, Walczak M, Ibiricu I, Schüchner S, Ogris E, Kraft C, et al. Mechanism and functions of membrane binding by the Atg5-Atg12/Atg16 complex during autophagosome formation. EMBO Journal. 2012;31. doi:10.1038/emboj.2012.278

332. Shintani T, Mizushima N, Ogawa Y, Matsuura A, Noda T, Ohsumi Y. Apg10p, a novel protein-conjugating enzyme essential for autophagy in yeast. EMBO Journal. 1999;18. doi:10.1093/emboj/18.19.5234

333. Ammerer G, Hunter CP, Rothman JH, Saari GC, Valls LA, Stevens TH. PEP4 gene of Saccharomyces cerevisiae encodes proteinase A, a vacuolar enzyme required for processing of vacuolar precursors. Mol Cell Biol. 1986;6. doi:10.1128/mcb.6.7.2490-2499.1986

334. Woolford CA, Daniels LB, Park FJ, Jones EW, van Arsdell JN, Innis MA. The PEP4 gene encodes an aspartyl protease implicated in the posttranslational regulation of Saccharomyces cerevisiae vacuolar hydrolases. Mol Cell Biol. 1986;6. doi:10.1128/mcb.6.7.2500

335. Bernard A, Jin M, Xu Z, Klionsky DJ. A large-scale analysis of autophagy-related gene expression identifies new regulators of autophagy. Autophagy. 2015;11. doi:10.1080/15548627.2015.1099796

336. Matoba K, Kotani T, Tsutsumi A, Tsuji T, Mori T, Noshiro D, et al. Atg9 is a lipid scramblase that mediates autophagosomal membrane expansion. Nat Struct Mol Biol. 2020. doi:10.1038/s41594-020-00518-w

337. Noda T, Kim J, Huang WP, Baba M, Tokunaga C, Ohsumi Y, et al. Apg9p/Cvt7p is an integral membrane protein required for transport vesicle formation in the Cvt and autophagy pathways. Journal of Cell Biology. 2000;148. doi:10.1083/jcb.148.3.465

338. Llinares E, Barry AO, André B. The AP-3 adaptor complex mediates sorting of yeast and mammalian PQ-loop-family basic amino acid transporters to the vacuolar/lysosomal membrane. Sci Rep. 2015;5. doi:10.1038/srep16665

339. Sun B, Chen L, Cao W, Roth AF, Davis NG. The Yeast Casein Kinase Yck3p is Palmitoylated, then Sorted to the Valcuolar Membrane with AP-3-dependent Recognition of a YXXΦ Adaptin Sorting Signal. Mol Biol Cell. 2004;15. doi:10.1091/mbc.E03-09-0682

340. Seaman MNJ, Marcusson EG, Cereghino JL, Emr SD. Endosome to Golgi retrieval of the vacuolar protein sorting receptor, Vps10p, requires the function of the VPS29, VPS30, and VPS35 gene products. Journal of Cell Biology. 1997;137. doi:10.1083/jcb.137.1.79

341. Hollenstein DM, Licheva M, Konradi N, Schweida D, Mancilla H, Mari M, et al. Spatial control of avidity regulates initiation and progression of selective autophagy. Nat Commun. 2021;12. doi:10.1038/s41467-021-27420-3

342. Hatakeyama R, de Virgilio C. A spatially and functionally distinct pool of TORC1 defines signaling endosomes in yeast. Autophagy. 2019. doi:10.1080/15548627.2019.1580107

343. Efe JA, Botelho RJ, Emr SD. Atg18 regulates organelle morphology and Fab1 kinase activity independent of its membrane recruitment by phosphatidylinositol 3,5-bisphosphate. Mol Biol Cell. 2007;18. doi:10.1091/mbc.E07-04-0301

344. Dove SK, Cooke FT, Douglas MR, Sayers LG, Parker PJ, Michell RH. Osmotic stress activates phosphatidylinositol-3,5-bisphosphate synthesis. Nature. 1997;390. doi:10.1038/36613

345. Cooke FT, Dove SK, McEwen RK, Painter G, Holmes AB, Hall MN, et al. The stress-activated phosphatidylinositol 3-phosphate 5-kinase Fab1p is essential for vacuole function in S. cerevisiae. Current Biology. 1998;8. doi:10.1016/s0960-9822(07)00513-1

346. Gary JD, Wurmser AE, Bonangelino CJ, Weisman LS, Emr SD. Fab1p is essential for PtdIns(3)P 5-kinase activity and the maintenance of vacuolar size and membrane homeostasis. Journal of Cell Biology. 1998;143. doi:10.1083/jcb.143.1.65

347. Hayakawa A, Hayes SJ, Lawe DC, Sudharshan E, Tuft R, Fogarty K, et al. Structural Basis for Endosomal Targeting by FYVE Domains. Journal of Biological Chemistry. 2004;279. doi:10.1074/jbc.M310503200

348. Kawamata T, Kamada Y, Kabeya Y, Sekito T, Ohsumi Y. Organization of the pre-autophagosomal structure responsible for autophagosome formation. Mol Biol Cell. 2008;19. doi:10.1091/mbc.E07-10-1048

349. Rostislavleva K, Soler N, Ohashi Y, Zhang L, Pardon E, Burke JE, et al. Structure and flexibility of the endosomal Vps34 complex reveals the basis of its function on membranes. Science (1979). 2015;350. doi:10.1126/science.aac7365

350. Schu P v., Takegawa K, Fry MJ, Stack JH, Waterfield MD, Emr SD. Phosphatidylinositol 3-kinase encoded by yeast VPS34 gene essential for protein sorting. Science (1979). 1993;260. doi:10.1126/science.8385367

351. Ohashi Y, Tremel S, Williams RL. VPS34 complexes from a structural perspective. Journal of Lipid Research. 2019. doi:10.1194/jlr.R089490

352. Suzuki SW, Emr SD. Membrane protein recycling from the vacuole/lysosome membrane. Journal of Cell Biology. 2018;217. doi:10.1083/jcb.201709162

353. Nice DC, Sato TK, Stromhaug PE, Emr SD, Klionsky DJ. Cooperative binding of the cytoplasm to vacuole targeting pathway proteins, Cvt13 and Cvt20, to phosphatidylinositol 3-phosphate at the pre-autophagosomal structure is required for selective autophagy. J Biol Chem. 2002;277. doi:10.1074/jbc.M204736200

354. Majerus PW, Kisseleva M v., Anderson Norris F. The role of phosphatases in inositol signaling reactions. Journal of Biological Chemistry. 1999. doi:10.1074/jbc.274.16.10669

355. Laporte J, Blondeau F, Buj-Bello A, Tentler D, Kretz C, Dahl N, et al. Characterization of the myotubularin dual specificity phosphatase gene family from yeast to human. Hum Mol Genet. 1998;7. doi:10.1093/hmg/7.11.1703

356. Parrish WR, Stefan CJ, Emr SD. Essential role for the myotubularin-related phosphatase Ymr1p and the synaptojanin-like phosphatases Sjl2p and Sjl3p in regulation of phosphatidylinositol 3-phosphate in yeast. Mol Biol Cell. 2004;15. doi:10.1091/mbc.E04-03-0209

357. Jin N, Chow CY, Liu L, Zolov SN, Bronson R, Davisson M, et al. VAC14 nucleates a protein complex essential for the acute interconversion of PI3P and PI(3,5)P2 in yeast and mouse. EMBO Journal. 2008;27. doi:10.1038/emboj.2008.248

358. Gary JD, Sato TK, Stefan CJ, Bonangelino CJ, Weisman LS, Emr SD. Regulation of Fab1 phosphatidylinositol 3-phosphate 5-kinase pathway by Vac7 protein and Fig4, a polyphosphoinositide phosphatase family member. Mol Biol Cell. 2002;13. doi:10.1091/mbc.01-10-0498

359. Yamamoto A, DeWald DB, Boronenkov I v., Anderson RA, Emr SD, Koshland D. Novel PI(4)P 5-kinase homologue, Fab1p, essential for normal vacuole function and morphology in yeast. Mol Biol Cell. 1995;6. doi:10.1091/mbc.6.5.525

360. Patton JL, Pessoa-Brandao L, Henry SA. Production and reutilization of an extracellular phosphatidylinositol catabolite, glycerophosphoinositol, by Saccharomyces cerevisiae. J Bacteriol. 1995;177. doi:10.1128/jb.177.12.3379-3385.1995

361. Angus WW, Lester RL. Turnover of inositol and phosphorus containing lipids in Saccharomyces cerevisiae; extracellular accumulation of glycerophosphorylinositol derived from phosphatidylinositol. Arch Biochem Biophys. 1972;151. doi:10.1016/0003-9861(72)90525-5

362. Yamagami K, Yamamoto T, Sakai S, Mioka T, Sano T, Igarashi Y, et al. Inositol depletion restores vesicle transport in yeast phospholipid flippase mutants. PLoS One. 2015;10. doi:10.1371/journal.pone.0120108

363. Harada Y, Tamura Y, Endo T. Identification of yeast Art5 as a multicopy suppressor for the mitochondrial translocator maintenance protein Tam41. Biochem Biophys Res Commun. 2010;392. doi:10.1016/j.bbrc.2010.01.024

364. Tamura Y, Harada Y, Nishikawa SI, Yamano K, Kamiya M, Shiota T, et al. Tam41 is a CDP-diacylglycerol synthase required for cardiolipin biosynthesis in mitochondria. Cell Metab. 2013;17. doi:10.1016/j.cmet.2013.03.018

365. Nomura W, Maeta K, Inoue Y. Phosphatidylinositol 3,5-bisphosphate is involved in methylglyoxal-induced activation of the Mpk1 mitogen-activated protein kinase cascade in Saccharomyces cerevisiae. Journal of Biological Chemistry. 2017;292. doi:10.1074/jbc.M117.791590

366. Nomura W, Aoki M, Inoue Y. Methylglyoxal inhibits nuclear division through alterations in vacuolar morphology and accumulation of Atg18 on the vacuolar membrane in Saccharomyces cerevisiae. Sci Rep. 2020;10. doi:10.1038/s41598-020-70802-8

367. Léon S, Erpapazoglou Z, Haguenauer-Tsapis R. Ear1p and Ssh4p are new adaptors of the ubiquitin ligase Rsp5p for cargo ubiquitylation and sorting at multivesicular bodies. Mol Biol Cell. 2008;19. doi:10.1091/mbc.E08-01-0068

368. Zhu L, Jorgensen JR, Li M, Chuang YS, Emr SD. ESCRTS function directly on the lysosome membrane to downregulate ubiquitinated lysosomal membrane proteins. Elife. 2017;6. doi:10.7554/eLife.26403

369. Li M, Rong Y, Chuang YS, Peng D, Emr SD. Ubiquitin-dependent lysosomal membrane protein sorting and degradation. Mol Cell. 2015;57. doi:10.1016/j.molcel.2014.12.012

370. Sardana R, Zhu L, Emr SD. Rsp5 ubiquitin ligase–mediated quality control system clears membrane proteins mistargeted to the vacuole membrane. Journal of Cell Biology. 2019;218. doi:10.1083/jcb.201806094

371. Feyder S, de Craene JO, Bär S, Bertazzi DL, Friant S. Membrane trafficking in the yeast Saccharomyces cerevisiae model. International Journal of Molecular Sciences. 2015. doi:10.3390/ijms16011509

372. Bowers K, Stevens TH. Protein transport from the late Golgi to the vacuole in the yeast Saccharomyces cerevisiae. Biochimica et Biophysica Acta - Molecular Cell Research. 2005. doi:10.1016/j.bbamcr.2005.04.004

373. Kahlhofer J, Leon S, Teis D, Schmidt O. The α-arrestin family of ubiquitin ligase adaptors links metabolism with selective endocytosis. Biology of the Cell. 2021. doi:10.1111/boc.202000137

374. O'donnell AF, Schmidt MC. AMPK-mediated regulation of alpha-arrestins and protein trafficking. International Journal of Molecular Sciences. 2019. doi:10.3390/ijms20030515

375. Shenoy SK, Lefkowitz RJ. Seven-transmembrane receptor signaling through beta-arrestin. Science's STKE : signal transduction knowledge environment. 2005. doi:10.1126/stke.2005/308/cm10

376. DeWire SM, Ahn S, Lefkowitz RJ, Shenoy SK. β-Arrestins and cell signaling. Annual Review of Physiology. 2007. doi:10.1146/annurev.physiol.69.022405.154749

377. Ahn S, Shenoy SK, Luttrell LM, Lefkowitz RJ. SnapShot: β-Arrestin Functions. Cell. 2020;182. doi:10.1016/j.cell.2020.07.034

378. Puca L, Chastagner P, Meas-Yedid V, Israël A, Brou C. α-arrestin 1 (ARRDC1) and β-arrestins cooperate to mediate Notch degradation in mammals. J Cell Sci. 2013;126. doi:10.1242/jcs.130500

379. Tian X, Irannejad R, Bowman SL, Du Y, Puthenveedu MA, von Zastrow M, et al. The αarrestin ARRDC3 regulates the endosomal residence time and intracellular signaling of the β2-adrenergic receptor. Journal of Biological Chemistry. 2016;291. doi:10.1074/jbc.M116.716589

380. MacGilvray ME, Shishkova E, Place M, Wagner ER, Coon JJ, Gasch AP. Phosphoproteome Response to Dithiothreitol Reveals Unique Versus Shared Features of Saccharomyces cerevisiae Stress Responses. J Proteome Res. 2020;19. doi:10.1021/acs.jproteome.0c00253

381. Breitkreutz A, Choi H, Sharom JR, Boucher L, Neduva V, Larsen B, et al. A global protein kinase and phosphatase interaction network in yeast. Science (1979). 2010;328. doi:10.1126/science.1176495

382. Hohmann S. Control of high osmolarity signalling in the yeast Saccharomyces cerevisiae. FEBS Letters. 2009. doi:10.1016/j.febslet.2009.10.069

383. Westfall PJ, Thorner J. Analysis of mitogen-activated protein kinase signaling specificity in response to hyperosmotic stress: Use of an analog-sensitive HOG1 allele. Eukaryot Cell. 2006;5. doi:10.1128/EC.00037-06

384. Nakamura T, Liu Y, Hirata D, Namba H, Harada SI, Hirokawa T, et al. Protein phosphatase type 2B (calcineurin)-mediated, FK506-sensitive regulation of intracellular ions in yeast is an important determinant for adaptation to high salt stress conditions. EMBO Journal. 1993;12. doi:10.1002/j.1460-2075.1993.tb06090.x

385. Cyert MS. Calcineurin signaling in Saccharomyces cerevisiae: How yeast go crazy in response to stress. Biochem Biophys Res Commun. 2003;311. doi:10.1016/S0006-291X(03)01552-3

386. Szopinska A, Degand H, Hochstenbach JF, Nader J, Morsomme P. Rapid response of the yeast plasma membrane proteome to salt stress. Molecular and Cellular Proteomics. 2011;10. doi:10.1074/mcp.M111.009589

387. Jiang Y, Broach JR. Tor proteins and protein phosphatase 2A reciprocally regulate Tap42 in controlling cell growth in yeast. EMBO Journal. 1999;18. doi:10.1093/emboj/18.10.2782

388. Jacinto E, Guo B, Arndt KT, Schmelzle T, Hall MN. TIP41 interacts with TAP42 and negatively regulates the TOR signaling pathway. Mol Cell. 2001;8. doi:10.1016/S1097-2765(01)00386-0

389. Boeckstaens M, Llinares E, van Vooren P, Marini AM aria. The TORC1 effector kinase Npr1 fine tunes the inherent activity of the Mep2 ammonium transport protein. Nat Commun. 2014;5. doi:10.1038/ncomms4101

390. Tate JJ, Rai R, de Virgilio C, Cooper TG. N- and C-terminal Gln3-Tor1 interaction sites: one acting negatively and the other positively to regulate nuclear Gln3 localization. Genetics. 2021;217. doi:10.1093/genetics/iyab017

391. Tate JJ, Tolley EA, Cooper TG. Sit4 and PP2A dephosphorylate nitrogen catabolite repression-sensitive Gln3 when TorC1 is up- as well as downregulated. Genetics. 2019;212. doi:10.1534/genetics.119.302371

392. Sun Z, Guerriero CJ, Brodsky JL. Substrate ubiquitination retains misfolded membrane proteins in the endoplasmic reticulum for degradation. Cell Rep. 2021;36. doi:10.1016/j.celrep.2021.109717

393. Liesche J, Marek M, Günther-Pomorski T. Cell wall staining with Trypan blue enables quantitative analysis of morphological changes in yeast cells. Front Microbiol. 2015;6. doi:10.3389/fmicb.2015.00107

394. Schmitt ME, Brown TA, Trumpower BL. A rapid and simple method for preparation of RNA from Saccharomyces cerevisiae. Nucleic Acids Res. 1990;18. doi:10.1093/nar/18.10.3091

395. Livak KJ, Schmittgen TD. Analysis of relative gene expression data using real-time quantitative PCR and the 2-ΔΔCT method. Methods. 2001;25. doi:10.1006/meth.2001.1262

396. Dohlman HG, Thorner JW. Regulation of G protein - Initiated signal transduction in yeast: Paradigms and principles. Annual Review of Biochemistry. 2001. doi:10.1146/annurev.biochem.70.1.703

397. Alvaro CG, Thorner J. Heterotrimeric G protein-coupled receptor signaling in yeast mating pheromone response. Journal of Biological Chemistry. 2016. doi:10.1074/jbc.R116.714980

398. Crespo JL, Helliwell SB, Wiederkehr C, Demougin P, Fowler B, Primig M, et al. NPR1 kinase and RSP5-BUL1/2 ubiquitin ligase control GLN3-dependent transcription in Saccharomyces cerevisiae. Journal of Biological Chemistry. 2004;279. doi:10.1074/jbc.M407372200

399. Urban J, Soulard A, Huber A, Lippman S, Mukhopadhyay D, Deloche O, et al. Sch9 Is a Major Target of TORC1 in Saccharomyces cerevisiae. Mol Cell. 2007;26. doi:10.1016/j.molcel.2007.04.020

400. Binda M, Péli-Gulli MP, Bonfils G, Panchaud N, Urban J, Sturgill TW, et al. The Vam6 GEF Controls TORC1 by Activating the EGO Complex. Mol Cell. 2009;35. doi:10.1016/j.molcel.2009.06.033

401. Raught B, Gingras AC, Sonenberg N. The target of rapamycin (TOR) proteins. Proc Natl Acad Sci U S A. 2001;98. doi:10.1073/pnas.121145898

402. Collins GA, Gomez TA, Deshaies RJ, Tansey WP. Combined chemical and genetic approach to inhibit proteolysis by the proteasome. Yeast. 2010;27. doi:10.1002/yea.1805

403. Guerriero CJ, Weiberth KF, Brodsky JL. Hsp70 targets a cytoplasmic quality control substrate to the san1p Ubiquitin ligase. Journal of Biological Chemistry. 2013;288. doi:10.1074/jbc.M113.475905

404. Li Y, Kane T, Tipper C, Spatrick P, Jenness DD. Yeast Mutants Affecting Possible Quality Control of Plasma Membrane Proteins. Mol Cell Biol. 1999;19. doi:10.1128/mcb.19.5.3588

405. Leskoske KL, Roelants FM, Emmerstorfer-Augustin A, Augustin CM, Si EP, Hill JM, et al. Phosphorylation by the stress-activated MAPK Slt2 down-regulates the yeast TOR complex 2. Genes Dev. 2018;32. doi:10.1101/gad.318709.118

406. Levy JMM, Towers CG, Thorburn A. Targeting autophagy in cancer. Nature Reviews Cancer. 2017. doi:10.1038/nrc.2017.53

407. Klionsky DJ, Petroni G, Amaravadi RK, Baehrecke EH, Ballabio A, Boya P, et al. Autophagy in major human diseases. EMBO J. 2021;40. doi:10.15252/embj.2021108863

408. Yang Y, Klionsky DJ. Autophagy and disease: unanswered questions. Cell Death and Differentiation. 2020. doi:10.1038/s41418-019-0480-9

409. Mizushima N, Levine B, Cuervo AM, Klionsky DJ. Autophagy fights disease through cellular self-digestion. Nature. 2008. doi:10.1038/nature06639

410. Saha S, Panigrahi DP, Patil S, Bhutia SK. Autophagy in health and disease: A comprehensive review. Biomedicine and Pharmacotherapy. 2018. doi:10.1016/j.biopha.2018.05.007

411. Lei Y, Xu X, Liu H, Chen L, Zhou H, Jiang J, et al. HBx induces hepatocellular carcinogenesis through ARRB1-mediated autophagy to drive the G1/S cycle. Autophagy. 2021;17. doi:10.1080/15548627.2021.1917948

412. Tan S, Lu Y, Xu M, Huang X, Liu H, Jiang J, et al. β-Arrestin1 enhances liver fibrosis through autophagy-mediated Snail signaling. FASEB Journal. 2019;33. doi:10.1096/fj.201800828RR

413. Wang P, Xu TY, Wei K, Guan YF, Wang X, Xu H, et al. ARRB1/β-arrestin-1 mediates neuroprotection through coordination of BECN1-dependent autophagy in cerebral ischemia. Autophagy. 2014;10. doi:10.4161/auto.29203

414. Kofoed M, Milbury KL, Chiang JH, Sinha S, Ben-Aroya S, Giaever G, et al. An updated collection of sequence barcoded temperature-sensitive alleles of yeast essential genes. G3: Genes, Genomes, Genetics. 2015;5. doi:10.1534/g3.115.019174

415. McCracken AA, Brodsky JL. Assembly of ER-associated protein degradation in vitro: Dependence on cytosol, calnexin, and ATP. Journal of Cell Biology. 1996;132. doi:10.1083/jcb.132.3.291

416. Klionsky DJ. Autophagy: From phenomenology to molecular understanding in less than a decade. Nature Reviews Molecular Cell Biology. 2007. doi:10.1038/nrm2245

417. Khmelinskii A, Knop M. Analysis of Protein Dynamics with Tandem Fluorescent Protein Timers. Methods in Molecular Biology. 2014;1174. doi:10.1007/978-1-4939-0944-5_13

418. Michaillat L, Mayer A. Identification of Genes Affecting Vacuole Membrane Fragmentation in Saccharomyces cerevisiae. PLoS One. 2013;8. doi:10.1371/journal.pone.0054160

419. Yoshikawa K, Tanaka T, Ida Y, Furusawa C, Hirasawa T, Shimizu H. Comprehensive phenotypic analysis of single-gene deletion and overexpression strains of Saccharomyces cerevisiae. Yeast. 2011;28. doi:10.1002/yea.1843

420. Altmann K, Westermann B. Role of essential genes in mitochondrial morphogenesis in Saccharomyces cerevisiae. Mol Biol Cell. 2005;16. doi:10.1091/mbc.E05-07-0678

421. Wiederhold E, Gandhi T, Permentier HP, Breitling R, Poolman B, Slotboom DJ. The yeast vacuolar membrane proteome. Molecular and Cellular Proteomics. 2009;8. doi:10.1074/mcp.M800372-MCP200

422. van Zutphen T, Todde V, de Boer R, Kreim M, Hofbauer HF, Wolinski H, et al. Lipid droplet autophagy in the yeast Saccharomyces cerevisiae. Mol Biol Cell. 2014;25. doi:10.1091/mbc.E13-08-0448

423. Hariri H, Rogers S, Ugrankar R, Liu YL, Feathers JR, Henne WM. Lipid droplet biogenesis is spatially coordinated at ER –vacuole contacts under nutritional stress . EMBO Rep. 2018;19. doi:10.15252/embr.201744815

424. Schütter M, Graef M. Localized de novo phospholipid synthesis drives autophagosome biogenesis. Autophagy. 2020. doi:10.1080/15548627.2020.1725379

425. Lang MJ, Martinez-Marquez JY, Prosser DC, Ganser LR, Buelto D, Wendland B, et al. Glucose starvation inhibits autophagy via vacuolar hydrolysis and induces plasma membrane internalization by down-regulating recycling. Journal of Biological Chemistry. 2014;289. doi:10.1074/jbc.M113.525782

426. Khmelinskii A, Keller PJ, Bartosik A, Meurer M, Barry JD, Mardin BR, et al. Tandem fluorescent protein timers for in vivo analysis of protein dynamics. Nat Biotechnol. 2012;30. doi:10.1038/nbt.2281

427. Khmelinskii A, Blaszczak E, Pantazopoulou M, Fischer B, Omnus DJ, Dez G le, et al. Protein quality control at the inner nuclear membrane. Nature. 2014;516. doi:10.1038/nature14096

428. Kong KYE, Fischer B, Meurer M, Kats I, Li Z, Rühle F, et al. Timer-based proteomic profiling of the ubiquitin-proteasome system reveals a substrate receptor of the GID ubiquitin ligase. Mol Cell. 2021;81. doi:10.1016/j.molcel.2021.04.018

429. Zbieralski K, Wawrzycka D. α-Arrestins and Their Functions: From Yeast to Human Health. Int J Mol Sci. 2022;23. doi:10.3390/IJMS23094988

430. Helle SCJ, Kanfer G, Kolar K, Lang A, Michel AH, Kornmann B. Organization and function of membrane contact sites. Biochimica et Biophysica Acta - Molecular Cell Research. 2013. doi:10.1016/j.bbamcr.2013.01.028

431. Phillips MJ, Voeltz GK. Structure and function of ER membrane contact sites with other organelles. Nature Reviews Molecular Cell Biology. 2016. doi:10.1038/nrm.2015.8

432. Elbaz Y, Schuldiner M. Staying in touch: The molecular era of organelle contact sites. Trends in Biochemical Sciences. 2011. doi:10.1016/j.tibs.2011.08.004

433. Kvam E, Goldfarb DS. Nucleus-vacuole junctions and piecemeal microautophagy of the nucleus in S. cerevisiae. Autophagy. 2007. doi:10.4161/auto.3586

434. Roberts P, Moshitch-Moshkovitz S, Kvam E, O'Toole E, Winey M, Goldfarb DS. Piecemeal microautophagy of nucleus in Saccharomyces cerevisiae. Mol Biol Cell. 2003;14. doi:10.1091/mbc.E02-08-0483

435. Madeira JB, Masuda CA, Maya-Monteiro CM, Matos GS, Montero-Lomelí M, Bozaquel-Morais BL. TORC1 Inhibition Induces Lipid Droplet Replenishment in Yeast. Mol Cell Biol. 2015;35. doi:10.1128/mcb.01314-14

436. Gray J v., Petsko GA, Johnston GC, Ringe D, Singer RA, Werner-Washburne M. "Sleeping Beauty": Quiescence in Saccharomyces cerevisiae . Microbiology and Molecular Biology Reviews. 2004;68. doi:10.1128/mmbr.68.2.187-206.2004

437. Fujimoto T, Ohsaki Y, Cheng J, Suzuki M, Shinohara Y. Lipid droplets: A classic organelle with new outfits. Histochemistry and Cell Biology. 2008. doi:10.1007/s00418-008-0449-0

438. de Virgilio C. The essence of yeast quiescence. FEMS Microbiology Reviews. 2012. doi:10.1111/j.1574-6976.2011.00287.x

439. Sun Y, Martin AC, Drubin DG. Endocytic Internalization in Budding Yeast Requires Coordinated Actin Nucleation and Myosin Motor Activity. Dev Cell. 2006;11. doi:10.1016/j.devcel.2006.05.008

440. Zahn R, Stevenson BJ, Schröder-Köhne S, Zanolari B, Riezman H, Munn AL. End13p/Vps4p is required for efficient transport from early to late endosomes in Saccharomyces cerevisiae. J Cell Sci. 2001;114. doi:10.1242/jcs.114.10.1935